



**National Library
of Canada**

**Bibliothèque nationale
du Canada**

Canadian Theses Service

Service des thèses canadiennes

Ottawa, Canada
K1A 0N4

NOTICE

The quality of this microform is heavily dependent upon the quality of the original thesis submitted for microfilming. Every effort has been made to ensure the highest quality of reproduction possible.

If pages are missing, contact the university which granted the degree.

Some pages may have indistinct print especially if the original pages were typed with a poor typewriter ribbon or if the university sent us an inferior photocopy.

Reproduction in full or in part of this microform is governed by the Canadian Copyright Act, R.S.C. 1970, c. C-30, and subsequent amendments.

AVIS

La qualité de cette microforme dépend grandement de la qualité de la thèse soumise au microfilmage. Nous avons tout fait pour assurer une qualité supérieure de reproduction.

S'il manque des pages, veuillez communiquer avec l'université qui a conféré le grade.

La qualité d'impression de certaines pages peut laisser à désirer, surtout si les pages originales ont été dactylographiées à l'aide d'un ruban usé ou si l'université nous a fait parvenir une photocopie de qualité inférieure.

La reproduction, même partielle, de cette microforme est soumise à la Loi canadienne sur le droit d'auteur, SRC 1970, c. C-30, et ses amendements subséquents.

**DYNAMIC MODELING AND SIMULATION ANALYSIS OF AN AGV
(CONCIC-2 AGV)**

Min Huang

**A THESIS
in the
DEPARTMENT OF MECHANICAL ENGINEERING**

**Presented in Partial Fulfillment of the
Requirement for the Degree of
Master of Engineering at
Concordia University
Montreal, Quebec, CANADA**

April, 1991

© Min Huang, 1991



National Library
of Canada

Bibliothèque nationale
du Canada

Canadian Theses Service Service des thèses canadiennes

Ottawa, Canada
K1A 0N4

The author has granted an irrevocable non-exclusive licence allowing the National Library of Canada to reproduce, loan, distribute or sell copies of his/her thesis by any means and in any form or format, making this thesis available to interested persons.

The author retains ownership of the copyright in his/her thesis. Neither the thesis nor substantial extracts from it may be printed or otherwise reproduced without his/her permission.

L'auteur a accordé une licence irrévocable et non exclusive permettant à la Bibliothèque nationale du Canada de reproduire, prêter, distribuer ou vendre des copies de sa thèse de quelque manière et sous quelque forme que ce soit pour mettre des exemplaires de cette thèse à la disposition des personnes intéressées.

L'auteur conserve la propriété du droit d'auteur qui protège sa thèse. Ni la thèse ni des extraits substantiels de celle-ci ne doivent être imprimés ou autrement reproduits sans son autorisation.

ISBN 0-315-64649-7

Canada

ABSTRACT

DYNAMIC MODELING AND SIMULATION ANALYSIS OF AN AGV (CONCIC-2 AGV)

Min Huang

Dynamic modeling and simulation analysis of CONCIC-2 AGV is presented in this thesis. The complete procedure of modeling the AGV system, and the different possible variation in its construction are discussed. A detailed study of the guidance system and velocity servo control loop together with the effect of these parameters on the AGV performance characteristics is conducted. "Optimal settings" of the tracking controller of CONCIC-2 AGV are proposed. The results of the simulation analysis are validated by the experimental data obtained from the on-board data acquisition facility of the CONCIC-2. The model is implemented in a Silicon Graphics Personal IRIS UNIX work-station, and gives visible realistic simulation results via the animation program.

A general procedure has been developed to formulate the motion equation for various types of wheel configurations. This is included in an appendix. Two specific cases of wheel configurations are discussed in detail.

TO MY PARENTS

ACKNOWLEDGEMENTS

I would like to thank my supervisor, Dr. R.M.H. Cheng, the director of the Center for Industrial Control, Concordia University, for many valuable discussions and advice over the past few years, and for his assistance in the successful completion of my thesis.

My own research has been built on and developed from the previous work of my colleagues in the CONCIC center. Ramesh Rajagopalan and Gilles Huard designed, built, and experimented with CONCIC-2 AGV, and have helped me with many technical aspects. Marian Surpaceanu provided the most important documentation for my thesis. Christine Nadeau and Eleanor Morris contributed much needed administrative assistance. All my friends, Farzam Ranjbaran, Simon Poon, Dinakara Karanth, Suresh Kabra, Mostafa Mehrabi, Mourad El-Mallah, Stuart Cassoff, Michael Ko, Wuxian Wu, and Cao Tuan, in the laboratories and in my office have helped brighten my days at Concordia.

Finally, I am most grateful to my parents, for their encouragement, support and love during all my years as a student. If it were not for them, I would not have been able to pursue the goal of higher education.

This work is supported by the Natural Sciences and Engineering Research Council of Canada in the form of a strategic grant No. STRO032709 awarded to Dr. R.M.H. Cheng.

TABLE OF CONTENTS

	Page
LIST OF FIGURES	x
LIST OF TABLES	xv
NOMENCLATURE	xvi
CHAPTER 1 INTRODUCTION	
1.1 The background	1
1.2 Description of CONCIC-2 and the scope of the thesis	9
CHAPTER 2 MODEL OF CONCIC-2 AGV SYSTEM	
2.1.1 Description	18
2.1.2 Assumptions for the dynamic modeling	22
2.2 A review of vehicle dynamics	24
2.3 Equations of motion for CONCIC-2	29
2.3.1.1 The AGV body	30
2.3.1.2 The forces on the AGV body	32
2.3.2.1 Casters	33
2.3.2.2 The forces on the casters	35
2.4 The equations of motion for the entire AGV	38
CHAPTER 3 FORMULATION OF EXTERNAL FORCES	
3.1 Tractive force	41
3.1.1 Formulation of tractive force	41
3.1.2 Tractive force of CONCIC-2 AGV	43
3.2 Rolling resistance (rolling friction)	45
3.2.1 A metal wheel on a metal rail	46
3.2.2 Rubber tires	48

3.2.3 Pneumatic tires	49
3.2.4 Rolling resistance of CONCIC-2 AGV	53
3.3 Lateral force	55
3.3.1 Side-friction force	56
3.3.2 Cornering force	58
3.3.3 The lateral force of CONCIC-2 AGV	63
3.4 The motion equations of CONCIC-2 AGV system with formulated external forces	66
CHAPTER 4 SERVO CONTROL SYSTEM		
4.1 Introduction	68
4.2 Servo control system of CONCIC-2 AGV	68
4.2.1 General description of LM628	70
4.2.2 Modeling the servo system of CONCIC-2 AGV	71
4.2.2.1 Trajectory Generator	71
4.2.2.2 Model for PID filter	73
4.2.2.3 Model for DAC	75
4.2.2.4 Model for Amplifier	76
4.3 Model for the drive motor	76
CHAPTER 5 GUIDANCE STRATEGY		
5.1 General description	80
5.2 Guidance system of CONCIC-2 AGV	82
5.2.1 The measurement of deviation (image analysis)	83
5.2.2 The guidance controller CONCIC-2 AGV	86

CHAPTER 6 SIMULATION AND ANALYSIS

6.1 Simulation program	90
6.2 The simulation and experiment results	95
6.2.1 Model validation	96
6.2.1.1 Validation of the AGV model		
with servo loops	96
6.2.1.2 Model validation with overall		
control system	99
6.2.2 A study of guidance system	109
6.2.2.1 The optimization of the guidance		
controller	109
6.2.2.2 The effect of the location of		
the camera sensor	123
6.2.2.3 The effect of the location of the		
virtual steering wheel	131
6.2.3 The study of servo control loop	136
6.2.3.1 The stability of the vehicle	136
6.2.3.2 The mismatch of the two		
servo loops	137
6.2.3.3 The acceleration constant a_s		
and the sensitivity of the		
control strategy with different		
initial orientation angle	144
6.2.4 The study of the geometric configuration	146
6.2.4.1 The wheel configuration	149

6.2.4.2 The relationship of the wheel-base and		
the radii of the drive wheel	152
6.2.4 The dynamic response of the casters	152
CHAPTER 7 CONCLUSION	157
REFERENCES	161
APPENDIX A THE GENERAL PROCEDURE FOR THE DEVELOPMENT OF EQUATIONS		
OF MOTION OF AGV WITH VARIOUS CONFIGURATIONS		
A.1 Introduction	166
A.2 Discussion of the initial model	167
A.3 Types of wheels of AGVs	168
A.4 The characteristics of wheels	168
A.5 Formulation of the external forces	172
A.6 Dynamic equation of AGVs	181
A.7 Case study		
A.7.1 Case study 1 -- CONCIC-2 AGV	184
A.7.2 Case study 2 -- Diamond shaped wheel base with		
fore- and -aft driving and steering	192
APPENDIX B THE CHARACTERISTIC OF WHEEL-DRIVE UNIT	217
APPENDIX C CHARACTERISTIC AND LIST OF COMMAND OF LM628.....		226

LIST OF FIGURES

	page
Fig. 1.1 The two basic configurations of AGV	8
Fig. 1.2 The schematic view of CONCIC-1 AGV	11
Fig. 1.3 The summation of major functions of CONCIC-1 AGV	12
Fig. 1.4 The implementation of CONCIC-1 AGV functions	12
Fig. 1.5 The photo of CONCIC-2 AGV	14
Fig. 1.6 The control scheme of CONCIC-2 AGV	15
Fig. 2.1 The physical description of CONCIC-2	19
Fig. 2.2 Load distribution of CONCIC-2 AGV	21
Fig. 2.3 Body-centered system	25
Fig. 2.4 CONCIC-2 AGV with body-centered system and all external forces	31
Fig. 2.5 AGV body subject to all the external forces	31
Fig. 2.6 Caster with body-centered system and external forces	34
Fig. 2.7 Base coordinate system and body-centered system of AGV	40
Fig. 3.1 Model of motor and load system	42
Fig. 3.2 Rolling resistance of a steel wheel [1]	47
Fig. 3.3 Rolling resistance of a pneumatic tire [45]	50
Fig. 3.4 The rolling resistance for conventional bias-ply and radial-ply tires at various speeds [45]	50
Fig. 3.5 Coefficient of rolling resistance at various inflation pressure [45]	52
Fig. 3.6 Coefficient of rolling resistance at various tire diameters [45]	52
Fig. 3.7 The curves for f_o and f_g [45]	54

Fig. 3.8 The cornering force for a pneumatic tire [7]	60
Fig. 3.9 The cornering force for conventional bias-ply and radial-ply tires at various slip angles [45]	60
Fig. 3.10 Cornering force at various normal reactions [45]	61
Fig. 3.11 Cornering force at various inflation pressures [7]	61
Fig. 3.12 Side-friction force on the caster	65
Fig. 4.1 Typical speed control for AGV	69
Fig. 4.2 Servo loop of CONCIC-2 AGV	69
Fig. 4.3 Velocity-profile generator	74
Fig. 4.4 Typical control loop with PID controller	74
Fig. 4.5 DAC-08 calibration curve	77
Fig. 4.6 Servo amplifier gain curve	77
Fig. 4.7 Equivalent circuit of dc motor	78
Fig. 5.1 The image window of the camera	85
Fig. 5.2 The definition of camera length and virtual steering wheel	88
Fig. 6.1 Timing control of the simulation program	91
Fig. 6.2 Flow chart of the simulation program	93
Fig. 6.3 Validation of the velocity servo loops (wheel-1)	98
Fig. 6.4 Validation of the velocity servo loops (wheel-2)	100
Fig. 6.5 Validation of the AGV with different controller gains (P) ...		102
Fig. 6.6 Validation of the AGV with different controller gains (P) ...		102
Fig. 6.7 Validation of the AGV with different controller gains (P) ...		103
Fig. 6.8 Validation of the AGV with different controller gains (P) ...		103

Fig. 6.9 Validation of the AGV with different initial conditions (P)	
(a) transient response	105
(b) velocity response of motor 2	106
(c) velocity response of motor 1	106
Fig. 6.10 Validation of the AGV with different initial conditions (P)	
(a) transient response	107
(b) velocity response of motor 2	108
(c) velocity response of motor 1	108
Fig. 6.11 Validation of the AGV with different velocity (PI)	110
Fig. 6.12 Validation of the AGV with different velocity (PI)	110
Fig. 6.13 Validation of the AGV with different velocity (PI)	111
Fig. 6.14 Validation of the AGV with different velocity (PI)	111
Fig. 6.15 3-D plot of AGV performance versus G_1 and G_2	113
Fig. 6.16 Comparison of AGV performance with various controllers	113
Fig. 6.17 3-D plot of AGV performance versus G_1 and G_2 ($\epsilon_d > 0$; $\epsilon_\theta > 0$; $V_y = 0.9$ m/s)	115
Fig. 6.18 3-D plot of AGV performance versus G_1 and G_2 ($\epsilon_d > 0$; $\epsilon_\theta < 0$; $V_y = 0.9$ m/s)	115
Fig. 6.19 3-D plot of AGV performance versus G_1 and G_2 ($\epsilon_d < 0$; $\epsilon_\theta > 0$; $V_y = 0.9$ m/s)	116
Fig. 6.20 3-D plot of AGV performance versus G_1 and G_2 ($\epsilon_d < 0$; $\epsilon_\theta < 0$; $V_y = 0.9$ m/s)	116
Fig. 6.21 3-D plot of AGV performance versus G_1 and G_2 ($V_y = 0.6$ m/s)	118
Fig. 6.22 3-D plot of AGV performance versus G_1 and G_2 ($V_y = 0.3$ m/s)	118
Fig. 6.23 Comparison of AGV performance with various velocities (PI) .. (experiment)	119
Fig. 6.24 3-D plot of AGV performance versus G_1 and G_2 (circular path; $R = 6$ m; $V_y = 0.6$ m/s)	121
Fig. 6.25 3-D plot of AGV performance versus G_1 and G_2 (circular path; $R = 6$ m; $V_y = 0.9$ m/s)	121
Fig. 6.26 3-D plot of AGV performance versus G_1 and G_2 (circular path; $R = 3.5$ m; $V_y = 0.3$ m/s)	122

Fig. 6.27 3-D plot of AGV performance versus G_1 and G_2 (circular path; $R = 3.5$ m; $V_y = 0.6$ m/s)	122
Fig. 6.28 AGV transient response with camera length = 0.69 m	124
Fig. 6.29 AGV transient response with camera length = 0.99 m	125
Fig. 6.30 AGV transient response with camera length = 1.89 m	126
Fig. 6.31 AGV transient response with camera length = 0.39 m	127
Fig. 6.32 AGV transient response with camera length = 0 m	128
Fig. 6.33 Comparison of AGV transient response with various camera length	130
Fig. 6.34 CONCIC-2 AGV and its equivalent tricycle	132
Fig. 6.35 Transient response of AGV with various equivalent wheel-base ($G_1 = 2.5$; $G_2 = 0.07$)	134
Fig. 6.36 Transient response of AGV with various equivalent wheel-base ($G_1 = 5.5$; $G_2 = 0.07$)	134
Fig. 6.37 Transient response of AGV with various equivalent wheel-bases at optimal controller settings	135
Fig. 6.38 (a) Current response of motor-1 and motor-2	138
Fig. 6.38 (b) Tractive force of the AGV	139
Fig. 6.38 (c) Centripetal force of AGV	139
Fig. 6.39 Mismatched cases of the servo loops (servo amplifiers)	141
Fig. 6.40 Transient response of AGV in perfectly matched and mismatched cases	142
Fig. 6.41 Transient response of AGV in perfectly matched and mismatched cases at optimal controller settings	143
Fig. 6.42 Transient response of AGV with various acceleration ... constants a_a (a - orientation error; b - position offset)	145
Fig. 6.43 Comparison of AGV performance with various acceleration constants a_a (experiment results)	147
Fig. 6.44 Transient response of AGV under 2 different initial orientation angles at a small a_a (0.048 m/s)	148
Fig. 6.45 Transient response of AGV with various wheel-spans	150

Fig. 6.46 Transient response of AGV with various wheel-bases	151
Fig. 6.47 Transient response of AGV with various wheel radii	153
Fig. 6.48 Response of casters (initial angle: front caster= 15° ; rear caster= 0°)	154
Fig. 6.49 Response of casters (initial angle: front caster= 0° ; rear caster= 15°)	154
Fig. 6.50 Performance of AGV with various caster angles -- simulation ..	155
(a - orientation error; b - position offset)	
Fig. 6.51 Performance of AGV with various caster angles	156
(Experiment results)	
Fig. A.1 A body-centered system and a 6 d-o-f rigid body	207
Fig. A.2 Velocity vectors and coordinates of a wheel	208
Fig. A.3 External forces of a drive wheel	209
Fig. A.4 External forces of a steering wheel	210
Fig. A.5 External forces of a steering-drive wheel	211
Fig. A.6 External forces of a caster	212
Fig. A.7 CONCIC-2 AGV	213
Fig. A.8 External forces of CONCIC-2 AGV	214
Fig. A.9 A diamond-shaped AGV in case study 2	215
Fig. A.10 External forces of the Diamond-shaped AGV	216
Fig. B.1 Motor-in-wheel-drive unit (plan view)	218
Fig. B.2 Motor-in-wheel-drive unit (side elevation)	219
Fig. B.3 Motor-in-wheel-drive unit (front elevation)	220
Fig. B.4 The characteristics of the driving motor	221
Fig. B.5 The steering unit	225
Fig. B.6 Steering motor characteristics	225

LIST OF TABLES

		Page
Table 2.1 The mass of the components of the CONCIC-2 AGV	21
Table 3.1 Coefficient of rolling resistance [46]	54
Table 3.2 Static coefficients of friction of tires on road surface (coefficients of tire-road interface friction) [1]	57
Table 3.3 The coefficients of cornering stiffness of tires [1]	62
Table 4.1 Summary of specifications of LM628	72
Table 6.1 The system parameters of CONCIC-2 AGV	97
Table B.1 Parameters of steering motor	225

NOMENCLATURE

a_a : Acceleration constant of velocity-profile generator.

a_{fx}, a_{fy} : Accelerations of front caster along x and y axis.

a_{rx}, a_{ry} : Accelerations of rear caster along x and y axis.

C_α : Lateral stiffness of the tire of driving wheel.

$d_{(f,r)}$: Offset of the casters (for front caster and rear caster).

D: Viscous damping constant of the driving motors.

F_{ij} : External forces of AGV, where $i = 1$ for left driving wheel;

$i = 2$ for right driving wheel;

$i = f$ for front caster;

$i = r$ for rear caster;

$j = t$ for tractive force;

$j = f$ for rolling resistance;

$j = c$ for cornering force;

$j = n$ for side-friction force;

F'_{ij} : Reaction forces from caster

$i = f$ for front caster;

$i = r$ for rear caster;

$j = x$ for the vector along x axis;

$j = y$ for the vector along y axis;

g: acceleration of gravity.

I_x, I_y, I_z : Moment of inertia about x,y,z axis of AGV body.

$I_{(1,2)}$: Current of driving motor (motor 1 and motor 2).

I_f, I_r (or I_c): Polar inertia of front and rear casters
about their pivot axle.

K_{DAC} : Gain of D/A converter.

k_1, k_2 : Coefficient of rolling resistance of driving wheels.

k_{c1}, k_{c2} : Coefficient of rolling resistance of casters.

k_p, k_i, k_d : Proportional, Integration, and Derivative gains for

PID filter of LM628 chip.

k_t : Torque constant of driving motor.

k_n : Side-friction coefficient.

k_c : Cornering force coefficient.

k_r : Coefficient of rolling resistance.

k_e : Voltage constant.

k : Wheel-base of CONCIC-2 AGV.

ℓ : Wheel-span of CONCIC-2 AGV.

m_f, m_r : Mass of the casters.

m_d : Mass of the Wheel-Drive unit.

m_v : Mass of the AGV main frame.

m : Total mass of AGV.

N : Normal reaction.

$N_{d(1,2)}$: Normal reaction at driving wheels (left and right).

N_f, N_r : Normal reaction at front and rear casters.

p : Angular velocity about x axis.

P_{xy}, P_{xz}, P_{yz} : Products of inertia about ox,oy; ox,oz; oy,oz.

q : Angular velocity about y axis.

r : Angular velocity about z axis.

r_d : Radius of driving wheel.

R : Resistance of driving motor.

T_{1f}, T_{2f} : Resistive torque at driving wheels.

T_g : Torque generated by motor.

T_{1m}, T_{2m} : Torque generated by the motor.
 T_{1t}, T_{2t} : Tractive torque at driving wheels.
 u : Linear velocity of P point along x axis within moving reference.
 U : Linear velocity of the origin of moving reference along x axis.
 V_x, V_y : Linear velocity of center of the mass of AGV.
 V_{cy} : Control linear velocity from the guidance strategy.
 v : Linear velocity of P point along y axis with moving reference.
 V : Linear velocity of the origin of the moving reference along y axis.
 V_{in} : Control signal to amplifier.
 V_m : Control voltage to the motor.
 V_1, V_2 : Linear velocities at two wheels.
 V_{fp}, V_{fv} : Velocity vector along and vertical to the principle plane of front caster.
 V_{rp}, V_{rv} : Velocity vector along and veertical to the principle plane of rear caster.
 w : Linear velocity of P point along z axis within moving reference.
 W : Linear velocity of the origin of moving reference along z axis.
 W_d : The weight of AGV main body and two driving wheels.
 x, y, z : the moving reference system.
 $\sum X, \sum Y, \sum Z$: The total external forces along x, y and z axis.
 $\bar{x}, \bar{y}, \bar{z}$: the base reference system.
 α : Sliding angle.
 β_f, β_r : Directional angle of side-friction forces at casters
(Angle between side-friction force and longitudinal axis of AGV).
 δ_f, δ_r : The directional angle of rolling resistance at casters
(Angle between caster's travel and the longitudinal axis of AGV)

n : Gear ratio.

θ_1, θ_2 : The angular displacement of driving wheels.

θ : Angular displacement of AGV yaw motion.

θ_{cs} : Control steering angle calculated by control strategy.

$\Omega_z (\omega_z)$: Angular velocities of the roll motion of AGV.

ω_{cz} : The command angular velocity from the guidance strategy.

CHAPTER 1 INTRODUCTION

1.1 The background

The Automated Guided Vehicles (AGVs) were first introduced in 1950s. According to the definition proposed by Müller in [31], the AGV system embraces all transport systems which are capable of functioning without driver operation. As a result of the continuous development, it was first possible in 1954 to use driverless battery-driven tractors in USA with inductive steering. In the following two decades, the AGV industry has been very successful in Europe and Japan.

Since 60s to the late of 70s approximately 200 AGVs, with total of approximately 1,300 induction-controlled vehicles, have been installed within the Federal Republic of Germany. As well as high shelf storage techniques, considerable development in the automation of internal logistics has been achieved. Most of these vehicles were used for transporting the parts between the assembly lines. Others were installed in the public services, such as post office and airport [31].

According to the *1986 Survey of Automated Guided Vehicle in Japanese Factory*, the first AGV in Japan was developed in 1963 by Daifuku Ltd. in Osaka [43]. Following the above Daifuku AGV, five famous companies were in this field. They were Shinko Electric, Murata Machinery, Nippon Yusoki, Tokyo Unpanki Ltd and Matsuda Kosan. Upto 1986, over 30 companies have worked on the AGV field, and over 15 companies made AGV in commercial base.

Today, after U.S. companies have noticed their successes with AGVs and given this technology another chance, the vehicles are finding uses in assembly and service in addition to material handling. AGVs now come in many

sizes and styles, ranging from large assembly platforms for heavy manufacturing to small experimental vehicles for flexible manufacturing. The largest employer of AGVs are still the automakers. GM's operation in Oshawa, Ontario, houses the world's largest concentration of AGVs. But the vehicle can also be found in electronics manufacturing, the postal service, hospitals, transportation systems, and newspaper publishing. The *Denver Post*, *Los Angeles Times*, and *Newsday*, a New York City metropolitan area daily newspaper, are either using or planning to use AGV systems in their facilities. *Newsday* is also considering installing an AGV system in a future mailroom [8]. AGV systems are growing rapidly because they complement the manufacturing trend towards flexibility. Unlike a conveyor line, an AGV can be sent to any station in the system's route, in any sequence, at any time, though the current generation of driverless transportation still follow mapped routes, they are easily reconfigured to meet changing production needs [46].

AGVs can be standalone or an integral part of a manufacturing system. Originally designed for horizontal transportation of palletized material, the current varieties of vehicle parallels that of industrial robots. Improved load movement is complemented with computer tracking of material. At the sophisticated end of the spectrum, an AGVs closes the traditionally open loop of material tracking on the shop floor. At the unsophisticated end, AGVs replace traditionally labor intensive fork-lift truck or manual movement of material.

Almost all the AGVs have these four characteristics: they are driverless, battery powered, automatically guided, and automatically positioned. Beyond these features, there are substantial variations in the

forms, functions, and controls of automatic guided vehicles. The main description of an AGVs is the vehicle style, and secondarily the control system. Other attributes include the type of guidance employed and the load adaptation [3].

According to the means of guidance implementation, AGVs can be classified as those which follow a continuous guide path, and those guided by a reference other than a continuous guide path. The latter case is sometimes called free ranging AGVs.

At present, The majority of AGVs in use belong to the first class, in which two sub categories can be defined:

- wire guided AGVs
- optically guided AGVs

Being the oldest and more established technology, wired guided AGVs are widely used in industry. Lack of path flexibility and the high cost associated with the wire path installation and maintenance have limited their commercial feasibility. The guide-paths consist of wires embedded in the factory floor. Each carrier has an antenna or coupler that detects the magnetic fields surrounding the guide wires which are energized at low voltages. The antenna generates an output signal corresponding to its location within the guide-path's magnetic field. To keep the antenna (and thus the vehicle) centered over the path, a control system on the carrier reads antenna signal strength and adjust the vehicle's steering mechanism to maintain a constant signal. There is a physical limitation to the magnetic field so generated fundamentally because of the inverse-square law. Consequently there is a physical lower limit to the deviation between the vehicle and the wire, therefore a lower limit to the highest speed

attainable by the type of guidance.

Optically guided AGVs follow lines on the floor, which can be painted or taped in order to define the path. Different ways of implementing optical guidance have been developed, such as camera vision guidance and photosensors based control.

In the photosensor based control, a photosensor tracks a fluorescent line on the floor. The AGV carries an ultra-violet light emitter to energize the guidance path that is previously prepared on the floor. This type of implementation suffers from the similar limitation as the magnetic coupler in the wire guidance in its limited path tolerance. AGVs of this type are more popular as slow-moving (less than 0.5 m/s) inter-office mail delivery carts.

Also in this category, camera vision guidance has more flexibility and higher speed using the technology of microprocessor (the highest speed can be more than 1 m/s). In these case, the path to be followed is prepared by taping or painting, the typical sensors may take the form of CDD cameras and 'cameras' employing light sensitive DRAMs (dynamic random access memory chip), etc. An on-board computer samples the deviation of the AGV related to the path sensed by the sensors, and steers the vehicle as to reduce the deviation. The main advantage of this guidance technique over wire guidance is that paths can be installed quickly and are easily alterable requiring less overhead. Another characteristic which distinguished optical guidance from wire guidance is the complexity of information that can be offered by the path. While a wire-track carries an AC signal or a fluorescent path which only defines the position of the path, an optical track can also provide additional information encoded in visual cues which can be

interpreted via appropriate software.

The study of free-ranging AGVs has been growing rapidly from early 80s. They are still poorly represented in the industry because of their low position accuracy and/or complex sensing and large data processing. Free-ranging AGVs use one or more of the following guidance techniques:

Dead-reckoning

The vehicle in this category calculates the position by keeping track of the rotational displacement and by referring to the initial position and orientation.

Reference Beacons

The vehicle travels within a field of operation which is defined by a network of reference beacons. As the vehicle moves it utilize a sensor to detect the location with respect to the beacons.

Dynamic optical targeting

The AGV emits a scanning optical beam, which is bounced back from an identifiable reflector. This is used in a triangulation process by which the relative position of the vehicle is determined.

Inertial navigation

The AGV uses gyroscope technology in order to navigate a predetermined path. This consists of setting up the gyroscope to detect the accelerations (linear and angular). The accelerations are used to compute the heading position of the AGV. Then the deviation is corrected by a servo mechanism. Because of the speed and acceleration limit of AGVs, the noise to the signal, as well as the high cost of the gyroscope make it difficult to be used in practice.

Mapping by camera vision or ultrasonic means

This technique consists of generating a reference map of the surroundings in which the position of the vehicle is known. The vehicle periodically generates an updated map of its surroundings, by using a camera or an ultrasonic device to delineate various objects and obstacles. These are compared with the reference map to estimate the position of the vehicle. Techniques using imaging of the surroundings suffer from complex and time consuming analysis which limits the speed of the vehicle. Also this type of system is often limited by the need for a easily analyzed environment.

In the above methods, the dead-reckoning is easiest to implement, but a slippage of the drive wheel or any random disturbance may lead to a cumulative position error.

The principle of the navigation is always an automated steering back on course based on the current position and the reference path (off-board physical path or memorized path and dynamic generated path). Thus, it becomes important to understand the dynamic effects of various design parameters on the steering action. Besides the means of guidance which are discussed above, there are other two critical parameters affecting the steering action of a AGV:

- Wheel configuration of AGVs
- Control strategy

In the early days, many AGVs were derived from industry trucks by adding sensor and controls. Now AGVs have been designed and built in factories and research laboratories with different type and different size in order to meet the application purposes. Propulsion and steering configurations for AGVs may be broadly categorized into two classes,

steer-drive and drive-drive or differential driving steering [33]. Steer-drive system rely on steering one or more of the wheels, which may or may not also function as drive wheels. The rotational speed of the driving motor is independent of the steering action. Drive-drive systems rely on the differential velocity of the two motorized wheels to provide steering. Typical examples of these are illustrated in Fig. 1.1. Fig. 1.1a presents a tricycle configuration, it can be found in [33] [28] [13] [18]. And Fig. 1.1b shows a differential configuration, the AGVs which are presented in [34] [21] [6] belong to this category. Sometimes variations on the geometry are made to meet certain application purposes, such as putting more casters in order to have better support of the vehicle or having the two driving wheels at back and two casters at the front in the case of drive-drive [17].

For industrial applications, the ability of the vehicle to turn in a small radius is an asset since this requires less turning area. With steer-drive configuration, the geometry of the vehicle poses a limit on the minimum radius of turning. It is not so with drive-drive configuration where the vehicle can turn on a spot literally.

The control strategies may be classified into two categories according to the two major classes of guidance methods. For free-ranging AGVs, the control strategy is usually made of two parts. One of them is the part called path planning. In the case of mapping by camera vision or ultrasonic means, the path planning part generates the reference map and decides the next destination. For the other cases in free-ranging AGVs, such as dead reckoning, dynamic optical targeting, and inertial navigation, this part of the control strategy calculates the current position of the vehicle using the message from the sensor. The path planning needs a computer system with

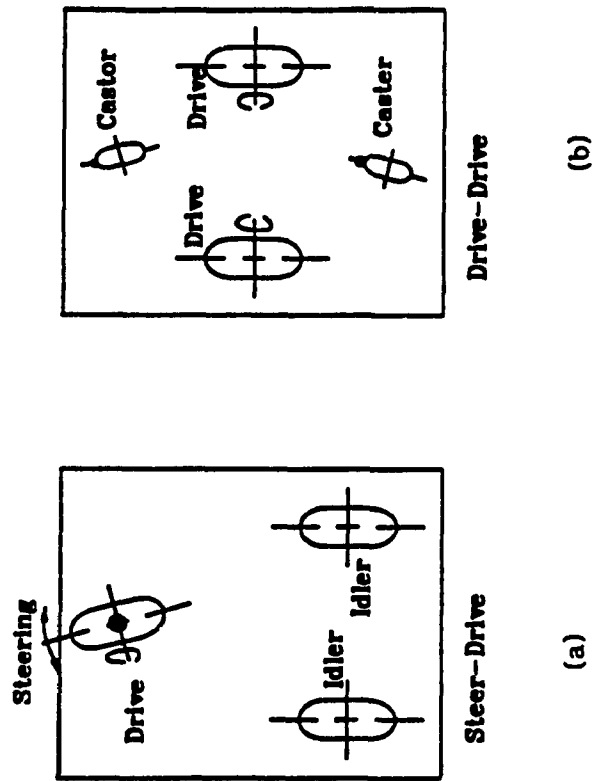


Fig. 1.1 The two basic configurations of AGV

a high computation speed, and it limits the highest speed of the AGVs. The another part of the control strategy of free-ranging AGVs is the guidance controller. In this case, the guidance controller steers the vehicle from the current position towards the destination or the target. Since the free-ranging guidance always has a destination point, the control is sometimes called destination-control. This type of control strategy are experienced in [34], [18], [23], [22], [18], [33]. For these AGVs which are guided by the continuous path, the control strategy only has the guidance controller. Since the sensor provides the deviation between the current position and the reference path, the guidance controller tries to eliminate the deviation. This type control is also called tracking regulation.

Many AGVs have been developed in the past 40 years. Some of them have been implemented in the real application, especially the wire-guided AGVs. Others are still in the research laboratory. These AGVs are built in different size, using different means guidance, and with different configurations. But little has been done on the investigation of the dynamics of this kind of system. In this thesis, a procedure is proposed for modeling the entire AGV system. And a intensive study on its dynamics, its guidance system, and its servo control are presented.

1.2 Description of CONCIC-2 AGV and the scope of the paper

In 1985, the Center for Industry Control within the Department of Mechanical Engineering, Concordia University developed the first AGV named CONCIC-1. The CONCIC-1 is a light-duty, high-speed AGV which is guided by camera vision and follows a floor guide path. It can be used as an automatic tractor or a unit load transporter. A schematic view of the

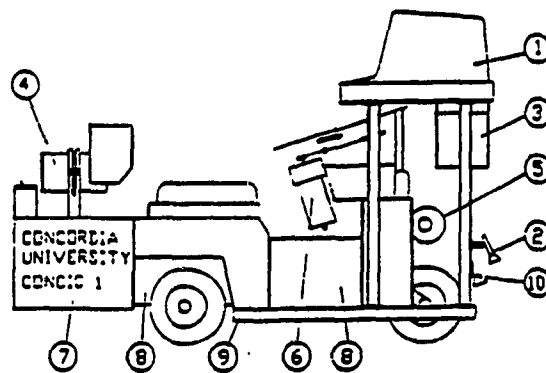
vehicle is shown in Fig. 1.2. The CONCIC-1 has a triangular wheel-base configuration with one drive-steer wheel in the front, and two caster wheels at the back. The major functions of the vehicle are summed up in Fig. 1.3.

- System Management involves user interface implementation.
Analysis and evaluation of the functional parameters and operations governing the system. logi
- Sensing insures guiding path perception, feedback signals acquisition and obstacle detection.
- Motion control guides the vehicle motion with a space time frame.
- Data Acquisition is an optional function used for experimental and research purposes.

These functions have been implemented as shown in Fig. 1.4 [3]. The controller has been designed and built as a modular structure comprising three microprocessors. These execute specific operations such as motion control or analysis of the guide path image. The use of a specialized processor working in parallel greatly improves the overall efficiency of the controller.

CONCIC-1 AGV worked well in various types of paths. But the tricycle mechanical configuration limits the turning radius so that the tracking at the corner of the path or the intersection becomes very difficult and more complex. The operation system which was written in the assembly language is not 'friendly', it is not easy to modify and study.

The Center of Industrial Control designed and built a second AGV called CONCIC-2 in 1988. This vehicle has a very flexible mechanical design which can develop a series of working prototypes of AGVs for the purpose of



1. Operator console: a Z-80 based, Northstar Advantage microcomputer which acts both as central controller and as operator interface.
2. Digital camera: a Micron Eye optic-ram camera which senses the optical guiding path.
3. Vision Subsystem Controller: a custom built image processor unit which contains the hardware necessary for camera interface, image analysis and communication with the central computer.
4. Vehicle Motion Controller: contains nine, wire-wrapped electronic component cards with one microprocessor, logic circuits, power supplies, and intermediate power stages, that implement motion control and other functions.
5. Drive mechanism: made up of a 0.6 HP DC motor which is engaged to the drive wheel via a belt and chain transmission.
6. Steering mechanism: made up of a 0.1 HP DC gearmotor which drives the steering axis via a chain drive.
7. Power circuitry: contains all the hardware for the drive switching power supply amplification stage, the steering motor linear amplifier and power distribution.
8. Power pack: made up of four 6V lead-acid industrial batteries connected in series.
9. Chassis.
10. Lights: a pair of flood light bulbs (rated @ 20 watts each).

Fig. 1.2 The schematic view of CONCIC-1 AGV

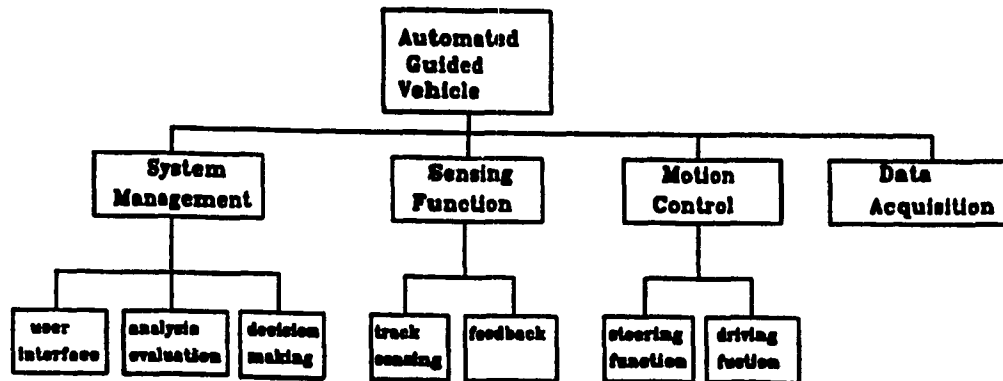


Fig. 1.3 The summation of major functions of CONCIC-1 AGV

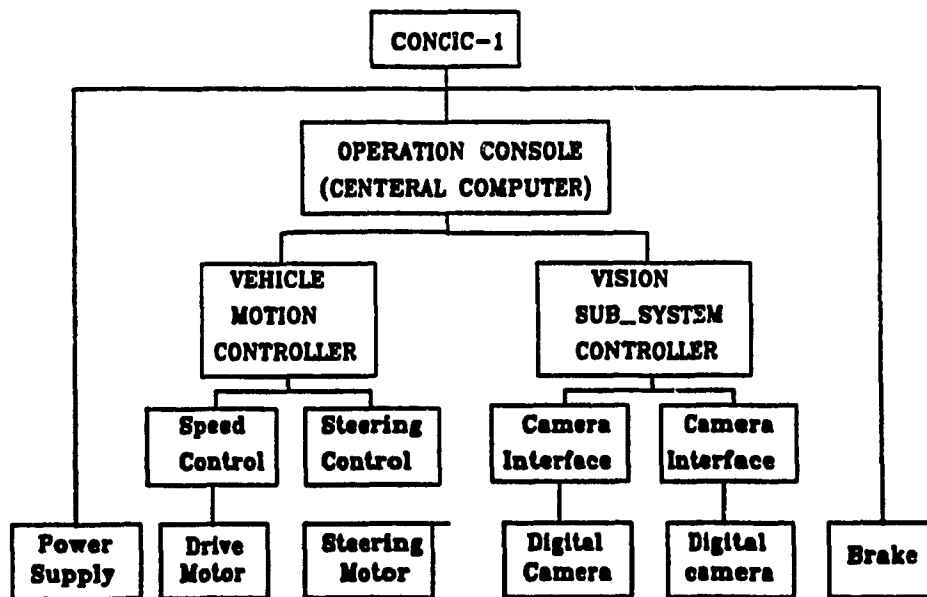


Fig. 1.4 The implementation of CONCIC-1 AGV functions

meeting different industrial needs by easy relocation of the wheel components. This flexible mechanical structure is also very useful for intensive investigation of the dynamic performance of AGVs for different wheel configurations.

The photograph in Fig. 1.5 shows the latest development. It features a chassis fabricated from aluminum tubing, to which are mounted two motorized wheel sets at mid-length, and casters in the fore-and-aft position. An on-board microcomputer unit serves as the main controller. Each motorized wheel is controlled by a velocity servo loop, and the loop is built with a LM628 servo controller, a DAC, and an amplifier. An optical camera is mounted at the front end of the vehicle, which is used to recognize the location of a taped track on the ground as well as a set of road junctions. There are additional features of interest, such as the ultrasonic sensors to detect obstacles, and a wireless device to communicate with the control station.

The control scheme of CONCIC-2 is shown in Fig. 1.6, the detail description is given in chapter 2.

This thesis presents a procedure of modeling an entire AGV system. The model consists the vehicle dynamics, and all the components in the servo control loop and the guidance system. It has a realistic structure as the real system, and presents the behavior of the system accurately. This model does not only demonstrates the dynamic behavior of the vehicle under different control parameters and wheel configurations, it also produces all the detailed information of the system during the operation. For example, the external forces, the motor currents and voltages, the final or midway control signal of the system. This information provides an efficient way of



Fig. 1.5 The photo of CONCIC-2 AGV

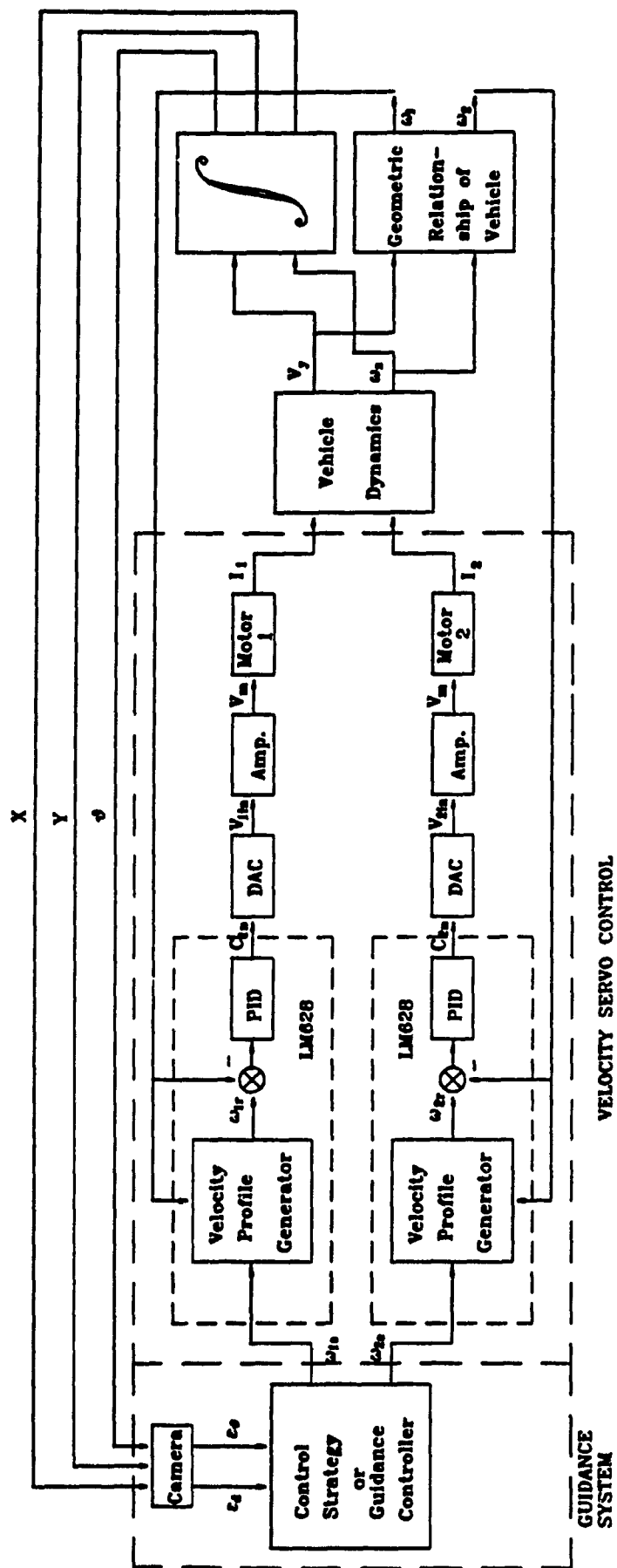


Fig. 1.6 The control scheme of CONCIC-2 AGV

designing and studying an AGV system since the model has been validated by the real system. An intensive study on some design operation variables is also presented in the thesis, such as the optimization of the controller, the location of the camera sensor, the location of the virtual steering wheel, and the acceleration constant of the LM628 chip. In the simulation program, a complex system is modeled in many blocks according to their physical function, it is easily alternated to become a new model of a new designed system.

The thesis is organized as follows.

Chapters 1 to 5 deal with the background of the AGV technology and modeling of CONCIC-2 AGV under the current configurations. In chapter 2 a review of vehicle dynamics is given, and the motion equation of the AGV is developed by applying the same method. Chapter 3 presents a study of external forces. Chapter 4 and chapter 5 give the model of the servo control loop and the guidance system respectively.

Chapter 6 presents the simulation and analysis of the results. The simulation has been carried out in the Personal IRIS UNIX work-station using "C" programming language, and the flowchart of the program is given. The study of the AGV with the simulation has been applied to different design and operation variables. The validation of the model is first done with only the servo loops, then with the completed control of the AGV. Using this realistic model, the study of the guidance controller, the location of the camera sensor, the location of the virtual steering wheel, together with the study of the servo loops and wheel configuration have been presented. An animation program makes it possible to have a visible performance of AGV simulation. The conclusion of the thesis is given in chapter 7.

Appendix A presents a generalized way to develop the motion equation of an AGV of different wheel configurations. The vehicle system is considered to have three degrees of freedom (forward, yaw and roll). Two applications of this generalized procedure are presented.

2.1.1 Description

The Center for Industrial Control of Concordia University has developed a series of working prototypes of AGVs for the purpose of meeting different industrial needs, and also for intensive investigation of the steady state and dynamic performance of AGVs of different mechanical, and control parameters.

The details of the physical description of the latest development -- CONCIC-2 AGV is given in Fig. 2.1. CONCIC-2 AGV has a rectangular prism body equipped with an autonomous system, including batteries, two motorized wheels, two casters, main controller (computer), optical camera sensor and servo system. The two casters locate in the front and rear to provide support of the weight of the vehicle and lead the direction. The caster has a molded rubber tire. The offset between the contact patch with the floor and the pivot point provide a moment to rotate the caster, and the bearing on the caster at the pivot point allows it to rotate freely. Two integral driving units are employed in CONCIC-2 AGV to power the two motorized wheels at the sides. These units are known as the motor-in-wheel-drive units (or simply called as motor-wheel unit). Each unit has a dc motor, a hardened rubber wheel, and a speed reduction gear arrangement with a gear ratio of 9.9:1. It also has a steering motor with speed reducer, and the gear ratio for the steering motor is 62.7:1. Each of the motorized wheel is controlled by a servo velocity control loop. The loop consists a LM628 chip, a DAC, and an amplifiers. The vehicle is steered by running the two motorized wheels at different speeds. The tracking control of the AGV is taken care of

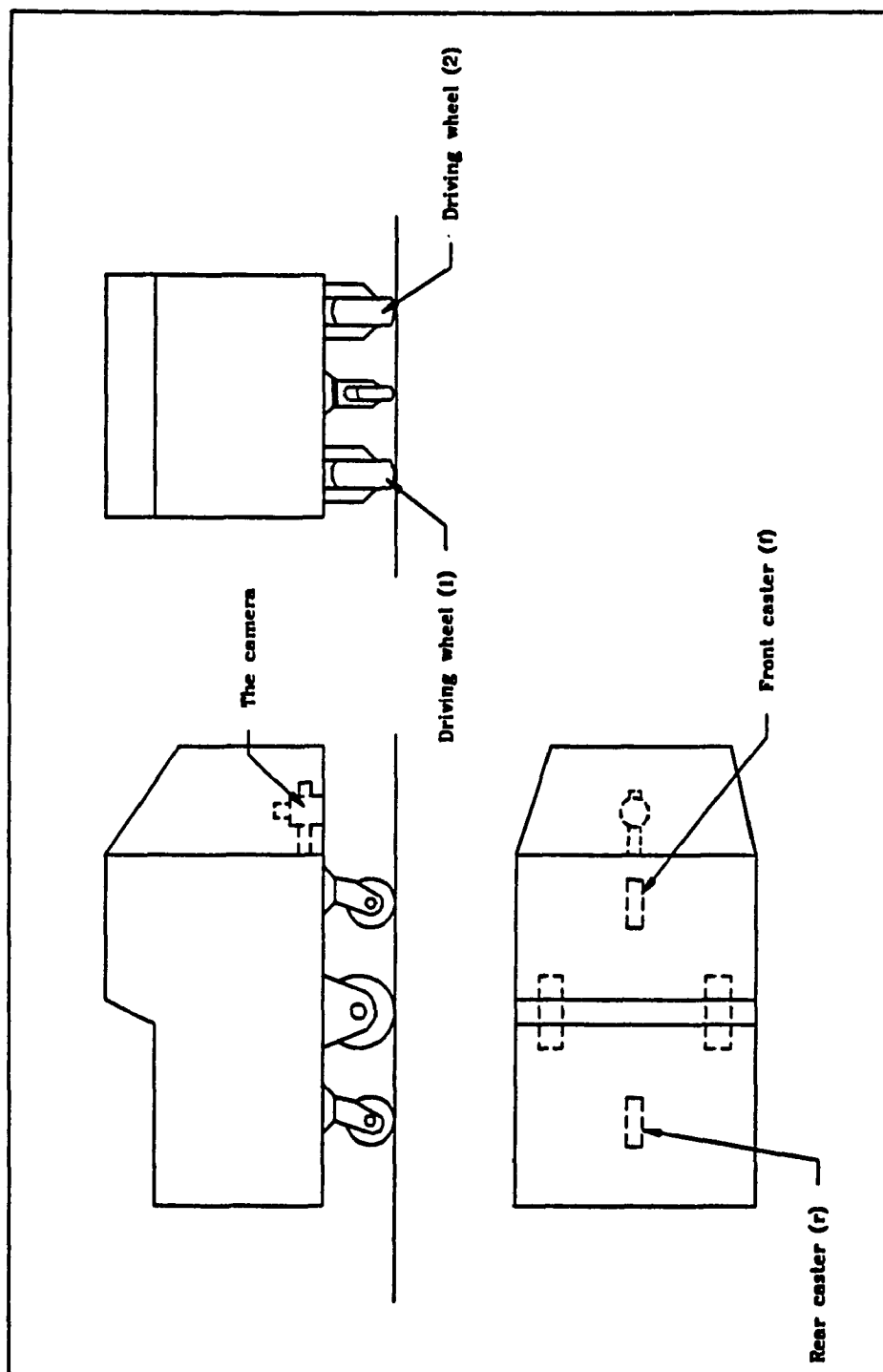


Fig. 2.1 The physical description of CONVIC-2

by the main controller (12Hz 80286 AT compatible) with the implementation of camera vision technique. The track to be followed by CONCIC-2 AGV is prepared on the floor by taping or painting. A IDETIX digitizing camera is used in CONCIC-2 AGV as the navigation sensor to detect the AGV's position related to the guided path. The 'camera' employs a IS32 optic Ram developed by Micron Technology, and has the ability to sense the image and translate into digital signals. The IS32 optic Ram consists of 65,536 light sensitive elements arranged into two arrays of 128 rows and 256 columns. When the reflected light from an object falls on a particular element, a capacitor which is connected to that element is discharged to zero volts. These capacitors are precharged to 5 Volts before the elements are exposed to light. The capacitors which have zero-charge are white pixels and are regarded to have logic 0. On the other hand, the non-discharged capacitors are black pixels with a logic value of 1. A controller board comes with the 'camera' communicates with the 8088, 80286 or 80386 processor. Pixel information is transferred from the controller to the PC memory using the Direct Memory Access (DMA). The image received from the pixels is about 30 m deep and 128 mm wide for CONCIC-2 Vehicle. The path width is 30 mm and this corresponds to 30 pixels approximately in the image window. The on-board computer samples the deviation of the vehicle relative to the path by this image, and steers the vehicle so as to reduce the deviation (position and orientation).

Fig. 2.2 shows the load distribution of CONCIC-2 AGV. The mass of each components is listed in Table 2.1. The components are arranged so that the mass-center is situated very closely to the geometrical center of the vehicle. In this case, the normal force endured by the four wheels are

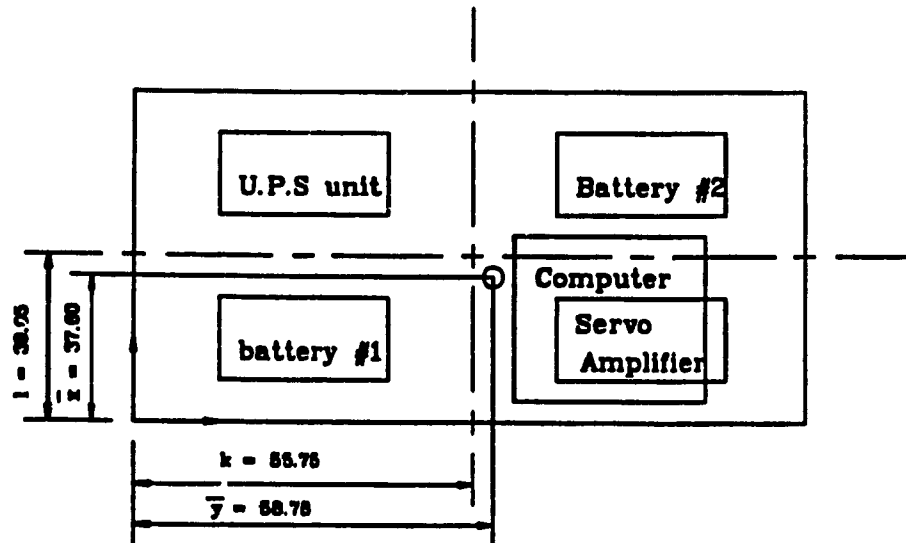


Fig. 2.2 Load distribution of CONCIC-2 AGV

Item	Quantity	Mass (kg)
Lower level frame	1	14.0
Upper level frame	1	5.4
Batteries with the holders	2	57.5
Wheel-drive units	2	16.0
Caster	2	2.7
Wheel mounting brackets	2	5.4
Computer	1	14.8
Servo-amplifiers	2	1.8
UPS-power supply	1	6.8
Total mass		124.4

Table 2.1 The mass of the components of the CONCIC-2 AGV

assumed to be identical. The normal reaction at the wheels and floor is calculated by

$$N_i = \frac{\text{weight of the vehicle body}}{4} + \text{Weight of the wheel (i)}$$

where the subscript i presents the location of the wheels:

$i = 1$ for the left motorized wheel;

$i = 2$ for the right motorized wheel;

$i = f$ for the front caster;

$i = r$ for the rear caster.

At this stage of development, CONCIC-2 is designed to work indoors in a typical manufacturing environment. Most of the time, the working surface is good enough to prevent side slip or longitudinal slip at the wheels. In another words, there exists enough friction between the wheels and the ground to prevent the vehicle from sliding. At the current configuration, CONCIC-2 AGV can be operated at the linear speed as high as 1.2 m/s.

2.1.2 Assumption for the dynamic modeling

To develop the motion equations of the system, CONCIC-2 AGV is considered as a collection of 3 interconnected rigid bodies. i.e. the AGV body (plus the two motorized wheels which are rigidly mounted to it) and the two casters. When the floor is assumed to be perfectly flat, and also can provide enough friction to prevent the longitudinal and side slip at the wheels, the AGV body can be considered as a rigid body with two degrees of freedom -- the forward translation and the yaw rotation. The casters have one more degree of freedom since it can rotate freely about the pivot axis.

For each of the rigid bodies, resistance (friction) forces act at the contact patch between this rigid body and the floor, and reaction forces

between adjacent rigid bodies. In the case of motorized wheel, the tractive force also exists between the wheel and the floor. The resistance (friction) is dependent on the characteristics of the tires and the condition of the floor. The reaction forces are the links between the rigid bodies. And the tractive forces are dependent on the characteristics of the motor in the motorized wheel. A detailed discussion of these forces will be given in Chapter 3.

From the above discussion and from section 2.1, the assumptions for developing the dynamic model of CONCIC-2 AGV system are made as follows:

- the vehicle body is considered to be a two degrees of freedom system,
- the vehicle has a symmetrical structure about the vehicle for-and-after plane,
- the location of the center of the mass coincides with the geometrical center of the vehicle,
- the weight support of the vehicle is equally distributed to all the wheels and casters,
- the wheels and casters roll without longitudinal or side slip,
- the casters take about 1% of the total mass, therefore their mass is considered negligible,
- the image window is assumed to have no limit in simulation,
- there is assumed to be no friction in the bearings of the casters,
- two casters are considered to have the same characteristics,
- the two motor-wheel units and their servo systems are considered to be identical.

2.2 A review of vehicle dynamics

Fig. 2.3 represents a body-centered system XYZ of a rigid body. Consider a typical point P(x, y, z) within the system moving with linear velocities u, v, w, in the X, Y, Z direction respectively. Let U, V, W be the instantaneous velocities of the origin in direction X, Y, Z and p, q, r be the rotational velocities about X, Y, Z. The direction of the angular velocities are defined by the right-hand rule.

The velocities of the point P can be presented as follows [7]:

$$\begin{aligned} u &= U - r \cdot y + q \cdot z \\ v &= V - p \cdot z + r \cdot x \\ w &= W - q \cdot x + p \cdot y \end{aligned} \quad (2.1)$$

Differentiating equations (2.1) with time, the acceleration \dot{u} , \dot{v} , and \dot{w} are :

$$\begin{aligned} \dot{u} &= \frac{du}{dt} = \dot{U} - \dot{r} \cdot y - r \cdot \dot{y} + \dot{q} \cdot z + q \cdot \dot{z} \\ \dot{v} &= \frac{dv}{dt} = \dot{V} - \dot{p} \cdot z - p \cdot \dot{z} + \dot{r} \cdot x + r \cdot \dot{x} \\ \dot{w} &= \frac{dw}{dt} = \dot{W} - \dot{q} \cdot x - q \cdot \dot{x} + \dot{p} \cdot y + p \cdot \dot{y} \end{aligned} \quad (2.2)$$

Substituting equations (2.2) with $\dot{x} = u$, $\dot{y} = v$, $\dot{z} = w$,

$$\begin{aligned} \dot{u} &= \dot{U} - \dot{r} \cdot y - r \cdot v + \dot{q} \cdot z + q \cdot w \\ \dot{v} &= \dot{V} - \dot{p} \cdot z - p \cdot w + \dot{r} \cdot x + r \cdot u \\ \dot{w} &= \dot{W} - \dot{q} \cdot x - q \cdot u + \dot{p} \cdot y + p \cdot v \end{aligned} \quad (2.3)$$

Replacing u, v, w in the equation of \dot{u} by equations (2.1):

$$\begin{aligned} \dot{u} &= \dot{U} - r \cdot (V - p \cdot z + r \cdot x) - \dot{r} \cdot y + q \cdot (W - q \cdot x + p \cdot y) + \dot{q} \cdot z \\ &= \dot{U} - r \cdot V + q \cdot W + r \cdot p \cdot z - r^2 \cdot x - \dot{r} \cdot y - q^2 \cdot x + p \cdot q \cdot y + \dot{q} \cdot z \\ &= \dot{U} - r \cdot V + q \cdot W - (r^2 + q^2) \cdot x + (p \cdot q - \dot{r}) \cdot y + (r \cdot p + \dot{q}) \cdot z \end{aligned} \quad (2.4)$$

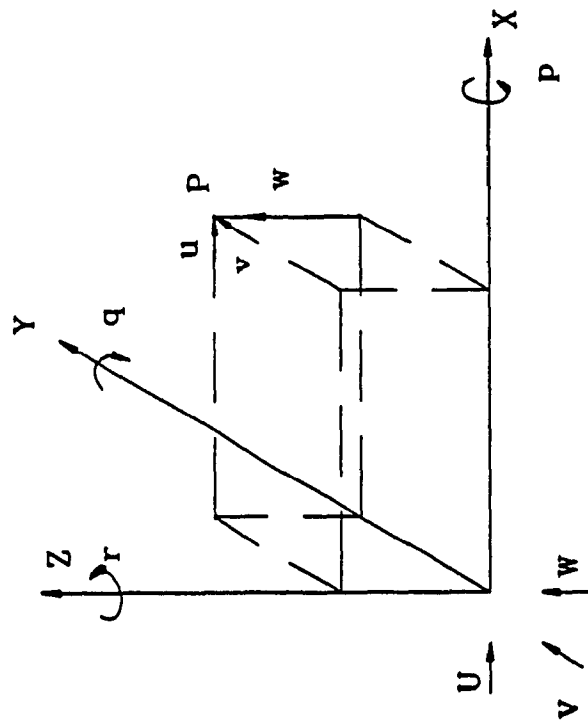


Fig. 2.3 Body-centered system

Hence equations (2.3) can be shown to be as follows:

$$\begin{aligned}\dot{u} &= \dot{U} - r \cdot V + q \cdot W - (q + r) \cdot x + (q \cdot p - r) \cdot y + (r \cdot p + q) \cdot z \\ \dot{v} &= \dot{V} - p \cdot W + r \cdot U - (p^2 + r^2) \cdot y + (r \cdot q - \dot{p}) \cdot z + (p \cdot q + \dot{r}) \cdot x \\ \dot{w} &= \dot{W} - q \cdot U + p \cdot V - (p^2 + q^2) \cdot z + (p \cdot r - \dot{q}) \cdot x + (q \cdot r + \dot{p}) \cdot y\end{aligned}\quad (2.5)$$

Equations (2.5) defines the accelerations of the point P(x,y,z) in a rigid body in terms of the accelerations and velocities of the origin of the body-centered system. Applying D'Alembert's principle, the equations of motion of the rigid body are:

$$\begin{aligned}\sum \delta m \dot{u} &= \sum X, \quad \text{the total external force in X direction.} \\ \sum \delta m \dot{v} &= \sum Y, \quad \text{the total external force in Y direction.} \\ \sum \delta m \dot{w} &= \sum Z, \quad \text{the total external force in Z direction.} \\ \sum \delta m (y \cdot \dot{w} - z \cdot \dot{v}) &= \sum L, \quad \text{the total external moment about x axis.} \\ \sum \delta m (z \cdot \dot{u} - x \cdot \dot{w}) &= \sum M, \quad \text{the total external moment about y axis.} \\ \sum \delta m (x \cdot \dot{v} - y \cdot \dot{u}) &= \sum N, \quad \text{the total external moment about z axis.}\end{aligned}\quad (2.6)$$

The moments and products of the inertia of rigid body are defined as

$$\begin{aligned}I_x &= \sum [\delta m (y^2 + z^2)] = \text{moment of inertia about OX} \\ I_y &= \sum [\delta m (x^2 + z^2)] = \text{moment of inertia about OY} \\ I_z &= \sum [\delta m (y^2 + x^2)] = \text{moment of inertia about OZ} \\ P_{yz} &= \sum (\delta m yz) = \text{product of inertia about OY and OZ} \\ P_{xz} &= \sum (\delta m xz) = \text{product of inertia about OY and OZ} \\ P_{xy} &= \sum (\delta m xy) = \text{product of inertia about OX and OY}\end{aligned}\quad (2.7)$$

If the origin of the body-centered system is defined to be at the center of the body, then

$$\sum(\delta mx) = \sum(\delta my) = \sum(\delta mz) = 0 \quad (2.8)$$

Substituting the equation of $\sum M$ in equations (2.6) by (2.5):

$$\begin{aligned} \sum M &= \sum[\delta m(z \cdot \dot{u} - x \cdot \dot{w})] \\ \sum M &= \sum \left[\delta m(z \cdot [\dot{U} - r \cdot V + q \cdot W - (q^2 + r^2) \cdot x + (q \cdot p - \dot{r}) \cdot y + \right. \\ &\quad \left. (r \cdot p + \dot{q}) \cdot z] - x \cdot [\dot{W} - q \cdot U + p \cdot V - (p^2 + q^2) \cdot z + \right. \\ &\quad \left. (p \cdot r - \dot{q}) \cdot x + (q \cdot r + \dot{p}) \cdot y] \right) \Big] \\ \sum M &= \sum(\delta mz) \cdot \dot{U} - \sum(\delta mz) \cdot r \cdot V - \sum(\delta mz) \cdot q \cdot W - (q^2 + r^2) \sum(\delta mxz) + \\ &\quad (q \cdot p - \dot{r}) \sum(\delta mzy) + (r \cdot p + \dot{q}) \sum(\delta mz^2) - \sum(\delta mx) \cdot \dot{W} + \sum(\delta mx) \cdot q \cdot U - \\ &\quad \sum(\delta mx) \cdot p \cdot V + (p^2 + q^2) \sum(\delta mxz) - (p \cdot r - \dot{q}) \sum(\delta mx^2) - \\ &\quad (q \cdot r + \dot{p}) \sum(\delta mxy) \end{aligned}$$

Collecting the terms in (2.7), and using equation (2.8), the external moment of a rigid body about Y axis $\sum M$ with a body-centered system located at its mass center can be written as:

$$\begin{aligned} \sum M &= - (q^2 + r^2) P_{xz} + (q \cdot p - r) P_{zy} + (r \cdot p + q) \sum(\delta mz^2) + \\ &\quad (p^2 + q^2) P_{xz} - (p \cdot r - q) \sum(\delta mx^2) - (q \cdot r - p) P_{xy} \end{aligned}$$

Thus

$$\sum M = I_y \dot{q} - (I_z - I_x) p \cdot r + (p^2 - r^2) P_{xz} - (q \cdot r + \dot{p}) I_{xy} + (q \cdot p - \dot{r}) P_{zy} \quad (2.9)$$

By following the same procedure, all the external forces and moments of a rigid body with a body-centered system located at its mass center can be obtained as:

$$\begin{aligned}
\Sigma X &= m(\dot{U} - r \cdot V + q \cdot W) \\
\Sigma Y &= m(\dot{V} - p \cdot W + r \cdot U) \\
\Sigma Z &= m(\dot{W} - q \cdot U + p \cdot V) \\
\Sigma L &= I_x \dot{p} - (I_y - I_z)q \cdot r + (r^2 - q^2)P_{yz} - (p \cdot q + \dot{r})P_{xz} + (p \cdot r - \dot{q})P_{xy} \\
\Sigma M &= I_y \dot{q} - (I_z - I_x)p \cdot r + (p^2 - r^2)P_{xz} - (q \cdot r + \dot{p})P_{xy} + (q \cdot p - \dot{r})P_{zy} \\
\Sigma N &= I_z \dot{r} - (I_x - I_y)q \cdot p + (q^2 - p^2)P_{xy} - (r \cdot p + \dot{q})P_{yz} + (r \cdot q - \dot{p})P_{xz}
\end{aligned} \tag{2.10}$$

When there is no overhead in the z axis, $W = \dot{W} = 0$. Equation (2.10) becomes:

$$\begin{aligned}
\Sigma X &= m(\dot{U} - r \cdot V) \\
\Sigma Y &= m(\dot{V} + r \cdot U) \\
\Sigma L &= I_x \dot{p} - (I_y - I_z)q \cdot r + (r^2 - q^2)P_{yz} - (p \cdot q + \dot{r})P_{xz} + (p \cdot r - \dot{q})P_{xy} \\
\Sigma M &= I_y \dot{q} - (I_z - I_x)p \cdot r + (p^2 - r^2)P_{xz} - (q \cdot r + \dot{p})P_{xy} + (q \cdot p - \dot{r})P_{zy} \\
\Sigma N &= I_z \dot{r} - (I_x - I_y)q \cdot p + (q^2 - p^2)P_{xy} - (r \cdot p + \dot{q})P_{yz} + (r \cdot q - \dot{p})P_{xz}
\end{aligned} \tag{2.11}$$

Furthermore, for a 3 d-o-f rigid body moving along x, y, and rotating about z, then the moments about x, and y axis are also considered to be balanced. Correspondingly $p = \dot{p} = 0$, $q = \dot{q} = 0$. The motion equations are:

$$\begin{aligned}
\Sigma X &= m(\dot{U} - r \cdot V) \\
\Sigma Y &= m(\dot{V} + r \cdot U) \\
\Sigma N &= I_z \dot{r}
\end{aligned} \tag{2.12}$$

Similarly for a 2 d-o-f rigid body moving along y and rotating about z, then $U = \dot{U} = 0$. From equations (2.12), the equation for 2 d-o-f are:

$$\begin{aligned}
\Sigma Y &= m \cdot \dot{V} \\
\Sigma N &= I_z \cdot \dot{r}
\end{aligned} \tag{2.13}$$

2.3 Equations of Motion for CONCIC-2

The CONCIC-2 AGV is a 2 d-o-f interconnected rigid body system. The equations of motion are derived by applying the vehicle dynamics in section 2.2 to the three independent rigid bodies, the AGV body with two motorized wheels mounted on it rigidly, and two casters which can rotate freely about the pivot axis. For the convenience, the following definitions are used in the later discussion. Main body of the vehicle is defined as the AGV without the four wheels. AGV body is referred to the main body of the vehicle with two motorized wheels.

Fig. 2.4 presents the entire AGV subject to all the external forces. These forces act at the contact patch of the two motorized wheels and the two casters. The forces can be classified in three categories:

- friction forces including rolling resistance and lateral forces;
- tractive forces;
- normal reaction forces.

The notation for the first two categories is F_{ij} , where the first subscript i stands for the location of the wheels or casters:

- 1 for the left motorized wheel;
- 2 for the right motorized wheel;
- f for the front caster;
- r for the rear cater.

where second subscript j stands for the type of force:

- f for the rolling resistance;
- n for the lateral force;
- t for the tractive force.

For the normal reaction forces, the following notation is used:

N_1 for the left motorized wheel;

N_2 for the right motorized wheel;

N_f for the front caster;

N_r for the rear caster.

A more detail discussion about the location of the forces and the reaction forces between the rigid bodies is presented in the following sections.

2.3.1.1 The AGV body

Fig. 2.5 presents the AGV body with the 2 casters replaced by reaction forces at their pivot points. A body-centered system xyz is located at the center of mass of the AGV body which is coincident with its geometric center. The y axis of the system is defined along the longitudinal axis of the vehicle body, and it is also the direction of AGV's travel at the mass center. The z axis is normal to the floor (Fig. 2.5), and the x axis is obtained by the right hand rule. V_y is linear velocity along y axis, and Ω_z is the angular velocity about Z axis. The direction of the angular velocity is also defined by the right hand rule.

For a 2 d-o-f rigid body, using equations (2.13), the equations of motion for AGV body are:

$$\begin{aligned} m \dot{V}_y &= \sum Y \\ I_z \dot{\Omega}_z &= \sum N \end{aligned} \quad (2.14)$$

where $\sum Y$ is the total force at the direction of travel of AGV, $\sum M$ is the total moment of the AGV body about the vertical axis z passing through the mass center. m is the mass of the main body of the vehicle with the two

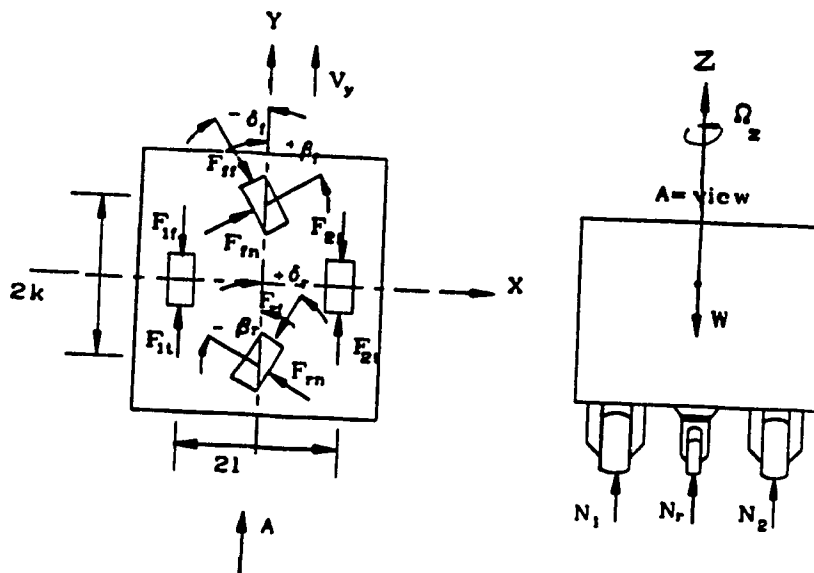


Fig. 2.4 CONCIC-2 AGV with body-centered system
and all external forces

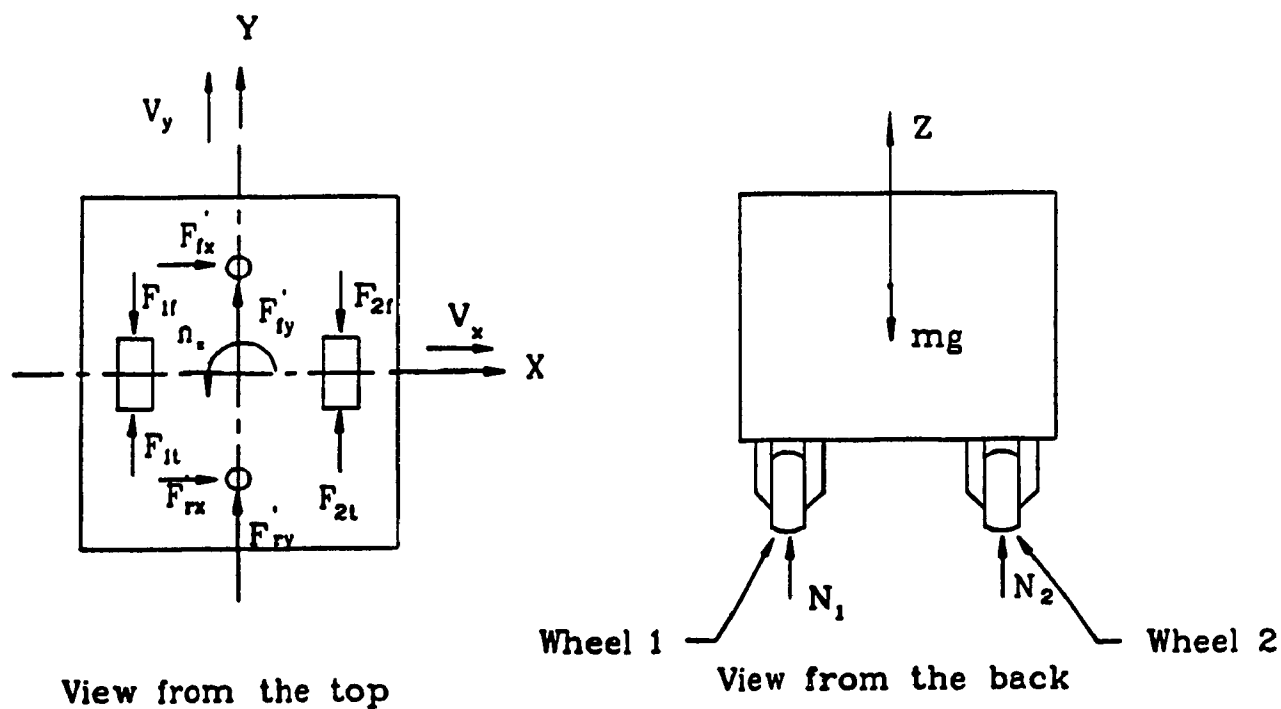


Fig. 2.5 AGV body subject to all the external forces

motorized wheels (the AGV body), and the I_z is the inertia of it about the z axis.

2.3.1.2 The forces on the AGV body

The forces on the AGV body act on:

- the 2 locations of which casters are pivoted on the AGV body;
- the contact patch between the motorized wheels and the the floor.

Since the friction at the bearing is negligible, the reaction forces at caster pivot are transferred from the casters to the AGV body. The reaction forces include the normal reaction between the body and the casters, and the forces caused by the rolling resistance and the lateral forces at the caster. The normal reaction N'_{fv} , N'_{rv} at front and rear casters respectively, are equal to quarter of the weight of the main body of the vehicle. The reaction of the rolling resistance and lateral forces of the caster are presented in two forces vectors F'_{ix} , F'_{iy} along x and y axis respectively ($i=f$ for front caster, and $i=r$ for rear caster).

At the contact patch of each motorized wheel, two kinds of forces are in action. A tractive force (F_{it}) is generated by the motor. It provides the driving and steering motion. This force acts in the direction of the wheel heading. Resistance force F_{1r} and F_{2r} are caused by the friction and the deformation of the wheels at the contact patch. It happens in the opposite direction of the wheel heading (Fig. 2.5).

From the external forces described above, the total external forces along the y-axis and the total moment about the z-axis can be obtained as:

$$\begin{aligned}\sum Y &= F_{1t} + F_{2t} - F_{1f} - F_{2f} + F'_{fy} + F'_{ry} \\ \sum M &= (F_{2t} - F_{1t})\ell + (F_{1f} - F_{2f})\ell + (F'_{rx} - F'_{fx})k\end{aligned}\quad (2.15)$$

where the ℓ is the wheel-span of the vehicle, and k is the wheel-base.

Substituting equations (2.14) by (2.15), the equations of motion of the AGV body are obtained as:

$$\begin{aligned}m \cdot \dot{V}_y &= F_{1t} + F_{2t} - F_{1f} - F_{2f} + F'_{fy} + F'_{ry} \\ I_z \cdot \dot{\Omega}_z &= (F_{2t} - F_{1t})\ell + (F_{1f} - F_{2f})\ell + (F'_{rx} - F'_{fx})k\end{aligned}\quad (2.16)$$

2.3.2.1 Casters

The casters have 3 d-o-f motion: the translation along x and y axis, and the rotation about z axis corresponding to the body-centered system at the AGV body. As shown in Fig. 2.6, the caster moves by following the pivot-point (the center of the axle which moves with the AGV body) and a rotation about the pivot-point.

Consider the case of the caster at the front, a system $x_f y_f z_f$ which is parallel to the system at AGV body is located in the center of mass of the front caster ($x_r y_r z_r$ for the rear caster). The center of mass is usually located somewhere between the center of the caster and pivot point. Let Δ be the distance between the origin of the system and the pivot point. Let the linear velocities along x_f and y_f be V_{xf} , V_{yf} , and the angular velocity of the caster about z_f be δ_f . The equations of motion of the front caster is derived from equation (2.12):

$$\begin{aligned}\sum X_f &= m_f (\dot{V}_{xf} - \delta_f \cdot V_{yf}) \\ \sum Y_f &= m_f (\dot{V}_{yf} + \delta_f \cdot V_{xf}) \\ \sum N_f &= I_{zf} \dot{\delta}_f\end{aligned}\quad (2.17)$$

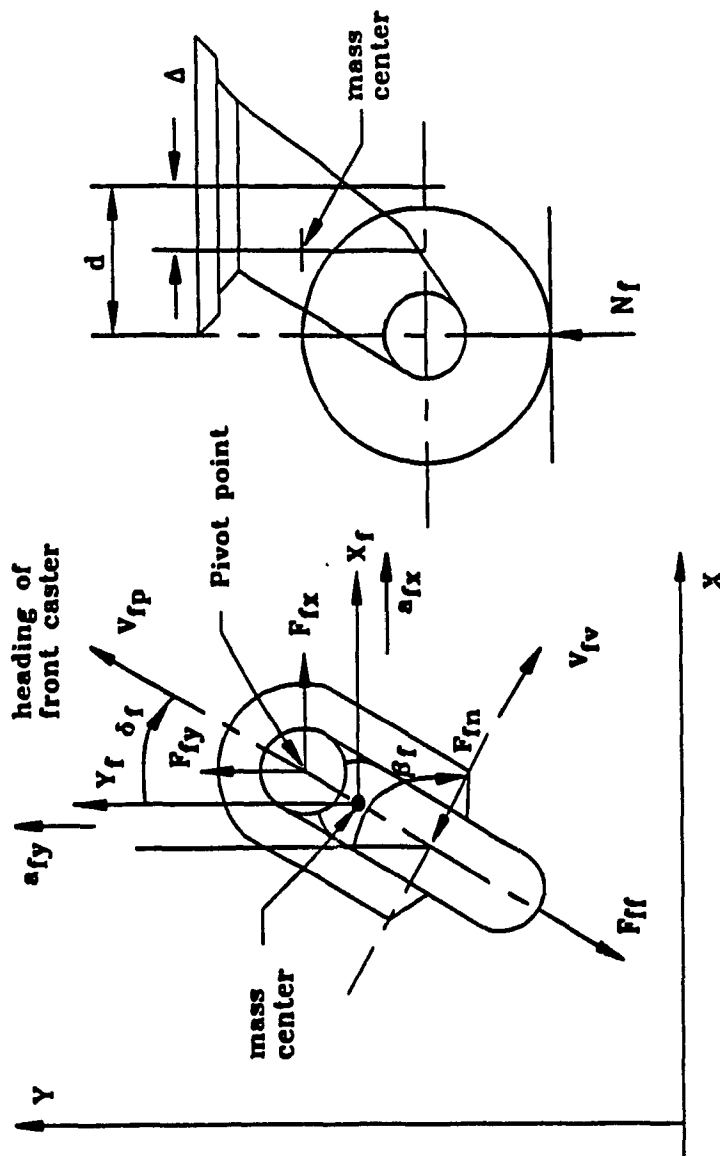


Fig. 2.6 Caster with body-centered system and external forces

where m_f is the mass of the caster, and I_{zf} is the moment of inertia of the caster about z_f . $\sum X_f$ is the total force along x_f , $\sum Y_f$ is the total force along the y_f , and the $\sum N_f$ is the total moment about the z_f axis.

Similarly at the rear caster, let the linear velocities along x_r and y_r be V_{xr} , V_{yr} , and the angular velocity of the caster about z_r be $\dot{\delta}_r$. The equations of motion of rear caster are:

$$\begin{aligned}\sum X_r &= m_r (\dot{V}_{xr} - \dot{\delta}_r \cdot V_{yr}) \\ \sum Y_r &= m_r (\dot{V}_{yr} + \dot{\delta}_r \cdot V_{xr}) \\ \sum N_r &= I_{zr} \ddot{\delta}_r\end{aligned}\tag{2.18}$$

where m_r is the mass of the front caster, and the I_{zr} is the moment of inertia of the front caster about z_r . $\sum X_r$ is the total force along x_r , $\sum Y_r$ is the total force along the y_r , and the $\sum N_r$ is the total moment about the z_r axis.

2.3.2.2 The forces on the casters

The forces at caster act at

- the pivot point which is connected to the AGV body through the pivot axle.
- the contact patch between the caster and floor.

As it is discussed in the section 3.2.1.1, the reaction between the caster and the AGV body at pivot point is also presented in three components,

- N'_{fv} : the normal reaction from the AGV body to the front caster;
- F'_{fx} : the reaction force at x_f direction;
- F'_{fy} : the reaction force at y_f direction.

Similarly for the rear caster,

- N'_{vr} : the normal reaction from the AGV body to the front caster;
- F'_{xr} : the reaction force at x_r direction;
- F'_{yr} : the reaction force at y_r direction.

Friction forces act at the contact patch between the caster and the floor. In the case of the front caster, the patch has two degrees of motion at the level plane. The linear velocity at the contact patch is presented by two velocity vectors, V_{fp} is the vector along the direction of the caster heading, and the vector V_{fv} is the vector vertical to it. When the direction of the caster heading is parallel to the velocity of pivot point, V_{fv} is zero, and there will be no lateral friction along this direction. Otherwise friction F_{fn} occurs in the direction against V_{fv} vector. The rolling friction F_{ff} lies in the opposite direction of V_{rp} .

The angle between y_f axis and the caster heading is defined as δ_f , the positive sign of the angle is defined as the clockwise. (Fig. 2.6). The angle between the y_f axis and force F_{fn} is presented by β_f , and

$$\beta_f = \delta_f + \pi/2 \quad (2.19)$$

Thus, for the caster:

$$\begin{aligned} \sum X_f &= -F_{ff} \sin(\delta_f) - F'_{fx} + F_{fn} \sin(\beta_f) \\ \sum Y_f &= -F_{ff} \cos(\delta_f) + F_{fn} \cos(\beta_f) - F'_{fy} \\ \sum N_{cf} &= F_{fn} \cdot (d - \Delta) + [F'_{xf} \cos(\delta_f) - F'_{yf} \sin(\delta_f)] \cdot \Delta \end{aligned} \quad (2.20)$$

Substituting equations (2.20) into (2.17), the equations of motion of front caster are:

$$m_f (\ddot{V}_{xf} - \dot{\delta}_f \cdot V_{yf}) = -F_{ff} \sin(\delta_f) - F'_{fx} + F_{fn} \sin(\beta_f) \quad (2.21a)$$

$$m_f (\ddot{V}_{yf} + \dot{\delta}_f \cdot V_{xf}) = -F_{ff} \cos(\delta_f) + F_{fn} \cos(\beta_f) - F'_{fy} \quad (2.21b)$$

$$I_{fz} \ddot{\delta}_f = F_{fn} \cdot (d - \Delta) + [F'_{xf} \cos(\delta_f) - F'_{yf} \sin(\delta_f)] \cdot \Delta \quad (2.21c)$$

For the rear caster, the equations of motion can be obtained similarly as:

$$m_r (\ddot{V}_{xr} - \dot{\delta}_r \cdot V_{yr}) = -F_{rf} \sin(\delta_r) - F'_{rx} + F_{rn} \sin(\beta_r) \quad (2.22a)$$

$$m_r (\ddot{V}_{yr} + \dot{\delta}_r \cdot V_{xr}) = -F_{rf} \cos(\delta_r) + F_{rn} \cos(\beta_r) - F'_{ry} \quad (2.22b)$$

$$I_{rz} \ddot{\delta}_r = F_{rn} \cdot (d - \Delta) + [F'_{xr} \cos(\delta_r) - F'_{yr} \sin(\delta_r)] \cdot \Delta \quad (2.22c)$$

The mass of caster is considered to be negligible in this analysis. $m_f = m_r = 0$. The left hand of (2.21a, b), and (2.22a, b) are all zero. Therefore the reaction forces between these bodies are as follows

$$\begin{aligned} F'_{fx} &= -F_{ff} \sin(\delta_f) + F_{fn} \sin(\beta_f) \\ F'_{fy} &= -F_{ff} \cos(\delta_f) + F_{fn} \cos(\beta_f) \\ F'_{rx} &= -F_{rf} \sin(\delta_r) + F_{rn} \sin(\beta_r) \\ F'_{ry} &= -F_{rf} \cos(\delta_r) + F_{rn} \cos(\beta_r) \end{aligned} \quad (2.23)$$

Substitute equations(2.23) into (2.21c)

$$\begin{aligned} I_{fz} \ddot{\delta}_f &= F_{fn} (d - \Delta) + [F'_{xf} \cos(\delta_f) - F'_{yf} \sin(\delta_f)] \cdot \Delta \\ &= F_{fn} (d - \Delta) + [-F_{ff} \sin(\delta_f) \cos(\delta_f) + F_{rn} \sin(\beta_f) \cos(\delta_f) \\ &\quad + F_{ff} \cos(\delta_f) \sin(\delta_f) - F_{rn} \cos(\beta_f) \sin(\delta_f)] \cdot \Delta \end{aligned}$$

Thus

$$I_{fz} \ddot{\delta}_f = F_{fn} (d - \Delta) + F_{rn} [\sin(\beta_f) \cos(\delta_f) - \cos(\beta_f) \sin(\delta_f)] \cdot \Delta \quad (2.24)$$

Substituting the equation (2.19) into (2.25) becomes

$$\begin{aligned}
 I_{fz} \ddot{\delta}_f &= F_{fn} (d - \Delta) + F_{rn} [\cos(\delta_f) \cos(\delta_r) + \sin(\delta_f) \sin(\delta_r)] \cdot \Delta \\
 &= F_{fn} (d - \Delta) + F_{fn} \Delta \\
 I_{fz} \ddot{\delta}_f &= F_{fn} \cdot d
 \end{aligned} \tag{2.25}$$

Similarly to the rear caster, the equation for the rotation about z_r axis is

$$I_{rz} \ddot{\delta}_r = F_{rn} \cdot d \tag{2.26}$$

2.4 The equation of motion for the entire AGV

Substituting the reaction forces F'_{fx} , F'_{fy} , F'_{rx} , and F'_{ry} of equations (2.23) into equations (2.16), the motion equations of the AGV main body can be obtained in terms of all the external forces acting on the vehicle.

$$\begin{aligned}
 m (\dot{V}_y + \Omega_z \cdot V_x) &= F_{1t} + F_{2t} - F_{1f} - F_{2f} - F_{ff} \cos(\delta_f) + \\
 &\quad F_{fn} \cos(\beta_f) - F_{rf} \cos(\delta_r) + F_{rn} \cos(\beta_r) \\
 I_z \dot{\Omega}_z &= (F_{2t} - F_{1t}) \cdot l + (F_{1f} - F_{2f}) \cdot l + (F_{rn} \sin(\beta_r) - \\
 &\quad F_{ff} \sin(\delta_r) - F_{fn} \sin(\beta_f) + F_{ff} \sin(\delta_f)) \cdot k
 \end{aligned} \tag{2.27}$$

where δ_f , δ_r may be determined by the following equations.

$$\begin{aligned}
 I_{fz} \ddot{\delta}_f &= F_{fn} \cdot d \\
 I_{rz} \ddot{\delta}_r &= F_{rn} \cdot d
 \end{aligned} \tag{2.28}$$

and the angles β_f and β_r are calculated by

$$\begin{aligned}
 \beta_f &= \delta_f + \pi/2 \\
 \beta_r &= \delta_r + \pi/2
 \end{aligned} \tag{2.29}$$

For a base reference system which is shown in Fig. 2.7, the coordinate of the AGV within it, is presented as

$$\begin{aligned}\bar{X} &= \bar{X}_0 + \int_0^t [V_x \cdot \cos(\theta - 90^\circ) + V_y \cdot \cos(\theta)] dt \\ \bar{Y} &= \bar{Y}_0 + \int_0^t [V_x \cdot \sin(\theta - 90^\circ) + V_y \cdot \sin(\theta)] dt \\ \theta &= \theta_0 + \int_0^t \Omega_z dt\end{aligned}\tag{2.30}$$

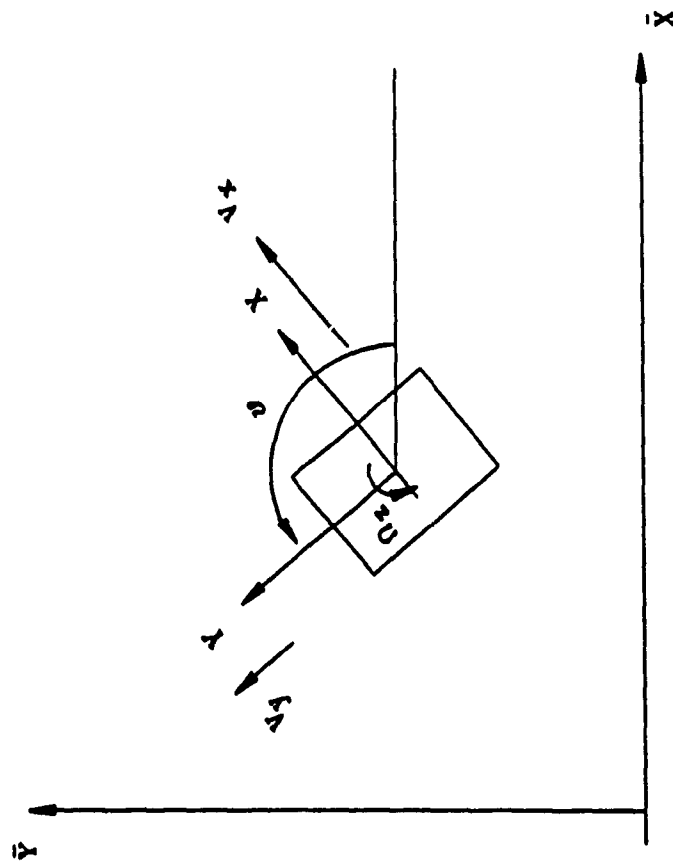


Fig. 2.7 Base coordinate system and body-centered system of AGV

CHAPTER 3

FORMULATION OF EXTERNAL FORCES

To generate analytical formulae to those external forces of vehicle may be the most difficult work for the dynamic modeling. As it was mentioned before, many external forces are dependent on the characteristics of wheels and floor. The formulae for these forces varies according to the wheels. All the external forces contributing in the motion equation of CONCIC-2 AGV are in three categories: tractive forces, lateral forces (cornering force and side-friction), rolling resistance. The following sections will give a detailed investigation of these three forces.

3.1 Tractive force

3.1.1 Formulation of tractive force

According to the configuration of differential drive-steering, the whole effort of the motion is provided by the forces between the two driving wheels and the working surface. The tractive force is the force which the motor can provide to the vehicle. And it is the only force which depends on the motor characteristic, but not the characteristics of the wheel and the floor.

The dc motor in the motor-wheel unit is a permanent magnet dc motor. From the torque-current curve [Appendix B], the torque generated by the motor T_g can be calculated in the following formula:

$$T_g = k_t I \quad (3.1)$$

Where I is the motor current, and k_t is defined as torque constant.

Fig. 3.1 gives a motor and load system. where J is the moment of inertia of motor referred to the motor shaft (with the wheel as the load in

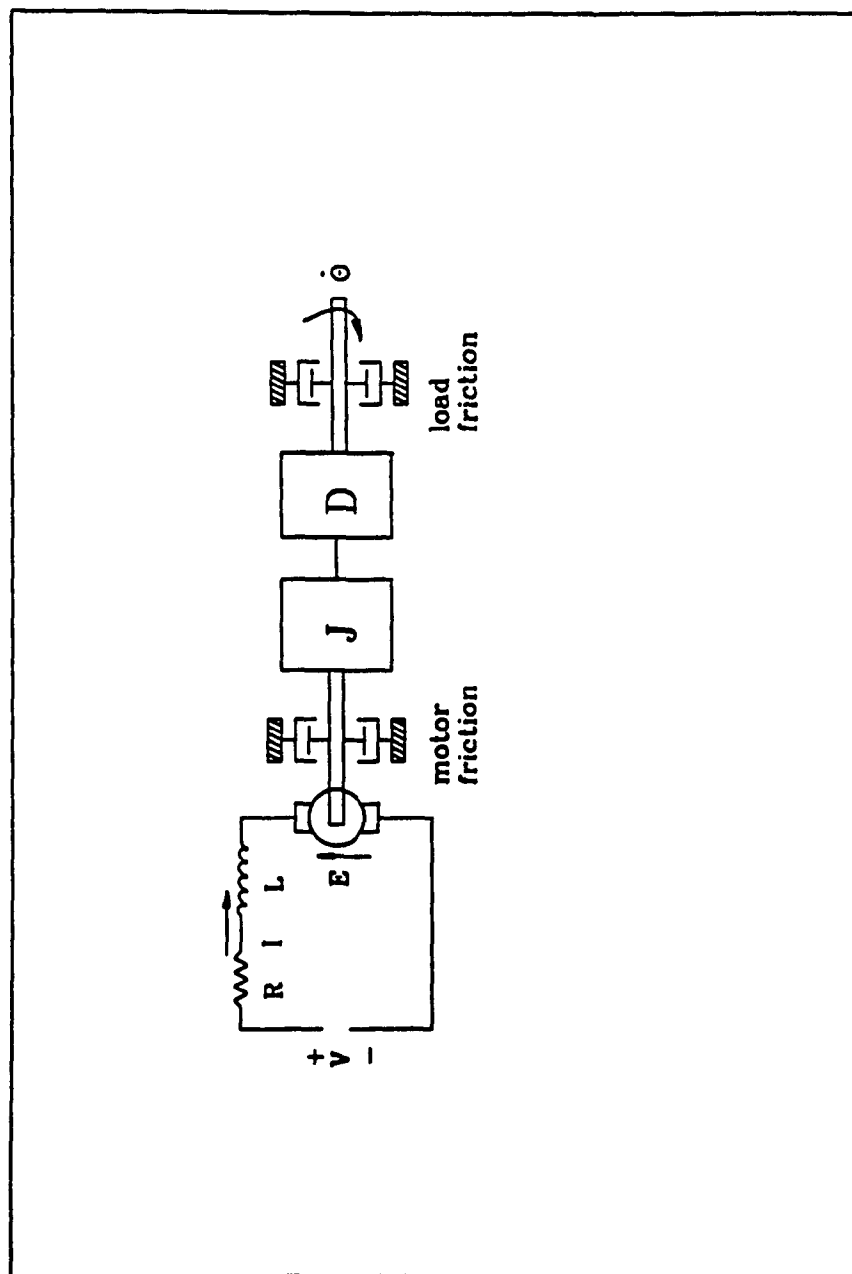


Fig. 3.1 Model of motor and load system

the case of CONCIC-2), D is viscous damping factor, T_f is the static friction torque, T_m is the load torque from the motor shaft, and θ is the angular displacement of the motor rotation.

The dynamic equation of this system is written as

$$T_s = J \frac{d^2\theta}{dt^2} + D \frac{d\theta}{dt} + T_f + T_m \quad (3.2)$$

Substituting T_s in equation (3.1) into equation (3.2)

$$T_m = k_t I - J \frac{d^2\theta}{dt^2} - D \frac{d\theta}{dt} - T_f \quad (3.3)$$

The torque transferred to the wheel from the motor shaft is

$$T_t = nT_m$$

where, n is gear ratio. And the tractive force at wheel and floor will be

$$\begin{aligned} F_t &= T_t / r_d = \frac{nT_m}{r_d} \\ &= \frac{n}{r_d} (k_t I - J \frac{d^2\theta}{dt^2} - D \frac{d\theta}{dt} - T_f) \end{aligned} \quad (3.4)$$

where r_d is the radius of the motorized wheel.

3.1.2 Tractive forces of CONCIC-2 AGV

For CONCIC-2 AGV, the tractive forces at the left motorized wheel(wheel 1) is obtained from equation (3.4)

$$F_{1t} = \frac{n_1}{r_{1d}} (k_{1t} I_1 - J_1 \frac{d^2\theta_1}{dt^2} - D_1 \frac{d\theta_1}{dt} - T_{1f})$$

where n_1 is the gear ratio, r_{1d} the radius of the wheel, J_1 the moment of inertia of the motor and wheel about the motor shaft, D_1 is the viscous damping factor, and the T_{1f} is the friction torque for the left motor-wheel unit.

Similarly for the right wheel (wheel 2), the tractive force is

$$F_{2t} = \frac{n_2}{r_{2d}} (k_{2t} I_2 - J_2 \frac{d^2 \theta_2}{dt^2} - D_2 \frac{d\theta_2}{dt} - T_{2f})$$

where n_2 , r_{2d} , k_{2t} , J_2 , D_2 , and T_{2f} are defined as same as above, but for wheel 2.

Since the two motor-wheel units are assumed to have the same characteristics. Let

$$n_1 = n_2 = n;$$

$$r_{1d} = r_{2d} = r_d;$$

$$k_{1t} = k_{2t} = k_t;$$

$$J_1 = J_2 = J;$$

$$T_{1f} = T_{2f} = T_f.$$

Therefore

$$\begin{aligned} F_{1t} &= \frac{n}{r_d} (k_t I_1 - J \frac{d^2 \theta_1}{dt^2} - D \frac{d\theta_1}{dt} - T_f) \\ F_{2t} &= \frac{n}{r_d} (k_t I_2 - J \frac{d^2 \theta_2}{dt^2} - D \frac{d\theta_2}{dt} - T_f) \end{aligned} \quad (3.5)$$

Let V_1 and V_2 be the linear velocity at the contact point of motorized wheel 1 and wheel 2. Then

$$\frac{d\theta_i}{dt} = n \frac{V_i}{r_d} \quad (i = 1, 2) \quad (3.6)$$

The accelerations are

$$\frac{d^2 \theta_i}{dt^2} = \frac{ndV_i}{r_d dt} \quad (3.7)$$

From the geometry of the vehicle

$$\begin{aligned} V_1 &= V_y - \ell \Omega_z \\ V_2 &= V_y + \ell \Omega_z \end{aligned} \quad (3.8)$$

Where ℓ is the wheel-span of CONCIC-2 AGV. Then

$$\begin{aligned}\frac{d^2\theta_1}{dt^2} &= \frac{n}{r_d}(\dot{V}_y - \dot{\Omega}_z) \\ \frac{d^2\theta_2}{dt^2} &= \frac{n}{r_d}(\dot{V}_y + \dot{\Omega}_z)\end{aligned}\quad (3.9)$$

Substituting equations (3.9) and (3.8) into (3.5), the tractive force of are

$$\begin{aligned}F_{1t} &= \frac{n}{r_d} [k_t I_1 - \frac{Jn}{r_d}(\dot{V}_y - \dot{\Omega}_z) - \frac{Dn}{r_d}(\dot{V}_y - \dot{\Omega}_z) - T_f] \\ F_{2t} &= \frac{n}{r_d} [k_t I_2 - \frac{Jn}{r_d}(\dot{V}_y + \dot{\Omega}_z) - \frac{Dn}{r_d}(\dot{V}_y + \dot{\Omega}_z) - T_f]\end{aligned}\quad (3.10)$$

3.2. Rolling resistance (rolling friction)

A perfect solid wheel has a point-contact with the hard floor at any given instant. The contact point has no relative motion with respect to the floor, the wheel eliminates the large friction which would arise if the load were in direct contact with the ground. In practice, however, it is not always the case. The contact of the wheel with the floor is rather a patch than a point because of the deformation at the wheel and the floor. Some resistance to the motion of the wheel exists. This resistance has two distinct causes. It is due

(1) to the fact that the wheel and ground may deform, with the result that the contact between wheel and ground takes place not at a single point, but over a certain patch,

(2) to a combined effect of bearing friction.

The rolling resistance is the friction caused by the second reason.

Rolling resistance is a force highly dependent upon the characteristics of the wheel and the condition of the floor. For a wheel with a rubber or

pneumatic tire, the rolling resistance of tires on hard floor is primarily caused by the hysteresis in tire material due to the deflection of the carcass while rolling [45]. Friction between the tire and the road caused by sliding, the resistance due to air circulating inside the tire in the case of pneumatic tire, and the fan effect of the rotating tire on the outside air also contribute to the rolling resistance of the tire, but they are secondary importance. For a solid wheel on a hard and smooth floor, the rolling resistance is caused by the displacement of the point of instantaneous rolling of the wheel because of the deformation of the wheel and the floor.

The ratio of the rolling resistance and the downward force at the wheel is usually defined as the coefficient of rolling resistance k_r .

$$k_r = \frac{R}{W}$$

The following gives more details for the three different types of wheels on the hard floor.

3.2.1 A metal wheel on a metal rail

In this case, the rolling resistance is caused by the deformation of wheel and track producing an elastic deformation, as shown in Fig. 3.2. This deformation causes the point of instantaneous rolling of the wheel to be always ahead of the point geometrically directly under the center axle of the wheel. The result is that the downward force to the surface and the normal reaction at the wheel exert a retarding torque which is known as rolling resistance torque. It is also can be presented as a horizontal force which is generally known as rolling resistance at wheel-road contact patch when tractive force is involved. The displacement of the instantaneous

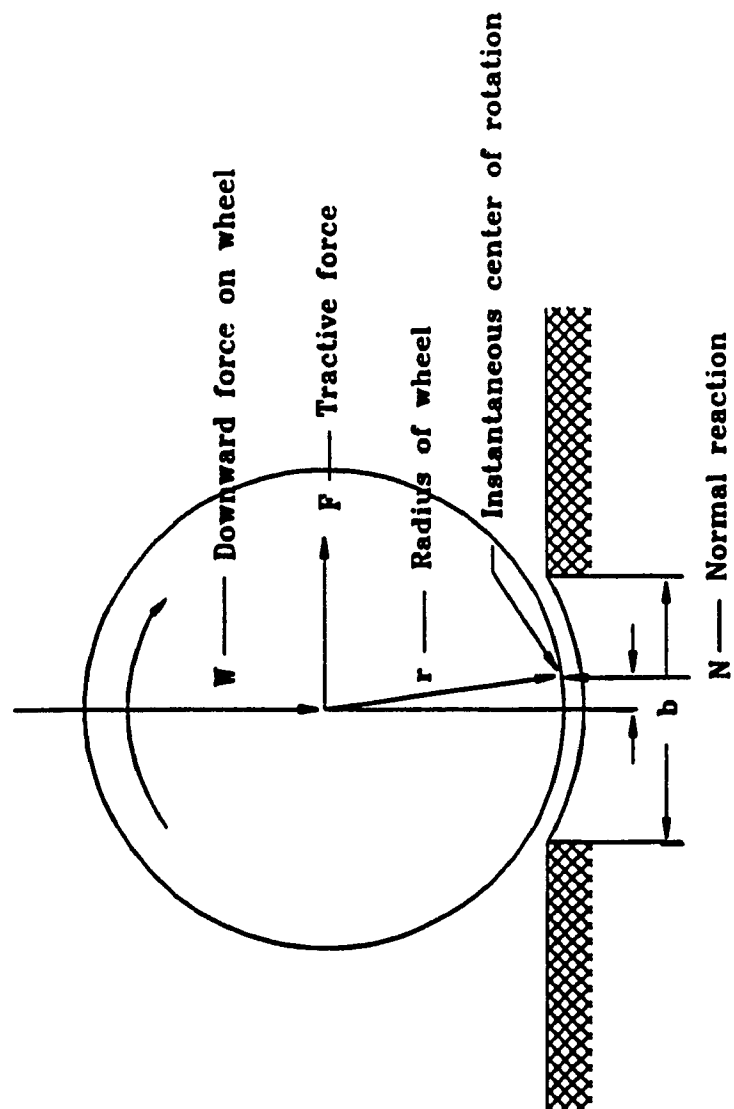


Fig. 3.2 Rolling resistance of a steel wheel [1]

center of rotation can be measured from experiments or calculated from some predicting formula [37].

The numerical value of the rolling resistance torque is the downward force between the wheel and road, which in steady state is the weight of the wheel plus its share of the weight of the vehicle, multiplied by the displacement of the instantaneous center of the rotation. Consequently, the resistance force is calculated as

$$\text{Resistance force} = \frac{\text{Weight} \times \text{Displacement of the instantaneous center}}{\text{Radius of the wheel}}$$

The coefficient of rolling resistance may be obtained as

$$\text{Rolling coefficient} = \frac{\text{Displacement of the instantaneous center}}{\text{Radius of the wheel}}$$

The displacement of the instantaneous center may be measured experimentally. For iron-iron contact, it is within a range of 0.002 mm to 0.005 mm.

3.2.2 Rubber tires

If the tire of the wheel is made elastic so that it can change shape sufficiently during passage over an obstacle, the motion of the wheel center may not be perceptibly affected, and the mass subjected to impact may be localized to the neighborhood of the point of contact. Thus, the use of rubber tires on an ordinary road greatly reduces the amount of energy wasted. Again, the rubber tire being elastic, instead of sinking into a road, it is flattened out. The area of contact with the floor being much larger, the pressure per unit area is less.

Resistance to rolling of a rubber tire is of the same nature as

discussed in the previous section. The amount of compression of the tire in contact with the ground being much greater than in the case of metal wheel on a metal rail, the rolling resistance is also greater. Archibald [1] introduces a formula to predict the rolling resistance in the form of

$$R = k_1(1 + k_2 V) \cdot W \quad (3.11)$$

where k_1 and k_2 are constants, V is linear velocity at the wheel, and W is the weight of the wheel and its share of the weight of the vehicle.

3.2.3 Pneumatic tires

A pneumatic-tired wheel rolling on the road exhibits more significant characteristics compared with the steel wheel on rails or the rubber wheel on the hard road. The flattening of the tire over equivalent distance b (Fig. 3.3) is greater for pneumatic tires, and therefore a much greater rolling resistance is observed.

A number of factors affect the rolling resistance of a pneumatic tire. The tire construction has a significant influence on its rolling resistance. Fig. 3.4 shows the difference of a conventional cross-ply tire and a radial-ply tire at various speeds [47]. Thicker treads and an increased number of carcass plies tend to increase the rolling resistance because of greater hysteresis losses. The materials of the tires also affect the rolling resistance. Tires made of synthetic rubber compounds generally have slightly higher rolling resistance than those made of natural rubber. Butyl rubber tires, which are shown to have better traction and road holding properties, have even higher rolling resistance than conventional synthetic rubber ones [45].

The surface condition is another important factor. On hard, smooth, dry

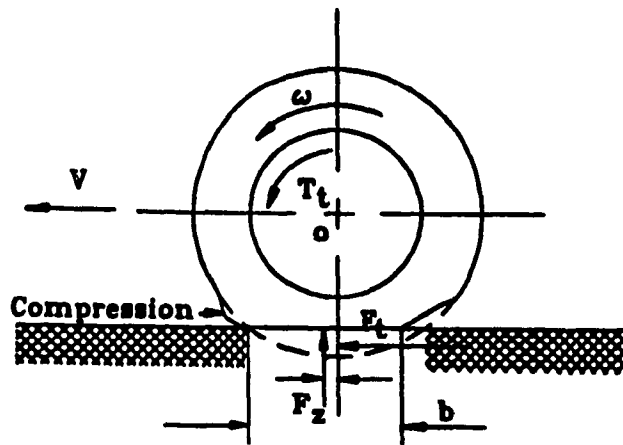


Fig. 3.3 Rolling resistance of a pneumatic tire [45]

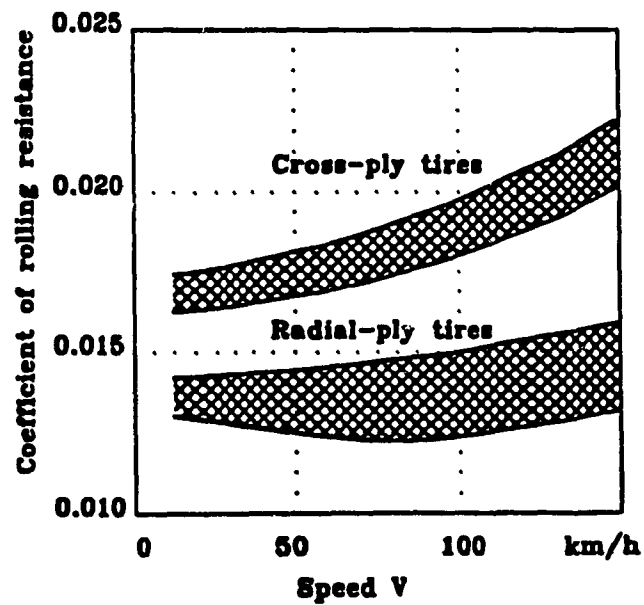


Fig. 3.4 The rolling resistance for conventional bias-ply and radial-ply tires at various speeds [45]

surfaces, the rolling resistance is considerably lower than that on a worn-out road. On wet floor, a higher rolling resistance is usually observed.

The inflation pressure of the pneumatic tire affects its deforming ability and thus the rolling resistance. On hard surfaces, the rolling resistance decreases slightly with the increase of the inflation pressure, as shown in Fig. 3.5 [45]. On deformable surfaces, such as sand, high inflation pressure results in increased of ground penetration work and therefore higher rolling resistance. Conversely, lower inflation pressure, while decreasing ground losses, increases the deflection of the tire and hence hysteresis losses. Therefore optimum pressure exists for the particular surface condition. Rolling resistance is also affected by linear speed at the wheel, because of the increase of energy in deforming the tread and of vibration in tire carcass with the increase of speed. The influence of speed on rolling resistance of a conventional cross-ply tire and a radial-ply tire is already illustrated in Fig. 3.4.

Other factors, such as operating temperature, tire diameter, and tractive forces also have an effect on the rolling resistance. For example, Fig. 3.6 [45] presents the effect of tire diameter on the coefficient of rolling resistance.

The complex relationship between the design and operating parameters of a tire and its rolling resistance make it extremely difficult, if not impossible, to develop an analytic method for predicting the rolling resistance. The measurement of a rolling resistance, therefore, relies almost entirely on experiments. Based on experimental results, many empirical formulae have been proposed for calculating rolling resistance of

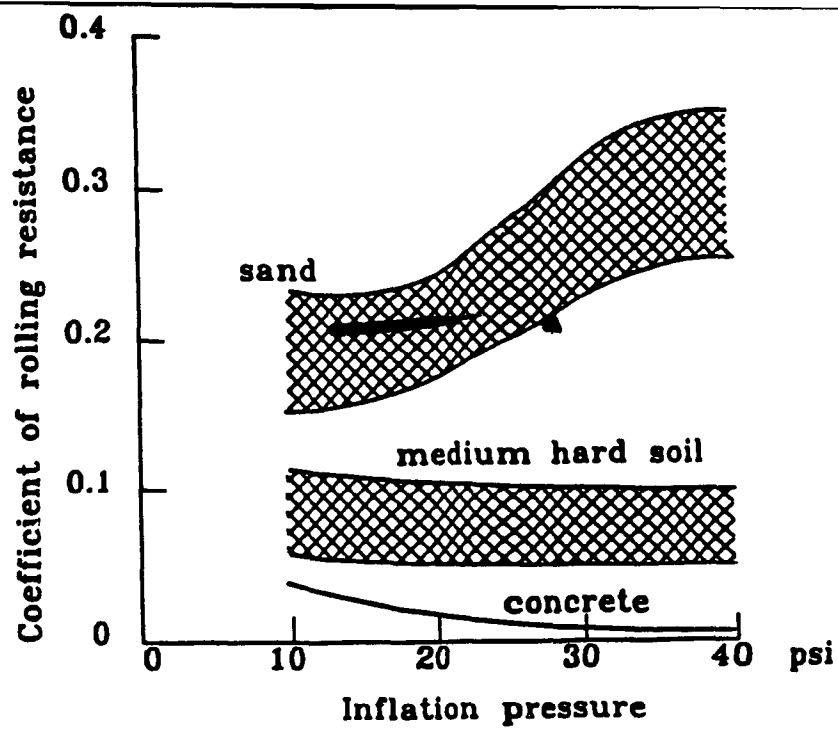


Fig. 3.5 Coefficient of rolling resistance at various inflation pressure [45]

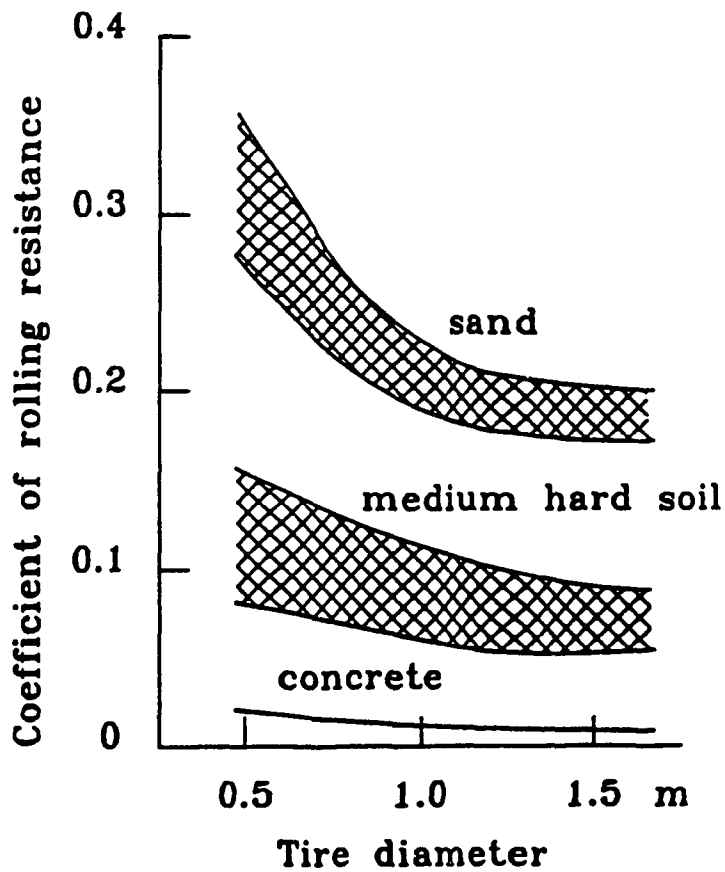


Fig. 3.6 Coefficient of rolling resistance at various tire diameter [45]

tires on hard surfaces. For instance, the coefficient of rolling resistance k_r for passenger car tires on concrete pavement may be calculated from the following formula introduced by Wang [45]:

$$k_r = f_o + f_s \left(\frac{V}{100} \right)^{2.5} \quad (3.12)$$

Where V is speed in km/h, and coefficients f_o and f_s depend on the inflation pressure and may be taken from Fig. 3.7.

In many cases, it is sufficient to consider the coefficient of rolling resistance to be a linear function of speed. For the most common range of inflation pressure (around 179 kPa or 26 psi), the following equation gives the coefficient of a passenger car tire on a concrete surface [45]:

$$k_r = 0.01 \left(1 + \frac{V}{160} \right) \quad (3.13)$$

According to Wang, the coefficient of rolling resistance k_r predicted by the above formula has a acceptable accuracy for speeds up to 128 km/h (80 mph).

Sometimes, even the effect of the speed can be ignored. For an example, Johnson [17] indicates there is a speed limit V_o for rolling resistance, under this limit rolling resistance is a function of velocity, beyond that, the effect of the speed can be ignored.

Table 3.1 lists some average value of k_r [47].

3.2.4 Rolling resistance of CONCIC-2 AGV

The case for CONCIC-2 AGV is that four hard rubber wheels run on a hard, smooth concrete surface. Referring to the discussion above, the coefficients of rolling resistance of the wheels may take the form of

$$k_r = k_1 (1 + k_2 V) \quad (3.14)$$

The coefficient of rolling resistance of motorized wheels and casters

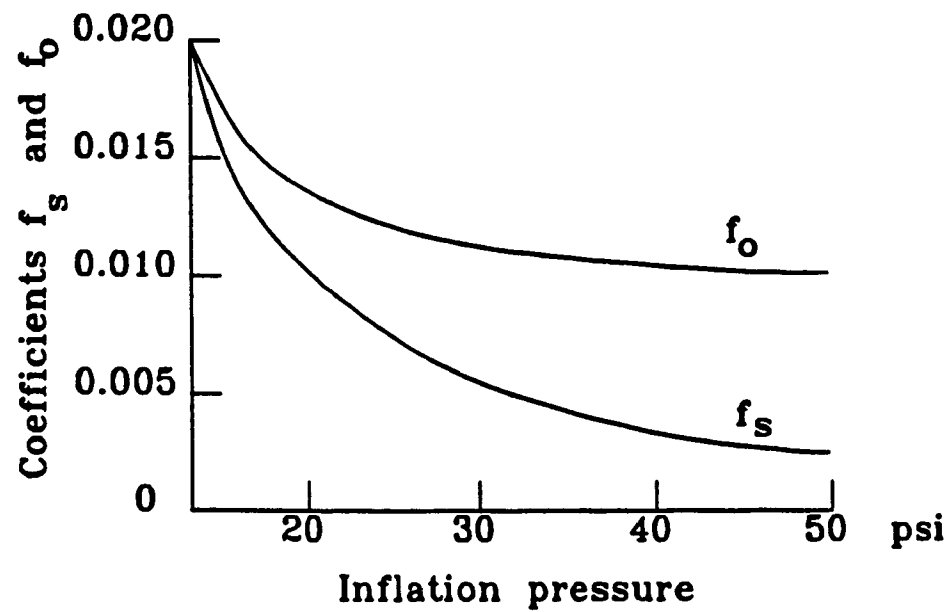


Fig. 3.7 The curves for f_o and f_s [45]

Coefficient of rolling resistance

Road surface	Coefficient of rolling resistance f
Tires on	
large paving stone	0.015
small paving stone	0.015
concrete, asphalt	0.015
rolled gravel	0.02
tarmacadam	0.025
dirt road	0.05
arable soil	0.1 ... 0.35
Off-highway wheels on	
arable soil	0.14 ... 0.24
Caterpillar tractor on	
arable soil	0.07 ... 0.12
Wheel on rail	0.001 ... 0.002

Table 3.1 Coefficient of rolling resistance [46]

of CONCIC-2 are not available from the manufacturer. For this thesis, these figures are estimated from the knowledge to reduce the deviation between the simulation and experiment results. Referring to Table 3.1, the coefficient of rolling resistance of metal wheel on rail is 0.001 - 0.002, and pneumatic tire on concrete road is 0.015. As a wheel with hard rubber tire, k_1 is chosen to be the average value as 0.007, and k_2 is taken as 0.01. The value of k_1 and k_2 effects the motor voltage and current of the drive-motor at steady state. Higher k_1 and k_2 required higher current and voltage, and the detailed illustration is given in chapter 6.

It is assumed that the four wheels of CONCIC-2 AGV have the same characteristics of rolling resistance, thus the formula of rolling resistance of the wheels of CONCIC-2 AGV is

$$F_{1r} = 0.007(1 + 0.01V_1) \cdot N_1 \quad (3.15)$$

and the notations are referred as the definition before.

Substitute V_1 and V_2 of equation (3.8) into equation (3.15), The rolling resistance for the motorized wheels are

$$\begin{aligned} F_{1r} &= k_1 (1 + k_2 V_y - k_2 \cdot \ell \cdot \Omega_2) \cdot N_1 \\ F_{2r} &= k_1 (1 + k_2 V_y + k_2 \cdot \ell \cdot \Omega_2) \cdot N_2 \end{aligned} \quad (3.16)$$

3.3 Lateral force

Lateral force is a force which acts perpendicularly to the wheel plane. It is created when the wheel tends to slip sideways (side-slip) or when the wheel is steered. The lateral force which is caused by the side-slip is also called side-friction, and that caused by the steer-action is usually called the cornering force. Lateral force is caused by friction and deformation at the contact patch between the wheel and the floor. Thus, as in the case of

rolling resistance, lateral force also varies with different type of wheels.

3.3.1 Side-friction force

When a vehicle negotiates with a relatively high speed or is subjected to other side disturbances, a horizontal force F_n is exerted on the wheels to prevent the vehicle sliding sideways. The force acts at the direction perpendicular to the wheel plane. When F_n is smaller than the active force F_a , the vehicle will slip sideways. This slipping is often experienced in greasy asphalt and smooth concrete at high speed.

The side-friction depends on the downward force on the wheel and the coefficient of friction k_n between the wheel and the floor. It is calculated by the following formula:

$$F_n = k_n \cdot N \quad (3.17)$$

where N is normal reaction at the wheel.

The coefficient of friction k_n varies with the material of wheels (or tires), the condition of the floor and the wheel (or tire), and other factors such as the downward load, etc. [32]. Table.3.2 lists some the coefficients of friction for different materials [49].

The side-friction affects the lateral stability of the vehicle. For example, on a hard, smooth, concrete surface, because of the greater deformation at the contact patch of the pneumatic tire, it provides greater side-friction than solid tires and hard rubber tires, thus the vehicle exhibits more lateral stability. But on soft mud roads, the pressure per square inch on the larger surface of a pneumatic tire in contact with the ground being much smaller, the tire is unable to force the mud from beneath it. It has no actual contact with the ground, but floats on a very thin

Static coefficients of friction of tires on road surface
(coefficients of tire-road interface friction)

Road speed	Tire condition	Road conditions		Puddles Depth of water approx. 2 mm	Wet Depth of water approx. 0.2 mm	Icy
		Dry	Heavy rain Depth of water approx. 1 mm			
		Static coefficient of friction μ_r				
50	new	0.85	0.55	0.5	0.55	0.1 and less
	worn ²	1	0.4	0.25	0.5	
90	new	0.8	0.3	0.05	0.6	—
	worn ²	0.95	0.1	0.05	0.2	
130	new	0.75	0.2	0	0.55	—
	worn ²	0.9	0.1	0	0.2	

Table 3.2 Static coefficients of friction of tires on road surface
(coefficients of tire-road interface friction) [1]

layer of mud. the coefficient of friction at this case is very small, a sharp turn may cause side slip.

3.3.2 Cornering force

The cornering force is caused by the steering action of the wheels. In the case of a solid tire on a hard surface, the cornering force is very small because of the small contact area (point contact). The resistance of the steering action is in the form of a small friction moment, and it is considered to be negligible.

When the plane of a wheel with a pneumatic tire is steered not to be in line with the path of motion, a deformation and displacement of the contact patch occurs which gives a lateral force and a moment which attempt to realign the wheel in the direction of wheel heading. And the front portion of the contact patch is parallel to the direction of motion and eventually slides to the center line of the wheel and at rear portion of the patch (Fig. 3.8). For a small steering angle, the whole contact patch is substantially parallel to the direction of rolling, but as the angle increases that portion moves forward until at an angle of 12° to 15° the whole area is sliding and the lateral force reaches the maximum. The distribution of the forces between the tire and the road are shown in Fig. 3.8. It is seen that the lateral force increases from the front to the rear of the contact length for some angles, and the offset of the resultant lateral force produces the aligning torque about the vertical axis. The offset is called the pneumatic trail, and the resultant lateral force is defined as cornering force. The product of cornering force and pneumatic trail determines the aligning torque. The aligning torque helps the steered

tire return to the original position after negotiating a turn. At large angles of steer the lateral forces are progressively limited by the sliding which occurs at the rear part of the contact path.

The relationship between the slip angle and the cornering force of various types of tires under a variety of operation conditions have been investigated quite extensively. Fig. 3.9 shows some typical plots of the cornering force as a function of the slip angle for bias-ply tire and a radial-ply tire. It is seen that for slip angle below certain value, such as 4° in Fig. 3.9, the cornering force is approximately proportional to the slip angle. Beyond the angle, the cornering force increases at a lower rate and reaches the maximum value where the tire begins sliding laterally. That angle (as 4° in the example) is defined as limit-angle in this thesis. In order to compare the cornering behavior of different tires, a parameter called cornering stiffness C_α is used, which is defined as the derivative of the cornering force F_c with respect to the slip angle α [17].

$$C_\alpha = \frac{\partial F_c}{\partial \alpha}$$

or

$$F_c \approx C_\alpha \cdot \alpha \quad 0 < \alpha < \text{limit-angle} \quad (3.18)$$

A number of factors affect the cornering behavior of pneumatic tires. The most important are the normal load and the inflation pressure of the tire. Fig. 3.10 and Fig. 3.11 show these changes for a small car tire [7].

The cornering stiffness is obtained through experimental data. Table.3.3 lists some cornering stiffness for different tires in different conditions [44].

Rubber tires have properties that lies between the solid wheels and the wheels with pneumatic tires. When the tire is made of hard rubber, it

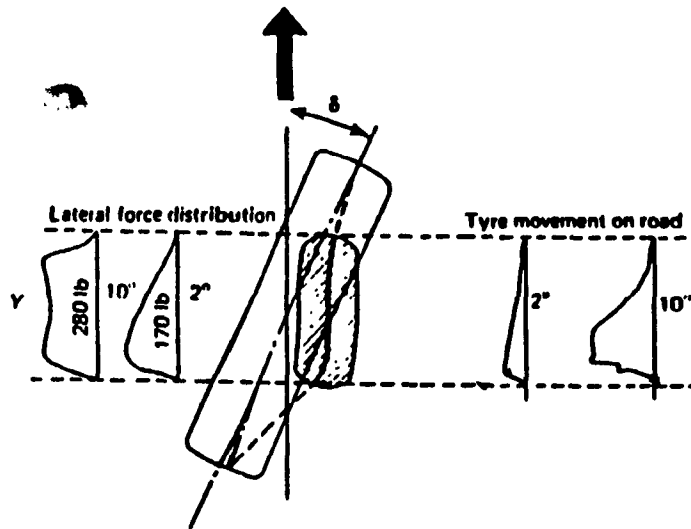


Fig. 3.8 The cornering force for a pneumatic tire [7]

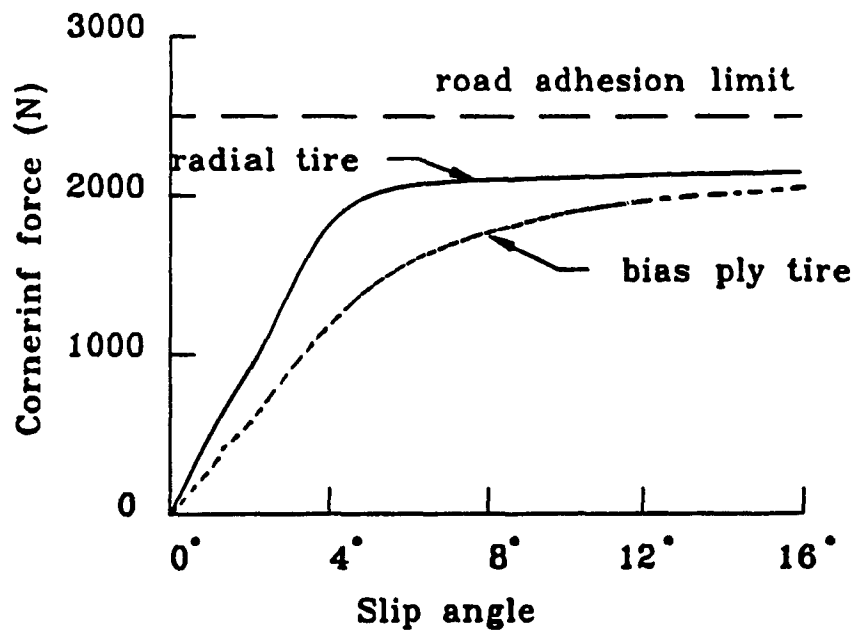


Fig. 3.9 The cornering force for conventional bias-ply and radial-ply tires at various slip angles [45]

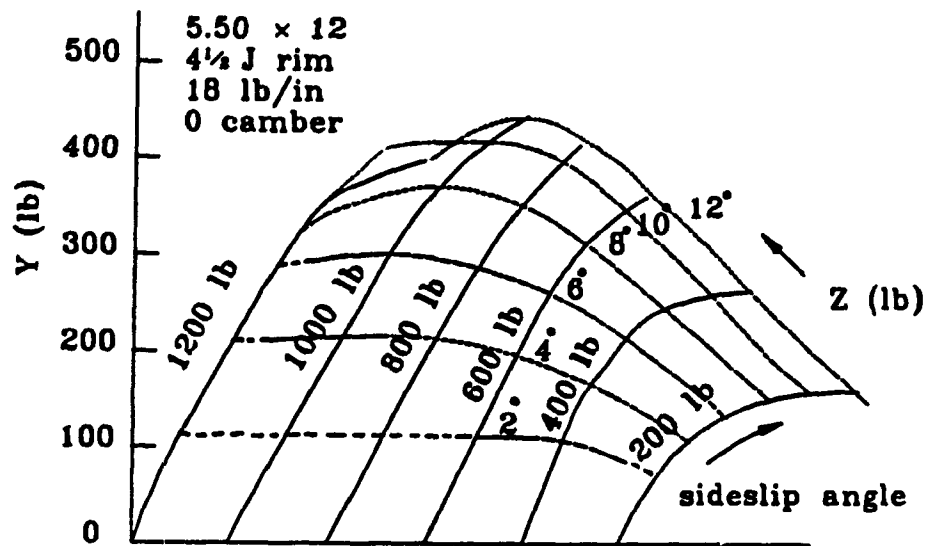


Fig. 3.10 Cornering force at various normal reaction [45]

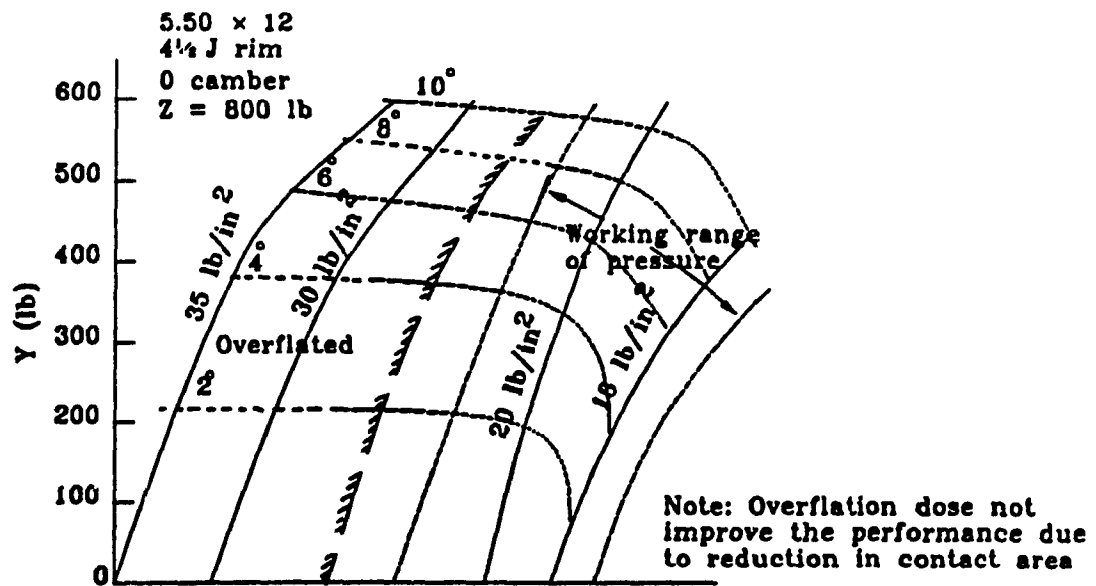


Fig. 3.11 Cornering force at various inflation pressure [7]

Reference	Tyre	Ground conditions	Tyre pressure, kPa	Vertical load, kN	Test conditions	Lateral force definition*	Cornering stiffness coefficients at various tyre slip angles			Comments
							0°	10°	20°	
Ipek (1959)	7.00 x 16 tractor front	Asphalt	303	3.4 6.9 9.8		T T T	0.103 0.105 0.143	0.018 0.024 0.031		measured up to 11° slip angle
	10 x 28 tractor rear	Asphalt	80	6.9	with treadbars without treadbars	T T	0.094 0.160	— —	— —	measured up to 8° slip angle
	7.50 x 16 multi-rib ot tractor front	Sandy loam	276	10.2 14.9		T T	0.086 0.066	— —	— —	measured up to 15° slip angle
		Silty clay	276	10.2 14.7		T T	0.036 0.039	— —	— —	
Taylor and Hirtwhistle (1966)	5.50 x 16 tractor front	Sandy clay soil bin	101	3.9		T	0.033	0.017	—	coefficient decreased slightly over vertical force range 1.0-3.9 kN
		Concrete	101			T	0.053	—	—	
	6.00 x 20 tractor front	Sandy clay	101	3.4		W	0.022	—	—	constant up to 15°
Baker and Collins (1972)	11 x 28 tractor rear	Moist pasture	not recorded	not recorded	cross ply 45° tread cross-ply 23° tread radial-ply 45° tread	T T T	— — —	— — —	— — —	15300 N/rad cornering stiffness 7800 N/rad cornering stiffness 7650 N/rad cornering stiffness
Arick (1973)	7.50 x 18 tractor front	Sandy loam in soil bin (14% moisture content)	101	3.2	no slip 35% slip no slip 35% slip	W W W W	0.031 0.021 0.029 0.017	0.031 0.021 0.029 0.017	0.031 0.021 0.029 0.017	driven wheels coefficient constant up to maximum measured slip angle of 25°
	12.50 x 20 cross country vehicle	Sandy loam in soil bin (14% moisture content)	101	5.2	no slip 25% slip	W W	0.026 0.020	0.026 0.020	0.026 0.020	driven wheels - linear up to 20° slip angle
	7.50 x 16 tractor front	Grass on soft ground (100 lbf/in² cone index)	151	1.4 2.7 4.3 5.5		T T T T	0.069 0.055 0.075 0.055	0.042 0.038 0.047 0.034	— — — —	
		Stubble		1.4 2.7 4.3 5.5		T T T T	0.075 0.058 0.061 0.058	0.051 0.040 0.040 0.040	— — — —	
Schwanhart (1981)	7.50 x 18	Dry road	Not recorded	3		Not recorded	0.13 0.05 0.03 0.07 0.03	0.016 0.018 0.018 0.033 0.013	-0.016 -0.003 -0.012 -0.004 0.004	
		Wet road								
		Dry sandy loam								
		Meadow								
		Ploughed field								
Kraft and Phillips (1981)	5.00 x 5	Clayed silt, cone index 30-46	Not recorded	0.6		W	0.07	0.05	0.03	Average of 23 tests
	8.50 x 10	Buckshot clay, cone index 37-74	Not recorded	6.5		W	0.03	0.02	0.01	
Gee-Clough and Sommer (1981)	4.00 x 8 smooth implement tyre	Loam (12% moisture) cone index 300 kPa cone index 550 kPa cone index 900 kPa	117	1.0		W	0.066 0.10 0.13	0.035 0.032 0.015	0.015 0.009 0.001	
McAllister et al (1981)	7.50 x 16 tractor front	Stubble on sandy clay loam. Cone index 1034 kPa	212 406	6.0 10.0		W W	0.060 0.015	0.017 0.016	0.005 0.010	
		Stubble on clay. Cone index 794 kPa	212 406	6.0 10.0		W W	0.040 0.023	0.023 0.018	0.013 0.014	
	7.50 x 16 implement	Stubble on sandy clay loam. Cone index 1034 kPa	212	6.0		W	0.048	0.021	0.010	
		Stubble on clay. Cone index 794 kPa	212	6.0		W	0.037	0.020	0.011	

Table 3.3 The coefficients of cornering stiffness of tires [1]

behaves like a solid tire with a greater friction. But a softer rubber under relatively more load also exhibits deformation at the contact patch. It has similar characteristics to a pneumatic tire, and the cornering force can be calculated by the formula (3.18).

3.3.3 The lateral force of CONCIC-2 AGV

The motorized wheels of CONCIC-2 AGV are located in the lateral center line of the AGV, and the vehicle is steered by varying the velocity of these two wheels. There are no steering action involved in these two driving wheels. The cornering force are therefore zero. Since the model assumed no side-slip at the motorized wheels, side-friction is assumed to balance the centripetal force at any time.

The casters are located in the longitudinal axis of the vehicle. When the velocity vector at the pivot point is not align with the wheel plane of the caster, the pivot point led the caster sideways as well as forward. As the results, a side-friction acts at the contact patch to prevent side-slip. The offset of the caster and the side friction results a torque to force the caster to rotate about the pivot point until its plane is in line with the velocity vector of the pivot point.

The side-friction of the casters can be calculated by using the formula (3.17).

$$F_{ln} = k_n \cdot N_l \quad (3.19)$$

The coefficient of friction of the casters is not available from the manufacturer for CONCIC-2, it is chosen as 0.01 though, the validation of the model. From the definition of side-friction, the direction of the force is always oppositely to the trend of side-slip and to align the caster to the

direction of the velocity vector at the pivot point. Referring to section 2.3.2.2, the positive direction of side-friction is defined along the angle β_1 , or in other words, the positive direction of F_n is to have the caster rotate clockwise about the pivot point ($\delta > 0$). When the angle between the +Y axis and the velocity vector at pivot point is defined as α_1 , α_1 is calculated by (3.20) for CONCIC-2.

$$\begin{aligned}\alpha_f &= \arctan\left(\frac{-k \cdot \Omega_z}{V_y}\right) \\ \alpha_r &= \arctan\left(\frac{k \cdot \Omega_z}{V_y}\right)\end{aligned}\quad (3.20)$$

and the difference between the velocity vector of the pivot point and the caster heading is

$$(\alpha_1 - \delta_1)$$

When $(\alpha_1 - \delta_1) > 0$, then F_{ln} acts in the positive direction (Fig. 12). Otherwise, F_{ln} acts in the negative direction when $(\alpha_1 - \delta_1) < 0$. In the case of $(\alpha_1 - \delta_1) = 0$, there is no side-friction on the caster since the caster is in line with the velocity vector of the pivot point. Thus the sign of the lateral force is calculated by the following formula:

$$\arctan\left(\frac{-k \cdot \Omega_z}{V_y}\right) - \delta_f \quad (3.21)$$

where k is the wheel-base of the CONCIC-2 vehicle.

So the formula of the side-friction of casters of CONCIC-2 AGV may be written as

$$\begin{aligned}F_{fn} &= k_n \cdot N_f \cdot \text{sign}\left[\arctan\left(\frac{-k \cdot \Omega_z}{V_y}\right) - \delta_f\right] \\ F_{rn} &= k_n \cdot N_r \cdot \text{sign}\left[\arctan\left(\frac{k \cdot \Omega_z}{V_y}\right) - \delta_r\right]\end{aligned}\quad (3.22)$$

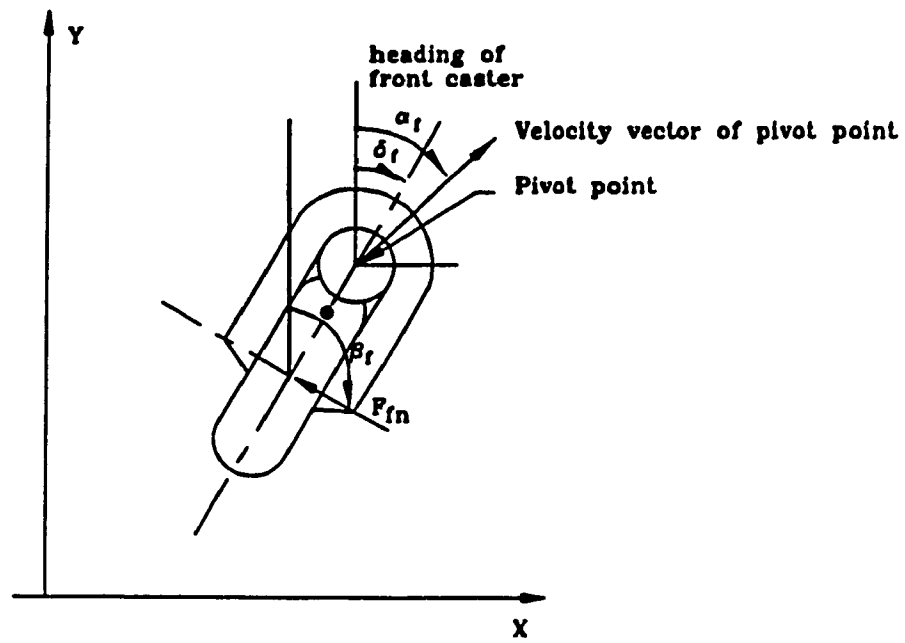


Fig. 3.12 The side friction force at caster

3.4 The equations of motion of CONCIC-2 AGV system with formulated forces

The external forces on the motorized wheels are summarized in the follows:

$$\begin{aligned}
 F_{1t} &= \frac{n}{r_d} [k_t I_1 - \frac{Jn}{r_d} (\dot{V}_y - \ell \dot{\Omega}_z) - \frac{Dn}{r_d} (V_y - \ell \Omega_z) - T_f] \\
 F_{2t} &= \frac{n}{r_d} [k_t I_2 - \frac{Jn}{r_d} (\dot{V}_y + \ell \dot{\Omega}_z) - \frac{Dn}{r_d} (V_y + \ell \Omega_z) - T_f] \\
 F_{1f} &= k_1 (1 + k_2 V_y - k_2 \ell \Omega_z) \cdot N_1 \\
 F_{2f} &= k_1 (1 + k_2 V_y + k_2 \ell \Omega_z) \cdot N_2
 \end{aligned} \tag{3.23}$$

where $k_1 = 0.007$, $k_2 = 0.01$.

Substituting the above equations into equations (2.27), the equations of motion of the AGV body are

$$\begin{aligned}
 (m + \frac{2n^2 J}{r_d^2}) \dot{V}_y &= \frac{nk_t}{r_d} (I_1 + I_2) - (\frac{2n^2 D}{r_d^2} + 2 k_1 k_2 N_d) V_y \\
 &\quad - 2 k_1 N_d - F_{ff} \cos(\delta_f) + F_{fn} \cos(\beta_f) - F_{rf} \cos(\delta_r) + F_{rn} \cos(\beta_r) \\
 (I_z + \frac{2n^2 \ell^2}{r_d^2}) \dot{\Omega}_z &= \frac{\ell \cdot n \cdot k_t}{r_d} (I_2 - I_1) - (\frac{2n^2 D}{r_d^2} + 2 k_1 k_2 N_d) \ell^2 \Omega_z \\
 &\quad + k [F_{rn} \sin(\beta_r) - F_{rf} \sin(\delta_r) - F_{fn} \sin(\beta_f) + F_{ff} \sin(\delta_f)]
 \end{aligned} \tag{3.24}$$

The external forces acting at casters are:

$$\begin{aligned}
 F_{fn} &= k_n \cdot N_f \cdot \text{sign}[\arctan(\frac{-k \cdot \Omega_z}{V_y}) - \delta_f] \\
 F_{rn} &= k_n \cdot N_r \cdot \text{sign}[\arctan(\frac{-k \cdot \Omega_z}{V_y}) - \delta_r] \\
 F_{rf} &= k_1 (1 + k_2 V_{fp}) \cdot N_f \\
 F_{rf} &= k_1 (1 + k_2 V_{rp}) \cdot N_r
 \end{aligned} \tag{3.25}$$

Substituting the above forces into the equations (2.28), the equations of

motion of casters are:

$$\begin{aligned} I_{fz} \ddot{\delta}_f &= k_n \cdot N_f \cdot d \cdot \text{sign}[\arctan(\frac{-k \cdot \Omega_z}{V_y}) - \delta_f] \\ I_{rz} \ddot{\delta}_r &= k_n \cdot N_r \cdot d \cdot \text{sign}[\arctan(\frac{-k \cdot \Omega_z}{V_y}) - \delta_r] \end{aligned} \quad (3.26)$$

where $k_1 = 0.007$, $k_2 = 0.01$, and $k_n = 0.01$.

And β_f and β_r are calculated by

$$\begin{aligned} \beta_f &= \delta_f + 90^\circ \\ \beta_r &= \delta_r + 90^\circ \end{aligned} \quad (3.27)$$

CHAPTER 4 SERVO CONTROL SYSTEM

4.1 Introduction

Closed-loop velocity control (velocity servo control loop) provides smooth vehicle operation and consistent performance of the guidance control software. A typical speed control loop is shown in Fig. 4.1. It includes a servo controller, a power amplifier, the servo motor, and the speed sensor. The servo controller is used to eliminate the error between the speed set-point and the real speed which is detected by the speed sensor. When a digital controller is used as the servo controller, the digital signal is converted to an analog signal by a DAC. This analog signal is amplified by the power amplifier in order to drive the servo motor. Servo controllers are now available on the market. These controllers usually have an independent processor, and some interface to the host computer and amplifiers. LM628 is a servo controller which is used by CONCIC-2 AGV, and more details about the chip is given in section 4.2.1.

4.2 Servo control system of CONCIC-2 AGV

CONCIC-2 AGV servo control system consists a LM628 chip, an DAC and a amplifier (Fig. 4.2). The host processor communicates with LM628 through an I/O port to facilitate programming a trapezoidal velocity profile and a digital compensation filter. The DAC output of LM628 interface with an external D/A converter to produce the signal that is power amplified and applied to the motor. An incremental encoder at the motorized wheel provides feedback for closing the servo loop. The trapezoidal velocity profile generator calculates the reference velocity. During the operation, the LM628

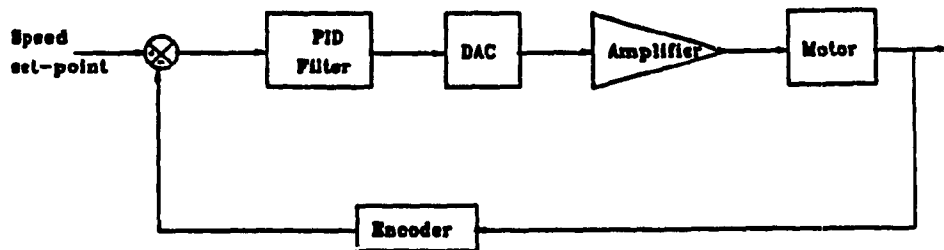


Fig. 4.1 Typical speed control for AGV

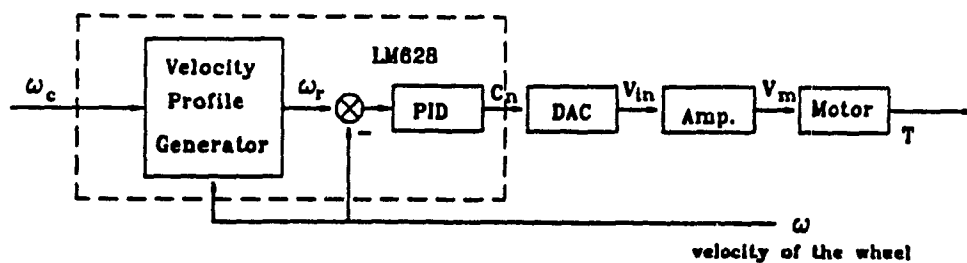


Fig. 4.2 Servo loop of CONCIC-2 AGV

subtracts the actual velocity from the reference velocity, and the resulting velocity error is processed by the digital filter to drive the motor to desired speed.

4.2.1 General description of LM628

The LM628 is a precision motion controller manufactured by National Semi-conductor Corporation. The LM628 is a dedicated motion-control processor designed for use with a servo motor and servo mechanisms which provides an incremental feedback signal. The chip includes elements such as host-interface, PID filter, and position feedback processor. These elements perform the intensive real-time computational task required by a fast performance digital motion control. It can be operated at both velocity and position modes. The host control software interface is facilitated by a high-level command set. The chip also provides a real-time programmable host interrupts (Appendix C). It has 32-bit position, velocity, acceleration registers. The trapezoidal velocity profile generator has a programmable acceleration downloaded from host processor. The coefficients of PID filter are also programmable. An incremental encoder is installed on the shaft of the motorized wheel. Three inputs are provided: two quadrature signal inputs, and an index pulse input. The quadrature signals are used to keep track of the position of the motor. The output from the LM628 to the DAC can either a latched eight-bit parallel output or a multiplexed 12-bit output. The 8-bit can be directly connected to a non-in or out-latching D/A converter, the 12-bit output can be demultiplexed using an external 8-bit and a input latching 12-bit D/A converter. As an external servo controller from the host processor, the LM628 operates at a high sampling time as 341

μ s. It also decreases sample time for the overall control by removing the servo controller from the host computer, so as to improve the performance of the overall control which is carried out by the host processor.

Table 4.1 provides a brief summary of the specifications offered by LM628.

4.2.2 Modeling the servo system of CONCIC-2 AGV

Since the dynamics of electronic parts are much smaller than mechanical parts, so the dynamic responses of the electronic parts in the CONCIC-2 AGV servo system are neglected in the modeling.

The functions of the electronic parts and the control software in the servo control system are obtained through experiments. The mid-way control signals are measured to derive the functions. The experiment results and the mathematic formulae for CONCIC-2 AGV servo system are presented.

4.2.2.1 Trajectory Generator

The trapezoidal velocity profile generator computes the reference velocity of motor versus time. The motor accelerates to the command velocity at specified acceleration rate and maintains the value until command to change to a new velocity.

This function is executed at each sampling interval. the specified acceleration value is added to the current desired velocity to generate a new desired velocity (unless the command velocity has been reached).

$$\omega(n) = \omega(n - 1) + a_a \cdot T_{ss} \quad (4.1)$$

Where $\omega(n)$ is the motor velocity at sampling time n , a_a is the desired acceleration, and T_{ss} is the sampling interval of the servo control loop.

Features:

- 32-bit position, velocity, and acceleration registers
- 750 kHz encoder-state capture rate
- 341 μ s sampling interval
- Programmable digital PID filter with 16-bit coefficients
- 8 or 12 bit DAC output data (LM628)
- 8-bit sign-magnitude PWM output data (LM629)
- Internal trapezoidal velocity profile generator
- Velocity, target position, and filter parameters may be changed during motion
- Position and velocity modes of operation
- Real-time programmable host interface
- Quadrature incremental encoder interface with index pulse input
- Programmable derivative sampling interval (341 μ s to 87,381 μ s, or $341.33 \times 256 \mu$ s)
- 6 MHz clock frequency

Table 4.1 Summary of specifications of LM628

This can be illustrated in Fig. 4.3.

The acceleration a_a is a programmable parameter from the host computer. Larger acceleration gives faster response but higher starting current. In chapter 6, a more detailed discussion of choosing acceleration of trajectory profile generators is presented.

4.2.2.2 Model for PID filter:

Having over 50 years of history, PIDs are still the most popular controllers in the field of industrial control. A typical control system with PID controller is presented in Fig. 4.4.

The transfer function of the controller is

$$G(s) = K_p + \frac{K_i}{s} + K_d \cdot s \quad (4.2)$$

There are several way to implement PID controller into digital computers.

The LM628 uses a digital Proportional Integral Derivative (PID) filter to compensate the control loop.

The following discrete-time equation illustrates the control performed by LM628 (Appendix C)

$$C[i] = k_p e[i] + k_i \sum_0^n e[i] + k_d \{e[i] - e[i - 1]\} \quad (4.3)$$

Where $C[i]$ is the motor control signal output at sample time i , $e[i]$ is the velocity error at sample time n and k_p , k_i , k_d are the discrete-time PID controller gains. Again, k_p , k_i , k_d are also input from the host computer, and proper values for the three parameter have to be tuned to get the best performance of the servo system. The parameters of CONCIC-2 AGV are chosen as $k_p = 100$, $k_i = 225$, and $k_d = 50$ by experiments. Another important parameter, integration-limit, is introduced to minimize integral or reset

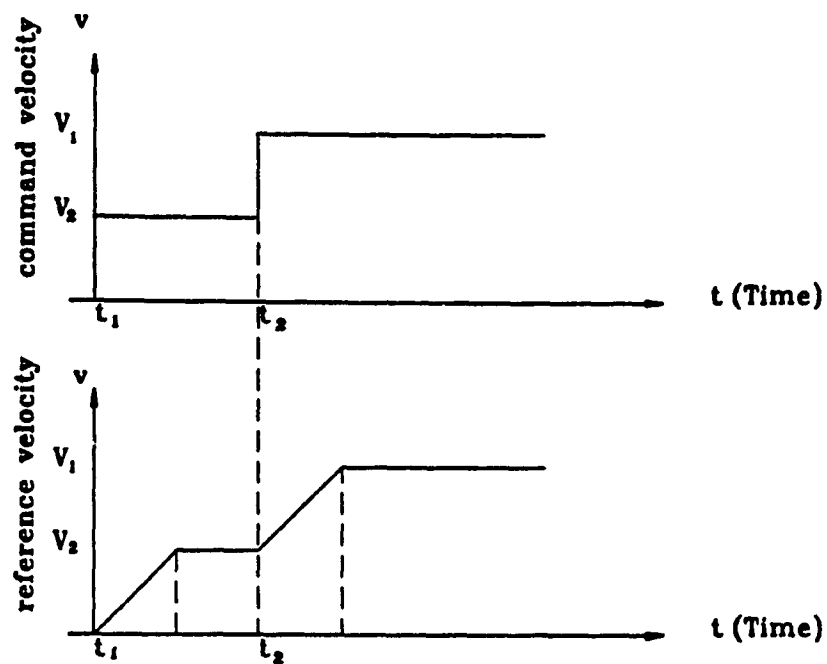


Fig. 4.3 Velocity-profile generator

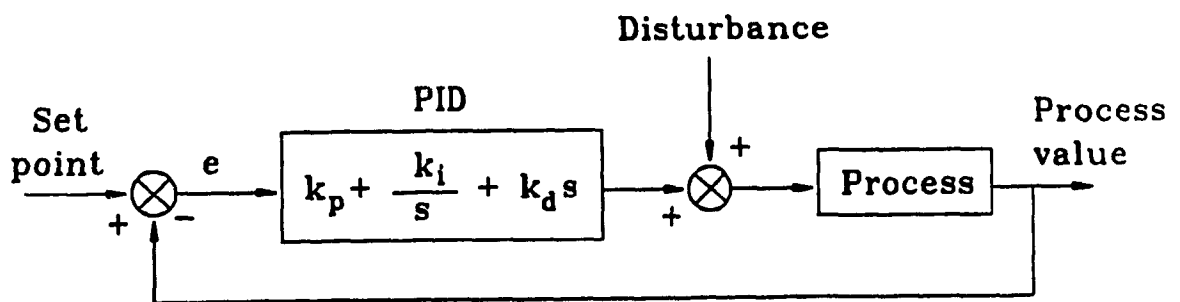


Fig. 4.4 Typical control loop with PID controller

"wind-up" (an overshooting effect of integral action). The Integration-limit constrains the contribution of the integration term

$$k_i \cdot \sum_{x=0}^n e(x)$$

The limit of CONCIC-2 is 30.

4.2.2.3 Model for DAC:

A Digital Analog Converter (DAC) functions a linear data conversion from digit data to analog signal. The servo system contains a 8-bit DAC. The 8-bit digital control signal from the LM628 is converted into analog voltage signal by this converter. The input-output relationship of a 8-bit DAC is represented in Fig. 4.5. The converter gives a linear voltage output of a range of -9.2 to +9.2 volts. Corresponding to the 8-bit digital value which starts with the minimum value (0) to the maximum value (256). The output voltage will be zero at the digital value of 128, which means if the control voltage from the servo system is zero (output from the power amplifier), the output digital value to the DAC has to be 128, and this simple data converting is taken care of by the operation software in the host computer.

The mathematical models of the above relationships may be written as

$$\text{Digital value input of DAC (x)} = \text{Output from Amp. (C}_n\text{)} + 128$$

$$\text{Voltage output of DAC (y)} = 0.0725 \cdot x - 9.2$$

So the conversion coefficient of DAC (K_{DAC}) which is defined as the ratio between y and C_n is derived as

$$y = 0.0725 \cdot x - 9.2$$

$$y = 0.0725 \cdot (C_n + 128) - 9.2 = 0.0725 \cdot C_n - 0.08$$

$$K_{DAC} = \frac{y}{C_n} \approx 0.0725 \quad (4.4)$$

4.2.2.4 Model for Amplifier:

The output of DAC is amplified by a power amplifier in order to drive the motor. The gain of the amplifier takes a important part in the servo system. Since the output of the amplifier is the input voltage of the servo motor, and the range of input voltage of the motor is from - 24 V to + 24 V. Therefore the amplifier has been chosen for the servo loop in order to let the motor work within this range.

Fig. 4.6 presents the characteristic of the power amplifier.

As shown in the graph the relationship between the input voltage and the output voltage is not linear. To develop the mathematical expression for it, we use three pieces of straight lines to fit the curve in the range of -24 volts to +24 volts.

The linear approximation is made as

$$\begin{aligned} V_m &= 4.5 V_{in} & V_{in} &\leq 1.28 \text{ (volt)} \\ V_m &= 6.74(V_{in} - 0.39) & 1.28 < V_{in} &\leq 2.5 \text{ (volts)} \\ V_m &= 9(V_{in} - 1) & V_{in} &> 2.5 \text{ (volts)} \end{aligned} \quad (4.5)$$

where V_{in} is the output signal from DAC, V_m is the voltage signal to the motor.

4.3 The model of drive motor

The two driving motors of motor-wheel units are permanent magnet (PM) brush type 24 volts dc motors. An equivalent circuit is proposed by the [48] as Fig. 4.7. The motor is approximated by the resistance R , the inductance L , and the internal generated voltage E_g which is proportional to the motor speed ω , or

$$E_g = k_o \cdot \omega \quad (4.6)$$

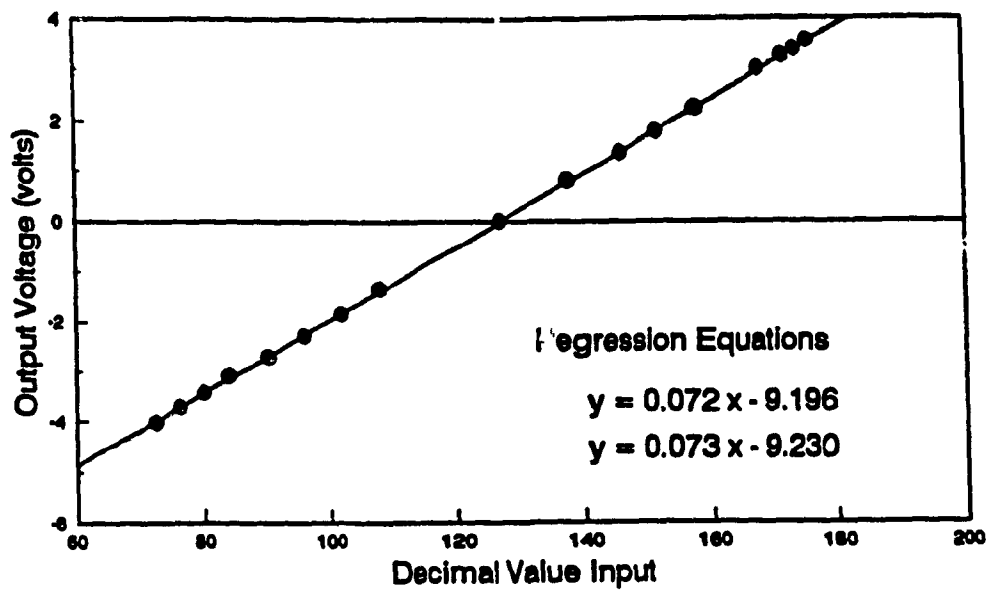


Fig. 4.5 DAC-08 calibration curve

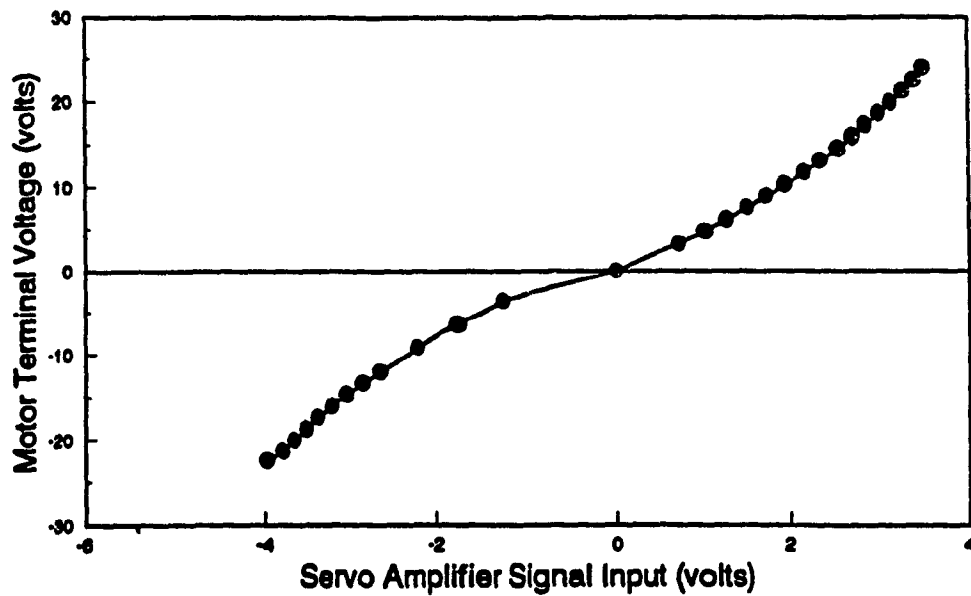


Fig. 4.6 Servo amplifier gain curve

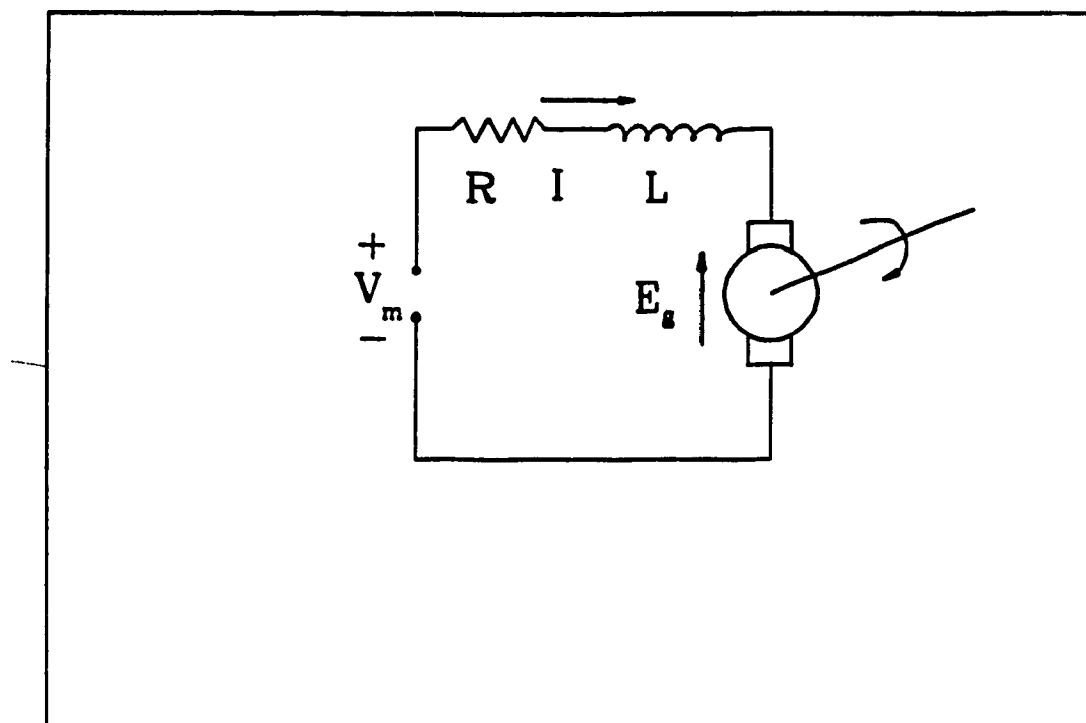


Fig. 4.7 Equivalent circuit of dc motor

Thus the electrical equation of the motor may be written as

$$V_m = L \frac{dI}{dt} + R \cdot I + E_g \quad (4.7)$$

Substituting equation (4.6) into (4.7), the electrical equation of the motor is obtained as

$$V_m = L \cdot \frac{dI}{dt} + R \cdot I + k_g \cdot \omega \quad (4.8)$$

CHAPTER 5 GUIDANCE SYSTEM

5.1 General description

The objective of a guidance system of an AGV is to steer the vehicle back on course based on the derivation between the current position of the vehicle and the reference. As in the definition introduced in chapter 1, the guidance system includes the sensor and the control strategy. Various control strategies (or control laws) have been developed based on the different implementation of guidance. Based on the survey, the control strategies can be classified into two categories. For free-ranging AGVs, the control strategy includes path planning and the guidance controller of destination control. And the control strategies of the AGVs which follow a continuous reference track have only the guidance controller of regulation tracking.

In destination control, the control variable for the overall loop is a point of the reference path. This method directly controls the trajectory of the vehicle. It is often seen in a guidance system with a non-continuous reference path. But in regulation tracking, the control variable for the overall system is the deviation between the vehicle and the reference path (track). This method attempts to eliminate the errors between the vehicle and the track without time or distance limitation. It does not require a specific trajectory for the AGV to approach the guide track. It is often seen in the guidance of the AGV with a continuous guidance track.

The guidance of the vehicle (either destination control or regulation tracking) is finally carried out by the corresponding servo control loops of different configurations. For example, the servo variables are the steering

angles for tricycle configuration, and the two differential speeds of the two motorized wheels for differential drive steering. The guidance controller is defined to be present the relationship between the servo variables. The output of the guidance controller can be either directly or indirectly servo variables of the vehicle. The destination control needs to control all the servo variables of the vehicle in order to control the trajectory. And the regulation tracking only needs to control some of the servo variables since the continuous reference track provides a continuous message to regulate the vehicle. Compared with the destination control, the guidance controller of regulation tracking is much simpler. The following gives some examples for a tricycle configured vehicle using both destination control and regulation tracking.

Destination control.

In [21], Y. Kanayama et al. introduced a control law for AGV control by using PID controller. Assuming the current position and the reference position of a vehicle are $p_c(x_c, y_c, \theta_c)$ and $p_r(x_r, y_r, \theta_r)$ respectively, then the error vector between them is defined as

$$e_x = (x_r - x_c)\cos\theta_c + (y_r - y_c)\sin\theta_c$$

$$e_y = (y_r - y_c)\cos\theta_c + (x_r - x_c)\sin\theta_c$$

$$e_\theta = \theta_r - \theta_c$$

The classic PID filter is used to generate vehicle's forward velocity and angular command velocity with the error vector. The guidance controller is presented in following equations:

$$V_{cy} = k_1 \cdot e_x + k_2 \int e_x \cdot dt + k_3 \frac{de_x}{dt}$$

$$\omega_{cz} = k \cdot e_y + k_5 \int e_y \cdot dt + k_6 \frac{de_y}{dt} + k_7 \cdot e_\theta + k_8 \int e_\theta \cdot dt + k_9 \frac{de_\theta}{dt}$$

Regulation tracking

A linear controller was proposed by Cheng et al. for the CONCIC-1 vehicle in 1984. This controller is designed based on tricycle configured vehicle with a optical camera as sensor. It may also be applied to other type of AGV which follows a continuous path and has the capability to provide the deviation between the vehicle and track. The guidance controller is presented as follows

- The deviation between the vehicle and track is presented into two terms:

the position offset ϵ_d is defined as the perpendicular distance between the track and the center of the sensor (camera in the case of CONCIC-1).

the orientation error ϵ_θ is defined as the angle between the longitudinal axis of the vehicle and the track.

- The steering angle θ_s for a tricycle is

$$\theta_s = G_1 \cdot \epsilon_d + G_2 \cdot \epsilon_\theta$$

where the G_1 and G_2 are constants.

5.2 Guidance system of CONCIC-2 AGV

CONCIC-2 AGV employs a relatively inexpensive camera vision technique. An optical camera was installed at the head of the vehicle to pick up the

deviation of the vehicle related to the reference track or the signals on the ground. The track to be followed in this case is prepared on the floor by painting, taping or fabricated in loops or circuits linking all possible sources and destinations which vehicles are to serve. The sensor is IDETIX digitizing camera from Micron Technology with an IS32 optic ram. A camera controller board provides the interface from the camera to the 8088, 80286, or 80386 microprocessors. Pixel information is transferred from the controller to the PC memory using the Direct Memory Access (DMA). Also on the controller board there is a 63701 micro controller which has a 8 bit port for transferring data between the PC and internal memory of 63701. There are 18 bytes data to be downloaded to the micro controller from PC to determine the size of the image window and the other parameters for the next image [35]. This type of sensor has the advantages of being able to focus on the path, while having a controllable width of view by changing the distance between the camera and the ground. The deviation of the vehicle from the track is calculated by the PC using the image, and a digital controller is implemented in the on-board computer to steer the vehicle so as to reduce the deviation (position and orientation) together with the two servo loops.

5.2.1 The measurement of deviation (image analysis)

The IS32 optic ram has two arrays of 128 rows and 256 columns of light sensitive elements. The upper array of 64x256 elements is used only for the CONCIC-2 navigation. The image received only from the alternate elements in a row and hence the image window is actually 64x128 pixels. The camera is fitted with 8 mm lens. The distance between the lens and the ground is approximately 200 mm. At this distance, the actual size corresponding to the

image window is about 30 mm deep and 128 mm width. In other words, one pixel stands for about 1 mm in the width and about 0.5 mm in depth. The track is about 30 mm in width and about 30 pixels in the image window.

The track of CONCIC-2 AGV can be straight lines, circles, and any kinds of curves. Since there are limit speeds for the two motorized wheels, the radius of curvature of the track also has a limit. The smallest radius of curvature for experiments of CONCIC-2 is about 1.75 m. The image window of the camera is about 30mm deep, it is reasonable to approximate the track seen by the camera as a straight line (see Fig.5.1). So the location and the orientation of the track within the camera window can be presented by an equation in the form of

$$y = m x + c \quad (5.1)$$

where y and x are the coordinates of the image window in meters [35]. This coordinate system is parallel to the body-centered system of the AGV body since the camera is mounted on the longitudinal axis of the vehicle. m is slope of the image of the track, and c is offset the center line of the image of the track. The deviation of CONCIC-2 AGV from the guidance track is defined by two errors ϵ_d and ϵ_θ (position error and orientation error), and their definitions are as follows:

- Position error ϵ_d :** It is defined as the perpendicular distance between the center line of the track and the camera image window center line along the lateral center line of the camera image window.
- Orientation error ϵ_θ :** It is the angle between the direction of travel of the vehicle and the direction pointed to by the track.

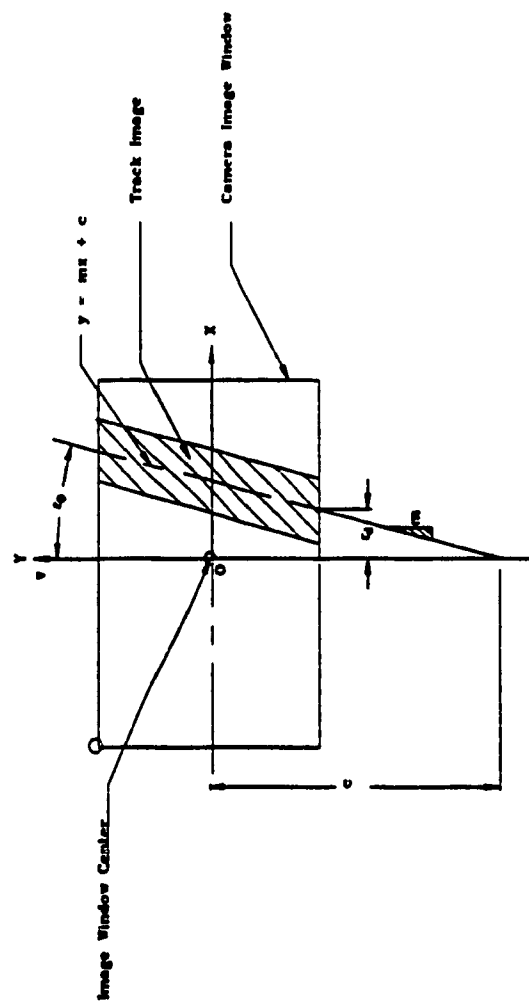


Fig. 5.1 The image window of the camera

Referring to the equation (5.1) and Fig. 5.1, the position error ϵ_d and the orientation error ϵ_θ have some relationship with m and c in the equation of the image of the track. ϵ_d equal to x in the equation (5.1) when y equals to zero, and the ϵ_θ is the arctangent of the slop of the image $1/m$.

$$\begin{aligned}\epsilon_d &= -\frac{c}{m} \\ \epsilon_\theta &= \cotan^{-1}(1/m)\end{aligned}\tag{5.2}$$

From the above, it is seen that the deviation of the vehicle from the track is calculated from the image of the track in the camera window. Thus the location of the camera is an important consideration. Chapter 6 presents some simulation experiments about the effects of camera location on the dynamic response of the vehicle.

5.2.2 The guidance controller of CONCIC-2 AGV

CONCIC-2 AGV uses a regulation tracking method in its guidance. The guidance controller attempts to eliminate the deviation of the vehicle from the track. In other words, the outputs of the controller are the variables to steer back the vehicle to the track base upon ϵ_d and ϵ_θ detected by the camera sensor. The direct approach is to regulate the two speed of the two motorized wheels based on the deviation. CONCIC-2 uses a indirect approach which is discussed below.

For a tricycle configured vehicle with a steering wheel in the front, the direction of vehicle travel is determined by the steering wheel with a certain steering angle. If the vehicle is found off the track, it can be eventually driven back to the track by steering the front wheel towards the track. This approach is used by the CONCIC-2 vehicle. The guidance controller presents the relationship between the deviation and the steering

angle as in the following formula

$$\theta_{cs} = G_1 \cdot \epsilon_d + G_2 \cdot \epsilon_\theta \quad (5.3)$$

where G_1 and G_2 are called as the offset gain and orientation gain of the controller respectively.

In the control of CONCIC-2 AGV, a steering wheel is considered to be located virtually somewhere on the longitudinal axis of the vehicle. This steering wheel is defined as virtual steering wheel. In the current design, the virtual steering wheel is assumed to be located in the position of the front caster [Fig. 5.2]. Thus the CONCIC-2 AGV can be considered as a tricycle with a steering wheel at the location of front caster and two rear wheels at the location of two motorized wheels. Then at a steering angle as θ_{cs} , the corresponding angular velocity of the vehicle is calculated as follows.

$$\omega_{cz} = \frac{V_y \cdot \tan \theta_{cs}}{L} \quad (5.4)$$

where V_y is the linear velocity at the geometrical center of the vehicle, and the L is the wheel-base of the equivalent tricycle-configured vehicle (the distance from the contact point of the steering wheel to the center of the two rear wheels). Since the caster have a offset between the pivot point and normal axis through the center of the caster, the wheel-base will be changed. Hence the equivalent wheel-base for CONCIC-2 AGV is as:

$$L_{ae} = k - d(1 - \cos \theta_{cs}) \quad (5.5)$$

where k , d are defined as before.

Then the control angular velocity of the vehicle is

$$\omega_{cz} = \frac{V_y \cdot \tan \theta_{cs}}{L_{ae}} \quad (5.6)$$

Being a differential drive steering configuration, the angular velocity of CONCIC-2 is obtained by varying the speed at two motorized wheels. To obtain a angular velocity as ω_{cz} , the speed at two motorized wheel of the vehicle are calculated by equations (5.7) from the geometrical relationship of the AGV.

$$V_{c1} = V_y - \omega_{cz} \cdot l \quad (5.7)$$

$$V_{c2} = V_y + \omega_{cz} \cdot l \quad (5.7)$$

In summary, the control strategy of CONCIC-2 AGV is as follows:

- 1) Obtain the equivalent steering angle from the deviation

$$\theta_{cs} = G_1 \cdot \varepsilon_d + G_2 \cdot \varepsilon_\theta \quad (5.8)$$

- 2) Calculate the corresponding angular velocity of CONCIC-2 AGV

$$l_{ae} = k + d(1 - \cos\theta_{cs}) \quad (5.9)$$

$$\omega_{cz} = \frac{V_y \cdot \tan\theta_{cs}}{l_{ae}} \quad (5.10)$$

- 3) Calculate the control velocities for the two velocity servo loop

$$\begin{aligned} V_{c1} &= V_y - \omega_{cz} \cdot l \\ V_{c2} &= V_y + \omega_{cz} \cdot l \end{aligned} \quad (5.11)$$

CHAPTER 6 SIMULATION AND ANALYSIS

6.1 Simulation program

A simulation program has been implemented in a personal IRIS computer using C programming language. The AGV system consists of mechanical and electrical components, and there is also a combination of continuous and discrete time systems. Thus in the program, both logic and timing control have to be considered.

The timing control of the program presents the property of the multi sample digital control of the system. In the CONCIC-2 AGV, there are two important sample intervals for the two types of control systems. The two velocity servo loops which are built with a LM628 motion controller, a DAC, and a power amplifier have relatively high sampling rates. The LM628 chip provides a sampling rate of about $341 \mu\text{s}$ which ensures the fast performance of the servo loop. The regulation tracking loop which includes the image processing, the guidance controller, and the velocity servo loop has a much lower sampling rate. The sample interval for the regulation tracking loop is about 50 ms, which is almost 170 times longer than that of servo loops. And the image processing takes the major part of this 50 ms. These two sampling intervals are implemented by two feed-back counters in the simulation program as two zero-order-holds. The basic timing of the simulation is the integral step for solving the dynamic equation in a digital computer. All the feed-back counters are based upon the integral step which is chosen as 0.00005 s ($50 \mu\text{s}$) in simulation. As is shown in Fig. 6.1, the feedback counter for the velocity servo loop is calculated by

$$\frac{\text{sampling interval of velocity servo loop } 341 \mu\text{s}}{\text{integral step of simulation } 50 \mu\text{s}} \approx 7$$

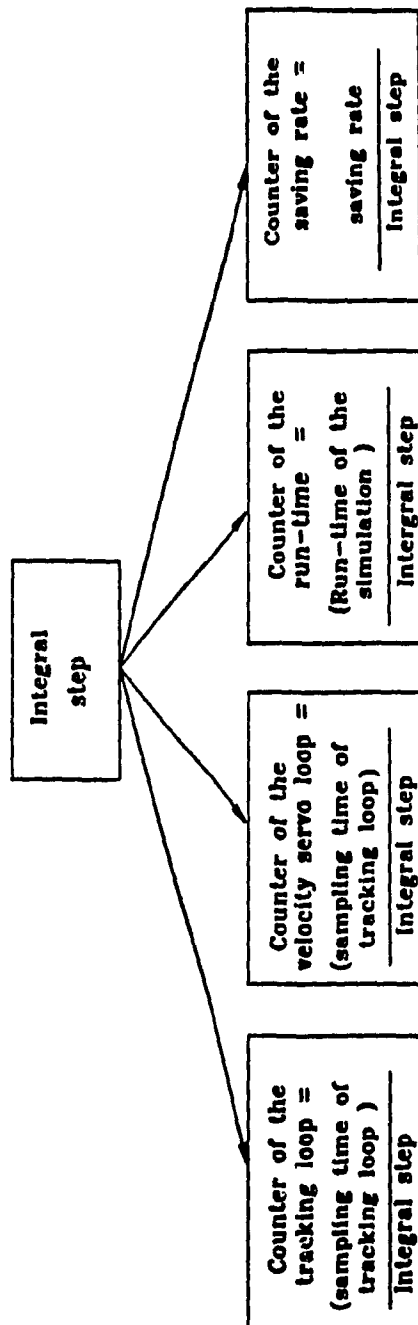


Fig. 6.1 Timing control of the simulation program

This simply means that the servo loop samples data at every 7 integral steps which is about 341 μ s. Similarly to the regulation tracking loop, the feedback counter is calculated by

$$\frac{\text{sampling interval of regulation tracking } 50 \text{ ms}}{\text{integral step of simulation } 50 \mu\text{s}} = 1000$$

The simulation program consists of 2 ".c" source files, a header file, and an input data file. One of the ".c" source file is agv.c. It is the main program of the simulation, including the AGV dynamics, the velocity servo loops, and the timing control. The program is designed to be in modular form. The motion equation of the AGV is implemented using both Range-Kutta and Euler methods. And the simulation results indicate that Euler method gives about the same accuracy as Range-Kutta and need much less time for running the same test at the integral step as 0.0005 s. The guidance system of the vehicle is implemented in the image.c file which contains the image analysis and guidance controller. The system parameters are defined in the header file para.h. Some operation data such as the initial position of the vehicle, the linear speed, and the acceleration constant, etc., are input from the data file input.dat.

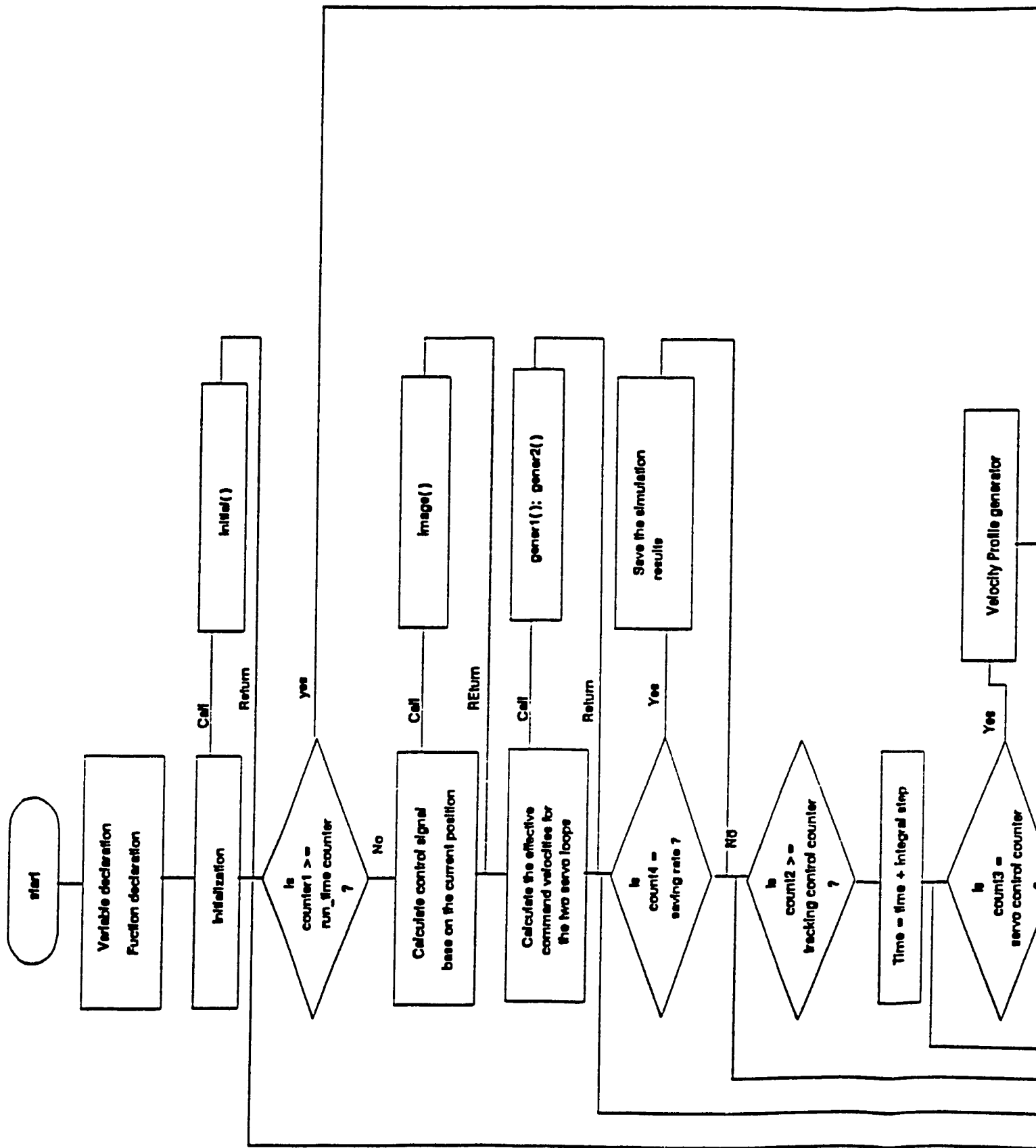
The flowchart of the program is shown in Fig. 6.2, and all the subroutines are listed as follows:

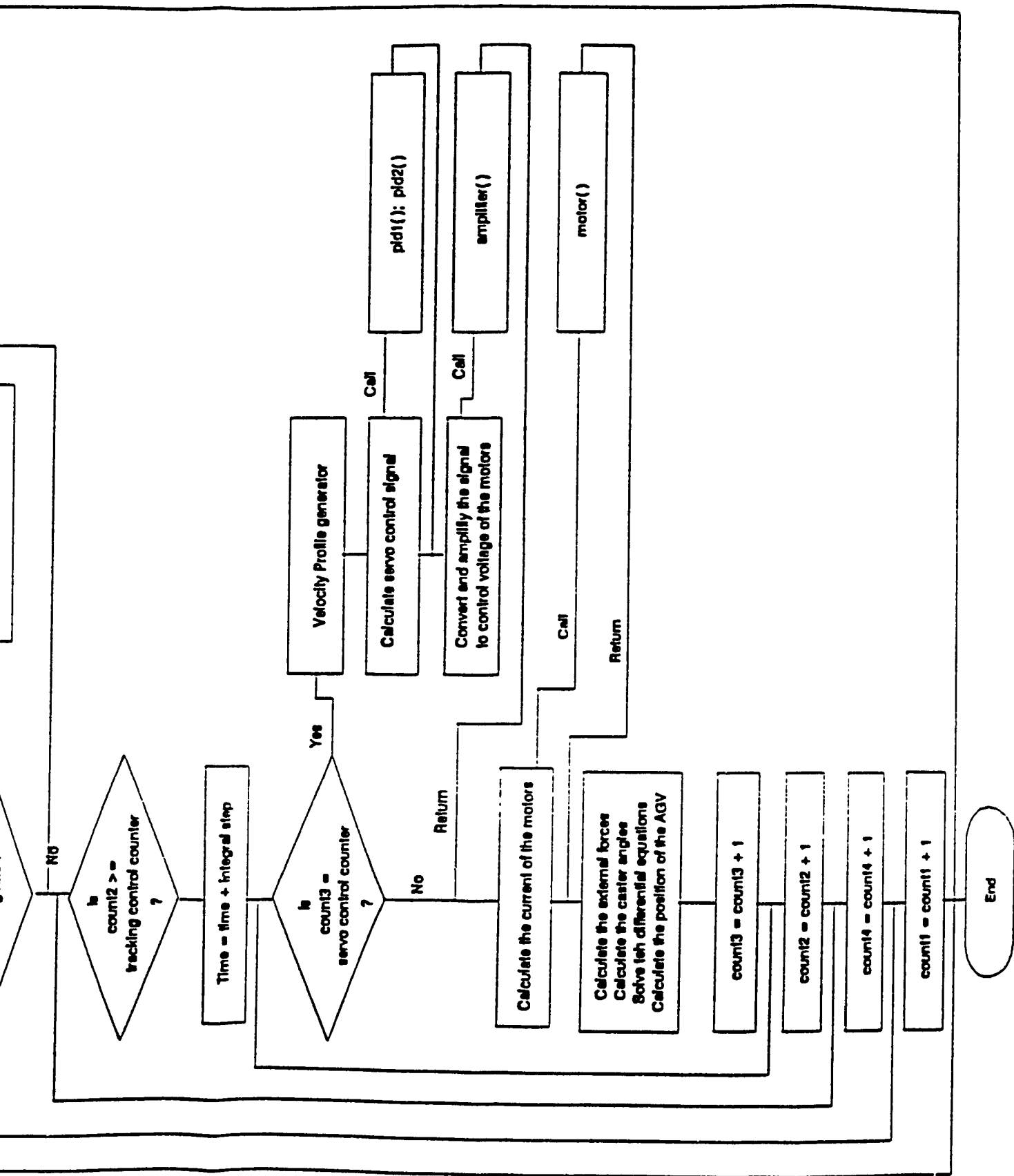
●initial(char *Fname)

Input the initial position of the AGV and the operation parameters. Initialize the working variables of the program.

●double image(double cgx, double cgy, double cx, double cy, double theta, double Rt, double V_des, double gain1, double gain2)

This program calculates the errors at the front and the rear camera, and outputs the control signal (the corresponding steering





rate of the equivalent tricycle) from the control strategy.

The inputs are:

cgx: x coordinate of the C.G of the vehicle in base system;

cgy: y coordinate of the C.G of the vehicle in base system;

cx: x coordinate of the front camera in base system;

cy: y coordinate of the front camera in base system;

theta: orientation angle of the vehicle in base system;

Rt: radius of the circular profile;

V_des: predefined linear velocity;

gain1: offset proportional control gain;

gain2: orientation gain.

● *pid1(double x, double y)* and *pid2(double x, double y)*

Implementation of the PID filter, the input variables are the current and previous errors, and the output is the control signal.

● *amplifier(double x)*

Implementation of the power amplifier of the servo system, the input of the function is the input signal of the amplifier, and the output is the amplified signal.

● *motor(double x, double y, double z)*

This subroutine represents the electrical characteristics of the driving DC motors, the inputs of the function are the previous motor voltage input, previous motor current and the current velocity. The output is the current from the motor.

● *sign(double x, double y)*

The *sign* function gives the sign of the difference of the two input values.

•gener1(double x) and gener2(double x)

This subroutine presents the geometric relationship of this type of vehicle, the input is the corresponding steering angle, and the outputs are the velocity commands for the servo control loops.

6.2 Simulation and experiment results

The simulation is carried out to investigate the guidance strategy, the servo control, and other properties of the CONCIC-2 vehicle. The results are organized into several sections such as model validation, study of guidance system, study of velocity servo loop, and the dynamics of the casters.

In the section on model validation, tests were done under different conditions to validate the model for the AGV at both tracking and servo loops. Study of guidance system covers the study on the AGV dynamics by changing settings of the guidance controller, the location of the camera, and the effects by the position of equivalent steering wheel. The mismatch of the two velocity servo control loops and some important properties of the LM628 chip are discussed in the section of the study of velocity servo loops. And the investigation on the contribution of the dynamics of caster to the overall system is given in section 6.2.4.

The study of CONCIC-2 AGV can be done with any type of continuous track. However, it is felt that the most stringent test for a vehicle of this type is its ability to realign itself rapidly after being subject to a sudden deviation in a straight path. This test is similar to investigating the transient response of a control system subject to a step-input or a step-disturbance.

For the purpose of this exercise, the vehicle is initially stationary

(zero speed) alongside a straight track, with a non-zero offset from the track. A step speed command is given, and the behavior of the vehicle is observed and recorded for a range of values of offsets, control parameters G_1 and G_2 , acceleration constants of the velocity profile generator, angles of the casters, and vehicle configuration.

Table 6.1 lists the design and operation parameters of the vehicle and the conditions for all experimental runs (without special specifications).

6.2.1. Model Validation

The advantage of this model is that it presents the real system accurately. It does not only present the characteristics of the system but also provides the exact values of the system. The model is examined in two levels:

- 1) Validation of the velocity servo loops,
- 2) Validation of the overall control system.

The details are presented in the following sections.

6.2.1.1 Validation of AGV model with velocity servo loops

In this case the validation of the model was done when the AGV only operated at velocity servo control loops. The vehicle is initially stationary, and the inputs to the vehicle are the two velocity commands to the servo loops. The outputs are the reference speeds of the wheels.

Fig. 6.3 presents the reference speed and the real speed of wheel 1 in both of the simulation and the experiment at 40 rpm (0.314 m/s). In the figure, the smooth line represents the simulation results, and the line with dot symbol presents the experiment data which is recorded by the on-board

<p>VEHICLE</p> <p>total mass moment of inertia wheel base wheel span distance between pivot point and camera</p> <p>MOTOR-WHEEL UNIT</p> <p>mass moment of inertia (refer to motor shaft) gear ratio radius of the wheel static friction of motor viscous damping factor torque constant voltage constant resistance of motor inductance of motor coefficient of rolling friction</p> <p>CASTER</p> <p>mass of caster polar moment of inertia offset coefficient of rolling friction coefficient of side friction</p> <p>SERVO LOOP</p> <p>gain of DAC gains of PID filter integral limit of PID filter</p>	<p>$m = 124.4 \text{ (kg)}$ $I_z = 14.6 \text{ (kg.m}^2\text{)}$ $k = 0.39 \text{ (m)}$ $l = 0.26 \text{ (m)}$ $l_c = 0.3 \text{ (m)}$</p> <p>$m_d = 9.5 \text{ (kg)}$ $J = 0.0025 \text{ (kg.m}^2\text{)}$ $n = 9.9$ $r_d = 0.075 \text{ (m)}$ $T_f = 0 \text{ (N.m)}$ $D = 0.0001 \text{ (N.m.s/rad.)}$ $k_t = 0.114 \text{ (N.m/A)}$ $k_g = 0.163 \text{ (Volt.s/m)}$ $R = 0.602 \text{ (}\Omega\text{)}$ $L = 0.0047 \text{ (H)}$ $k_1 = 0.007; k_2 = 0.01 \text{ (s/m)}$</p> <p>$m_c = 2.4 \text{ (kg)}$ $I_c = 0.001 \text{ (kg.m}^2\text{)}$ $d = 0.04 \text{ (m)}$ $k_{c1} = 0.007; k_{c2} = 0.01 \text{ (s/m)}$ $k_n = 0.01$</p> <p>$k_{dac} = 0.073$ $k_p = 225; k_i = 100; k_d = 50$ ± 30</p>
---	--

Table 6.1 The system parameters of CONCIC-2 AGV

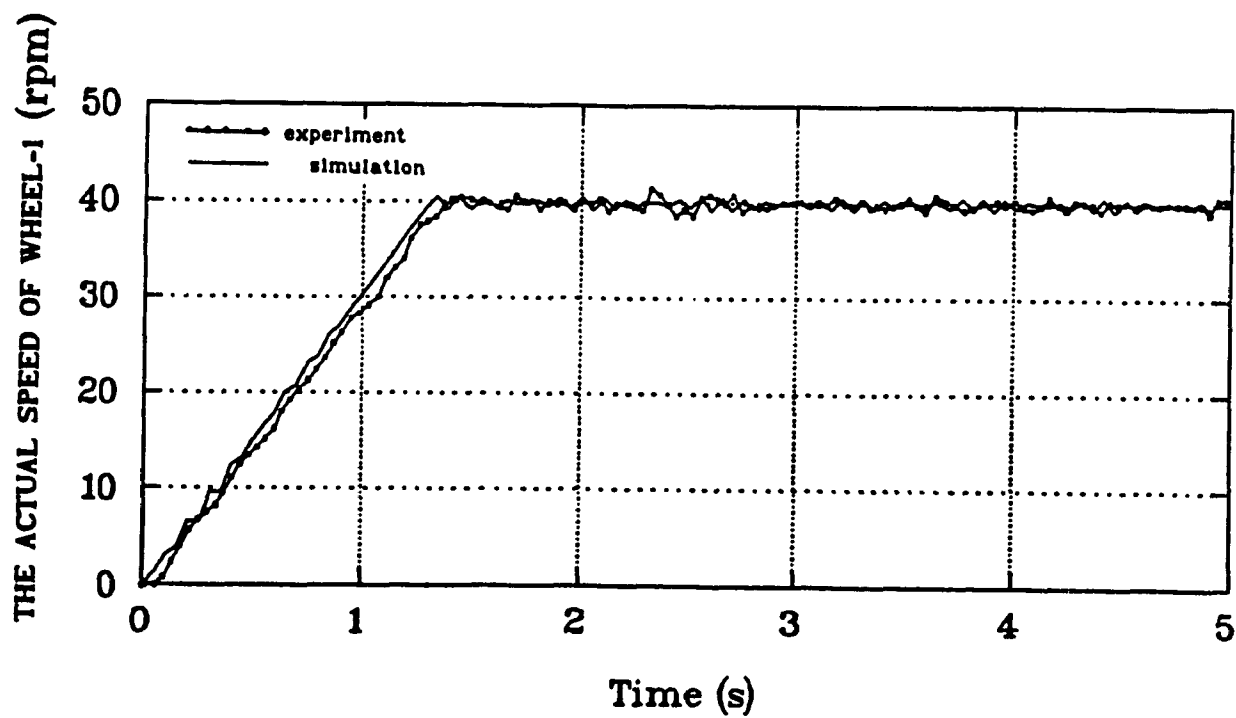
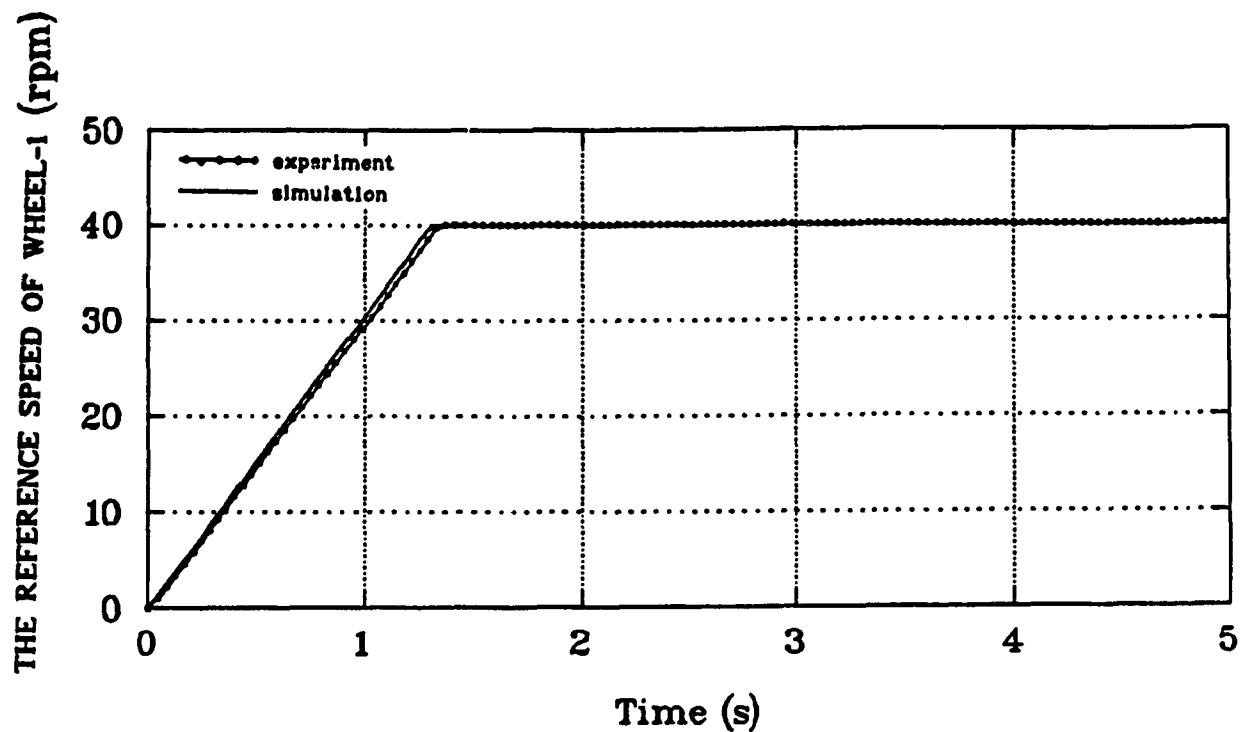


Fig. 6.3 Validation of the velocity servo loops
(wheel-1)

data-acquisition facility. The results show that the simulation and the experiments data are very close in both the reference speed and real speed curves. Only at the transient period, the real system responds little slowly than the model (less than 1 rpm). Compared to the reference speed curve, the real speed has a oscillation with small amplitude. Both the simulation and experiment illustrate this property. Similarly Fig. 6.4 shows the reference speed command and the real speed for wheel 2. The results also illustrate the realism of the model. The model of the AGV with only the servo loops is validated. Note the initial ramp is derived from the acceleration constant $a_a = 0.25 \text{ m/s}^2$.

6.2.1.2 Model validation with overall control system

For the complete model for the CONCIC-2 AGV, the following experiments were done to validate the dynamic model.

The track is a straight line, and the vehicle is initially stationary with an initial deviation from the reference track (position offset and orientation error). The tests were done under different initial conditions and different operational parameters, such as velocity, controller gains, acceleration constant a_a of servo loop etc. For the convenience of discussion, the results are presented in two groups:

- 1) AGV with a linear (proportional) guidance controller,
- 2) AGV with a PI (proportional and integral) guidance controller.

1) With linear guidance controller

A linear guidance controller is presented in the formula as

$$\theta_s = G_1 \epsilon_d + G_2 \epsilon_\theta \quad (6.1)$$

and the proportional gains are G_1 and G_2 .

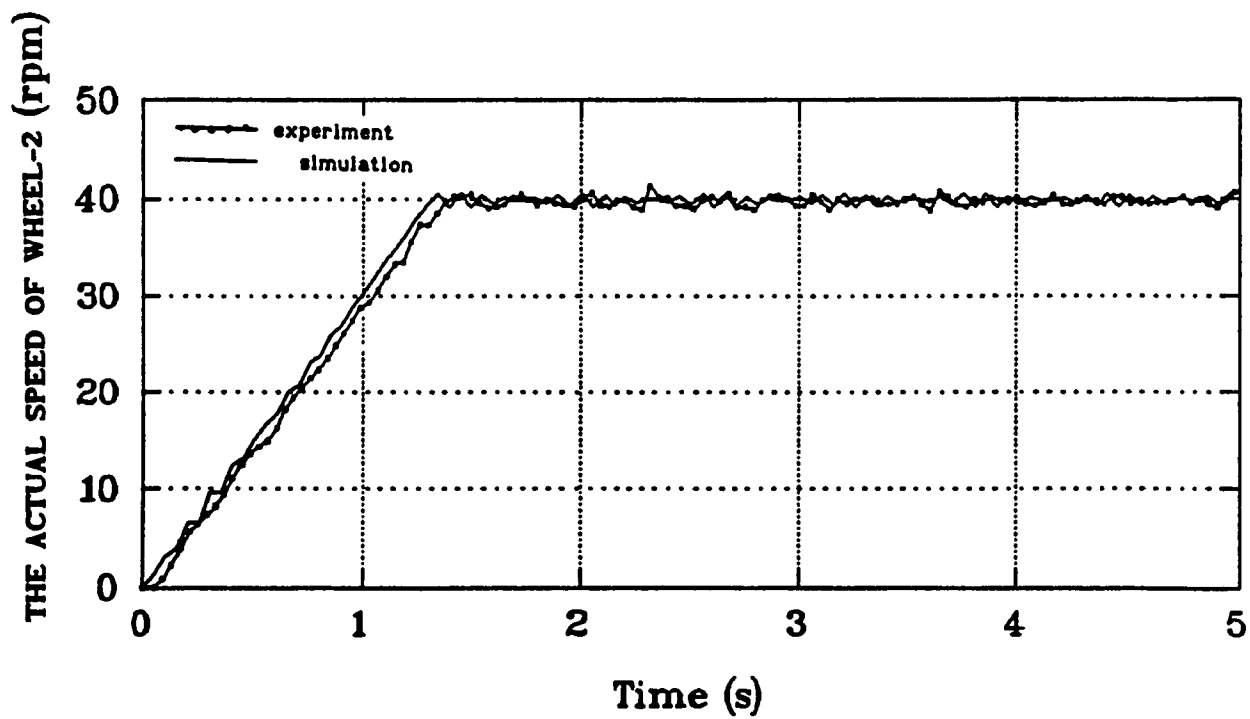
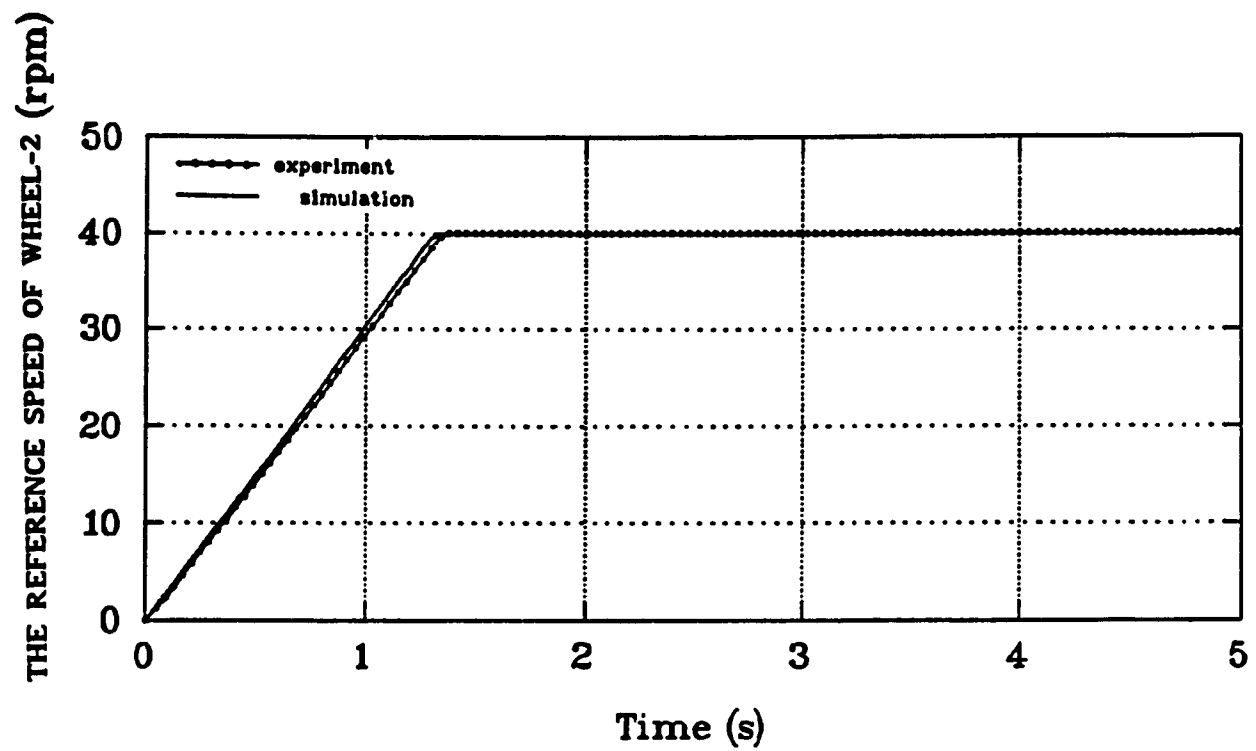


Fig. 6.4 Validation of the velocity servo loops (wheel-2)

Fig. 6.5 presents both the experiments and simulation results under the conditions of:

the step input linear velocity is 0.471 m/s;

the acceleration constant of the servo loop is 0.25 m/s^2 ;

the initial condition of AGV are:

position offset = 2 (cm),

orientation error = 8° .

The offset gain and the orientation gain for the guidance controller are 1.0 and 0 respectively. The plots in the figure are the position offset versus time. It is shown that the vehicle is going at the initial orientation angle in the first 2.5 s. In other words, the tracking regulation only acts after the first 2.5 s. This 2.5 s is defined as the response time for the CONCIC-2 AGV. It is a factor due to the vehicle's inertia and the property of the servo loop as will be discussed later. The simulation results are very well matched with the experiment. Similarly, tests in Fig. 6.6, Fig. 6.7 and Fig. 6.8 were done under same conditions except that the offset gain is increased to 2.5, 5.0, and 7.5 respectively. It is observed, the model accurately represents the real system at different controller gains. The time taken by the vehicle to attain the maximum offset error reduces slightly with the increase of the offset gain. Comparing with the real experiments, the simulation gives a more smooth trajectory. The simulation presents less disturbance than the real experiment.

The above four tests were done at the same initial conditions and a acceleration constant of 0.25 m/s^2 . The following gives some examples at different initial conditions, with the acceleration constant of the servo loop set at 0.05 m/s^2 . Fig. 6.9 gives the results for a test with:

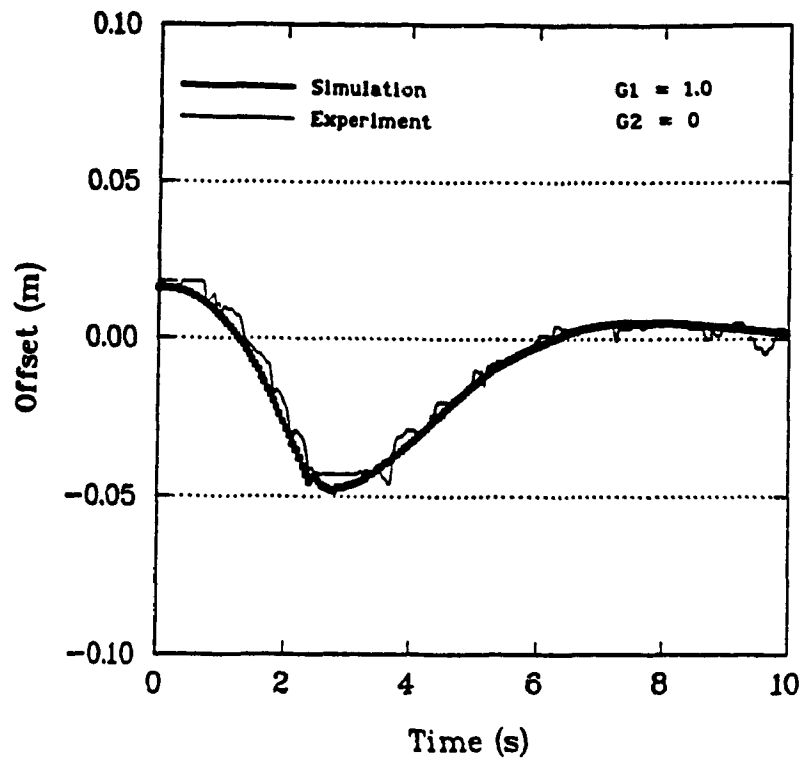


Fig. 6.5 Validation of the AGV with different controller gains (P)

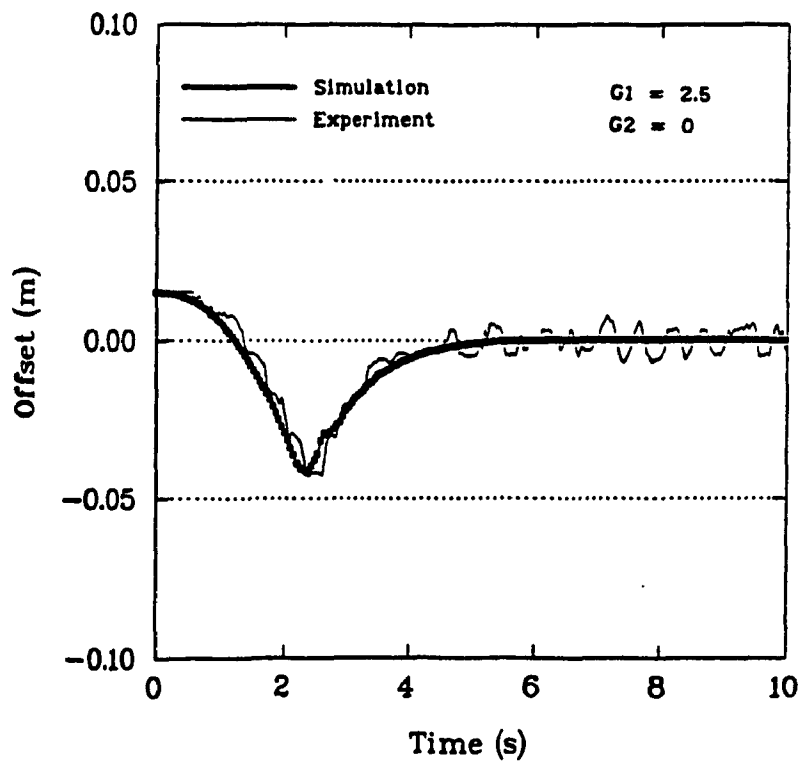


Fig. 6.6 Validation of the AGV with different controller gains (P)

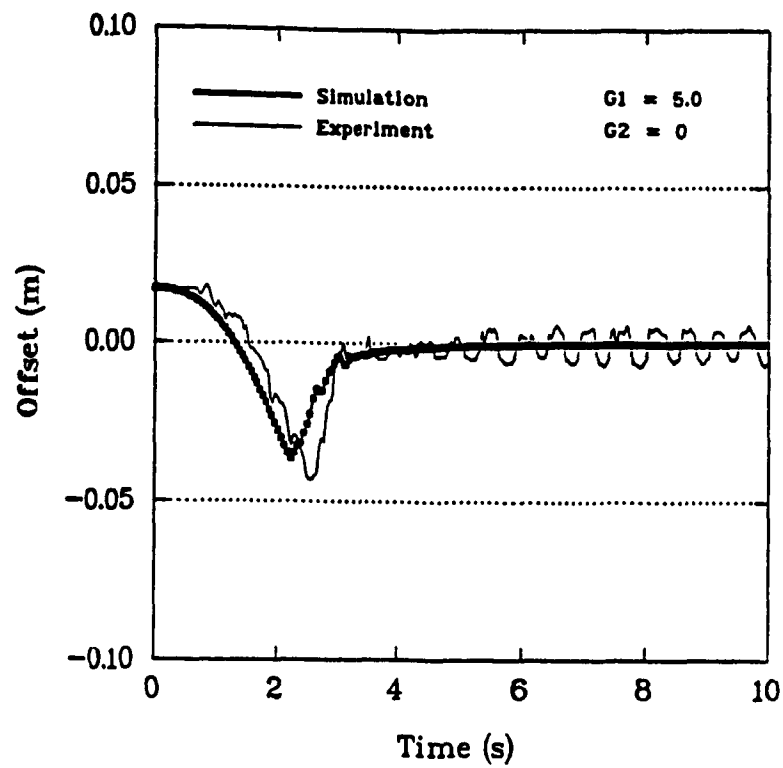


Fig. 6.7 Validation of the AGV with different controller gains (P)

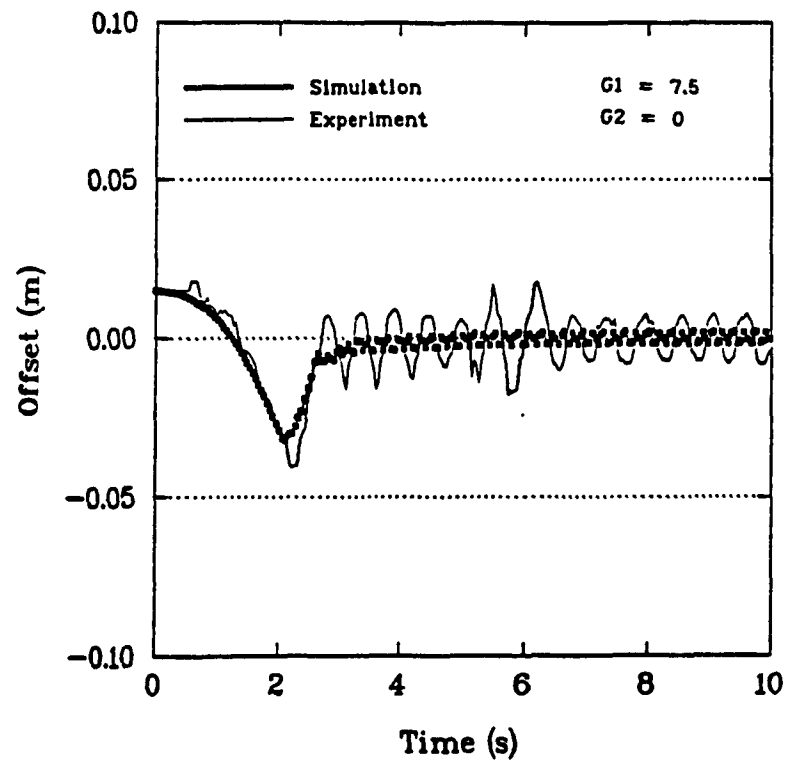


Fig. 6.8 Validation of the AGV with different controller gains (P)

initial conditions:

position offset = 4 cm; orientation error = 0,

linear velocity: 0.431 m/s,

acceleration constant of servo loop: 0.05 m/s^2 ,

the guidance controller gains:

$$G_1 = 9.0, G_2 = 0.5.$$

Plot 6.9 (a) presents the response of the position offset to the track, (b) and (c) present the velocity response at two motorized wheels (wheel 1 and wheel 2). The simulation results agree with the experiments very well in the offset and velocity response curves. It is also seen that the response time of the vehicle is increased to about 9.5 s comparing to the previous tests. The two motorized wheels speed up from zero at the same acceleration until one of them has reached the required linear velocity. During this period of time, the orientation angle of the vehicle does not change. The vehicle travels along a straight line and crosses the track, giving rise to a big overshoot Fig. 6.9.(a). This response time depends on the acceleration constant of the servo loop. More discussion is given in section 6.2.3. Fig. 6.10 presents a similar test except the initial conditions are:

position offset = 3 cm; orientation error = 4° ,

and the guidance controller gains are

$$G_1 = 3.5; G_2 = 0.5.$$

All the experiments and simulation tests shown above confirm the validity of the model. It is realistic in predicting the dynamic behavior of the AGV under different initial conditions, different linear controller, and different acceleration constants. The next section gives more tests with a PI controller at different speeds.

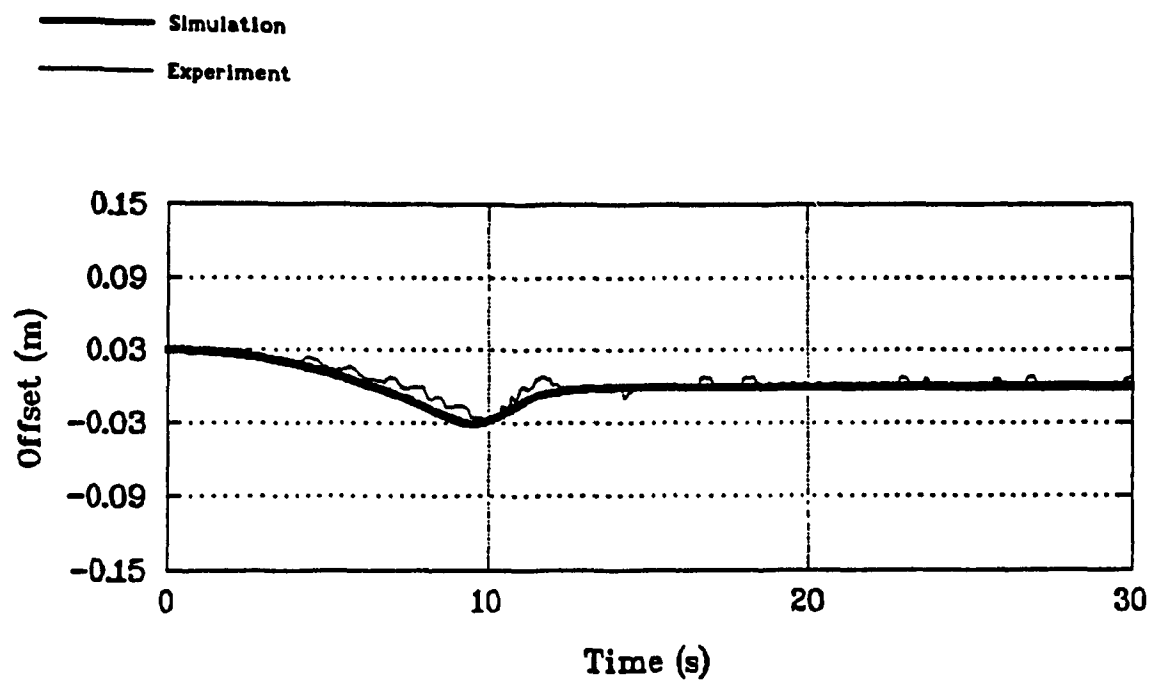


Fig.6.9 (a) transient response

Fig. 6.9 Validation of the AGV with different initial conditions (P)

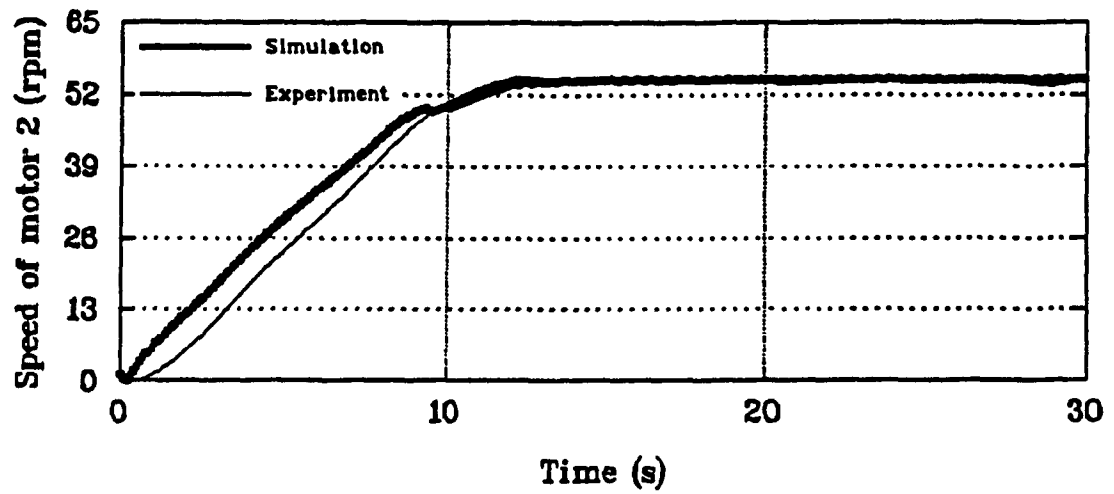


Fig.6.9 (b) velocity response of motor 2

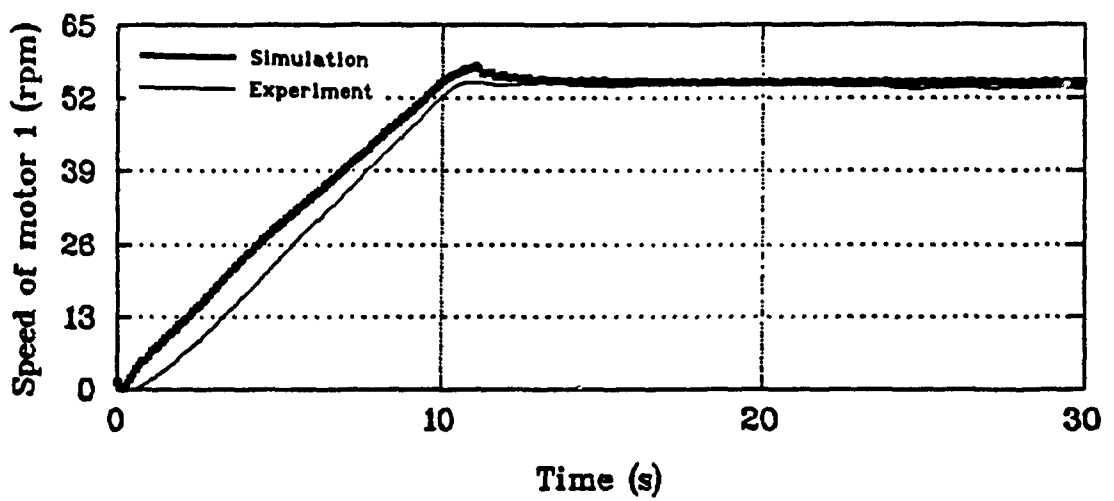


Fig.6.9 (c) velocity response of motor 1

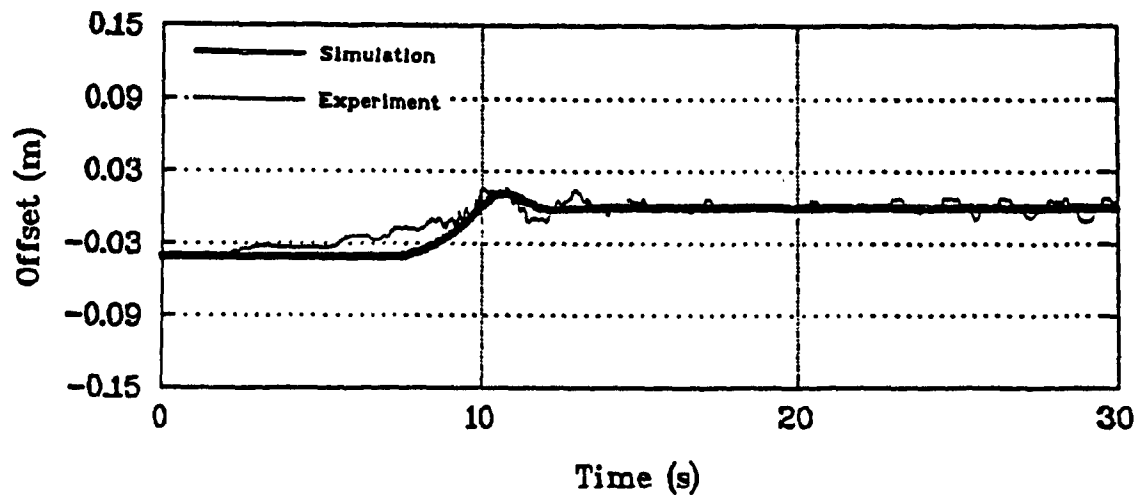


Fig.6.10 (a) transient response

Fig. 6.10 Validation of the AGV with different initial conditions (P)

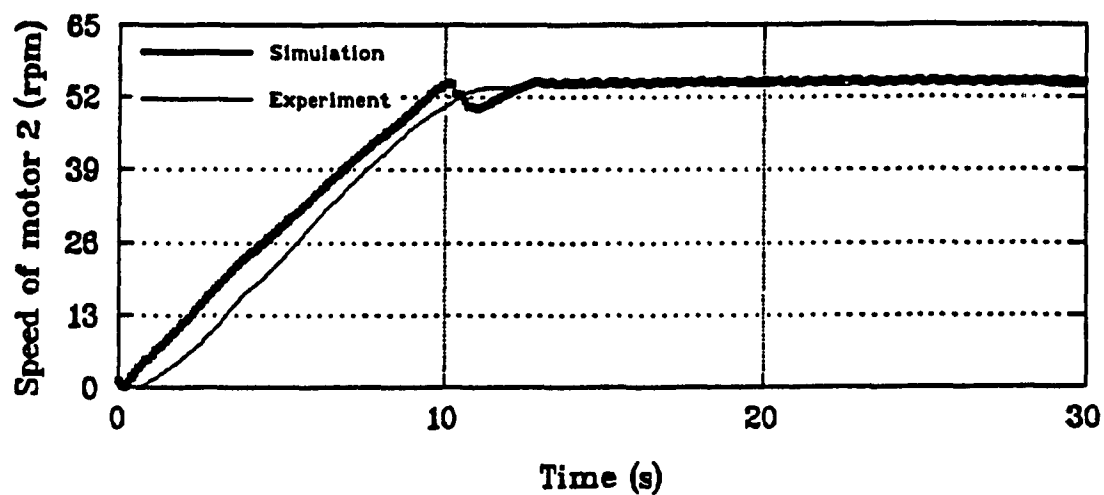


Fig. 6.10 (b) velocity response of motor 2

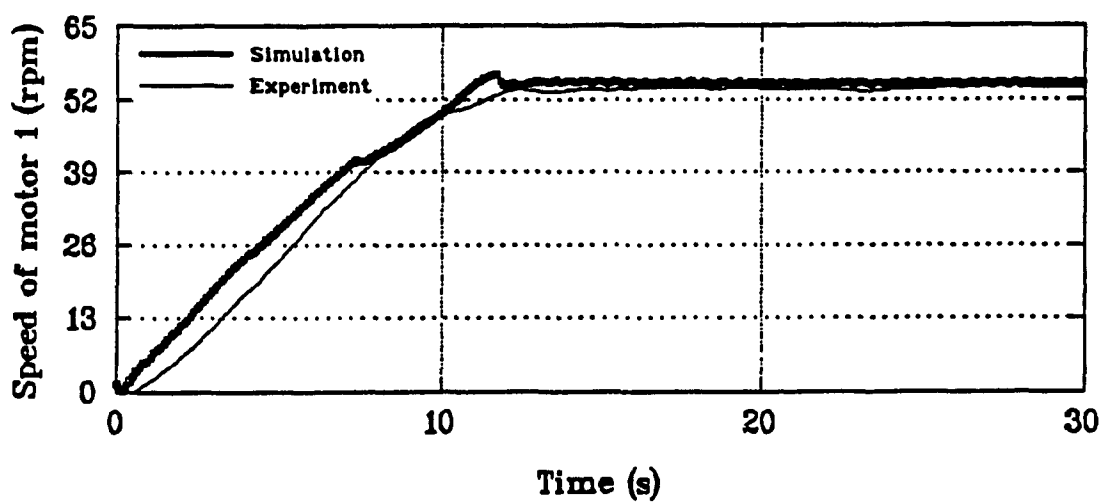


Fig. 6.10 (c) velocity response of motor 1

2) With PI controller

The following experiments validates the model at different speeds with a PI guidance controller. The PI guidance controller is presented as follows

$$\theta_s = G_1 \epsilon_d + \int G_{11} \epsilon_d dt + G_2 \epsilon_\theta \quad (6.2)$$

where G_1 is the linear offset gain which is chosen as 2.5, G_{11} is the integral offset gain which is 0.07, and the orientation gain G_2 is 0. The tests are done under the same initial condition as

offset = 2 cm;

orientation = 7° ,

and acceleration constant of 0.25 m/s^2 .

Fig. 6.11 shows the test at speed of 0.157 m/s. The simulation result is very close to the experiment, similarly at speed of 0.314, 0.628, and 0.785 m/s as shown in Fig. 6.12, Fig. 6.13, and Fig. 6.14 respectively. These tests further prove the reality of the model. Comparing Fig. 6.12 with Fig. 6.6, with the same offset gain G_1 , the overshoot of the transient response has been reduced very slightly by the PI controller (about 0.5 cm)

In the next section, a detailed discussion on the optimal design of control strategy is given.

6.2.2 A study of guidance system

In the guidance system of CONCIC-2 AGV, there three factors effects the vehicle behavior, the location of the camera sensor, the location of the effective steering wheel, and the gains of the guidance controller.

6.2.2.1 The optimization of the guidance controller

The optimization of the control strategy was carried out by considering

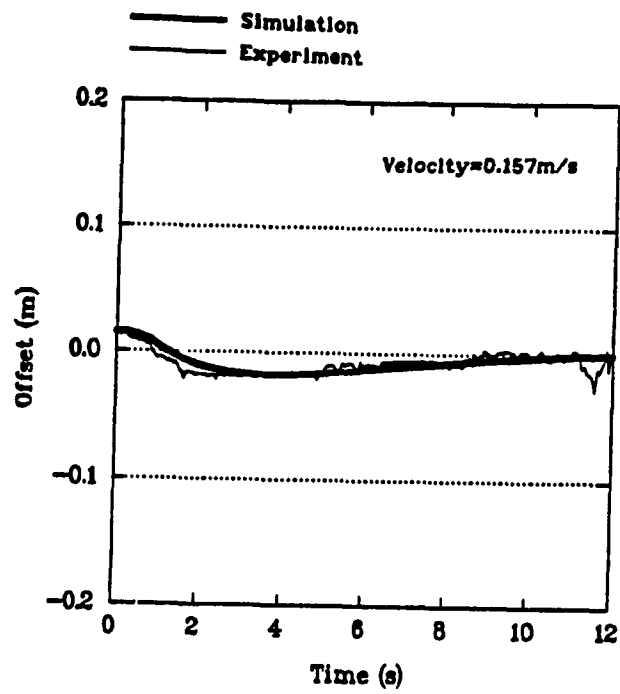


Fig. 6.11 Validation of the AGV with different velocity (PI)

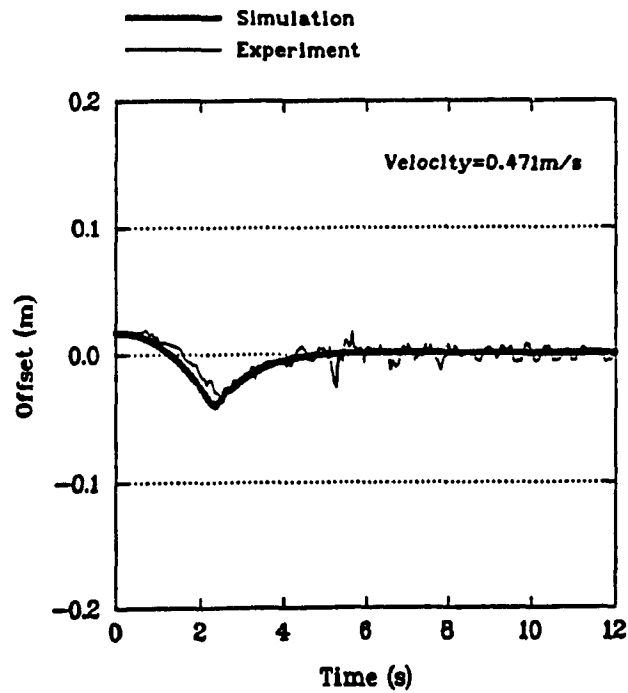


Fig. 6.12 Validation of the AGV with different velocity (PI)

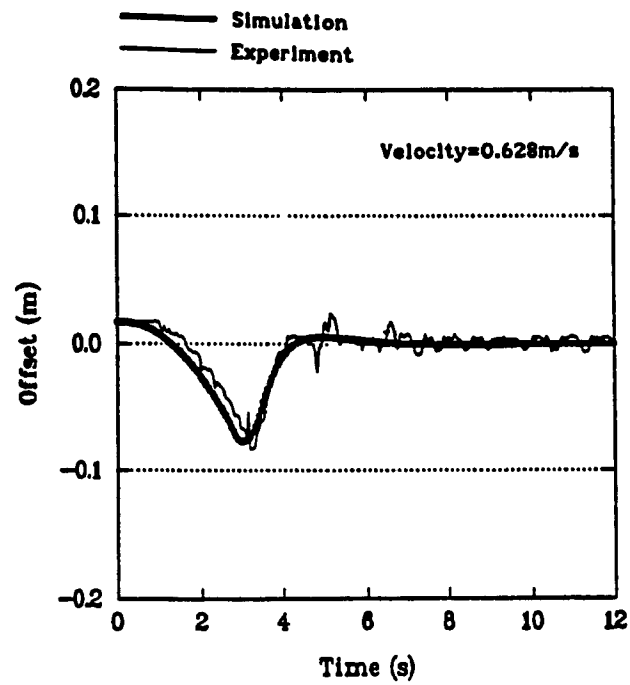


Fig. 6.13 Validation of the AGV with different velocity (PI)

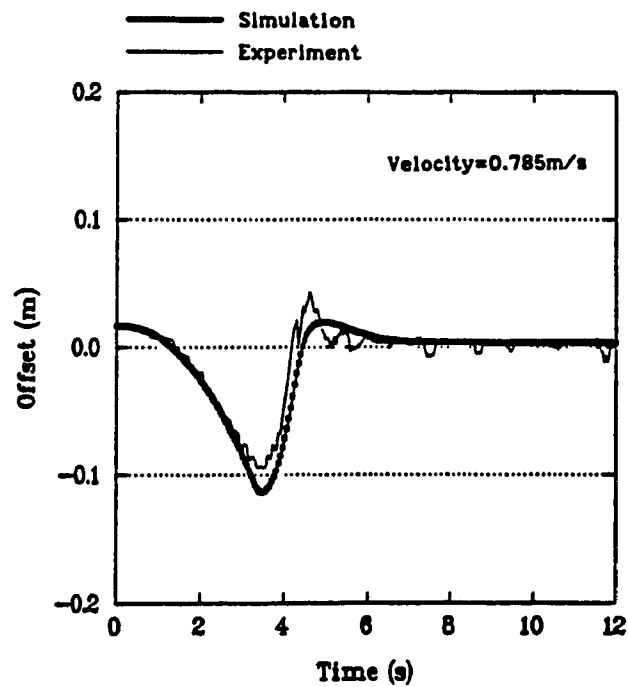


Fig. 6.14 Validation of the AGV with different velocity (PI)

the minimization of the summation of the error squared at both ends of the vehicle, where error refers to the offset error. Fig. 6.15 presents a 3-D graph of the error squared versus two controller gains G_1 and G_2 of CONCIC-2 AGV under the conditions of speed of 0.431m/s and a straight line guide-path. This 3-D graph shows that the 'optimal' setting of this control strategy spreads a relatively wide range of G_1 and G_2 . A large 'optimal' area presents a very stable performance of this control law at these conditions. The experiments also demonstrate this conclusion as shown in Fig. 6.16. All the tests are done at the same initial condition and the same linear velocity. When the proportional control gain G_1 changes from 2.5 to 7.5 and orientation control G_2 stays the same (0), the performance of the vehicle changes slightly.

In the experiments it is also observed that the 'optimal' settings change with the linear speed of the vehicle and the curvature of the guide-path. One constant controller setting is not always suitable for all kinds of operations and guide-paths. It also raises a question of the design of a suitable control strategy for the AGV which changes with some of the operational parameters. The following paragraph attempts to provide a good understanding of the changes of the 'optimal settings' of the controller at different operation conditions, and proposes some important factors in the controller design.

A. For a straight line guide-path

In this section we will investigate some of the properties of the guidance strategy with the different initial conditions and different forward velocities.

Performance vs G_1 & G_2

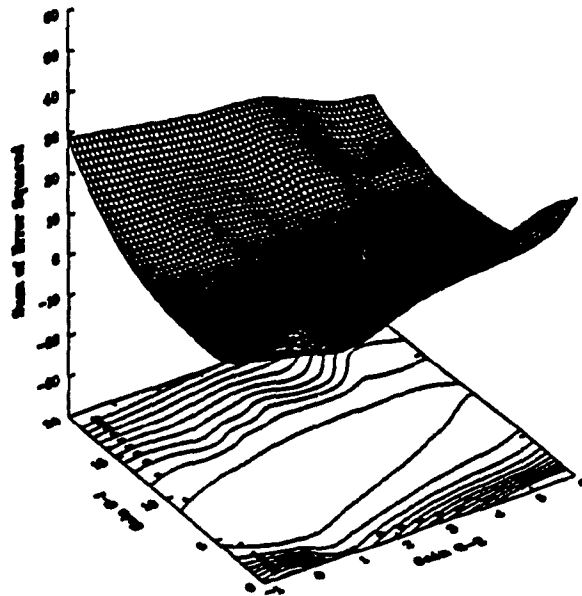


Fig. 6.15 3-D plot of AGV performance versus G_1 and G_2

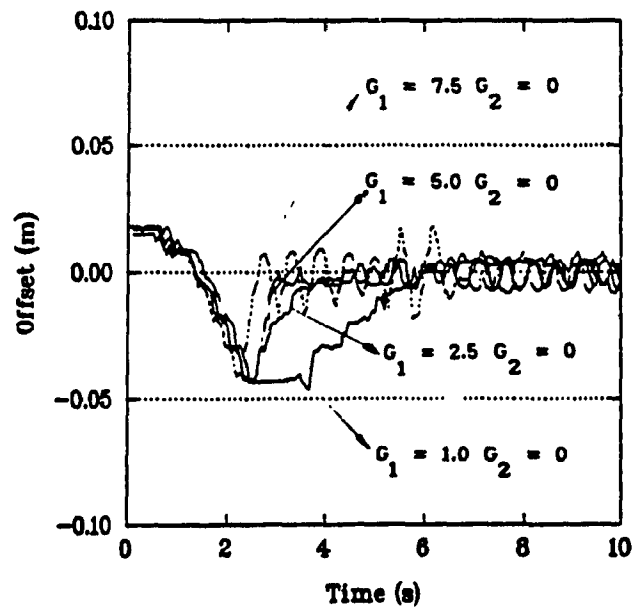


Fig. 6.16 Comparison of AGV performance with various controllers

The following chart indicates the different cases for the initial conditions:

1	2	3	4
$\epsilon_d > 0$	$\epsilon_d > 0$	$\epsilon_d < 0$	$\epsilon_d < 0$
$\epsilon_\theta > 0$	$\epsilon_\theta < 0$	$\epsilon_\theta > 0$	$\epsilon_\theta < 0$

The simulation tests are done under the following conditions for all the cases:

the forward-velocity command is 0.9 m/s

the position offset is about 2 cm

the orientation error is about 7° .

From the simulation, one can observe that the different combinations of errors does effect the optimal setting of the controller. Fig. 6.17, Fig. 6.18, Fig. 6.19, and Fig. 6.20 present the simulation tests which are done at the initial conditions as in case 1, case 2, case 3, and case 4 respectively. The results show that the different position conditions have little effect on the offset controller gain (G_1), but quite significantly on the orientation control gain (G_2). The contour plot shows that when the offset and orientation error have different signs, the 'optimal area' shifts to the right. In other words, the optimal settings for the controller have a related greater orientation gain compared with the case in which the offset and orientation gain have the same signs. As it is shown in the figures, a controller with settings as

$$G_1 = 2.5;$$

$$G_2 = 0;$$

Performance vs G1 & G2

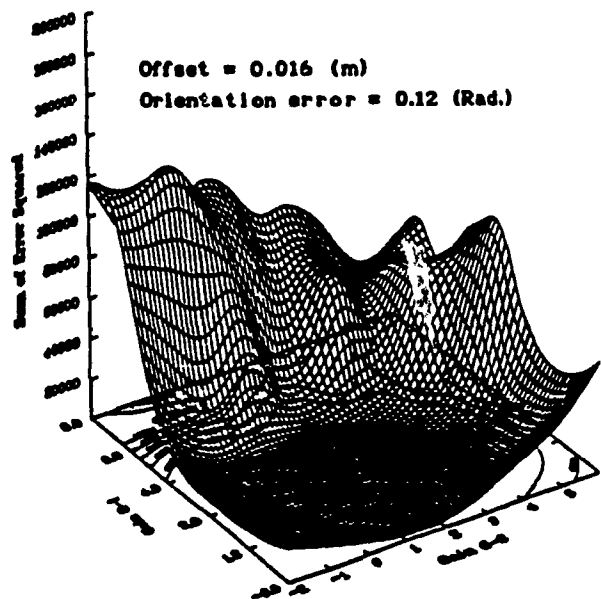


Fig. 6.17 3-D plot of AGV performance versus G_1 and G_2
($\epsilon_d > 0$; $\epsilon_\theta > 0$; $V_y = 0.9$ m/s)

Performance vs G1 & G2

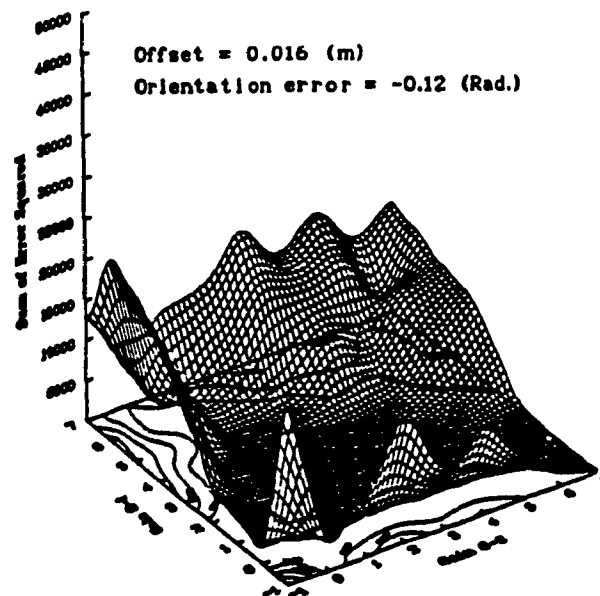


Fig. 6.18 3-D plot of AGV performance versus G_1 and G_2
($\epsilon_d > 0$; $\epsilon_\theta < 0$; $V_y = 0.9$ m/s)

Performance vs G1 & G2

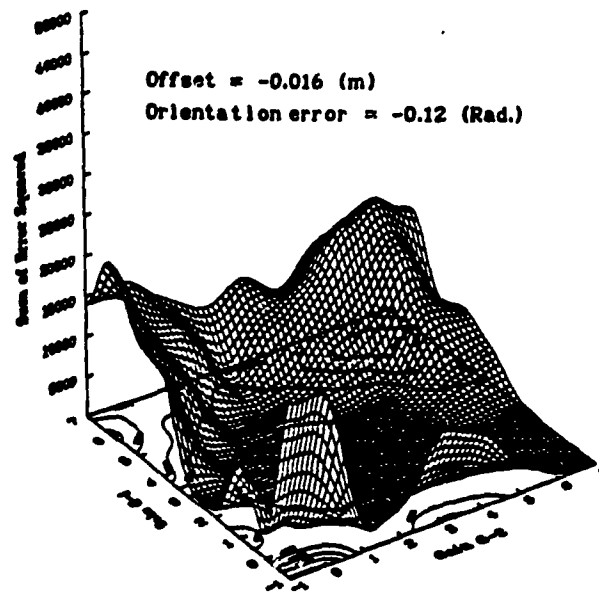


Fig. 6.19 3-D plot of AGV performance versus G_1 and G_2
($\epsilon_d < 0$; $\epsilon_\theta > 0$; $V_y = 0.9$ m/s)

Performance vs G1 & G2

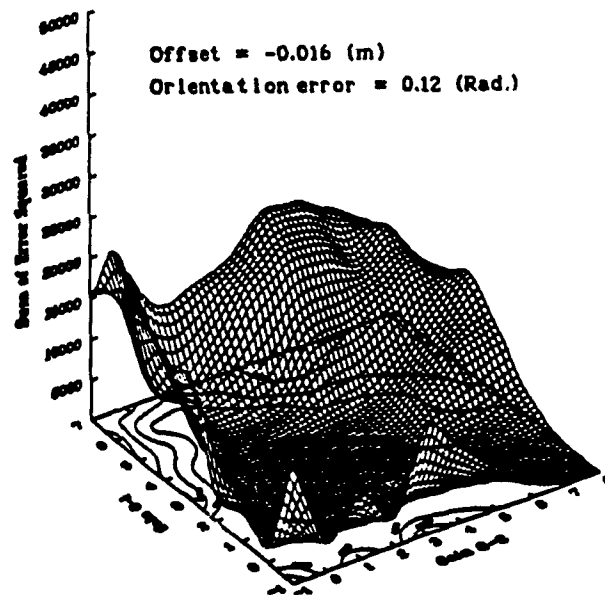


Fig. 6.20 3-D plot of AGV performance versus G_1 and G_2
($\epsilon_d < 0$; $\epsilon_\theta < 0$; $V_y = 0.9$ m/s)

are within the optimal range in Fig. 6.17 and Fig. 6.19, but out of the optimal range in Fig. 6.18 and Fig. 6.20. The orientation control gain is more sensitive to the error condition.

More simulation were carried out to study the change of optimal area of the controller with the increase of the linear velocity of the vehicle. The tests are done at same initial conditions of

the position offset: 2 cm;

the orientation error: 7° .

Fig. 6.21 shows the 'optimal area' of controller setting at 0.6 m/s linear velocity and Fig. 6.22 shows the 'optimal area' at 0.3 m/s linear velocity. Compared with Fig. 6.17 which is the 'optimal area' of AGV at 0.9 m/s velocity under the same conditions, It is noticed that the 'optimal area' covers a greater region when the speed of AGV is lower. In other words, the AGV becomes more stable at lower speeds.

Some real-time experiments have been done to substantiate the above conclusion. The experiments are done under the following conditions:

the initial offset: 2 cm

the initial orientation angle: 7° ;

the controller gains: $G_1 = 2.5$, $G_{11} = 0.07$, and $G_2 = 0$;

As observed in Fig. 23, the vehicle becomes more unstable when the velocity is higher. Thus, the optimal settings of the controller have to be considered under different working speeds.

Not only do the linear speed and initial condition affect the control ability of the vehicle, the curvature of the path is another important factor which affects the 'optimal area' of the controller settings. The following tests were performed to explain this property.

Performance vs G1 & G2

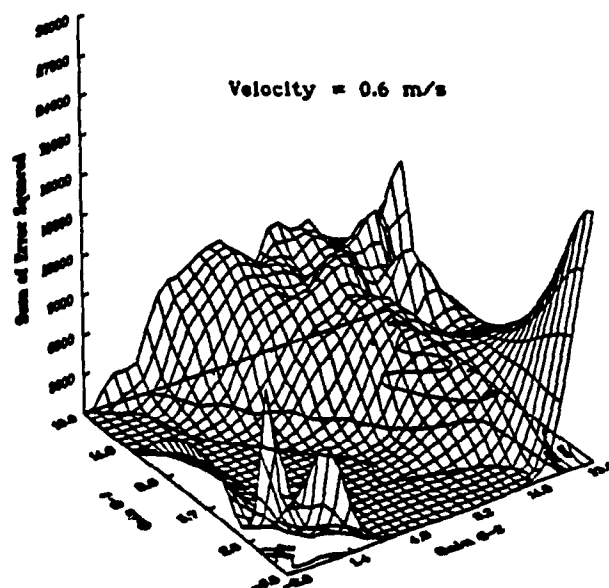


Fig. 6.21 3-D plot of AGV performance versus G_1 and G_2
($V_y = 0.6$ m/s)

Performance vs G1 & G2

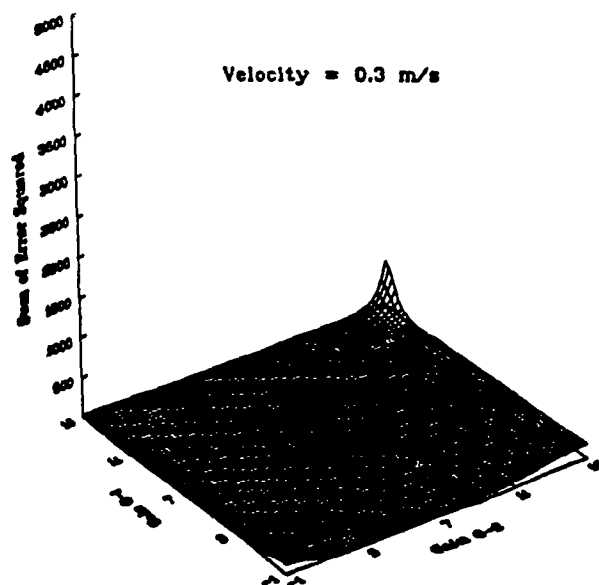


Fig. 6.22 3-D plot of AGV performance versus G_1 and G_2
($V_y = 0.3$ m/s)

Performance Comparison for Various Velocities (PI)

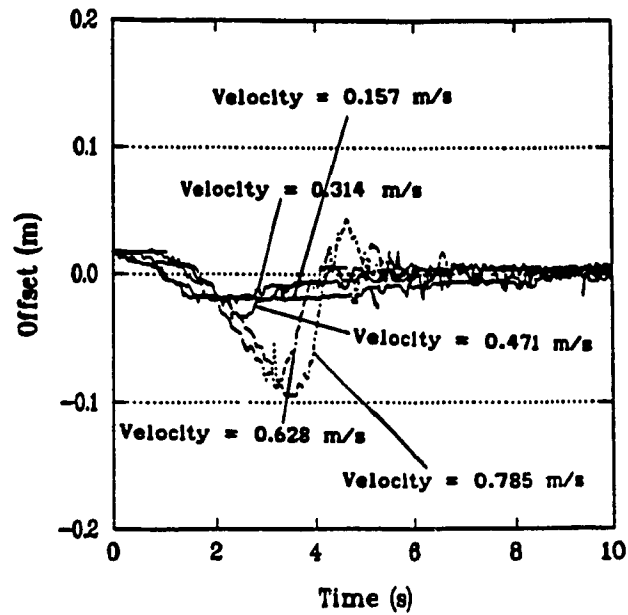


Fig. 6.23 Comparison of AGV performance with various velocities (PI) (experiment)

B. Circular guide-path

We used a circular path to examine the change of the optimal settings of the controller under the different curvatures. The tests are done at same initial condition and same speed with different radii of circular path.

The simulation show that the control ability becomes more sensitive to the vehicle speed associated with the the radius of the path. It is also noticed that the optimal area was shift to the right significantly when the radius of the path is not infinite. Fig. 6.24 and Fig. 6.25 present the AGV performance versus controller setting G_1 and G_2 at 0.6 and 0.9 m/s velocity with a circular path of a 6 m diameter. Fig. 6.26 and Fig. 6.27 is a same test at velocity 0.3 m/s and 0.6 m/s with a circular path of 3.5 m diameter. Comparing Fig. 6.25 with the same test under straight line profile (Fig. 6.21), the optimal area of the controller gains in the circular path covers a considerable larger region than it does in a straight line in the region of higher gains. But in the region of lower gains, the response of AGV is much more stable with a straight line profile than with a circular profile. At the same velocity, the smaller radius of the circular path also reduces the optimal area of the controller gains. As they were shown in Fig. 6.24 and Fig. 6.27, when the radius decreased from 6 m to 3.5 m, the optimal area reduced significantly.

The above results indicate that the vehicle has a better control-ability at larger radii and lower speed. For a small circular path (a path with a small radius of curvature), low speed is required to eliminate the position and orientation error.

Performance vs G1 & G2

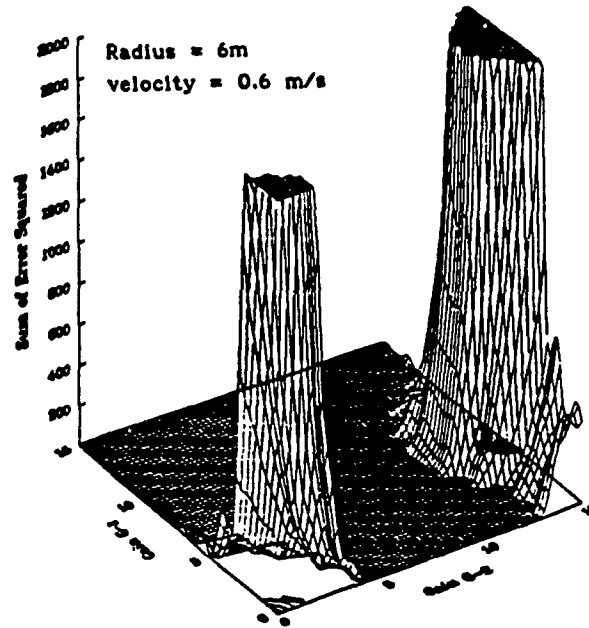


Fig. 6.24 3-D plot of AGV performance versus G_1 and G_2
(circular path; $R = 6$ m; $V_y = 0.6$ m/s)

Performance vs G1 & G2

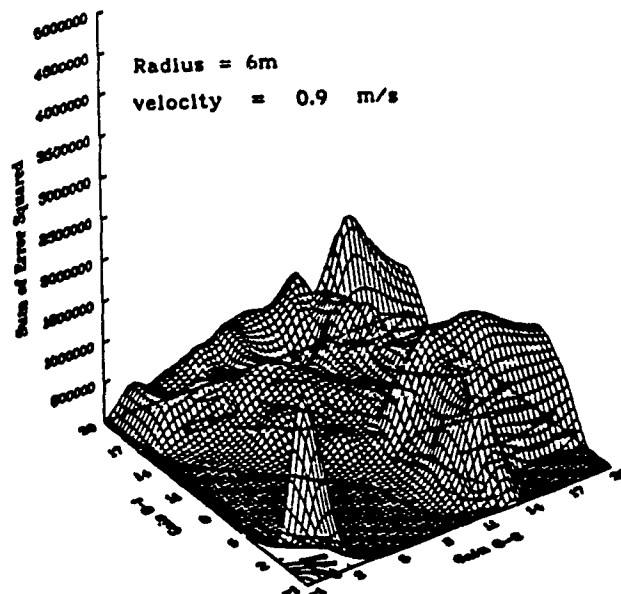


Fig. 6.25 3-D plot of AGV performance versus G_1 and G_2
(circular path; $R = 6$ m; $V_y = 0.9$ m/s)

Performance vs G1 & G2

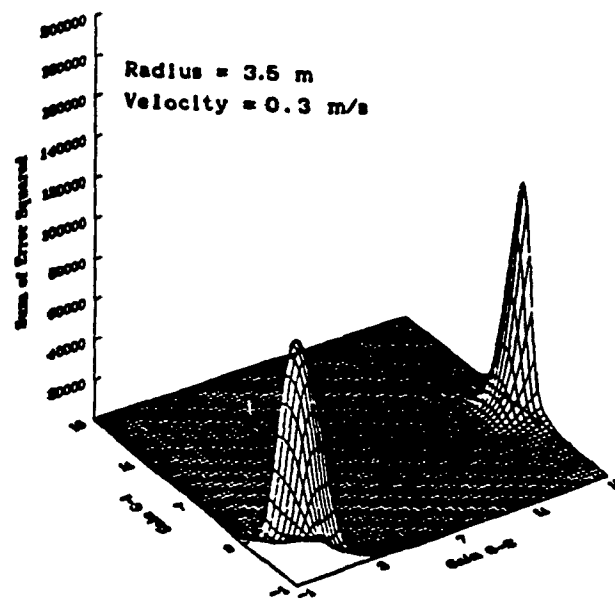


Fig. 6.26 3-D plot of AGV performance versus G_1 and G_2
(circular path; $R = 3.5$ m; $V_y = 0.3$ m/s)

Performance vs G1 & G2

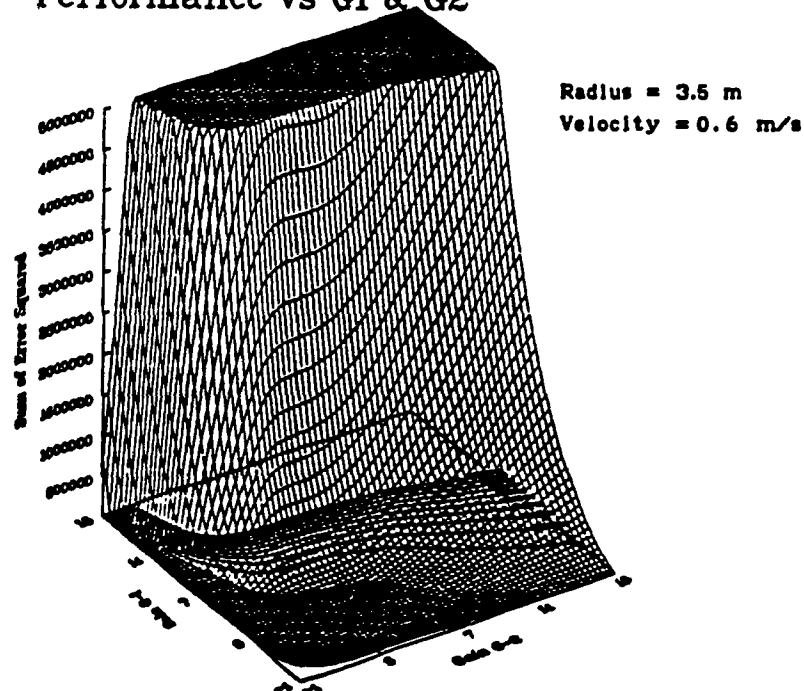


Fig. 6.27 3-D plot of AGV performance versus G_1 and G_2
(circular path; $R = 3.5$ m; $V_y = 0.6$ m/s)

6.2.2.2 The effect of the location of the camera sensor

The location of the camera determines where to measure the deviation between the vehicle and the track and where to minimize the deviation. Whether the linear guidance controller (6.1) or the PI controller (6.2) is used, the deviation of the camera from the track e_d and the e_q are the most effective factors for the guidance. It is felt that by putting the camera in front of the vehicle, better performance may be obtained. The following figures illustrate this property.

Fig. 6.28, Fig. 6.29, Fig. 6.30, Fig. 6.31 and Fig. 6.32 present the trajectory of the vehicle under the same initial condition and the same controller gains, but different camera location. Fig. 6.28, Fig. 6.29, Fig. 6.30 have a very smooth response with the camera in front of the front center of mass at 0.69 m, 0.99 m, and 1.89 m respectively. When the camera is installed close to the position of the front caster, the vehicle starts to have small oscillations as shown in Fig. 6.31. When the camera is at the center of mass, then the vehicle becomes unstable (Fig. 6.32). It is shown that when the camera is further from the center of mass, smoother and more stable response is observed. The distance between the camera and the center of the mass along the longitudinal axis is defined as camera length [Fig. 5.2]. The above results may be explained as follows. Consider the differential configuration of CONCIC-2 AGV, the motion of the vehicle at every instant is a rotation about a point somewhere on the lateral axis of the vehicle. The trajectory of any point on the vehicle contains a series of arcs, so does the trajectory of the camera. The radii of curvature of these arcs depend on the distance between the point and the center of instantaneous rotation of the vehicle. When this distance is shorter, the

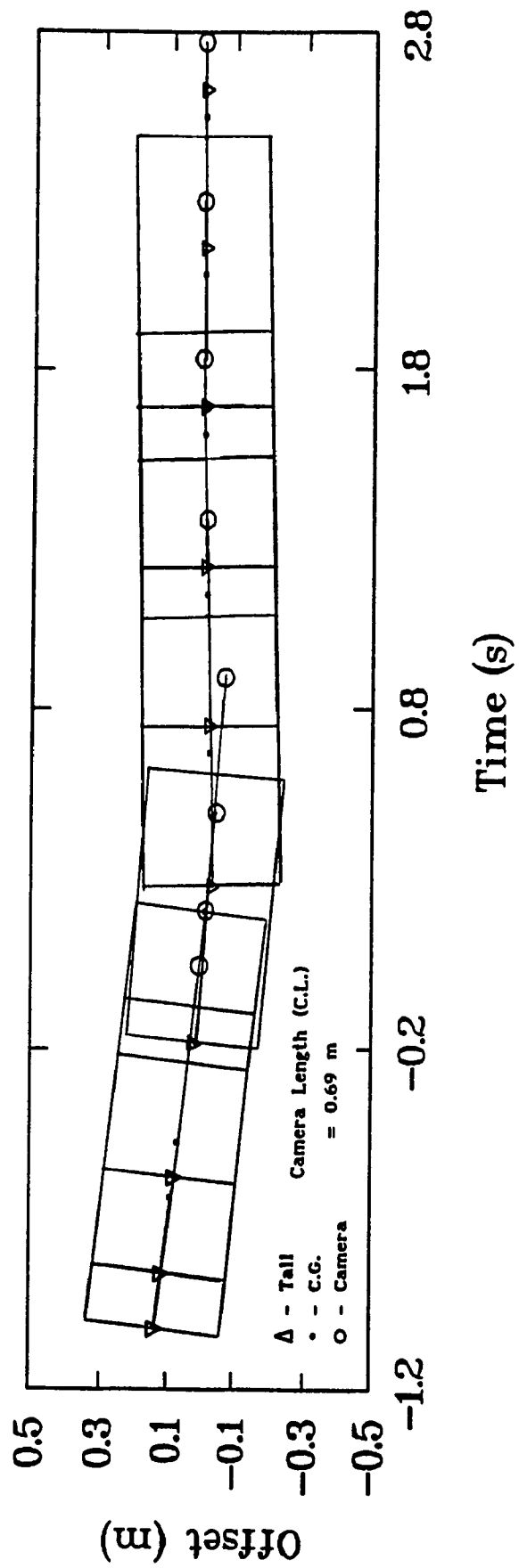


Fig. 6.28 AGV transient response with camera length = 0.69 m

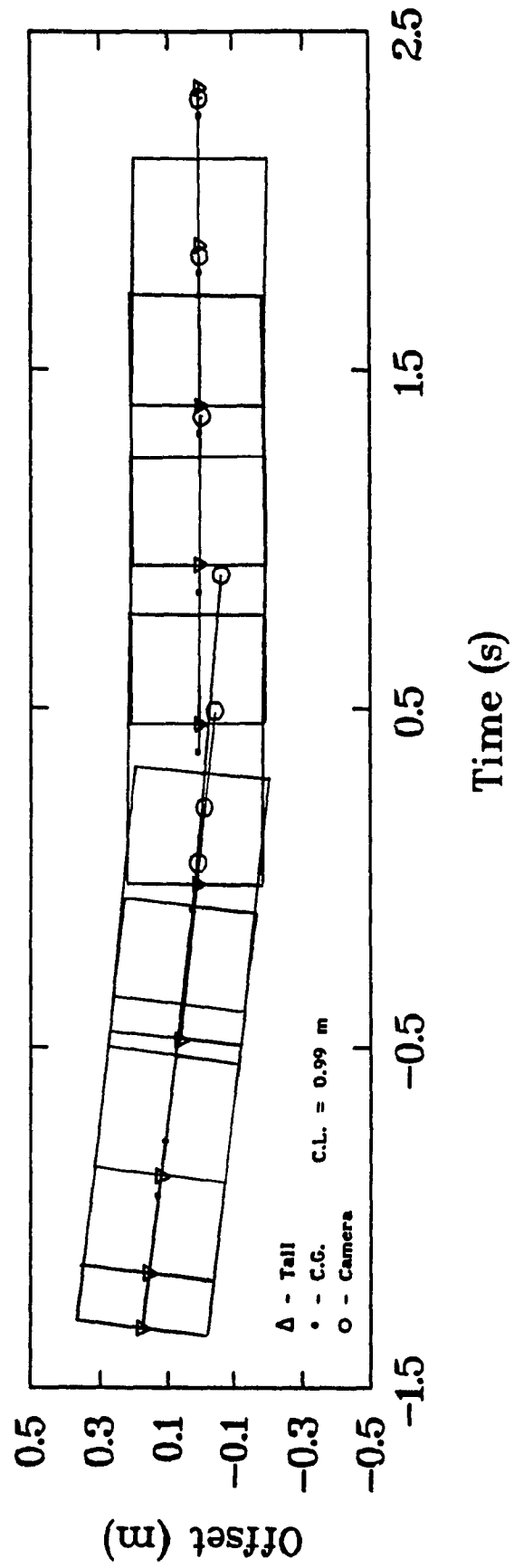


Fig. 6.29 AGV transient response with camera length = 0.99 m

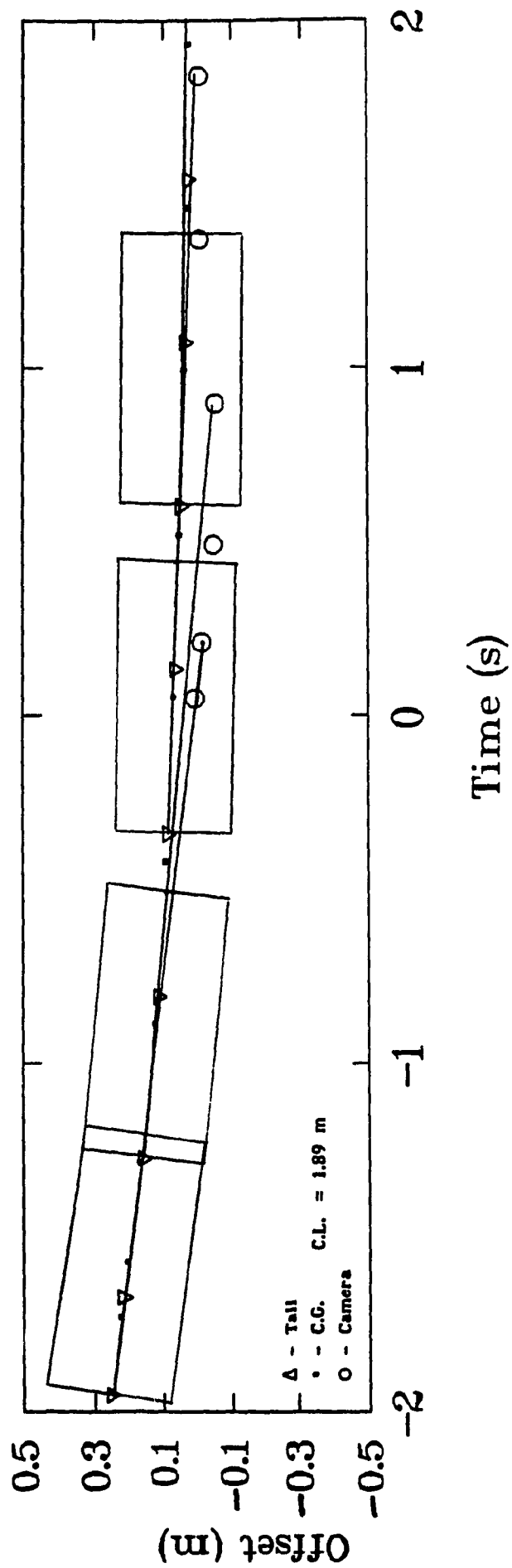


Fig. 6.30 AGV transient response with camera length = 1.89 m

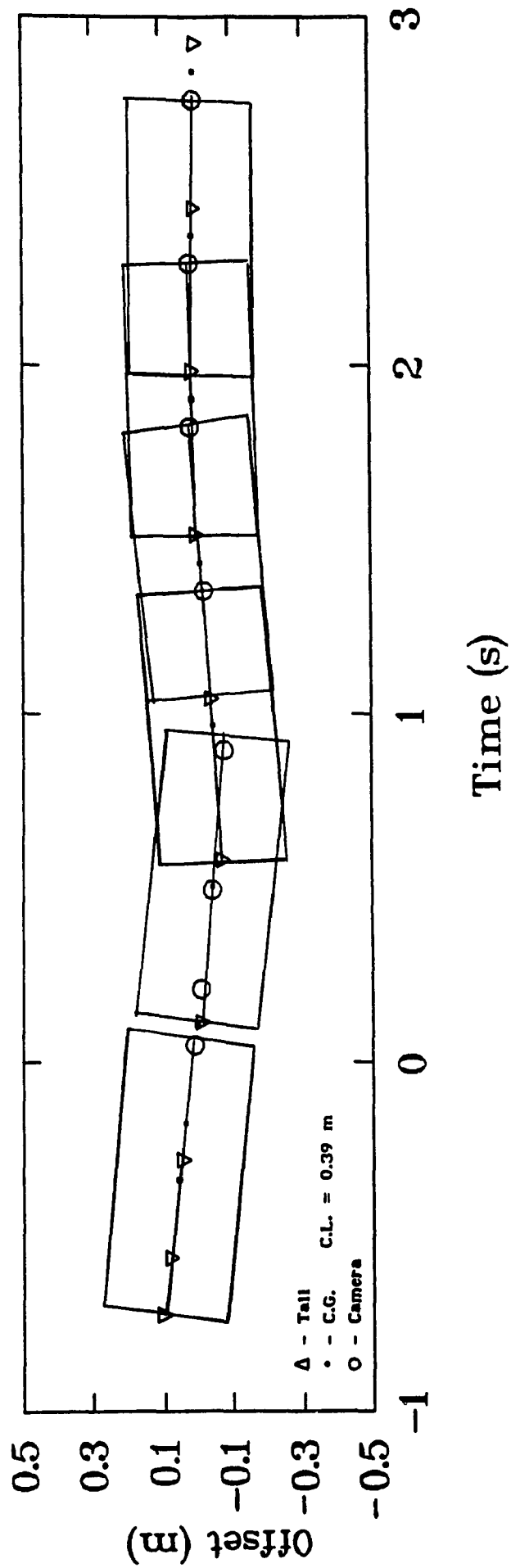


Fig. 6.31 AGV transient response with camera length = 0.39 m

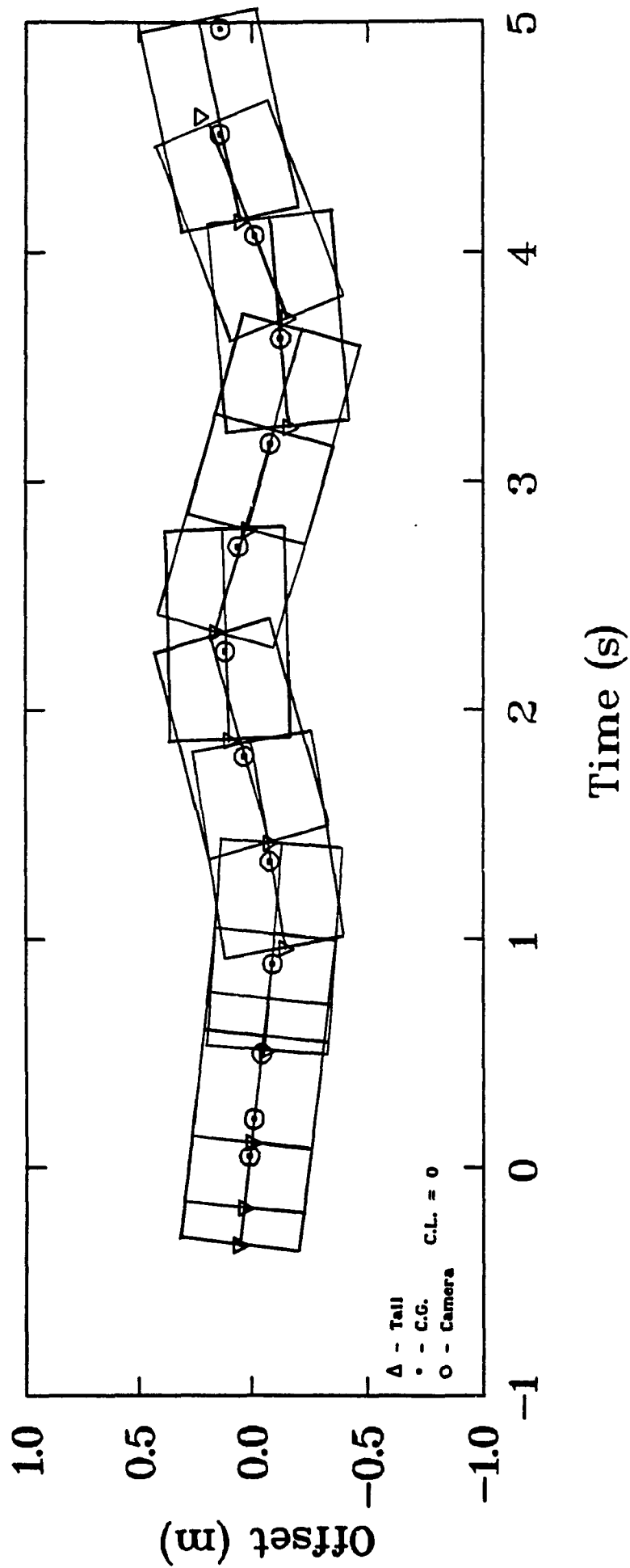


Fig. 6.32 AGV transient response with camera length = 0 m

trajectory of the point will consists of arcs with smaller radii of curvature. When the camera length is shorter, the distance between the camera and the center of instantaneous rotation of the vehicle is shorter. Consequently the trajectory of the camera is made of smaller arcs. The camera detects the errors along its trajectory. So the error message along the trajectory made of small arcs changes rapidly and more frequently. All of these make the control less stable. On the contrary, when the camera length is longer, the trajectory is made of arc with greater radius of curvature. The change of the errors along the trajectory is smoother and less frequent, therefore more stable performance is observed as shown in the simulation. The comparison of the trajectories of the camera is presented in the Fig. 6.33.

Longer camera length can make the vehicle response smoother and faster. But the performance of the vehicle does not change proportional with the camera length. As it is shown in Fig. 6.33, when the camera length changed from 0.69 m to 1.89 m, the AGV performance changed very slightly. At the same time, the total length of the vehicle increased from 1 m to about 2.3 m, thus working space for the AGV is much larger. Therefore, there is a limitation for increasing the camera length.

The trajectory of the camera can also be smoothed by increasing the radius of instantaneous rotation by reducing the controller gains or adjusting the location of virtual steering wheel. But these will reduce the control angular velocity at the same time, and increase the transient time of AGV. The transient time is defined as the time for the AGV to first come back right on the track from the initial stationary.

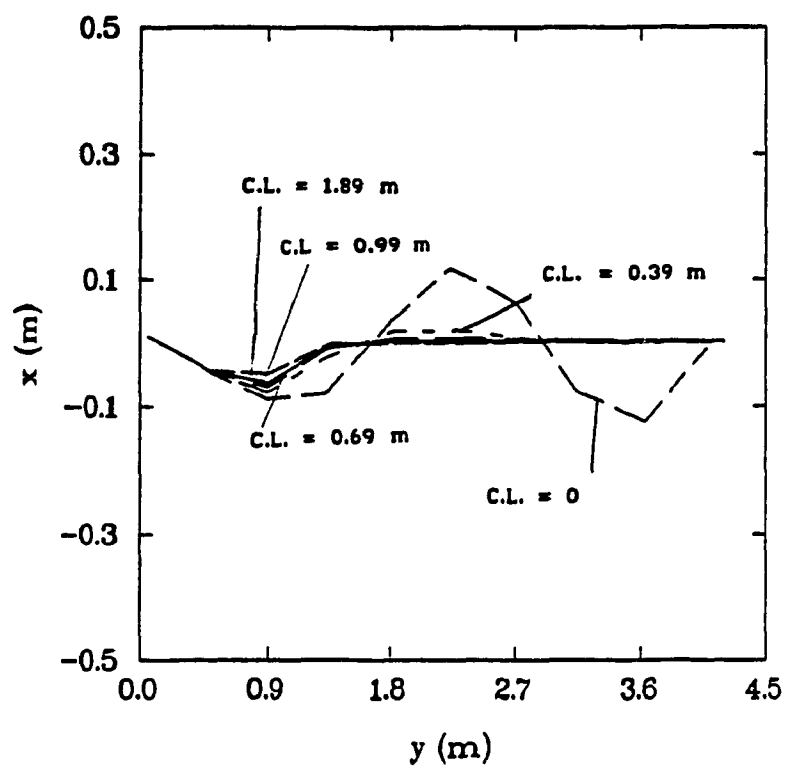


Fig. 6.33 Comparison of AGV transient response with various . camera length

6.2.2.3 The effect of the location of the virtual-steering wheel

CONCIC-2 AGV uses an indirect regulation tracking method for guidance. The output of the guidance controller is an effective steering angle, and it is transferred into the driving speeds of two motorized wheels through the geometric relationship of an equivalent tricycle [Fig. 6.34]. The location of the virtual steering wheel determines the configuration of the equivalent tricycle. The dynamic behavior will change when this location is changed. The relationship between the equivalent steering angle and the driving speeds of the two motorized wheels is presented in the following two equations (6.3) and (6.4) referring to chapter 5.

$$\omega_{cz} = \frac{V_y \cdot \tan \theta_{cs}}{l_{ae}} \quad (6.3)$$

$$\begin{aligned} V_{c1} &= V_y - \omega_{cz} \cdot l \\ V_{c2} &= V_y + \omega_{cz} \cdot l \end{aligned} \quad (6.4)$$

When the equivalent wheel-base l_{ae} is larger, the control steering rate ω_{cz} is smaller. In other words, the instantaneous radius of the rotation of the vehicle is greater, and a slower response of the AGV is observed.

Fig. 6.35 shows some simulation tests of the vehicle when the equivalent wheel-base l_{ae} is 3.9 m, and 0.39 m and 0.04 m accordingly. The initial conditions for the vehicle are

position offset = 1.6 cm;

orientation error $\approx 6^\circ$,

the acceleration constant for these tests is

$$a_a = 0.25 \text{ m/s}^2,$$

and the controller gains are

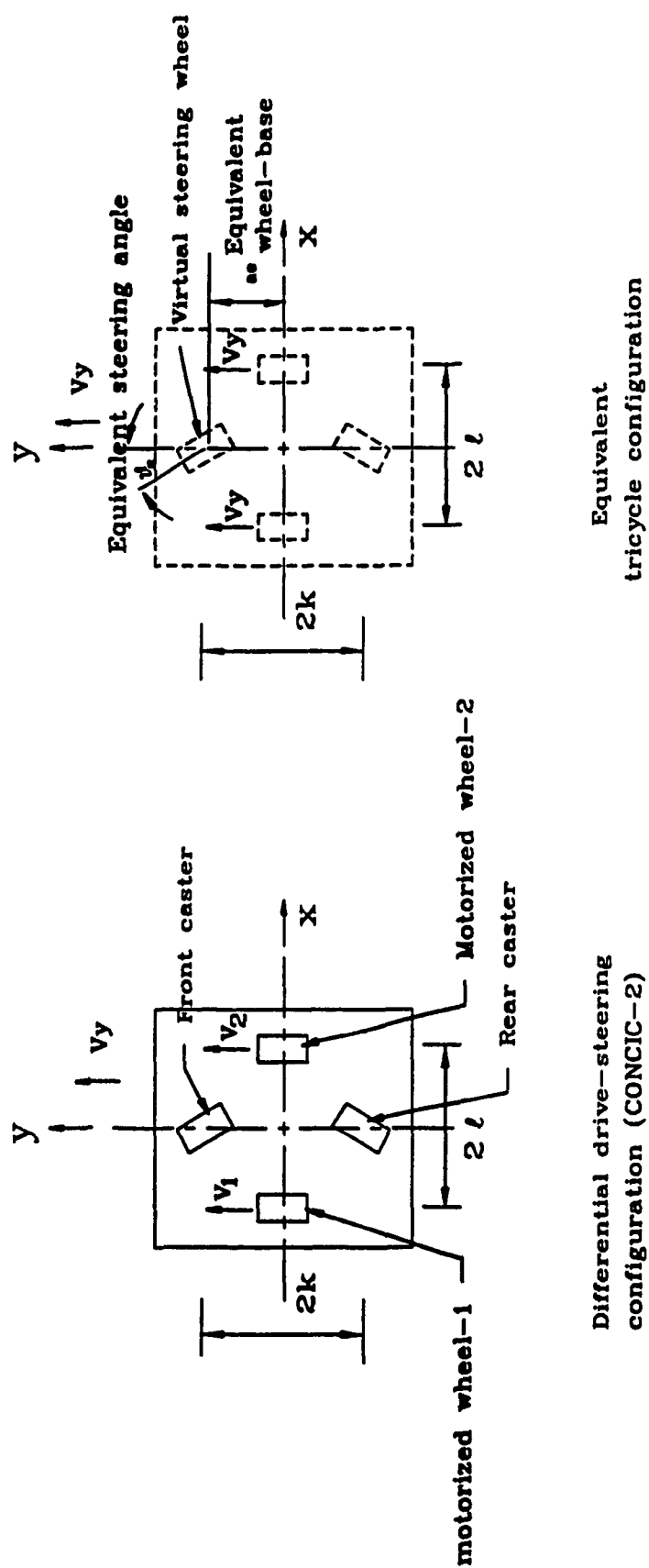


Fig. 6.34 CONCIC-2 AGV and its equivalent tricycle

$$G_1 = 2.5; G_{11} = 0.007$$

$$G_2 = 0.$$

As it is seen in the figure, when ℓ_{ae} equals to 0.39 m, the vehicle has a overshoot of 7 cm and settles down in about 2 m distance. When ℓ_{ae} is increased to 3.9 m (about 10 times the original length), a much slower response of the vehicle is observed. In this case, the vehicle has a 13 cm overshoot, and takes a distance of more than 10 m to get settle down. When ℓ_{ae} is reduced to 0.04 m (about 1/10 of the original length), the AGV has a faster response, with some transient oscillations. The overshoot for this case has been reduced to about 2.5 cm.

The longer equivalent wheel-base, the slower the response of the AGV is. The response, however, can be improved by increasing the controller gains as it is shown in the Fig. 6.36. A Smaller equivalent wheel-base ℓ_{ae} improves the response of the vehicle, but it also makes the vehicle less stable at higher gains. Fig. 6.36 presents the AGV response of previous three cases with $G_1 = 5.5$. The results shows that the higher gain improves the response at $\ell_{ae} = 3.9$ m. But at $\ell_{ae} = 0.04$ m, the vehicle becomes unstable. Fig. 6.37 presents the behavior of the AGV at optimal controller settings for each individual case. The results show that, even in the case of optimal settings, the vehicle with longer equivalent wheel-base still takes more time to response. This is simply because the vehicle with a longer wheel-base has a smaller steering rate. Consequently, the radius of the instantaneous rotation of the vehicle is larger, and the difference between the velocities of the two wheels is less. Since the average of the two velocities yields the linear velocity of the vehicle, the velocity of the slower wheel is higher in the case of longer wheel-base. Consequently

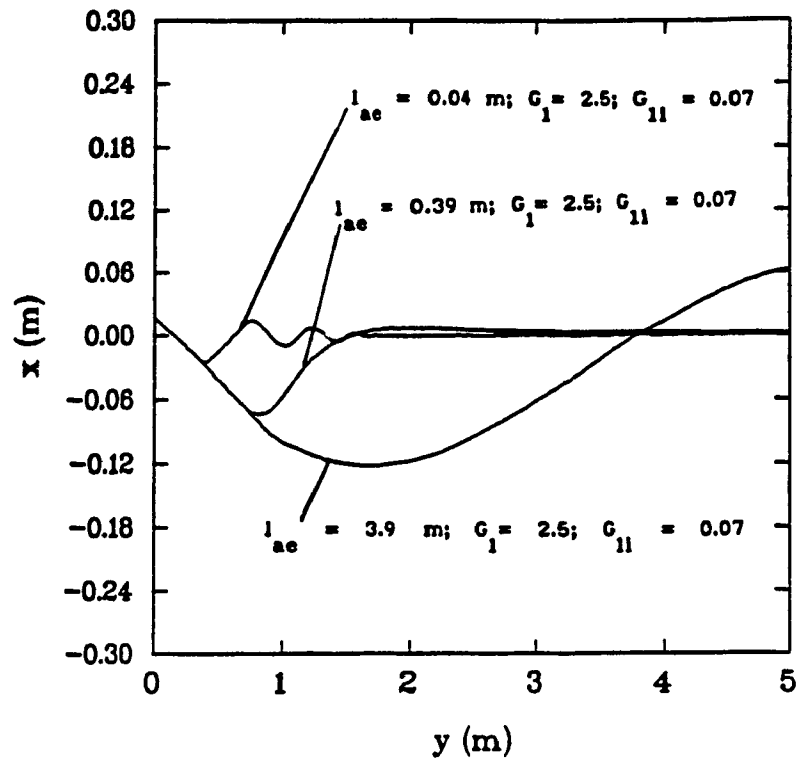


Fig. 6.35 Transient response of AGV with various equivalent wheel-base ($G_1 = 2.5; G_2 = 0.07$)

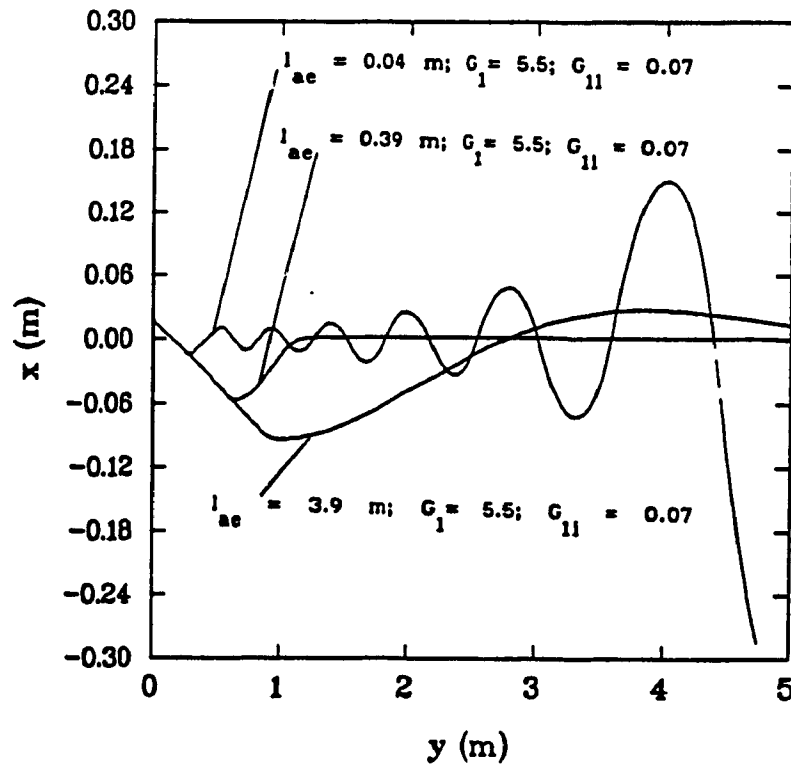


Fig. 6.36 Transient response of AGV with various equivalent wheel-base ($G_1 = 5.5; G_2 = 0.07$)

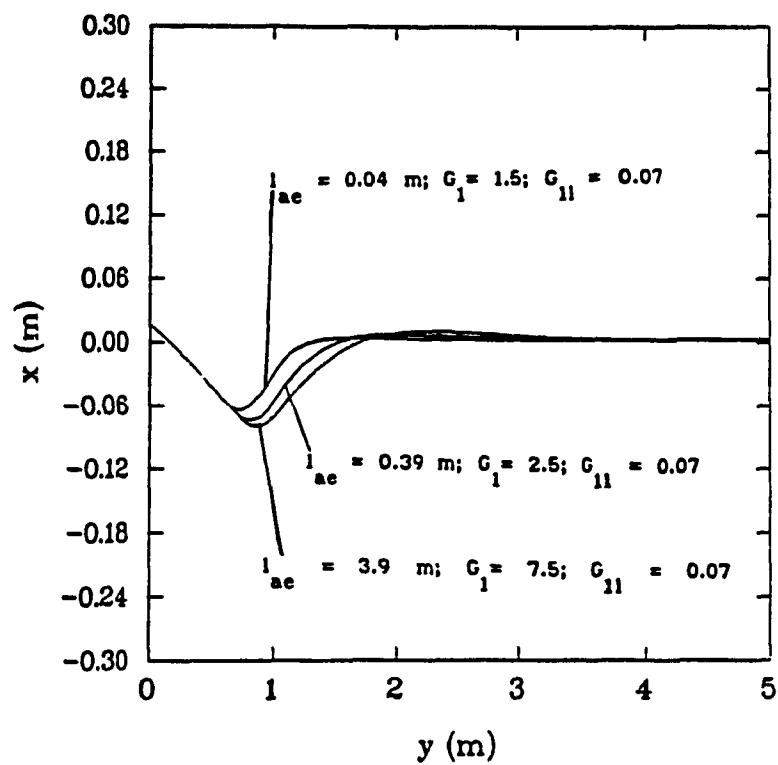


Fig. 6.37 Transient response of AGV with various equivalent wheel-bases at optimal controller settings

the time for the servo loop to reach the lower one in the two velocities is longer. The vehicle takes a longer time to respond. It is also shown that the shorter wheel-bases make the vehicle respond faster but less stable in the high gains, and it also makes the vehicle more sensitive to the initial conditions.

The discussion of the above two sections shows that the longer camera length makes the vehicle respond smoother and have less overshoot, and the shorter equivalent wheel-base makes the vehicle respond faster but less stably. For the CONCIC-2 AGV, the camera length is 0.69 m. From Fig. 6.35, Fig. 6.36, and Fig. 6.37, the relative best equivalent wheel-base may be about 0.39 m, which is about half of the camera length.

6.2.3. The study of servo control loop

6.2.3.1 The stability of the vehicle

In the above simulations, assumptions were made that there is *no slippage at the wheels* and that *there is always enough power provided by the motors*. But in real life, there are some physical constraints which go against these assumptions. For instance,

- 1) the upper limit of starting current and the working current;
- 2) the upper limit of the static friction at the wheels.

The limit of the starting current is dictated by the characteristic of the driving motor. For the CONCIC-2 AGV, the maximum starting current of the driving motor is 36 Amp (Appendix B). The second constrain depends on the characteristic of the tire and the working surface. The static friction at the contact patch can be represented as two vectors: One acting along the direction against the heading of the wheel (or the direction of tractive

force), and the other along the lateral axis. When the tractive force is bigger than the limiting friction, there will be longitudinal slippage at the contact patch. Similarly for the case of side-slip, when the second vector of the static force is smaller than the centripetal force at the wheel, the wheel will slip sideways. The coefficient of the static friction is estimated to be 0.2 for the motorized wheels in both directions (see Table 3.2).

Fig. 6.38 (a), (b), and (c) presents the transient response of the motor currents, the tractive force, and the centripetal force of the AGV operating under the following conditions:

initial position offset: 3 cm;

initial orientation error: 12° ;

linear velocity: 0.431;

acceleration constant: 0.048 m/s^2 ;

and controller gains G_1 and G_2 : 3.5, 0.5 respectively.

In this case, the maximum starting current of the AGV is about 15 A, which is well below the limit as 36 A. The maximum tractive force and the centripetal force are about 8 N and 5 N respectively, which are less than 50% of the limiting static friction. The assumptions are well validated in this case. In general, these assumptions are valid for CONCIC-2 AGV operation at its normal working speeds of under 1 m/s.

6.2.3.2 The mismatch of the two servo loops

In the real life, it is difficult to expect the servo loops to match perfectly in their characteristics. For example, the amplifier may become degenerated with time, and the two servo loops become mismatched. The

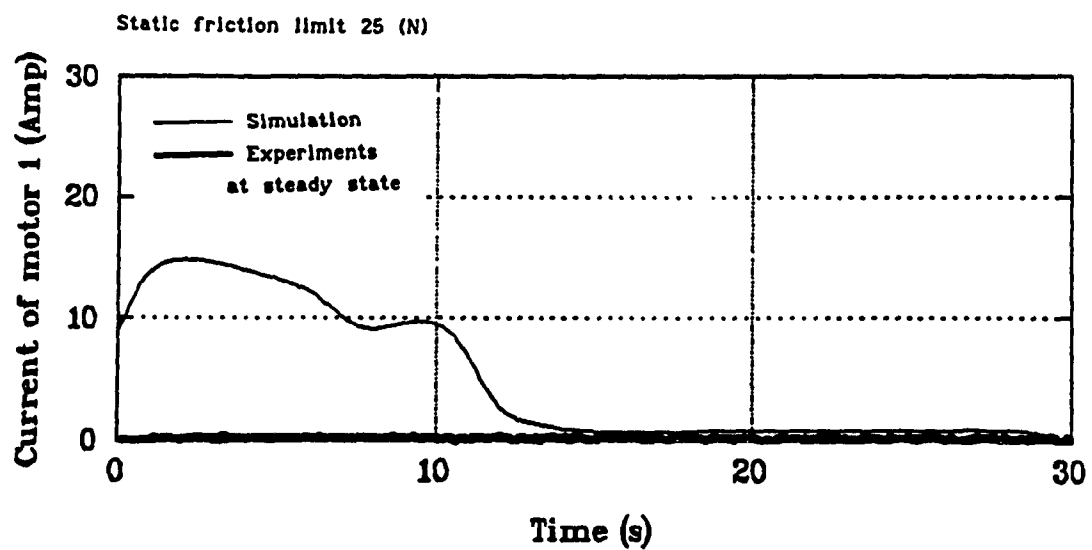
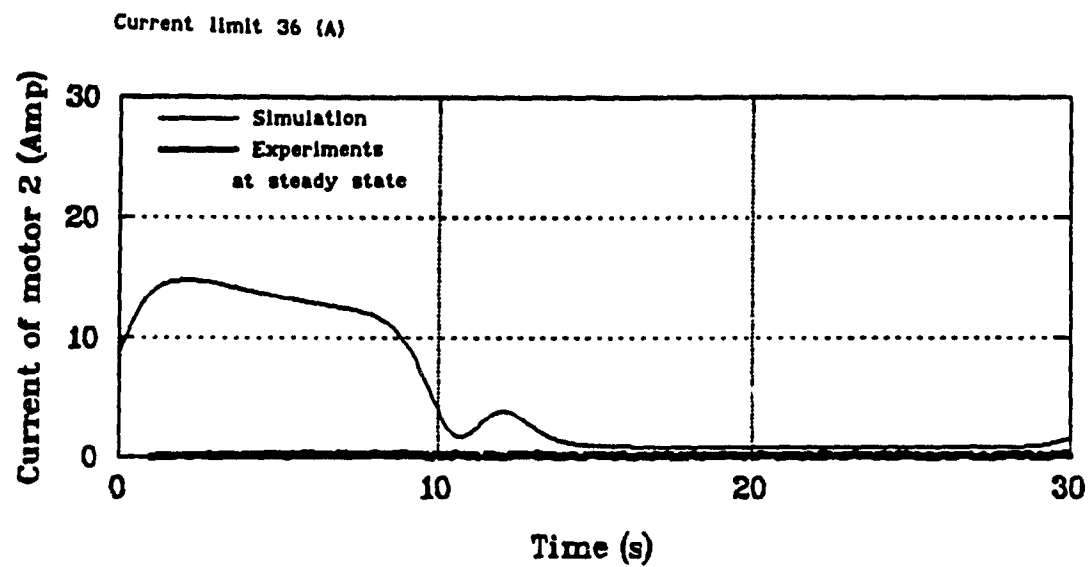


Fig. 6.38 (a) Current response of motor-1 and motor-2

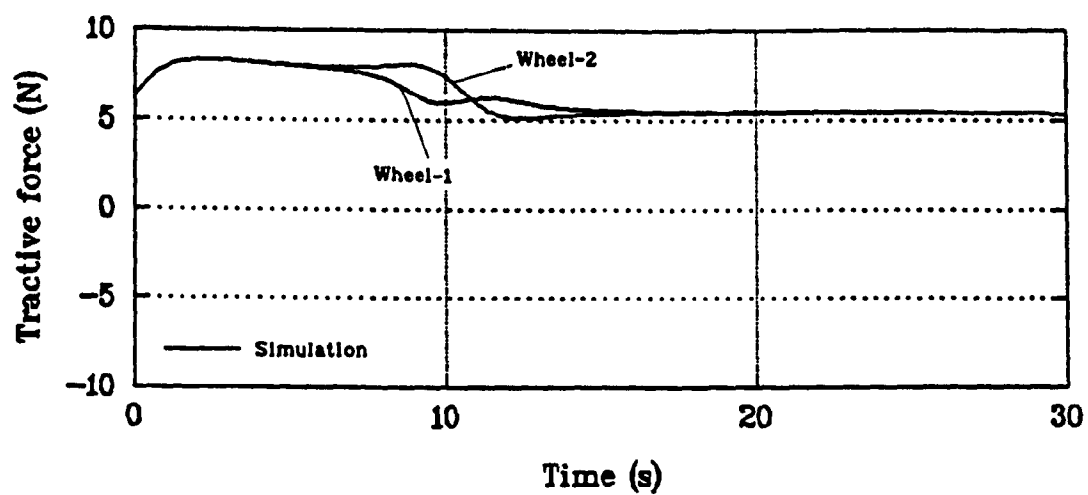


Fig. 6.38 (b) Tractive force of the AGV

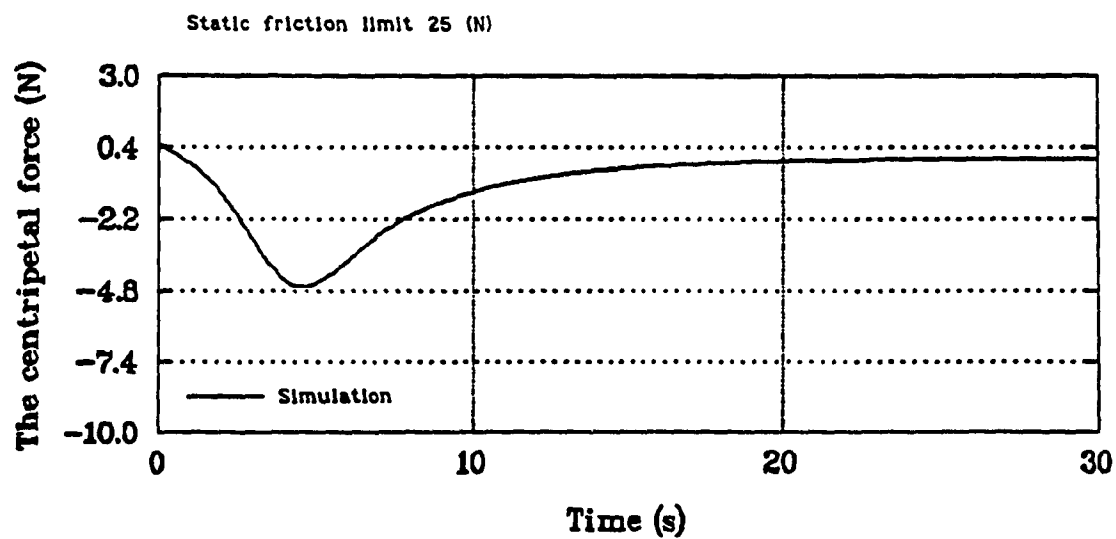


Fig. 6.38 (c) Centripetal force of AGV

following figure gives some cases of mismatched servo loops in terms of amplifiers. In Fig. 6.39, the continuous line presents the characteristics of the amplifier in the servo loop of wheel 1, and the dashed line presents the characteristics of the amplifier in the servo loop of wheel 2. Case 1 and case 2 show the two linear mismatched cases, and case 3 and case 4 show two kinds of nonlinear ones. The maximum deviation between the two curves is 20%.

Fig. 6.40 shows the performance of the vehicle in these cases under the conditions:

initial position offset = 2 cm;

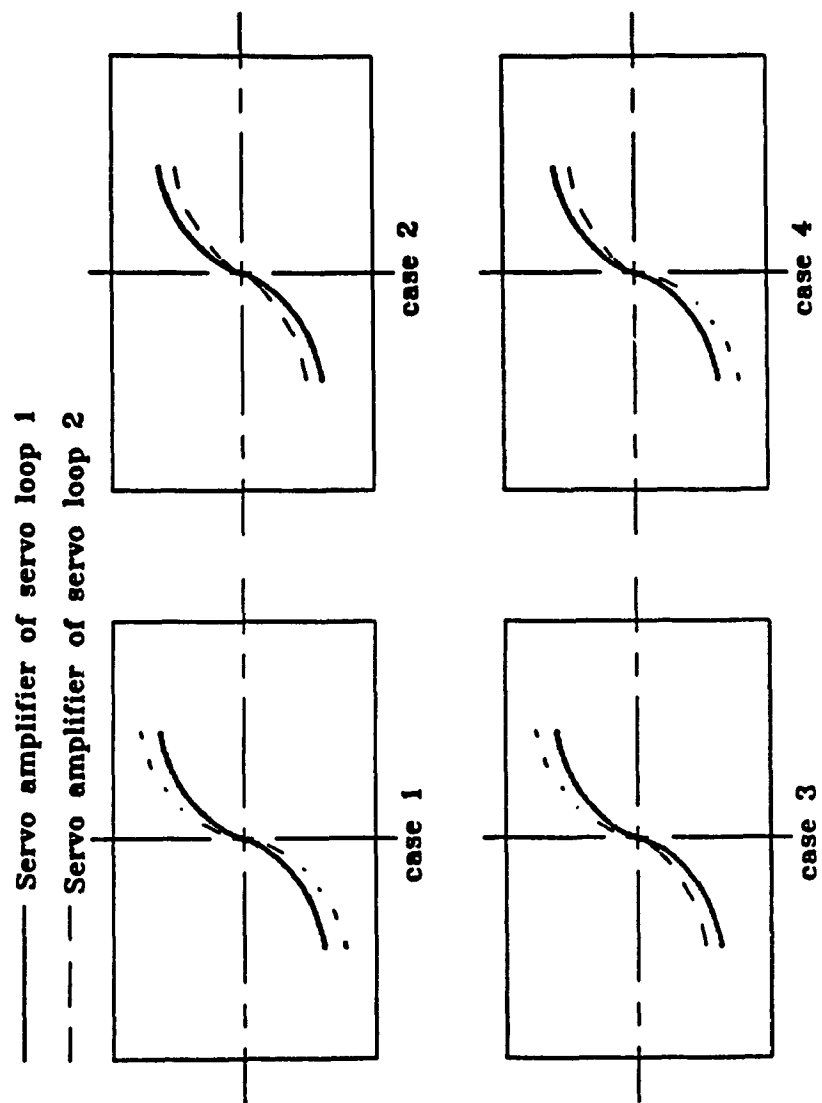
initial orientation error = 0.12 rad;

$G_1 = 2.5$; $G_{11} = 0.007$; and $G_2 = 0$,

$a_a = 0.25 \text{ m/s}^2$.

The line with dot symbol presents the performance in the case of perfectly matched pair. The results show that the mismatching of the servo loop affects the performance of the vehicle in most of the cases. In case 1, it is seen that the vehicle has a bigger overshoot. And at case 2 the vehicle responses very slowly and has a offset in the steady state. The performance of the vehicle at case 3 almost has no difference compared with the case of the perfectly matched pair. But in case 4 the vehicle again responds slowly and has an offset in the steady state.

Further simulation also shows that by increasing the proportional and integral gains of the guidance controller, the overshoot and offset can be reduced. Fig. 6.41 presents the results for the above cases when the proportional and integral controller gains G_1 and G_{11} of the guidance controller is increased to 5.5 and 0.7 respectively. Notable improvement is



Note: For all the cases, the maximum deviation between the two loops is 20%

Fig. 6.39 Mismatched cases of the servo loops (servo amplifiers)

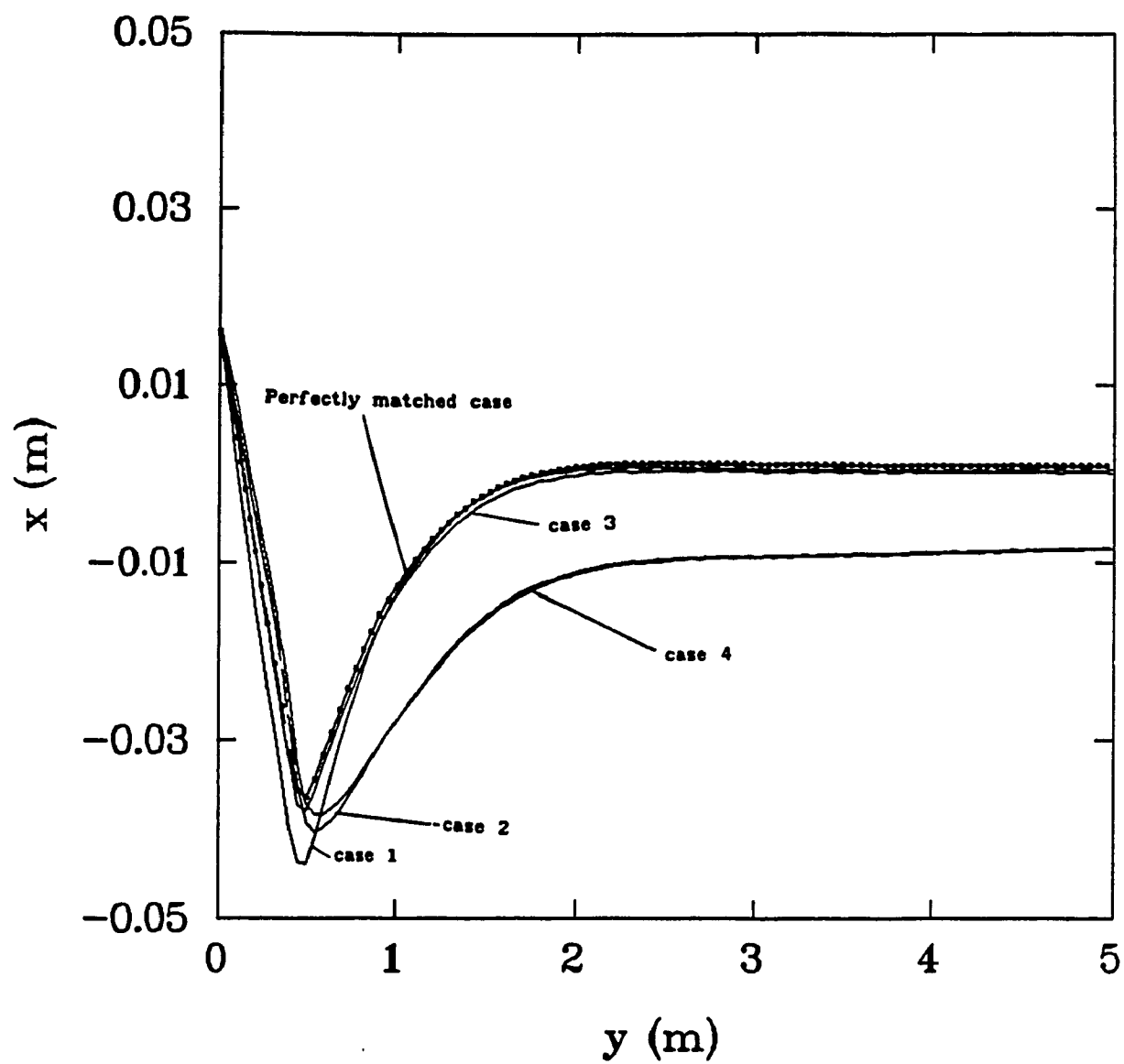


Fig. 6.40 Transient response of AGV in perfectly matched and mismatched cases

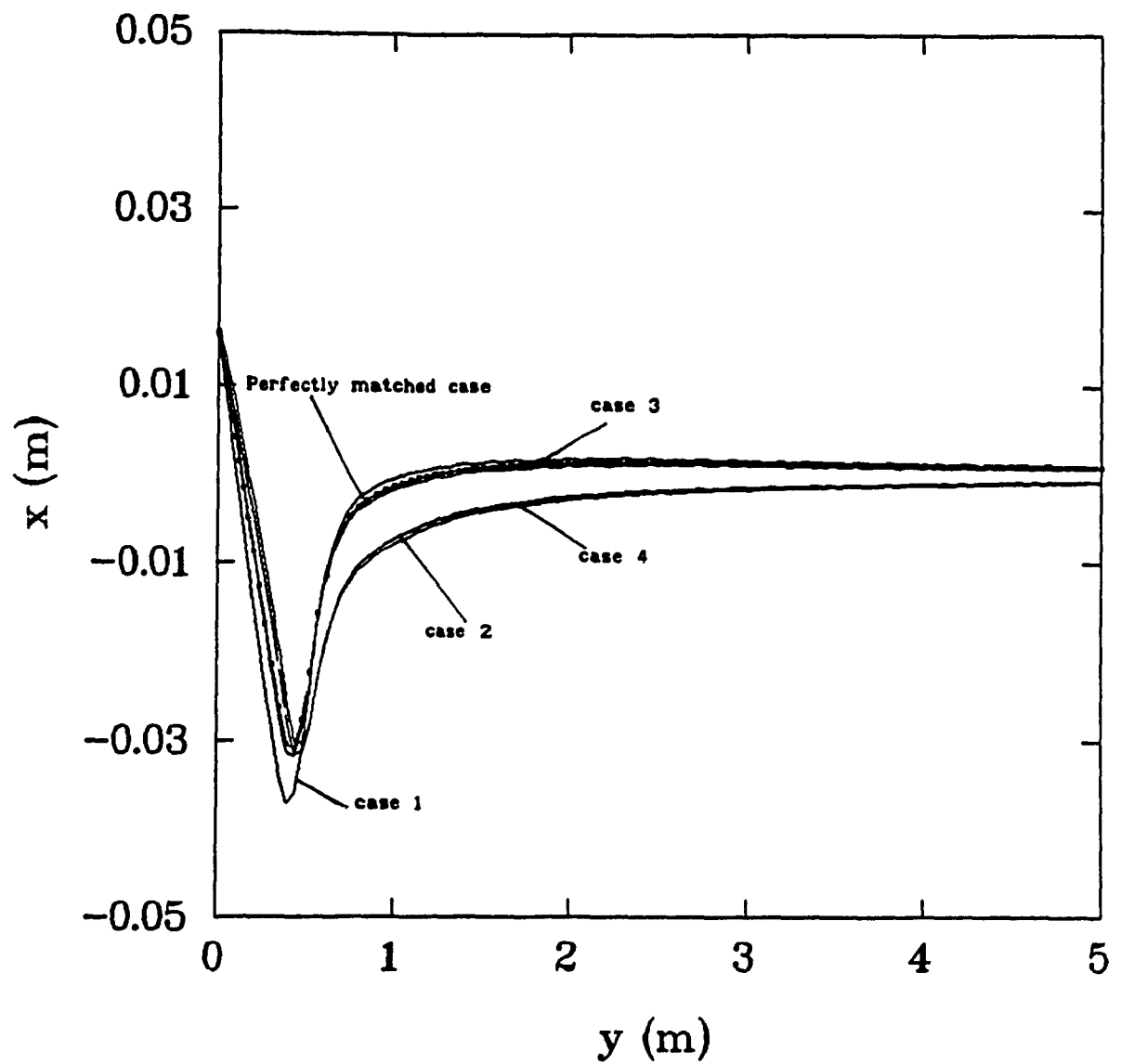


Fig. 6.41 Transient response of AGV in perfectly matched and mismatched cases at optimal controller settings

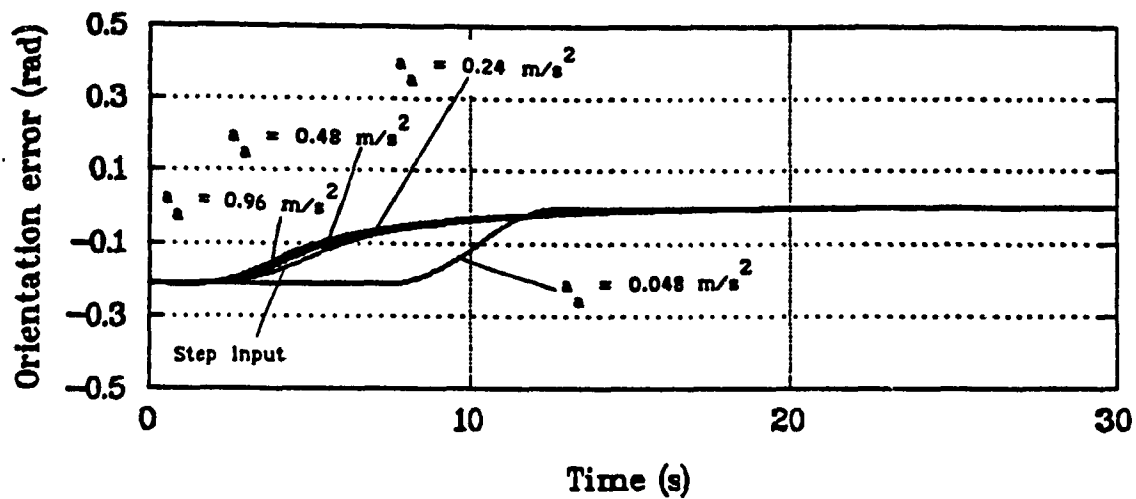
observed. For case 1, the overshoot has been reduced from 4.5 cm to 3.8 cm. For case 2 and case 4, response time has become much less, and the offset has been eliminated after approximately 8 m (not shown).

6.2.3.3 The acceleration constant a_a and the sensitivity of the control strategy to different initial orientation angles

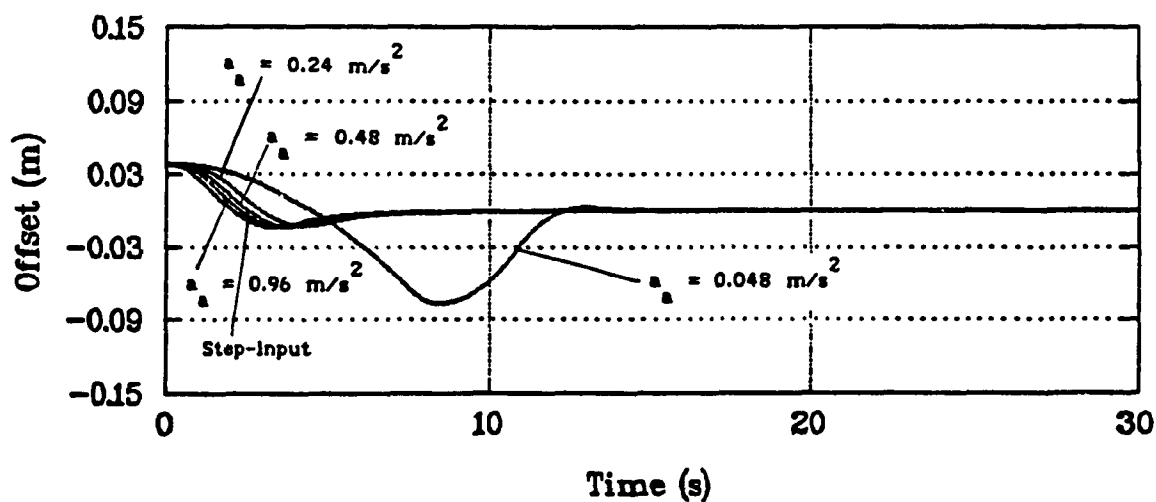
The servo-control loop of the CONCIC-2 contains a LM628 chip, a D/A converter, a power amplifier and an encoder which provide the feed-back signal from the motor. The control parameters of the servo-control loop are the control settings of the PID filter and the acceleration constant for the velocity-profile-generator. Both functions are included in the LM628, and these parameters are programmable from the main computer.

Once the settings of the PID filter and the amplifier are chosen, the starting current is dependent on the error between the reference velocity and the actual velocity of the wheel. From the previous chapters, it is known that the reference velocity builds up at a constant acceleration (or deceleration) a_a to the command velocity. At smaller a_a , the reference velocity as provided by the velocity profile generator of the LM628 changes slowly. Consequently, as the maximum velocity error is decreased, so does the input voltage to the motor. In this case, the AGV also has a slower response and a longer transient time. That this is so has been observed in both the simulation and the experiments.

Fig. 6.42 shows some simulation results to illustrate the effecting of different a_a . Fig. 6.42 (a) is the response of the orientation angle of the AGV, and Fig. 6.42 (b) is the offset response of the AGV. The tests have been done under the following conditions:



(a) - orientation error



(b) - position offset

Fig. 6.42 Transient response of AGV with various acceleration constant a_a

initial position offset: 3 cm;

initial orientation error: 12° ;

linear velocity: 0.471 m/s;

controller gains G_1 : 3.5 and G_2 : 0.5.

In Fig. 6.42, when a_a is 0.048 m/s^2 , the transient time of the vehicle is about 12 s, and the vehicle trajectory has a large overshoot of about 7 cm. When a_a increases to 0.24 m/s^2 , the transient time decreased to about 6 s, and only about 1.5 cm overshoot is observed. And it is also seen that there is a limitation for the AGV to respond to a_a beyond a certain value (about 0.25 m/s^2). Experiments also demonstrate similar results shown in Fig. 6.43. This limitation may be due to the time constant of the motor and vehicle dynamics. Another factor that prevents the vehicle from having a higher acceleration constant is the limiting starting current. The study through the simulation shows that the starting current increases significantly with the increase of the acceleration constant. 0.25 m/s^2 has been observed to be the best value of a_a for the CONCIC-2 AGV, by both simulation and experiments. In the case of low accelerations, the response of AGV is very sensitive to the initial orientation error because of the long transient time. This has been demonstrated in Fig. 6.44.

6.2.4. The study of the geometric configuration

The study of geometric configuration presented here includes two parts:

1) the wheel configuration;

2) the relationship between the wheel-span and the radius of the wheel.

Performance Comparison for Various Acceleration

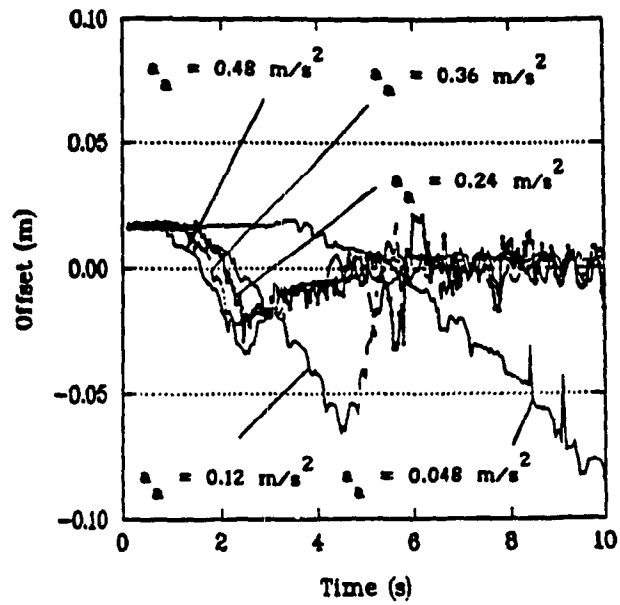


Fig. 6.43 Comparison of AGV performance with various acceleration constant a_a (experiment results)

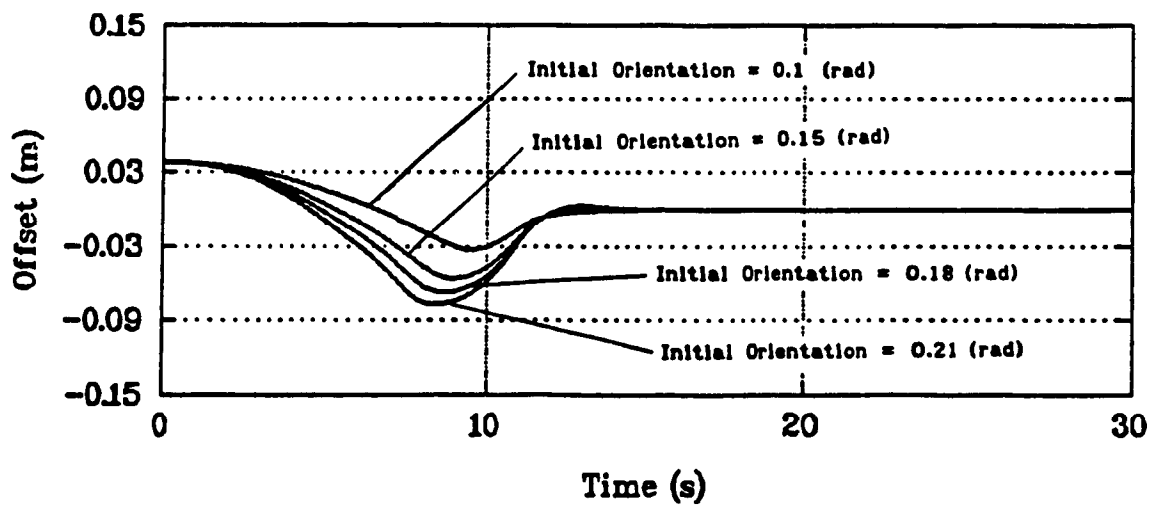
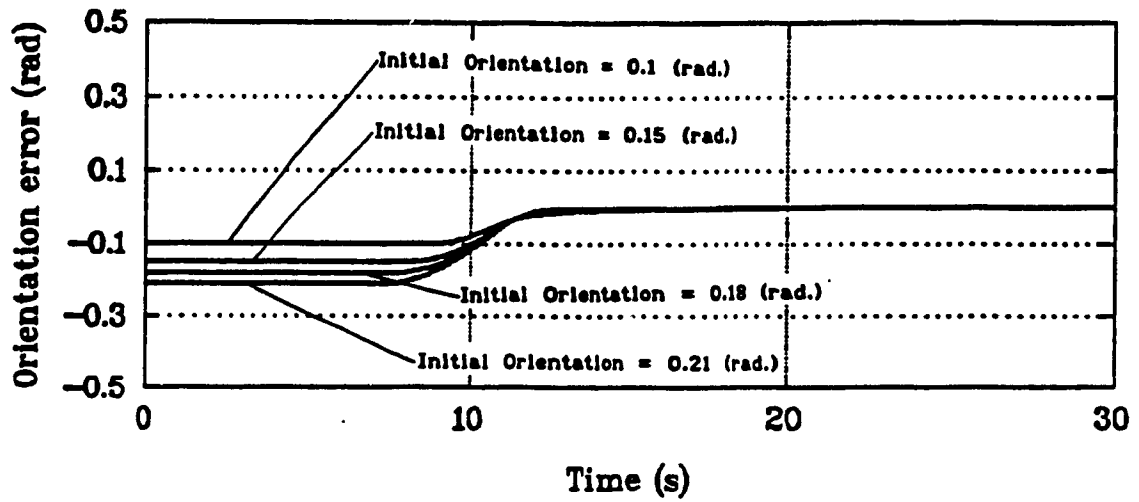


Fig. 6.44 Transient response of AGV under different initial orientation angle at a small a_x (0.048 m/s²)

6.2.4.1 The wheel configuration

The rectangular body of the AGV is designed to meet the needs of the applications and to fit the working environment. The four wheels are located near the four sides of the rectangular prism body in order to have a good support of the weight. This section discusses the effects of the wheel location on the behavior of the vehicle.

Fig. 6.45 presents the simulations for different wheel-spans l while the wheel-base k is fixed. The line with dot symbol is the trajectory of the vehicle with normal wheel-span (0.26 m). The results indicate that changes in the wheel-span has no significant effect on the behavior of the vehicle. When the wheel-span decreases by 50% (0.13 m), the overshoot of the trajectory of the vehicle increases slightly (by about 5%). And when the wheel-span increases by 100% (0.52 m), the trajectory of the AGV has slightly less overshoot (by about 5%) and with slight oscillations. The change of the wheel-span thus has little effect on the response of the vehicle.

Once the wheel-span of the vehicle is chosen, the wheel-base can be selected accordingly. The results in Fig. 6.46 show the trajectory of the vehicle with changes in the wheel-base. The plot with the dotted symbol is the trajectory of the vehicle at current wheel-base (0.39 m). When the wheel-base increase 100% (0.78 m), the overshoot of the trajectory decreases slightly (by 5%), but the vehicle takes longer time to eliminate the deviation. On the contrary, when the wheel-base decreases to 0.18 m, the overshoot of the trajectory increases by 5% and the vehicle takes much less time to steer itself back to the path. The simulation investigation indicates that the wheel-base may be chosen to be a littler longer than the

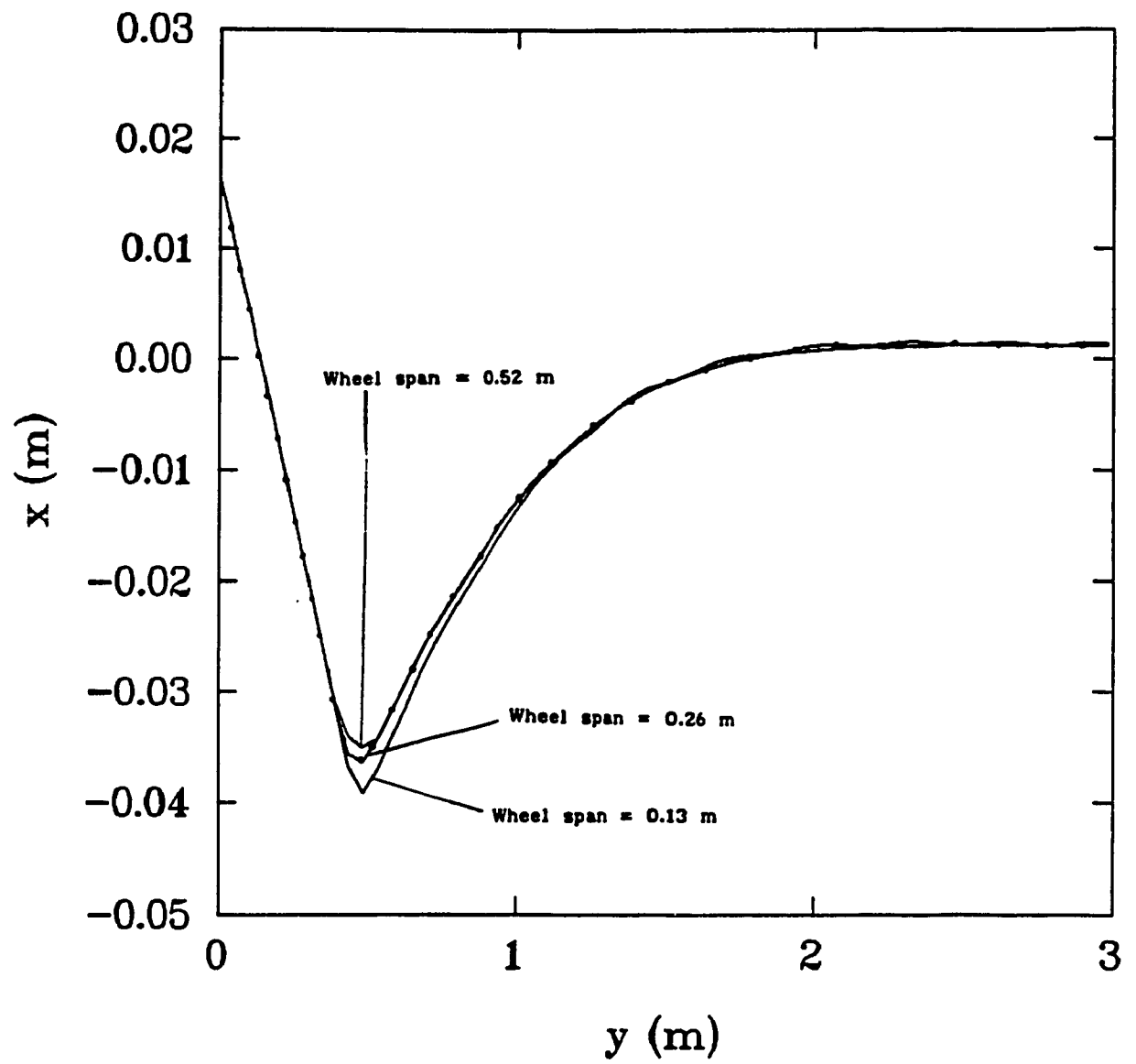


Fig. 6.45 Transient response of AGV with various wheel-spans

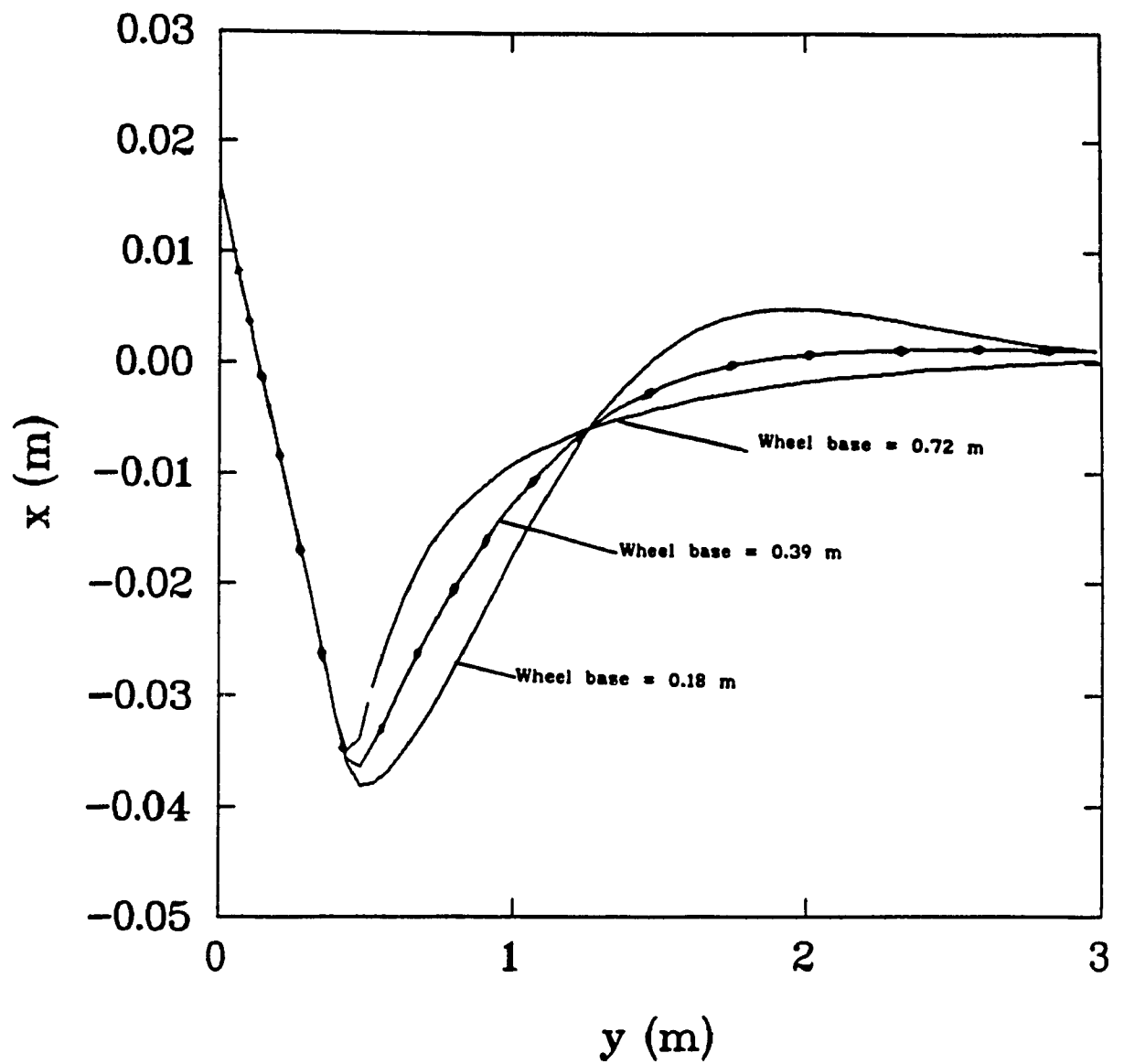


Fig. 6.46 Transient response of AGV with various wheel-bases

wheel-span in order to obtain a smooth response.

6.2.4.2 The relationship of the wheel-span and the radius of the drive wheel

The radius of the drive wheel is a minor factor that may affect the vehicle behavior. Since a small drive wheel requires a fast rotation of the motor and a high motor current output, so the smallest radius of the drive wheel is chosen based on how much energy it can provide and how fast it rotates. On the other hand, the simulation study shows that the radius of the motorized wheel can not be too large either. The results in Fig. 6.47 indicate this limitation. For the CONCIC-2 AGV, when the radius of the motorized wheel is increased from 0.075 m to 0.15 m, the AGV starts to have oscillations. Otherwise, within the limits, the dynamics of the AGV does not change significantly with different radii of the wheels.

6.2.5. The dynamic response of the casters

In this section, we will discuss the contribution of the casters to the AGV dynamics.

The casters are used to carry the weight of the AGV. In CONCIC-2 AGV, the casters have a small mass compared to the mass of the entire system. It is observed that the dynamics of the caster has an insignificant effect on the system behavior. Fig. 6.48, and Fig. 6.49 show the simulation response of the casters at two different initial caster angles with otherwise the same vehicle initial conditions. The AGV dynamic response however is not noticeably affected by the difference of caster response in both cases (Fig. 6.50). Experiments also confirm this observation (see Fig. 6.51). It means that we can ignore the initial caster angles for the CONCIC-2 AGV. This helps to simplify the dynamic modeling.

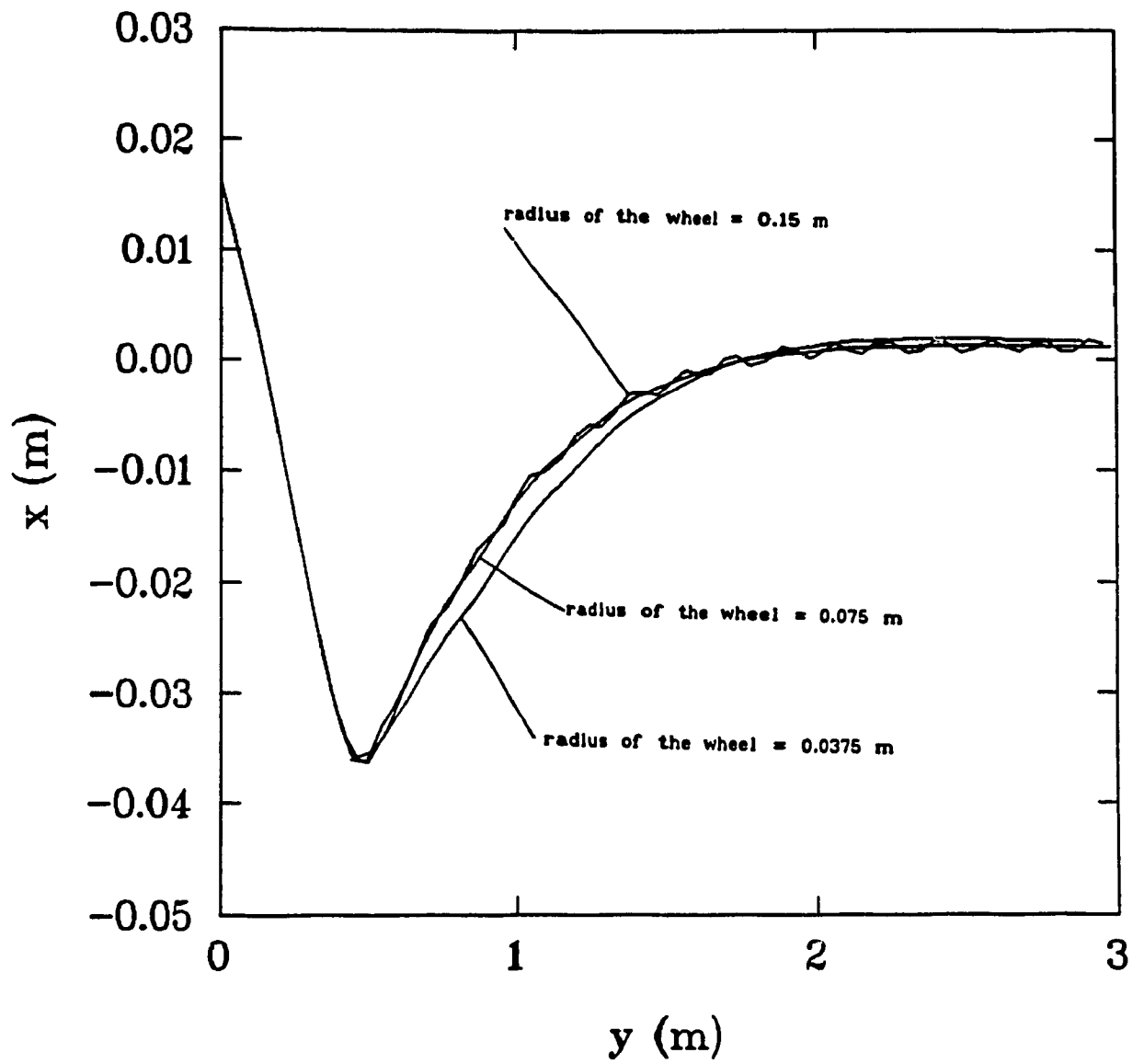


Fig. 6.47 Transient response of AGV with various wheel radii

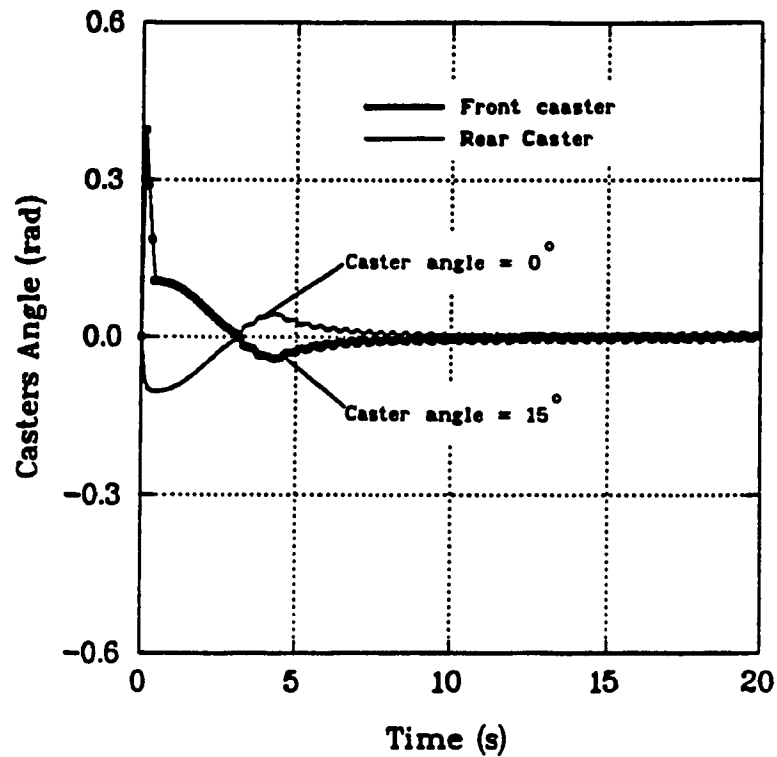


Fig. 6.48 Response of casters
(initial angle: front caster=15°; rear caster=0°)

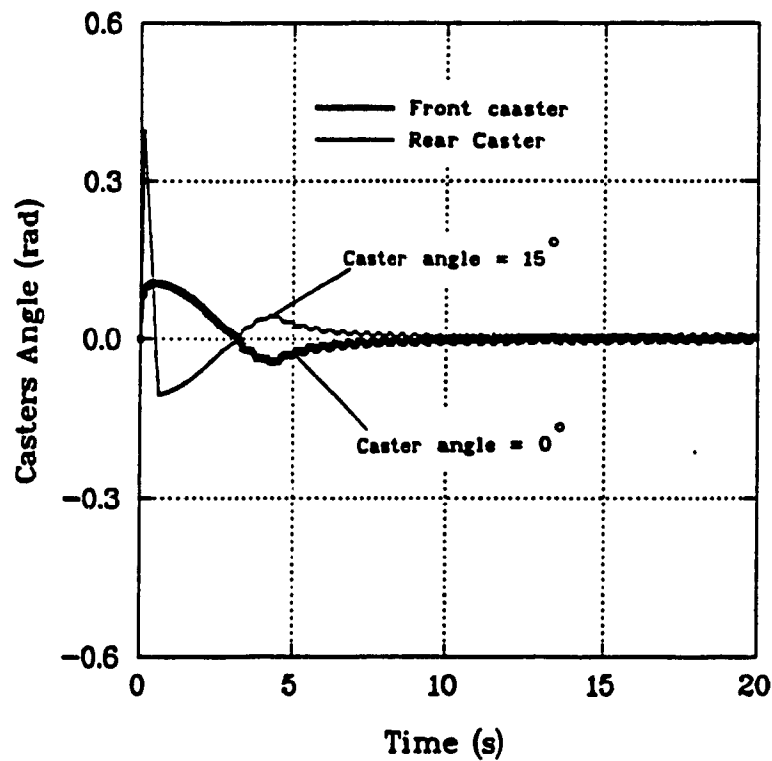


Fig. 6.49 Response of casters
(initial angle: front caster=0°; rearcaster=15°)

AGV performance with different caster angles
(simulation)

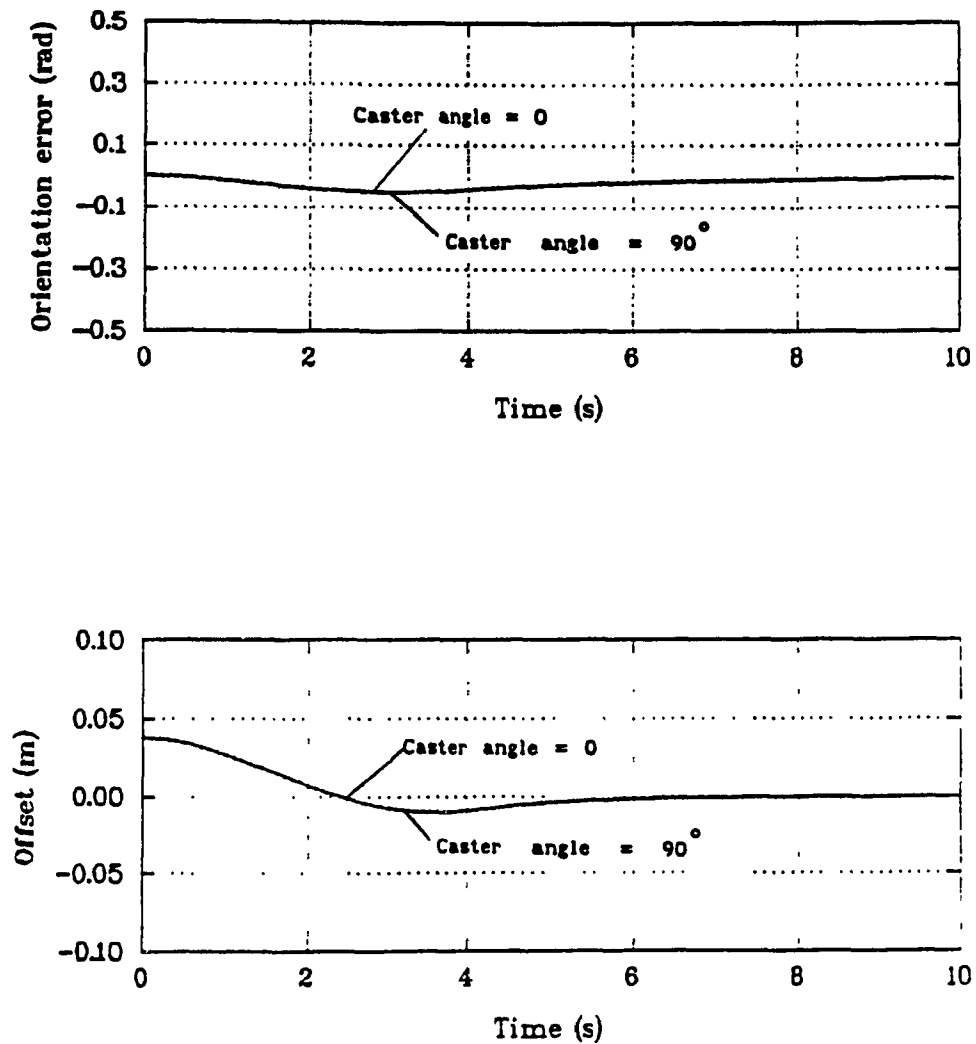


Fig. 6.50 Performance of AGV with various caster angles -- simulation
(a - orientation error; b - position offset)

Performance with Various Caster Angles

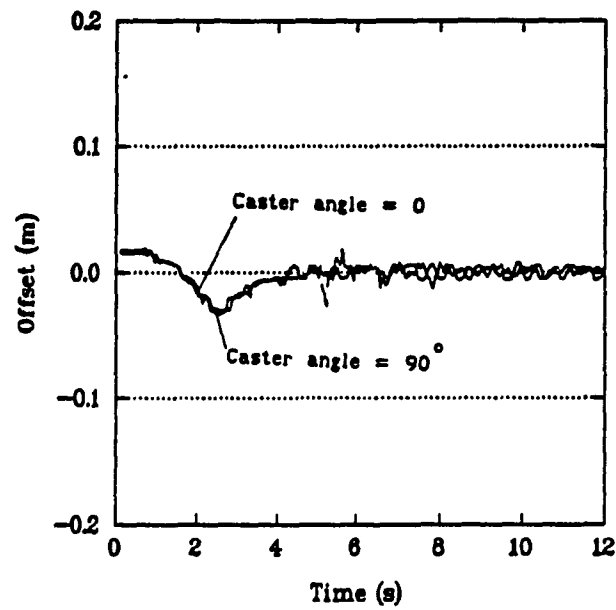


Fig. 6.51 Performance of AGV with various caster angles
(Experiment results)

CHAPTER 7 CONCLUSION AND FUTURE WORK

In this thesis, a complete dynamic model of CONCIC-2 AGV system is presented, validated by experiments. This is followed by an experimental and simulation investigation into the characteristics of the vehicle. The parameters of this model are obtained from experiments and manufacturers specifications. An intensive study of guidance control and servo control is presented.

The model is validated in two levels:

- 1) the servo loop;
- 2) the overall control system.

The simulation results show a very good agreement with experimental results for different operating and control conditions, such as different controller initial conditions, different velocities, and different acceleration constants of the velocity profile generator in the LM628.

For a straight-line profile, the optimal settings of the guidance controller is observed to be within a range of G_1 and G_2 (optimal area); there is no single optimal setting as such. This range is found to be influenced by the vehicle speed, and the initial conditions. The lower the vehicle speed, the larger the optimal area is. The combination of the initial conditions is found to have a significant effect on the orientation gain. The orientation gain is observed to be higher in the case in which the position offset ϵ_d and the orientation error ϵ_θ had opposite signs. On the other hand, when ϵ_d and ϵ_θ had the same signs the optimal settings of the guidance controller had lower orientation gains.

For a circular path, the optimal area of the guidance controller is found to be affected by the radii of the path. Compared with the straight-line profile, the most significant phenomenon observed in the circular path with non-infinite radius is the poorer control ability at lower gains. Also the optimal area becomes smaller when the radius of the circular path decreases. It is also more sensitive to the vehicle speeds.

With certain controller settings, the transient responses of the vehicle are affected by many design parameters, such as the location of the camera sensor and the location of the virtual steering wheel. From the study, it is observed that the vehicle has a smooth response and less overshoot when the camera length is longer. However, the price to pay is an increase of total vehicle length; and more space is required by the AGV. On the contrary, shorter camera lengths make more compact vehicles. And these vehicles tend to be less stable. The location of the virtual steering wheel is another factor which is found to affect the transient response of the AGV. When the virtual steering wheel is located further away from the center of mass, the AGV responds slower and requires higher gains to achieve the optimal performance. On the other hand when the virtual steering wheel is close to the center of mass, the AGV has a faster response and needs lower gains, and a more restricted 'optimal area' for the guidance controller. Another factor which is found to affecting the transient response significantly is the programmable acceleration constant a_a of the LM628 chip. The AGV has a faster response at a high acceleration constant. At low a_a , it is observed that the vehicle is more sensitive to the initial orientation angles, while the response time increases. With increasing a_a , it is found that there is a limiting value for a_a , above which the response

time does not reduce any further. This phenomenon is not due to the limitation of the power rating. The simulation study also demonstrated that the mismatched characteristics in the two servo loops can cause certain undesirable offsets at steady state. These offsets, however, can be eliminated by choosing larger controller gains.

The study of the geometry structure of CONCIC-2 is also presented in the thesis. For a wheel-base of 0.39 m, the wheel-span is found to have insignificant effect on the response of the AGV. But for a fixed wheel-span of 0.26 m, it is observed that the longer wheel-bases, the slower and smoother the vehicle responds. And the radii of the driving wheels should not be too large, otherwise it tends to make the vehicle less stable.

The proposed model has the advantages of having a realistic structure, an accurate performance compared with real-time experiments, and an ease of modification. It has a modularized structure which makes the complicated system easy to understand. The modularized model provides a convenient and easy way to implement any kind of new design, and gives all the possible variables of the system. With the animation program, a visible and animated 'cartoon' gives a good representation of the vehicle response.

The dynamic model presented in this thesis is for a 2 d-o-f AGV with differential drive. The vehicle considered for the analysis does not have suspension system, and is operated on a flat concrete floor at low speeds. This kind of model is realistic and sufficient for the CONCIC-2 AGV as it has been shown in the thesis. If it is desired to provide the vehicle with suspension then, more degrees of freedom should be considered, and hence the dynamic model need to be refined. Furthermore, if a vehicle with a wheel-base configuration other than the differential drive is employed, then

changes need to be incorporated in the model. Considering these issues, an approach to the development of a generic model is proposed. In Appendix A, the author proposed a general procedure for developing the equations of motion of a AGV of 4 d-o-f with various wheel configurations. No implementation of this approach has been included in this thesis. However, this general approach can be used as a basis for continued research into AGVs. It is also proposed that a design procedure for AGVs, and more investigation on the suspension system and cornering stability of AGVs may be developed in the future study.

REFERENCE

- [1] Archibald, S., *Bicycles and Tricycles*, MIT Press, 1979.
- [2] Beer, F.P., Johnston, E.R. *Mechanics for Engineering Statics and Dynamics*, McGraw-Hill Book Company, 1988.
- [3] Cheng, R.H.M., Courbet, Y., Surpaceanu, M., Favreau, P., Fahim, A., *Investigation of an Automated Guided Vehicle (AGV) Driven by Camera Vision*, Intelligent Autonomous Systems, An International Conference, Amsterdam, Netherlands, Dec. 8-11, 1986, pp. 162-167.
- [4] Cheng, R.M.H., Huang, M., *A Study of Guidance Strategy of an AGV System Using the Simulation of the Dynamic Model*, Proc. of Thirteenth IASTED International Symposium, ROBOTICS AND MANUFACTURING, Santa Barbara, USA, Nov. 13-15, 1990, pp. 13-17.
- [5] Cheng, R.M.H., Huang, M., Sankar, T.S., *Dynamic Simulation of CONCIC-2 Vehicle*, Accepted by IFToMM -- Eighth World Congress on the Theory of Machines and Mechanisms, Prague, CZECHOSLOVAKIA, Aug. 26 - 31, 1991.
- [6] Culley, G., Baldur, R., *Experiments with a Free Wheel Approach to AGV Navigation*, Proc. of Robots 12 Conference, Detroit, June, 1988.
- [7] Ellis, J.R., M. Sc. (Eng). Ph.D., *Vehicle Dynamics*, BUSINESS BOOKS LIMITED, London, 1969.
- [8] Evans, B., *AGVs Begin to Leave The Beaten Path*, Mechanical Engineering, November 1988, pp. 38-41.
- [9] Gratetinger, T.J., Krough, B.H., *Evaluation and Time-Scaling of Trajectories for Wheeled Mobile Robotics*. Trans. ASME, JDMC, Vol. 111, June 1989, pp. 222-231
- [10] Hatwal, H., and Mikulcik, E.C., *Some Inverse Solutions to an Automobile Path-Tracking Problem with Input Control of Steering and Brakes*, Vehicle

System Dynamics, Vol. 15, 1986, pp. 61-71.

[11] Hatwal, H., and Mikulcik, E.C., *An Optimal Control Approach to the Path Tracking Problem for an Automobile*, Transaction of CSME, Vol. 10, No. 4, 1986, pp. 233-241.

[12] Hayhoe, G.F., *A driver model based on the Cerebellar Model Articulative Controller*, Vehicle System Dynamics, Vol.8, No.1, 1979, pp. 49-72.

[13] Hemami, A., Mehrabi, M.G., and Cheng, R.M.H., *A New Control Strategy for Tracking in Mobile Robots and AGVs*, Proc. of the 1990 IEEE international conference on Robotics and Automation, Cincinnati, Ohio, May 13-18, 1990.

[14] Horton, D.N.L., Crolla, D.A., *The Handling Behavior of Off-Road vehicles*, Int. J. of Vehicle Design. Vol.1.5, U.K., 1984.

[15] Huissoon, J.P., *Motor Control for AGVs With Differential Drive Steering*, Proc. of IASTED Conference on Robotics And Automation, Santa Barbara, California, U.S.A., 1988.

[16] Johnson, B.W., and Aylor, J.H., *Modeling of Wheelchair Dynamics for The Design of a Microcomputer-Based Controller*, Proc. of Industrial Electronics and Control Instrumentation Society Meeting (IECI), 1981, pp. 70-75.

[17] Johnson, B.W. *Microcomputer-based Adaptive Control for a Electric Wheel-chair Guidance System*. Ph.D. Thesis, University of Virginia, University Microfilms International, 1983.

[18] Julliere, M., Marce, L., and Perrichot, H., *A Guidance System for a Vehicle Which has to Follow a Memorized Path*, Proceedings of the 2nd International Conference on Automated Guided Vehicle Systems, and 16th IPA Conference, Stuttgart, W. Germany, June 7-9, 1983

[19] Julliere, M., Marce, L., and Place, H., *A Guidance System for a Mobile Robot*, 13th ISIR/Robots 7 Conference, Chicago, Illinois, April 17-21, 1983.

- [20] Kanayama, Y., and Miyake, N., *Trajectory Generation for Mobile Robots*, Robotics Research, The Third International Symposium, Cambridge, MA, MIT Press, 1986 pp. 334-340.
- [21] Kanayama, Y., Nilipour, A., and Leim, C.A., *A Locomotion control method For Autonomous Vehicles*, Proc. of IEEE International Conference on Robotics and Automation, Vol. 2, Philadelphia, PA, 1988, pp. 1314-1317.
- [22] Kanayama, Yutaka, Hartman, B.I., *Smooth Local Path-Planning for Autonomous Vehicles*, Submitted to the AAAI-88 National Conference on Artificial Intelligence, St. Paul, Minnesota, August 22-26, 1988
- [23] Kanayama, Y., Yuta, S.I., *Vehicle Path Specification by a Sequence of Straight Lines*, IEEE J. of Robotics and Automation, Vol.4, June 1988.
- [24] Kanayama, Y., Kimura, Y., Miyazaki, F., and Noguchi, T., *A Stable Tracking Control Method for an Autonomous Mobile Robot*, Proc. of IEEE International Conference on Robotics and Automation, Cincinnati, Ohio, May 13-18, 1990.
- [25] Kim, O.H., *Optimal steering control of an Auto-Guided-Vehicle with two motored wheels*, Trans. Inst. M. C. Vol 9, No 2, April-June 1987, pp. 58-63.
- [26] Krogh, B.H., and Feng, D., *Dynamic Generation of Subgoals for Autonomous Mobile Robots Using Local Feedback Information*, IEEE Trans. on Automatic Control, Vol. 34, No. 5, May, 1989, pp. 483-493
- [27] Larcombe, M.H.E., *Tracking Stability of Wire Guided Vehicles*, 1st Int. Conf. on Automated Guided Vehicle systems, Stratford-upon-Avon, U.K., 1981, pp. 137-144.
- [28] Legouis, T., Laniville, A., Bourassa, P., Payre, G. *Characterization of Dynamic Vehicle Stability Using Two Models of Human Pilot Behavior*. Vehicle System Dynamics, Vol. 5, No. 1, 1986.

- [29] Marinov, J., Nakov, O., Grozdanov, V., and Stefanov, St., *On a System for Microprocessor Remote Control and Guidance of an Adaptive Vehicle*, proc. of International Conference on Advanced Robotics, Tokyo, Japan, 1985, pp. 445-450.
- [30] Müller, Thomas, Dr.-Ing, *Automatic Guided Vehicles*, IFS (Publications) Ltd, UK, Springer-Verlag, Berlin, Heidelberg, New York, 1983.
- [31] Nakano, E., Koyachi, N., Agari, Y., and Hirooka, S., *Sensor System of a Guideless Autonomous Vehicle in a Flexible Manufacturing System*, Proc. of 15th International Symposium on Industrial Robots, Tokyo, Japan, 1985.
- [32] Nathoo, N.S., Healey, A.J, *Coupled Vertical_Lateral Dynamics of a Pneumatic Tired Vehicle: Part1 - A Mathematical Model*, Trans. of ASME, JDSMC, Vol. 100, Dec. 1978.
- [33] Nelson, W.L., Cox, I.J., *Local Path Control for an Autonomous Vehicle*, Proc. of IEEE International conference on Robotics and Automation, Vol. 2, Philadelphia, PA, 1988, pp. 1504-1510.
- [34] Okazaki, M., Tomikawa, H., Sudare, M., Terada, K., *New Guidance System For Automated Navigational Vehicle*, Proc. Japan-U.S.A. Symposium On Flexible Automation, Control and Design in Robotics, Vehicles and Flexible Manufacturing Systems, Osaka, Japan, July 14-18, 1986.
- [35] Rajagopalan, R., Huard, G., *System report on CONCIC-2 AGV: Design, Control and Theory of Operation*, Internal Report #CIC-0024, Concordia University, MTL. QUEBEC, 1989.
- [36] Rathbone, R.R., Valley, R.A. Jr., Kindlmann, P.J., *Beacon-Referenced Dead Reckoning: A versatile Guidance System*, J. of ROBOTICS ENGINEERING, Dec. 1986, pp. 11-16.
- [37] Sharp, R.S., *The Stability and Control of Motorcycle*, Journal of

Mechanical Engineering Science, Vol. 13, No. 5, 1971.

[38] Shung, J.B., Stout, G., Tomizuka, M., and Auslander, D.M., *Dynamic Modeling of a Wheelchair on a Slope*, Trans. of the ASME, J. of Dynamic Systems, Measurement, and Control, Vol. 105, June, 1983, pp. 101-106.

[39] Shung, J.B., Tomizuka, M., Auslander, D., and M., Stout, G., *Feedback Control and Simulation of a Wheelchair*, Trans. of the ASME, Vol. 105, June 1983, pp. 96-100.

[40] Sung, E., Loon, N.K., and Yin, Y.C., *Parallel Linkage Steering for an Automated Guided Vehicle*, IEEE Control System Magazine, Oct. 1989, pp. 3-8.

[41] Surpceanu, M., *A Study of the Lateral Stability for a Diamond-shaped AGV*, Internal report in CIC, Concordia University, MTL, QUEBEC, 1988.

[42] Tousi, S., Gajaj, A.K., Soedel, W., *On the Stability of a Flexible Vehicle Controlled by a Human Pilot*, Vehicle System Design, Vol. 17, Feb. 1988, pp. 37-56.

[43] Tsumura, T., *Survey of Automated Guided Vehicle in Japanese Factory*, Proc. of IEEE International Conf. on Robotics and Automation, San Francisco, CA, Vol. II, 1986, pp. 1329-1334.

[44] Whitt, F.R., and Wilson, D.G., *Bicycling Science*, MIT. Press, 1967

[45] Wong, J.Y., Ph.D., *Theory of Ground vehicle.*, JOHN WILEY & SONS, 1978.

[46] Zygmunt, Jeffrey, *Guided Vehicle Set Manufacturing in Motion*, High Technology, DEC 1986, Page 16-21.

[47] *Automotive Hand Book*, BOSCH

[48] *DC Motors, Speed Controls and Servo Systems.* an Engineering handbook by ELECTRO-CRAFT CORPORATION, 1984.

APPENDIX A

GENERAL PROCEDURE OF DYNAMICS OF AGV

A.1 INTRODUCTION

For a specific configuration, the motion equations of the AGV can be developed in many ways. The method in dynamic analysis — "Body-centered system" which is based on D'Alemberts principle, gives a general the equations of motion of a 6 d-o-f rigid body as follows:

$$\begin{aligned}
 \sum X &= m(\dot{U} - r V + q W) \\
 \sum Y &= m(\dot{V} - p W + r U) \\
 \sum Z &= m(\dot{W} - q U + p V) \\
 \sum L &= I_x \dot{p} - (I_y - I_z)rq + P_{yz}(r^2 - q^2) - P_{xz}(pq + \dot{r}) + P_{xy}(pr - \dot{q}) \\
 \sum M &= I_y \dot{q} - (I_z - I_x)rp + P_{xz}(p^2 - r^2) - P_{xy}(qr - \dot{p}) + P_{zy}(qp - \dot{r}) \\
 \sum N &= I_z \dot{r} - (I_x - I_y)qp + P_{xy}(q^2 - p^2) - P_{yz}(rp + \dot{q}) + P_{xz}(rq - \dot{p})
 \end{aligned}
 \tag{A.1.1}$$

Where $\sum X$, $\sum Y$, $\sum Z$, $\sum L$, $\sum M$, and $\sum N$ are the total forces along X, Y, Z axis and the total moments about X, Y, Z axis respectively. U, V, W are the linear velocities of the center of mass along X, Y, Z, and p, q, r are the angular velocities of the rigid body about X, Y, Z axis (Fig. A.1).

In each particular case of developing the equations of motion of a vehicle, the most difficult part may be to formulate the external forces at all wheels associated with the wheel configuration. In this appendix, a procedure is developed by classifying the wheels and the forces on it, further to develop the equations of motion with the corresponding coordinates. Once the configuration of the vehicle is desired, the equations of motion can be obtained by following the procedure with wheels and the

coordinates.

A.2 DISCUSSION OF THE INITIAL MODEL

Equations (A.1.1) are the motion equations of a 6 d-o-f rigid body. In the modeling of a vehicle, the degrees of freedom of the vehicle may be less, considering the working situations. Usually AGVs are design to work on the floor which is a flat and smooth surface. Therefore the movement along the direction Z which is normal to the surface may be considered to be negligible. In another word, $W = 0$ and $\dot{W} = 0$ in the equations.

In this study, the pitch motion of the vehicle is also considered to be negligible. It results $p = 0$ and $\dot{p} = 0$.

Thus, the motion equation for such a vehicle is written as

$$\begin{aligned}\sum X &= m(\dot{U} - r V) \\ \sum Y &= m(\dot{V} + r U) \\ \sum M &= I_y \dot{q} + P_{xz} r^2 - P_{xy} q r + P_{yz} \dot{r} \\ \sum N &= I_z \dot{r} + P_{xy} q^2 - P_{yz} \dot{q} + P_{xz} r q\end{aligned}\tag{A.2.1}$$

More assumptions are made as follows:

- 1) The normal reactions at every wheels are known before the formulation.
- 2) The steering action is considered as an angle input. In other words, the steering motor reacts to the command immediately without dynamic delay.
- 3) The center of mass of the vehicle is located at the geometric center of the vehicle.
- 4) The tires of steering and driving wheels are rubber tires.
- 5) There is no longitudinal slippage at the wheels.

A.3 TYPES OF WHEELS ON THE VEHICLE

The equations of motion of a 4 d-o-f rigid body are presented in (A.2.1), where $\sum M$, $\sum N$, $\sum X$ and $\sum Y$ are the external moments and forces acting on the rigid body.

For a AGV, the wheels used in the operation can be classified into four categories.

- 1) driving wheel
- 2) steering wheel
- 3) steering and driving unit
- 4) caster

Associated with the vehicle configuration and load distribution, the external forces and moments at these wheels dominate the motion of the vehicle.

A.4 THE CHARACTERISTICS OF WHEELS

In dynamic modeling of an AGV using the method of body-centered system, the vehicle is considered as a system of a number of rigid bodies. The steering-wheels, the drive-wheels, and the steering-driving units are considered as part of the main body because they are mounted rigidly to the vehicle body. Casters can rotate about their axle freely, they are considered being individual rigid bodies, and have their own equations of motion. The equations of motion are obtained by applying the body-centered system to each of the rigid bodies.

All the forces at the AGV main body are the reaction forces and moments at casters axles and the external forces at contact points of driving and steering wheels and the working floor. The reaction force from the caster

are derived from the equations of motion of the casters. A body-centered system is located in the center of the mass of the AGV main body. The y axis of the body-centered system coincides with the longitudinal axis of the vehicle pointing to the travel of the AGV, the z axis is vertical to the working floor pointing up, and the x axis is determined by the right-hand rule. The body-centered systems of the casters are parallel to the system of the AGV main body. At contact point of each wheels, the external forces may be represented in three vectors, F_x , F_y , and F_z corresponding to the centered body system of the AGV main body (Fig. A.2). Description of F_x , F_y , and F_z for each type of wheels are driven in the following discussion.

The notations of the forces used in this appendix are as follows:

F_{jx} is the total force vector at j wheel along X axis,

$j = d, s, ds, c;$

F_{jy} is the total force vector at j wheel along Y axis,

$j = d, s, ds, c;$

N_j is the normal reaction at j wheel, $j = d, s, ds, c;$

F'_{cx} is the reaction force along X axis at caster;

F'_{cy} is the reaction force along Y axis at caster;

N'_c is the reaction force along the Z axis at caster;

F_{jr} is rolling resistance at wheel j ($j = d, s, ds, c$);

F_{jt} is tractive force at wheel j ($j = d, ds$);

F_{jl} is lateral force at wheel j ($j = d, ds, s$);

F_{jn} is side-friction force at wheel j ($j = c$);

where

d ----- for driving wheel;

s ----- for steering wheel;

ds ----- for driving and steering unit;

c ----- for caster.

Driving wheel

A driving wheel offers the tractive effort to the vehicle. It is mounted to the main frame in the direction of the AGV travel. Three forces act on the driving wheels. There are tractive force F_{dt} , friction F_{df} and lateral force F_{dl} (Fig. A.3).

Then force vectors are

$$\begin{aligned} F_{dx} &= - F_{dl} \\ F_{dy} &= F_{dt} - F_{df} \end{aligned} \quad (A.4.1)$$

Steering wheel

A steering wheel leads the direction of the motion by rotate about Z axis. But unlike caster, steering wheel can not rotate freely. It can transfer torques to the AGV main body. At every instant, the steering wheel is equivalently fixed to the vehicle main body at an angle. The angle between the direction of y axis and the travel of the steering wheel is defined as α which has the sign shown in Fig. A.3. There are a friction force F_{sf} along the travel of the wheel and a lateral force F_{sl} which is vertical to the travel of the wheel (Fig. A.4).

And the force vectors are

$$\begin{aligned} F_{sx} &= F_{sl} \sin(\alpha_s - 90^\circ) - F_{sf} \sin(\alpha_s) \\ F_{sy} &= F_{sl} \cos(\alpha_s - 90^\circ) - F_{sf} \cos(\alpha_s) \end{aligned} \quad (A.4.2)$$

Drive-steering unit

This is a unit which combines driving and steering together. It is used widely in the industrial AGV because of its compact structure. The forces act on it also can be considered as adding a tractive force F_{dst} to a

steering wheel which has a steering angle as α_{ds} (Fig. A.5).

Then the force vector of a drive-steering unit are

$$\begin{aligned} F_{dsx} &= F_{ds\ell} \sin(\alpha_{ds} - 90^\circ) + (F_{dst} - F_{dsf}) \sin(\alpha_{ds}) \\ F_{dsy} &= F_{ds\ell} \cos(\alpha_{ds} - 90^\circ) + (F_{dst} - F_{dsf}) \cos(\alpha_{ds}) \end{aligned} \quad (A.4.3)$$

Caster

Because of its free rotating, a caster is a independent rigid body apart from the main body of AGV. The external force on caster are transferred to AGV main body through the pivot axle as reaction forces N'_c , F'_{cx} , and F'_{cy} in the Z, x, and y directions. The external forces on the caster are rolling resistance F_{cf} , normal reaction N_c , and side-friction force F_{cn} (Fig. A.6). The side-friction is a friction force which is vertical to the travel of the caster. The difference between lateral force and sliding force is that lateral force is produced by the deformation of tire at contact patch with working surface, and sliding friction is because of the sliding trend of the wheel [A.8]. When the mass of the caster is neglected, then the reaction forces may be presented in terms of external forces referring to chapter 3 of the thesis.

$$\begin{aligned} F'_{cx} &= F_{cx} = F_{cn} \sin(\alpha_c - 90^\circ) - F_{cf} \sin(\alpha_c) \\ F'_{cy} &= F_{cy} = F_{cn} \cos(\alpha_c - 90^\circ) - F_{cf} \cos(\alpha_c) \end{aligned} \quad (A.4.4)$$

And

$$J_c \ddot{\alpha}_c = F_{cn} \cdot d$$

A.5 FORMULATION OF THE EXTERNAL FORCES

Once the wheel configuration of the AGV is known, the coordinates of each wheel are known too. The motion equations of the AGV main body are obtained from the external and reaction forces associating with their coordinates. The inputs of the motion equations are the currents of the driving motor and the steering angles, the outputs are the velocities of the vehicle.

Let m , n , ℓ , k be the number of the driving wheels, the steering wheels, the driving-steering unit, and the casters. $F[i]$ is defined as the force at wheel number i .

Then substituting all the external and reaction forces into equations (A.2.1), then

$$\begin{aligned}
 \sum X &= \sum_{i=1}^m F_{dx}[i] + \sum_{i=1}^n F_{sx}[i] + \sum_{i=1}^{\ell} F_{dsx}[i] + \sum_{i=1}^k F_{cx}[i] \\
 \sum Y &= \sum_{i=1}^m F_{dy}[i] + \sum_{i=1}^n F_{sy}[i] + \sum_{i=1}^{\ell} F_{dsy}[i] + \sum_{i=1}^k F_{cy}[i] \\
 \sum N &= -\sum_{i=1}^m F_{dx}[i] Y_d[i] - \sum_{i=1}^n F_{sx}[i] Y_s[i] - \sum_{i=1}^{\ell} F_{dsx}[i] Y_{dsx}[i] \\
 &\quad - \sum_{i=1}^k F_{cx}[i] Y_{cx}[i] + \sum_{i=1}^m F_{dy}[i] X_d[i] + \sum_{i=1}^n F_{sy}[i] X_s[i] \\
 &\quad + \sum_{i=1}^{\ell} F_{dsy}[i] X_{ds}[i] + \sum_{i=1}^k F_{cy}[i] X_c[i] \\
 \sum M &= -\sum_{j=1}^{m+n+\ell+k} N_j[i] X_j[i] - h_g \left\{ \sum_{i=1}^m F_{dx}[i] + \sum_{i=1}^n F_{sx}[i] + \sum_{i=1}^{\ell} F_{dsx}[i] + \sum_{i=1}^k F_{cx}[i] \right\} \\
 &\quad (j=d, s, ds, c)
 \end{aligned} \tag{A.5.1}$$

Where h_g is the vertical distance between the mass center of the vehicle and the working floor.

A detail discussion about calculation of rolling resistance, tractive

force, lateral force, side-friction have been presented in chapter 3 of the thesis.

The formula for the tractive force is

$$F_{1t} = \frac{n}{r_d} \left(k_t I_1 - \frac{Jn}{r_d} \cdot \dot{v}_j - \frac{Dn}{r_d} \cdot v_j - T_f \right) \quad (A.5.2)$$

Where k_t is the torque constant for the driving motor, J is the moment of inertial of the rotor and wheel, D is the damping constant, and T_f is the static friction torque.

The formula for the rolling resistance is

$$F_{jr} = (k_{j1} + k_{j2} \cdot v_j) N_j \quad (j = d, ds) \quad (A.5.3)$$

where k_{j1} , k_{j2} are coefficients of rolling resistance.

The side-friction always attempts to align the caster to follow the velocity of pivot point. The formula of it is in the form of (A.5.4).

$$F_{cn} = k_{cn} \cdot N_c \text{sign}(\theta_c) \quad (A.5.4)$$

where θ_c is the angle between caster travel and velocity of pivot point, and k_{cn} is the coefficient of friction.

For the cornering force, the formula is

$$F_{jl} = \theta_j \cdot C_j \quad (j = s, ds, d) \quad (A.5.5)$$

where θ_j ($j = d, s, ds$) is the slip angle which is defined to be the angle between the wheel travel and the velocity vector at that point. C_j is defined as the cornering stiffness.

General expression of F_x and F_y vectors of four types of wheels can be obtained based on those formula.

The wheels are located within the body-centered system with coordinates (x_j, y_j) and $j = d, s, ds, c$ and angle α_j as shown in Fig. A.2. The angle α_j is defined as the angle between the travel of AGV and the travel of the

wheel.

Then the velocity vectors along X and Y axis (V_{jx} and V_{jy}) at the point (x_j, y_j) are:

$$\begin{aligned}
 V_{jy} &= V + r \cdot \sqrt{(x_j^2 + y_j^2)} \sin[\text{atan}(x_j / y_j) + 90^\circ] \\
 &= V + r \cdot \sqrt{(x_j^2 + y_j^2)} \cos[\text{atan}(x_j / y_j)] \\
 V_{jx} &= U + r \cdot \sqrt{(x_j^2 + y_j^2)} \cos[\text{atan}(x_j / y_j) + 90^\circ] \\
 &= U - r \cdot \sqrt{(x_j^2 + y_j^2)} \sin[\text{atan}(x_j / y_j)]
 \end{aligned}
 \tag{A.5.6}$$

Let

$$\begin{aligned}
 \sigma_{j1} &= \sqrt{(x_j^2 + y_j^2)} \cos[\text{atan}(x_j / y_j)] \\
 \sigma_{j2} &= -\sqrt{(x_j^2 + y_j^2)} \sin[\text{atan}(x_j / y_j)]
 \end{aligned}
 \tag{A.5.7}$$

Then

$$\begin{aligned}
 V_{jy} &= V + r \sigma_{j1} \\
 V_{jx} &= U + r \sigma_{j2}
 \end{aligned}
 \tag{A.5.8}$$

Also the velocity vector along and vertical to the travel of the wheels

V_{jl} and V_{jv} are:

$$\begin{aligned}
 V_{jl} &= V_{jy} \cos(\alpha_j) + V_{jx} \sin(\alpha_j) \\
 V_{jv} &= -V_{jy} \sin(\alpha_j) + V_{jx} \cos(\alpha_j)
 \end{aligned}
 \tag{A.5.9}$$

From the definition of θ_d , θ_s , θ_{da} , and θ_c , they can be calculated by the following equations.

$$\begin{aligned}
 \theta_c &= \text{atan}\left(\frac{U + r \sigma_{c2}[i]}{V + r \sigma_{c1}[i]}\right) - \alpha_c[i] \\
 \theta_s &= \text{atan}\left(\frac{U + r \sigma_{s2}[i]}{V + r \sigma_{s1}[i]}\right) - \alpha_s[i]
 \end{aligned}$$

$$\phi_{ds} = \text{atan}\left(\frac{U + r \sigma_{ds2}[i]}{V + r \sigma_{ds1}[i]}\right) - \alpha_{ds}[i]$$

$$\phi_d = C_d[i] \text{atan}\left(\frac{U + r \sigma_{d2}[i]}{V + r \sigma_{d1}[i]}\right)$$

Let $C\alpha_j = \cos(\alpha_j)$, $S\alpha_j = \sin(\alpha_j)$. Using equations (A.5.2) to (A.5.9), the external forces at four types of wheel may be calculated as:

1) Driving Wheels ($x_d[i]$, $y_d[i]$, 0)

$$\begin{aligned} F_{dt}[i] &= \frac{n[i]}{r_d[i]} \{k_t[i]I[i] - \frac{Jn[i]}{r_d[i]} \dot{V}_\ell - \frac{Dn[i]}{r_d[i]} V_\ell[i] - T_f[i]\} \\ &= \frac{nk_t[i]}{r_d[i]} I[i] - \frac{Jn^2[i]}{r_d[i]} V - \frac{Jn^2[i]}{r_d[i]} \sigma_{d1}[i] r - \frac{Dn^2[i]}{r_d[i]} V \\ &\quad - \frac{Dn^2[i]}{r_d[i]} \sigma_{d1}[i] r - \frac{n[i]}{r_d[i]} T_f[i] \end{aligned}$$

$$\begin{aligned} F_{df}[i] &= \{k_{d1}[i] + k_{d2}[i] V_\ell[i]\} N_d[i] \\ &= \{k_{d1}[i] + k_{d2}[i] V + k_{d2}[i] r\} N_d[i] \end{aligned}$$

$$F_{d\ell}[i] = -C_d[i] \phi_d[i] = -C_d[i] \text{atan}\left(\frac{U + r \sigma_{d2}[i]}{V + r \sigma_{d1}[i]}\right)$$

(A.5.10)

2) For steering wheels ($x_s[i]$, $y_s[i]$, $\alpha_s[i]$)

$$\begin{aligned} F_{sf}[i] &= \{k_{s1}[i] + k_{s2}[i] V_\ell[i]\} N_s[i] \\ &= \{k_{s1}[i] + k_{s2}[i] C\alpha_s[i] V + k_{s2}[i] S\alpha_s[i] U \\ &\quad + (k_{s2}[i] C\alpha_s[i] \sigma_{s1}[i] + k_{s2}[i] S\alpha_s[i] \sigma_{s2}[i]) r\} N_s[i] \end{aligned}$$

$$\begin{aligned} F_{s\ell}[i] &= C_s[i] \phi_{s\ell}[i] \\ &= C_s[i] \left\{ \text{atan}\left(\frac{U + r \sigma_{s2}[i]}{V + r \sigma_{s1}[i]}\right) - \alpha_s[i] \right\} \end{aligned}$$

(A.5.11)

3) For steering-driving units ($x_{ds}[i]$, $y_{ds}[i]$, $\alpha_{ds}[i]$)

$$\begin{aligned}
 F_{dst}[i] &= \frac{n[i]}{r_{ds}[i]} (k_t[i] l[i] - \frac{Jn[i]}{r_{ds}[i]} \dot{V}_\ell[i] - \frac{Dn[i]}{r_{ds}[i]} V_\ell[i] - T_f[i]) \\
 &= \frac{n k_t[i]}{r_{ds}[i]} l[i] - \frac{Jn^2[i]}{r_{ds}^2[i]} C\alpha_{ds}[i] \dot{V} - \frac{Jn^2[i]}{r_{ds}^2[i]} S\alpha_{ds}[i] \dot{U} \\
 &\quad - (\frac{Jn^2[i]}{r_{ds}^2[i]} C\alpha_{ds} \sigma_{ds1}[i] + \frac{Jn^2[i]}{r_{ds}^2[i]} S\alpha_{ds} \sigma_{ds2}[i]) \dot{r} \\
 &\quad - \frac{Dn^2[i]}{r_{ds}^2[i]} C\alpha_{ds}[i] V - \frac{Dn^2[i]}{r_{ds}^2[i]} S\alpha_{ds}[i] U - \frac{nT_f[i]}{r_{ds}[i]} \\
 &\quad - (\frac{Dn^2[i]}{r_{ds}^2[i]} C\alpha_{ds} \sigma_{ds1}[i] + \frac{Dn^2[i]}{r_{ds}^2[i]} S\alpha_{ds} \sigma_{ds2}[i]) r
 \end{aligned}$$

$$\begin{aligned}
 F_{dsf}[i] &= (k_{ds1}[i] + k_{ds2}[i] V_\ell[i]) N_{ds}[i] \\
 &= (k_{ds1}[i] + k_{ds2}[i] C\alpha_{ds}[i] V + k_{ds2}[i] S\alpha_{ds}[i] U \\
 &\quad + (k_{ds2}[i] C\alpha_{ds}[i] \sigma_{ds1}[i] + k_{ds2}[i] S\alpha_{ds}[i] \sigma_{ds2}[i]) r) N_{ds}[i] \\
 F_{ds\ell}[i] &= C_{ds}[i] \{ \text{atan}(\frac{U + r_{ds} \sigma_{ds2}[i]}{V + r_{ds} \sigma_{ds1}[i]}) - \alpha_{ds}[i] \}
 \end{aligned}$$

(A.5.12)

4) Casters ($x_c[i]$, $y_c[i]$, $\alpha_c[i]$)

$$\begin{aligned}
 F_{cf}[i] &= (k_{c1}[i] + k_{c2}[i] V_\ell[i]) N_c[i] \\
 &= (k_{c1}[i] + k_{c2}[i] C\alpha_c[i] V + k_{c2}[i] S\alpha_c[i] U \\
 &\quad + (k_{c2}[i] C\alpha_c[i] \sigma_{c1}[i] + k_{c2}[i] S\alpha_c[i] \sigma_{c2}[i]) r) N_c[i] \\
 F_{cn}[i] &= k_{cn}[i] N_c \text{ sign}(\text{atan}(\frac{U + r \sigma_{c2}[i]}{V + r \sigma_{c1}[i]}) - \alpha_c[i])
 \end{aligned}$$

$$J_c \ddot{\alpha}_c[i] = F_{cn}[i] \cdot d[i] \quad (\text{A.5.13})$$

where d is the offset of casters.

In order to simplify the equations, some expression are defined as follows:

$$\begin{aligned} K_{et_j}[i] &= \frac{n k_{jt}[i]}{r_j[i]} \\ M_{e_j}[i] &= \frac{j_j n^2[i]}{r_j^2[i]} \\ D_{e_j}[i] &= \frac{D n^2[i]}{r_j^2[i]} \end{aligned} \quad (A.5.14 \ a)$$

where $j = d, ds$

$$\begin{aligned} T_{e_j}[i] &= \frac{n}{r_j} T_f[i] \\ K_{j1}[i] &= k_{j1}[i] N_j[i] \\ K_{j2}[i] &= k_{j2}[i] N_j[i] \end{aligned} \quad (A.5.14. b)$$

where $j = d, s, ds, c$

$$K_{cn}[i] = k_{cn}[i] N_c[i] \quad (A.5.14. c)$$

And the force vectors along the x and y axis of all the wheels are:

1) Driving wheels

Since

$$\begin{aligned} F_{dt}[i] &= K_{et_d}[i] I_d[i] - M_{e_d}[i] \dot{V} - M_{e_d}[i] \sigma_{d1}[i] \dot{r} \\ &\quad - D_{e_d}[i] V - D_{e_d}[i] \sigma_{d1}[i] r - T_{ef_d}[i] \\ F_{df}[i] &= K_{d1}[i] + k_{d2}[i] V + K_{d2}[i] \sigma_{d1}[i] r \\ F_{dl}[i] &= -C_d[i] \operatorname{atan}\left(\frac{U + r \sigma_{d2}[i]}{V + r \sigma_{d1}[i]}\right) \end{aligned}$$

Substituting into equations (4.1), then

$$\begin{aligned}
 F_{dx}[i] &= -C_d[i] \operatorname{atan}\left(\frac{U + r \sigma_{d2}[i]}{V + r \sigma_{d1}[i]}\right) \\
 F_{dy}[i] &= K_{et_j}[i] I_d[i] - M_{e_d}[i] V - M_{e_d}[i] \sigma_{d1}[i] \dot{r} - \\
 &\quad (D_{e_d}[i] + k_{d2}[i])V - (D_{e_d}[i] \sigma_{d1}[i] + K_{d2}[i] \sigma_{d1}[i]) \dot{r} - \\
 &\quad T_{ef_d}[i] - K_{d1}[i]
 \end{aligned}
 \tag{A.5.15}$$

2) Steering wheels

Since

$$\begin{aligned}
 F_{sf}[i] &= K_{s2}[i] C_{\alpha_s}[i] V + K_{s2}[i] S_{\alpha_s}[i] U \\
 &\quad + K_{s2}[i] (C_{\alpha_s}[i] \sigma_{s1}[i] + S_{\alpha_s}[i] \sigma_{s2}[i]) r + k_{s1}[i] \\
 F_{sl}[i] &= C_s[i] \left\{ \operatorname{atan}\left(\frac{U + r \sigma_{s2}[i]}{V + r \sigma_{s1}[i]}\right) - \alpha_s[i] \right\}
 \end{aligned}$$

Substituting into equations (A.4.2), then

$$\begin{aligned}
 F_{sx}[i] &= -K_{s2}[i] C_{\alpha_s}[i] S_{\alpha_s}[i] V - K_{s2}[i] S_{\alpha_s}^2[i] U - \\
 &\quad K_{s2}[i] S_{\alpha_s}[i] (C_{\alpha_s}[i] \sigma_{s1}[i] + S_{\alpha_s}[i] \sigma_{s2}[i]) r \\
 &\quad - C_s[i] C_{\alpha_s}[i] \left\{ \operatorname{atan}\left(\frac{U + r \sigma_{s2}[i]}{V + r \sigma_{s1}[i]}\right) - \alpha_s[i] \right\} \\
 &\quad - K_{s1}[i] S_{\alpha_s}[i] \\
 F_{sy}[i] &= -K_{s2}[i] C_{\alpha_s}^2[i] V - K_{s2}[i] S_{\alpha_s}[i] C_{\alpha_s}[i] U - \\
 &\quad K_{s2}[i] C_{\alpha_s}[i] (C_{\alpha_s}[i] \sigma_{s1}[i] + S_{\alpha_s}[i] \sigma_{s2}[i]) r \\
 &\quad + C_s[i] S_{\alpha_s}[i] \left\{ \operatorname{atan}\left(\frac{U + r \sigma_{s2}[i]}{V + r \sigma_{s1}[i]}\right) - \alpha_s[i] \right\} \\
 &\quad - K_{s1}[i] C_{\alpha_s}[i]
 \end{aligned}$$

(A.5.16)

3) Steering-Driving Units

$$\text{Since } F_{dst}[i] = K_{et_{ds}}[i]I[i] - M_{e_{ds}}[i] C\alpha_{ds}[i] \dot{V} - M_{e_{ds}}[i] S\alpha_{ds}[i]\dot{U}$$

$$- M_{e_{ds}}[i] (C\alpha_{ds} \sigma_{ds1}[i] + S\alpha_{ds} \sigma_{ds2}[i]) \dot{r}$$

$$- D_{e_{ds}}[i] C\alpha_{ds}[i] V - D_{e_{ds}}[i] S\alpha_{ds}[i] U$$

$$- D_{e_{ds}}[i](C\alpha_{ds} \sigma_{ds1}[i] + S\alpha_{ds} \sigma_{ds2}[i]) r - T_{ef_{ds}}[i]$$

$$F_{dsf}[i] = K_{ds2}[i] C\alpha_{ds}[i] V + K_{ds2}[i] S\alpha_{ds}[i] U$$

$$+ K_{ds2}[i] (C\alpha_{ds}[i] \sigma_{ds1}[i] + S\alpha_{ds}[i] \sigma_{ds2}[i]) r + K_{ds1}[i]$$

$$F_{dsf}[i] = C_{ds}[i] \left(\frac{U + r \sigma_{ds2}[i]}{V + r \sigma_{ds1}[i]} - \alpha_{ds}[i] \right)$$

Substituting into equations (A.4.3), then

$$F_{dsx} = K_{et_{ds}}[i] S\alpha_{ds}[i] I[i] - M_{e_{ds}}[i] S\alpha_{ds}[i] C\alpha_{ds}[i] \dot{V} -$$

$$M_{e_{ds}}[i] S\alpha_{ds}^2[i] \dot{U} - M_{e_{ds}}[i] S\alpha_{ds}[i] (C\alpha_{ds} \sigma_{ds1}[i] + S\alpha_{ds} \sigma_{ds2}[i]) \dot{r}$$

$$- C\alpha_{ds}[i] S\alpha_{ds}[i] (D_{e_{ds}}[i] + K_{ds2}[i]) V -$$

$$S\alpha_{ds}^2[i] (D_{e_{ds}}[i] + K_{ds2}[i]) U -$$

$$S\alpha_{ds}[i] (D_{e_{ds}}[i] + K_{ds2}[i]) (C\alpha_{ds} \sigma_{ds1}[i] + S\alpha_{ds} \sigma_{ds2}[i]) r$$

$$- (T_{ef_{ds}}[i] + K_{ds1}[i]) S\alpha_{ds}[i] -$$

$$C_{ds}[i] C\alpha_{ds}[i] \left(\text{atan}\left(\frac{U + r \sigma_{ds2}[i]}{V + r \sigma_{ds1}[i]} \right) - \alpha_{ds}[i] \right)$$

$$\begin{aligned}
F_{dsy} = & K_{et_{ds}}[i] C\alpha_{ds}[i] I[i] - M_{e_{ds}}[i] C\alpha_{ds}^2[i] \dot{V} - \\
& M_{e_{ds}}[i] S\alpha_{ds}[i] C\alpha_{ds}[i] \dot{U} - \\
& M_{e_{ds}}[i] C\alpha_{ds}[i] (C\alpha_{ds} \sigma_{ds1}[i] + S\alpha_{ds} \sigma_{ds2}[i]) \dot{r} \\
& - C\alpha_{ds}^2[i] (D_{e_{ds}}[i] + K_{ds2}[i]) V - \\
& S\alpha_{ds}[i] C\alpha_{ds}[i] (D_{e_{ds}}[i] + K_{ds2}[i]) U - \\
& C\alpha_{ds}[i] (D_{e_{ds}}[i] + K_{ds2}[i]) (C\alpha_{ds} \sigma_{ds1}[i] + S\alpha_{ds} \sigma_{ds2}[i]) r \\
& - (T_{ef_{ds}}[i] + K_{ds1}[i]) C\alpha_{ds}[i] + \\
& C_{ds}[i] C\alpha_{ds}[i] \left(\text{atan}\left(\frac{U + r \sigma_{ds2}[i]}{V + r \sigma_{ds1}[i]} - \alpha_{ds}[i] \right) \right)
\end{aligned}
\tag{A.5.17}$$

4) Casters

Since

$$\begin{aligned}
F_{cf}[i] = & K_{c1}[i] + K_{c2}[i] C\alpha_c[i] V + K_{c2}[i] S\alpha_c[i] U \\
& (K_{c2}[i] C\alpha_c[i] \sigma_{c1}[i] + K_{c2}[i] S\alpha_c[i] \sigma_{c2}[i]) r \\
F_{cn}[i] = & K_{cn}[i] \text{sign}\left(\text{atan}\left(\frac{U + r \sigma_{c2}[i]}{V + r \sigma_{c1}[i]} - \alpha_c[i]\right)\right) \\
\ddot{\alpha}_c[i] = & F_{cn}[i] d[i]
\end{aligned}$$

Substituting into equations (A.4.4), then

$$\begin{aligned}
F_{cx}[i] = & - K_{c2}[i] C\alpha_c[i] S\alpha_c[i] V - K_{c2}[i] S\alpha_c^2[i] U \\
& - K_{c2}[i] S\alpha_c[i] (C\alpha_c[i] \sigma_{c1}[i] + S\alpha_c[i] \sigma_{c2}[i]) r \\
& - k_{cn}[i] N_c[i] C\alpha_c[i] - K_{c1}[i] S\alpha_c[i]
\end{aligned}$$

$$\begin{aligned}
F_{cy}[i] = & -K_{c2}[i] C\alpha_c[i] C\alpha_c[i] V - K_{c2}[i] S\alpha_c[i] C\alpha_c[i] U \\
& - K_{c2}[i] C\alpha_c[i] (C\alpha_c[i] \sigma_{c1}[i] + S\alpha_c[i] \sigma_{c2}[i]) r \\
& + k_{cn}[i] N_c[i] S\alpha_c[i] - K_{c1}[i] C\alpha_c[i]
\end{aligned}
\tag{A.5.18}$$

A.6 DYNAMIC EQUATION OF AGV

Once all the external forces are obtained, the dynamic equation can be write as

$$\begin{aligned}
m(\dot{U} - r V) &= \sum_{i=1}^m F_{dx}[i] + \sum_{i=1}^n F_{sx}[i] + \sum_{i=1}^{\ell} F_{dsx}[i] + \sum_{i=1}^k F_{cx}[i] \\
m(\dot{V} + r U) &= \sum_{i=1}^m F_{dy}[i] + \sum_{i=1}^n F_{sy}[i] + \sum_{i=1}^{\ell} F_{dsy}[i] + \sum_{i=1}^k F_{cy}[i] \\
B \dot{q} + E r^2 - F q r + D \dot{r} \\
&= -\sum_{j=1}^{m+n+\ell+k} N_j[i] X_j[i] - h_z \left(\sum_{i=1}^m F_{dx}[i] + \sum_{i=1}^n F_{sx}[i] + \sum_{i=1}^{\ell} F_{dsx}[i] + \sum_{i=1}^k F_{cx}[i] \right) \\
C \dot{r} + F q^2 - D \dot{q} + E r q \\
&= -\sum_{i=1}^m F_{dx}[i] Y_d[i] - \sum_{i=1}^n F_{sx}[i] Y_s[i] - \sum_{i=1}^{\ell} F_{dsx}[i] Y_{dsx}[i] \\
&\quad - \sum_{i=1}^k F_{cx}[i] Y_{cx}[i] + \sum_{i=1}^m F_{dy}[i] X_d[i] + \sum_{i=1}^n F_{sy}[i] X_s[i] \\
&\quad + \sum_{i=1}^{\ell} F_{dsy}[i] X_{ds}[i] + \sum_{i=1}^k F_{cy}[i] X_c[i]
\end{aligned}
\tag{A.6.1 a}$$

where $j = d, ds, s, c$.

Equations (A.6.1 a) presents the motion equation of a AGV with various wheel configuration. The procedure of developing the equations of motion of a specific wheel configuration using the above approach is summarized as follows:

Step 1 --- AGV system information

Input the vehicle configuration and collect the information in three aspects:

- 1) Number of wheels in each wheel type;
- 2) Assign a serial number to the wheels in each wheel type;
- 3) Give the coordinates for every wheel in Body Centered System.

Step 2 --- Calculate the system parameters

- 1) With the formula for σ_1 and σ_2 , calculate σ_{j1} and σ_{j2} for every wheel.

$$\sigma_{j1} = \sqrt{x_j^2 + y_j^2} \cos(\arctan(x_j / y_j))$$
$$\sigma_{j2} = - \sqrt{x_j^2 + y_j^2} \sin(\arctan(x_j / y_j))$$

- 2) Calculate friction constant for every wheel by equation

$$K_{j1} = k_{j1} N_j; \quad K_{j2} = k_{j2} N_j \quad j = d, s, ds, c$$

- 3) Calculate sliding constant for casters

$$K_{cn} = k_{cn} N_c$$

Step 3 --- formulate the forces

Calculate the force vectors F_{jx} , F_{jy} for each wheel using equations (A.5.4) to (A.5.8).

Step 4 --- Derive the dynamic equation of AGV

Substituting all forces above into equation (A.6.1 a)

$$\begin{aligned} m(\dot{U} - r V) &= \sum_{i=1}^m F_{dx}^{[i]} + \sum_{i=1}^n F_{sx}^{[i]} + \sum_{i=1}^{\ell} F_{dsx}^{[i]} + \sum_{i=1}^k F_{cx}^{[i]} \\ m(\dot{V} + r U) &= \sum_{i=1}^m F_{dy}^{[i]} + \sum_{i=1}^n F_{sy}^{[i]} + \sum_{i=1}^{\ell} F_{dsy}^{[i]} + \sum_{i=1}^k F_{cy}^{[i]} \end{aligned}$$

$$B \dot{q} + E r^2 - Fqr + D \dot{r}$$

$$= -\sum_{i=1}^{m+n+l+k} N_j[i] X_j[i] - h_g \left\{ \sum_{i=1}^m F_{dx}[i] + \sum_{i=1}^n F_{sx}[i] + \sum_{i=1}^l F_{dsx}[i] + \sum_{i=1}^k F_{cx}[i] \right\}$$

$$C \dot{r} + Fq^2 - D \dot{q} + E r q$$

$$\begin{aligned} &= -\sum_{i=1}^m F_{dx}[i] Y_d[i] - \sum_{i=1}^n F_{sx}[i] Y_s[i] - \sum_{i=1}^l F_{dsx}[i] Y_{dsx}[i] \\ &- \sum_{i=1}^k F_{cx}[i] Y_{cx}[i] + \sum_{i=1}^m F_{dy}[i] X_d[i] + \sum_{i=1}^n F_{sy}[i] X_s[i] \\ &+ \sum_{i=1}^l F_{dsy}[i] X_{ds}[i] + \sum_{i=1}^k F_{cy}[i] X_c[i] \end{aligned} \quad (A.6.1)$$

where $j = d, ds, s, c$.

In the following chapter, a study of two specific cases of using this general approach to develop the motion equations are presented.

A.7 CASE STUDY

A.7.1 CASE STUDY 1— CONCIC-2 AGV

The following discussion gives an example to use the general procedure to develop the equations of motion of the CONCIC-2 AGV. As it is described in the thesis, the CONCIC-2 AGV has two driving wheels at the sides and two caster in the front and rear (Fig. A.7). All the driving wheels are assumed to have the same characteristics, and so does the casters. Also the mass center is assumed to be the geometric center, and the roll movement is considered to be negligible during the operation. The external forces on the CONCIC-2 AGV are shown in Fig. A.8. Using the equations (A.6.1) the motion equations of CONCIC-2 vehicle are

$$\begin{aligned}\sum Y = m(\dot{V} + r U) &= \sum_1^{\ell} F_{dy}[i] + \sum_1^m F_{sy}[i] + \sum_1^n F_{dsy}[i] + \sum_1^k F_{cy}[i] \\ \sum N = I_z \dot{r} &= - \sum_1^{\ell} F_{dx}[i] \cdot Y_d[i] - \sum_1^m F_{sx}[i] \cdot Y_s[i] - \sum_1^n F_{dsx}[i] \cdot Y_{ds}[i] - \\ &\quad \sum_1^k F_{cx}[i] \cdot Y_c[i] + \sum_1^{\ell} F_{dy}[i] \cdot X_d[i] + \\ &\quad \sum_1^m F_{sy}[i] \cdot X_s[i] + \sum_1^n F_{dsy}[i] \cdot X_{ds}[i] + \sum_1^k F_{cy}[i] \cdot X_c[i]\end{aligned}\quad (A.7.1.1)$$

STEP ONE --- system information

Fig. A.7 shows the configuration of the AGV. It has

2 Driving wheels (left and right wheel---1,2); $\ell = 2$

2 casters (front and rear wheel---1,2); $k = 2$

with coordinates

left wheel $[-\ell, 0]$; right wheel $[\ell, 0]$;

front wheel $[k, 0]$; rear wheel $[-k, 0]$;

And $\delta[1]$ and $\delta[2]$ are the angles for two caster between their travel and

longitudinal axis of the AGV.

STEP TWO --- system parameters

With the formula of σ_{j1} and σ_{j2} :

$$\sigma_{j1} = \sqrt{(x^2 + y^2)} \cos[\text{atan2}(x / y)]$$

$$\sigma_{j2} = -\sqrt{(x^2 + y^2)} \sin[\text{atan2}(x / y)]$$

Thus for driving wheels:

$$\sigma_{d1}[1] = -\ell; \quad \sigma_{d2}[2] = 0;$$

$$\sigma_{d1}[1] = \ell; \quad \sigma_{d2}[2] = 0;$$

and

$$Ket[1] = \frac{nk_t[1]}{r_d[1]} = \frac{nk_t[2]}{r_d[2]} = Ket[2] = Ket;$$

$$Me[1] = \frac{Jn^2[1]}{r_d^2[1]} = \frac{Jn^2[2]}{r_d^2[2]} = Me[2] = Me;$$

$$De[1] = \frac{Dn^2[1]}{r_d^2[1]} = \frac{Dn^2[2]}{r_d^2[2]} = De[2] = De;$$

$$Tef[1] = \frac{n[1]}{r_d[1]} T_f[1] = \frac{n[2]}{r_d[2]} T_f[2] = Tef[2] = 0;$$

$$N_d[1] = N_d[2] = N;$$

$$k_{d1}[1] \cdot N = k_{d1}[2] \cdot N = K_1; \quad k_{d2}[1] \cdot N = k_{d2}[2] \cdot N = K_2;$$

$$k_{cn}[1] \cdot N_c[1] = K_{cn}[1]; \quad k_{cn}[2] \cdot N_c[2] = K_{cn}[2];$$

$$C_d[1] = C_d[2] = C.$$

And for casters:

$$\sigma_{c1}[1] = 0; \quad \sigma_{c2}[1] = -k;$$

$$\sigma_{c1}[1] = 0; \quad \sigma_{c2}[2] = k;$$

$$k_{c1} \cdot N_c[1] = k_{c1} N_c[2] = K_{c1}; \quad k_{c2} \cdot N_c[1] = k_{c2} \cdot N_c[2] = K_{c2}.$$

STEP THREE ----- formulate the force

Let

V_x ----- be the linear velocity along the X axis within the body centered system.

V_y ----- be the linear velocity along the Y axis within the body centered system.

Ω_z ----- be the angular velocity about the Z axis within the body centered system.

The external forces may be calculated by substituting the coordinate and parameters obtained in the previous steps into the equations.

For Driving wheels, from equation (A.5.15)

Y axis

$$\begin{aligned} F_{dy}[1] &= K_{et} \cdot I[1] - M_e \cdot \dot{V}_y + M_e \cdot \ell \cdot \dot{\Omega}_z - D_e \cdot V_y \\ &\quad + D_e \cdot \ell \Omega_z - K_2 \cdot V_y + K_2 \cdot \ell \cdot \Omega_z - K_1 \\ F_{dy}[2] &= K_{et} \cdot I[2] - M_e \cdot \dot{V}_y + M_e \cdot \ell \cdot \dot{\Omega}_z - D_e \cdot V_y \\ &\quad + D_e \cdot \ell \Omega_z - K_2 \cdot V_y + K_2 \cdot \ell \cdot \Omega_z - K_1 \end{aligned}$$

X axis

$$\begin{aligned} F_{dx}[1] &= -C \operatorname{atan}\left(\frac{V_x}{V_y - \Omega_z \cdot \ell}\right) \\ F_{dx}[2] &= -C \operatorname{atan}\left(\frac{V_x}{V_y + \Omega_z \cdot \ell}\right) \end{aligned}$$

For Caster, from equation (A.5.18):

X axis

$$\begin{aligned} F_{cx}[1] &= -K_{c1} \sin\delta[1] - K_{c2} \sin\delta[1] \cos\delta[1] V_y + \\ &\quad K_{c2} k \sin^2\delta[1] \Omega_z \\ &\quad - K_{cn}[1] \operatorname{sign}\left\{\operatorname{atan}\left(\frac{-\Omega_z k}{V_y}\right) - \delta[1]\right\} \cos\delta[1] \end{aligned}$$

$$F_{cx}[2] = -K_{c1} \sin \delta[2] - K_{c2} \sin \delta[2] \cos \delta[2] V_y - K_{c2} k \sin^2 \delta[2] \Omega_z \\ - K_{cn}[2] \text{sign}\left(\text{atan}\left(\frac{\Omega_z k}{V_y}\right) - \delta[2]\right) \cos \delta[2]$$

Y axis

$$F_{cy}[1] = K_{c1} \cos \delta[1] - K_{c2} \cos^2 \delta[1] V_y \\ + K_{c2} \cos \delta[1] \sin \delta[1] \cdot k \cdot \Omega_z \\ + K_{cn}[1] \text{sign}\left(\text{atan}\left(\frac{-\Omega_z k}{V_y}\right) - \delta[1]\right) \sin \delta[1] \\ F_{cy}[2] = K_{c1} \cos \delta[2] - K_{c2} \cos^2 \delta[2] V_y \\ - K_{c2} \cos \delta[2] \sin \delta[2] \cdot k \cdot \Omega_z \\ + K_{cn}[2] \text{sign}\left(\text{atan}\left(\frac{\Omega_z k}{V_y}\right) - \delta[2]\right) \sin \delta[2]$$

STEP FOUR ----- The dynamic equations

The dynamic equation is given in (A.6.1). Replacing V , U , r by V_x , V_y and Ω_z , then

$$\sum Y = m(\dot{V}_y + \Omega_z V_x) = \sum_1^{\ell} F_{dy}[i] + \sum_1^k F_{cy}[i] \\ \sum N = I_z \dot{\Omega}_z = - \sum_1^{\ell} F_{dx}[i] \cdot Y_d[i] - \sum_1^k F_{cx}[i] \cdot Y_c[i] + \sum_1^{\ell} F_{dy}[i] \cdot X_d[i] \\ + \sum_1^k F_{cy}[i] \cdot X_c[i]$$

Substituting the external forces into the above equations

$$\sum Y = K_{et}(I[1] + I[2]) - 2 M_o \dot{V}_y - 2 K_1 - K_{c1}(\cos \delta[1] + \cos \delta[2]) \\ - K_{c2} V_y (\cos \delta[1] \cos \delta[1] + \cos \delta[2] \cos \delta[2]) \\ - K_{c2} k \Omega_z (-\cos \delta[1] \sin \delta[1] + \cos \delta[2] \sin \delta[2]) \\ - (K_{cn}[1] \text{sign}\left(\text{atan}\left(\frac{-\Omega_z k}{V_y}\right) - \delta[1]\right) \sin \delta[1] \\ + K_{cn}[2] \text{sign}\left(\text{atan}\left(\frac{\Omega_z k}{V_y}\right) - \delta[2]\right) \sin \delta[2])$$

$$\begin{aligned}
\sum N = & [K_{et} (I[1] - I[2]) + 2 M_e \ell \dot{\Omega}_z + 2(D_e + K_2) \ell \Omega_z] \ell \\
& - [k K_{c1} (\sin \delta[1] - \sin \delta[2]) \\
& + k K_{c2} V_y (\sin \delta[1] \cos \delta[1] - \sin \delta[2] \cos \delta[2]) \\
& + k^2 K_{c2} \Omega_z (\sin^2 \delta[1] + \sin^2 \delta[2]) \\
& - k K_{cn} [1] \text{sign}(\text{atan}(\frac{-\Omega_z k}{V_y}) - \delta[1]) \cos \delta[1] \\
& + K_{cn} [2] \text{sign}(\text{atan}(\frac{\Omega_z k}{V_y}) - \delta[2]) \cos \delta[2]
\end{aligned}$$

Rearranging the equations

$$\begin{aligned}
m \dot{V}_y = & k_{et}(I[1] + I[2]) - 2M_e \dot{V}_y - 2(D_e + K_2) V_y - K_{c2} (\cos^2 \delta[1] \\
& + \cos^2 \delta[2]) V_y - K_{c2} k (-\sin \delta[1] \cos \delta[1] + \sin \delta[2] \cos \delta[2]) \Omega_z \\
& - 2 K_{c1} - K_{c1} (\cos \delta[1] + \cos \delta[2]) \\
& - K_{cn} [1] \text{sign}(\text{atan}(\frac{-\Omega_z k}{V_y}) - \delta[1]) \sin \delta[1] \\
& - K_{cn} [2] \text{sign}(\text{atan}(\frac{\Omega_z k}{V_y}) - \delta[2]) \sin \delta[2] \\
I_z \dot{\Omega}_z = & k_{et}(I[1] - I[2]) - 2M_e \ell^2 \dot{\Omega}_z + 2(D_e + K_2) \ell^2 \Omega_z \\
& - k K_{c2} (\sin \delta[1] \cos \delta[1] - \sin \delta[2] \cos \delta[2]) \\
& + k^2 K_{c2} (\sin^2 \delta[1] + \sin^2 \delta[2]) \Omega_z \\
& - k K_{c1} (\sin \delta[1] - \sin \delta[2]) \\
& - k K_{cn} [1] \text{sign}(\text{atan}(\frac{-\Omega_z k}{V_y}) - \delta[1]) \cos \delta[1] \\
& + k K_{cn} [2] \text{sign}(\text{atan}(\frac{\Omega_z k}{V_y}) - \delta[2]) \cos \delta[2]
\end{aligned}$$

Let

$$\sin \delta[1] = S\delta[1], \cos \delta[1] = C\delta[1];$$

$$\sin \delta[2] = s\delta[2], \cos \delta[2] = C\delta[2].$$

Then the equations can be written as

$$\begin{aligned}
 m \dot{V}_y &= k_{et}(I[1] + I[2]) - 2M_0 \dot{V}_y - 2(D_0 + K_2) V_y - K_{c2}(C^2\delta[1] \\
 &+ C^2\delta[2])V_y - K_{c2} k (-C\delta[1]S\delta[1] + C\delta[1]S\delta[2]) \Omega_z - 2 K_1 \\
 &- K_{c1}(C\delta[1] + C\delta[2]) \\
 &- K_{cn}[1]\text{sign}\left(\text{atan}\left(\frac{-\Omega_z k}{V_y}\right) - \delta[1]\right) S\delta[1] \\
 &- K_{cn}[2]\text{sign}\left(\text{atan}\left(\frac{\Omega_z k}{V_y}\right) - \delta[2]\right) S\delta[2] \\
 I_z \dot{\Omega}_z &= k_{et}(I[1] - I[2]) - 2M_0 \ell^2 \dot{\Omega}_z + 2(D_0 + K_2) \ell^2 \Omega_z \\
 &- k K_{c2}(S\delta[1]C\delta[1] - S\delta[2]C\delta[2])V_y \\
 &+ k^2 K_{c2}(S^2\delta[1] + S^2\delta[2]) \Omega_z \\
 &- k K_{c1}(S\delta[1] - S\delta[2]) \\
 &- k K_{cn}[1]\text{sign}\left(\text{atan}\left(\frac{-\Omega_z k}{V_y}\right) - \delta[1]\right) C\delta[1] \\
 &+ K_{cn}[2]\text{sign}\left(\text{atan}\left(\frac{\Omega_z k}{V_y}\right) - \delta[2]\right) C\delta[2]
 \end{aligned}
 \tag{A.7.1.2}$$

Comparison with the result of the regular approach

The equations of motion of the CONCIC-2 AGV developed in chapter 4 of the thesis using regular approach are

$$\begin{aligned}
 \left(m + \frac{2n^2 J}{r_d^2}\right) \dot{V}_y &= \frac{nk_t}{r_d} (I_1 + I_2) - \left(\frac{2n^2 D}{r_d^2} + 2 k_1 k_2 N_d\right) V_y \\
 &- 2 k_1 N_d - F_{ff} \cos(\delta_f) + F_{fn} \cos(\beta_f) - F_{rf} \cos(\delta_r) + F_{rn} \cos(\beta_r) \\
 \left(I_z + \frac{2n^2 J \ell^2}{r_d^2}\right) \dot{\Omega}_z &= \frac{\ell \cdot n \cdot k}{r_d} (I_2 - I_1) - \left(\frac{2n^2 D}{r_d^2} + 2 k_1 k_2 N_d\right) \ell^2 \Omega_z \\
 &+ k [F_{rn} \sin(\beta_r) - F_{rf} \sin(\delta_r) - F_{fn} \sin(\beta_f) + F_{ff} \sin(\delta_f)]
 \end{aligned}
 \tag{A.7.1.3}$$

where

$$F_{rn} = k_{cn} \text{sign}\left(\text{atan}\left(\frac{\Omega_z k}{V_y}\right) - \delta_r\right) N_r;$$

$$F_{fn} = k_{cn} \text{sign}\left(\text{atan}\left(\frac{-\Omega_z k}{V_y}\right) - \delta_f\right) N_f; \quad (\text{A.7.1.4})$$

$$F_{ff} = k_{c1} \{ 1 + k_{c2} [(V_y \cos \delta_f - \Omega_z \ell \sin \delta_f)] \} N_f$$

$$F_{rf} = k_{c1} \{ 1 + k_{c2} [(V_y \cos \delta_r + \Omega_z \ell \sin \delta_r)] \} N_r \quad (\text{A.7.1.5})$$

$$\beta_f = \delta_f + 90^\circ \quad (\text{A.7.1.6})$$

$$\beta_r = \delta_r + 90^\circ \quad (\text{A.7.1.7})$$

Therefore

$$\sin \beta_f = \cos \delta_f; \quad \cos \beta_f = -\sin \delta_f$$

$$\sin \beta_r = \cos \delta_r; \quad \cos \beta_r = -\sin \delta_r$$

Substituting the above into equations (A.7.1.3), then

$$\left(m + \frac{2n^2 J}{r_d^2}\right) \dot{V}_y = \frac{nk_t}{r_d} (I_1 + I_2) - \left(\frac{2n^2 D}{r_d^2} + 2k_2 N_d\right) V_y$$

$$- 2k_1 N_d - F_{ff} \cos(\delta_f) - F_{fn} \sin(\delta_f) - F_{rf} \cos(\delta_r) - F_{rn} \sin(\delta_r)$$

$$\left(I_2 + \frac{2n^2 \ell^2}{r_d^2}\right) \dot{\Omega}_z = \frac{\ell \cdot n \cdot k_t}{r_d} (I_2 - I_1) - \left(\frac{2n^2 D}{r_d^2} + 2k_2 N_d\right) \ell \Omega_z$$

$$+ k [F_{rn} \cos(\delta_r) - F_{rf} \sin(\delta_r) - F_{fn} \cos(\delta_f) + F_{ff} \sin(\delta_f)] \quad (\text{A.7.1.8})$$

From the definitions, K_{et} , D_e , M_e , K_{j1} , and K_{j2} are:

$$M_e = \frac{2n^2 J}{r_d^2} \quad K_{et} = \frac{nk_t}{r_d} \quad D_e = \frac{2n^2 D}{r_d^2}$$

$$K_{d1}[1] = K_{d1}[1] = k_1 N_d = K_{d1}$$

$$K_{d2}[1] = K_{d2}[2] = k_2 N_d = K_{d2}$$

$$K_{c1}[1] = k_{c2} N_f; \quad K_{c1}[2] = k_{c2} N_r$$

$$K_{cn}[1] = k_{cn} N_f; \quad K_{cn}[2] = k_{cn} N_r$$

Substituting these expressions into equations (A.7.1.5), (A.7.1.6) and (A.7.1.8), they are written as:

$$\begin{aligned}
(m + M_e)\dot{V}_y &= K_{et}(I_1 + I_2) - 2(D_e + K_{d2})V_y \\
&\quad - 2K_{d1} - F_{ff}\cos(\delta_f) - F_{fn}\sin(\delta_f) - F_{rf}\cos(\delta_r) - F_{rn}\sin(\delta_r) \\
(I_z + M_e \ell^2)\dot{\Omega}_z &= K_{et} \ell (I_2 - I_1) - (D_e + 2K_{d2})\ell^2\Omega_z + \\
&\quad k [K_{cn}[2]\sin(\delta_r) - F_{rf}\sin(\delta_r) - K_{cn}[1]\cos(\delta_f) + F_{ff}\cos(\delta_f)]
\end{aligned} \tag{A.7.1.9}$$

And

$$\begin{aligned}
F_{ff} &= K_{c1}[1] + K_{c2}[1][(V_y \cos \delta_f - \Omega_z \ell \sin \delta_f)] \\
F_{rf} &= K_{c1}[2] + K_{c2}[2][(V_y \cos \delta_r + \Omega_z \ell \sin \delta_r)] \\
F_{rn} &= K_{cn}[2]\text{sign}\left(\text{atan}\left(\frac{\Omega_z k}{V_y}\right) - \delta_r\right); \\
F_{fn} &= K_{cn}[1]\text{sign}\left(\text{atan}\left(\frac{-\Omega_z k}{V_y}\right) - \delta_f\right);
\end{aligned} \tag{A.7.1.10}$$

Substituting (A.7.1.10) into (A.7.1.9), and with

$$C\delta_r = \cos \delta_r; C\delta_f = \cos \delta_f; S\delta_r = \sin \delta_r; S\delta_f = \sin \delta_f$$

Then the motion equations of CONCIC-2 obtained by the regular approach are

$$\begin{aligned}
(m + M_e)\dot{V}_y &= K_{et}(I_1 + I_2) - (2D_e + 2K_{d2} - K_{c2}[1]C^2\delta_f + K_{c2}[2]C^2\delta_r)V_y \\
&\quad - K_{c2} k (-S^2\delta_f + S^2\delta_r)\Omega_z \\
&\quad - 2K_{df} - K_{ff}[1]C\delta - K_{rf}[2]C\delta + \\
(I_z + M_e \ell^2)\dot{\Omega}_z &= K_{et} \ell (I_2 - I_1) - (2D_e + 2K_{d2})\ell^2\Omega_z \\
&\quad + (K_{c2}[1]S^2\delta_f + K_{c2}[1]S^2\delta_r)k^2\Omega_z \\
&\quad + k K_{c2} S\delta_r - k K_{c1}[1] C\delta_f] \\
&\quad + k K_{cn}[2]\text{sign}\left(\text{atan}\left(\frac{\Omega_z k}{V_y}\right) - \delta_r\right) S\delta_r \\
&\quad - k K_{cn}[1]\text{sign}\left(\text{atan}\left(\frac{-\Omega_z k}{V_y}\right) - \delta_f\right) C\delta_f
\end{aligned} \tag{A.7.1.11}$$

Comparing equations (A.7.1.11) with (A.7.1.2), and take note that $\delta_f = \delta[1]$ and $\delta_r = \delta[2]$, the results of the two approach are the same.

7.2 CASE STUDY 2— DIAMOND SHAPED WHEEL BASE WITH FORE-AND-AFT DRIVING AND STEERING

This section presents the equations of motion of a diamond-shaped AGV with a driving wheel in the front and a steering wheel at the rear using the two approaches. In this case, the AGV is considered to have 3 d-o-f (forward, lateral, and yaw), and the center of mass is also assumed locating in the geometrical center of the AGV. The equations of motion are first developed by the regular approach, then followed by the general approach. The comparison of the results of the two approach are presented as well.

Regular approach

Fig. A.9 shows this diamond-shaped wheel-configuration AGV. The vehicle is steered by the steering wheel in the front and driven by the driving wheel in the rear. There are two casters on the two sides of the AGV. The steering wheel is located in the front AGV body on the longitudinal axis. The driving wheel in the rear is mounted rigidly to the AGV body on the longitudinal axis.

The velocities of the AGV are defined as:

V_y ----- linear velocity of AGV along y axis in body centered system.

V_x ----- linear velocity of AGV along x axis in body centered system.

Ω_z ----- angular velocity of AGV about z axis in body centered system.

Then the velocities along and vertical to the travel of the wheel are:

$$\begin{aligned} V_{cf1} &= (V_y - \Omega_z \ell) \cos\beta_1 + V_x \sin\beta_1 \\ V_{cf2} &= (V_y + \Omega_z \ell) \cos\beta_2 + V_x \sin\beta_2 \\ V_{sf} &= V_y \cos\alpha + (V_x - \Omega_z k) \sin\alpha \end{aligned} \quad (A.7.2.1)$$

The equations of motion of the AGV is written as

$$\begin{aligned} \sum X &= m(\dot{V}_x - \Omega_z V_y) \\ \sum Y &= m(\dot{V}_y - \Omega_z V_x) \\ \sum N &= I_z \dot{\Omega}_z \end{aligned} \quad (A.7.2.2)$$

Where $\sum X$, $\sum Y$ are the summation of the forces along x and y axis, and $\sum N$ is the summation of the moments about the z axis.

The external forces acting on the vehicle is presented in Fig. A.10. Therefore, $\sum X$, $\sum Y$ and $\sum N$ may be obtained in terms of external forces. They are:

$$\begin{aligned} \sum X &= -F_{d\ell} - F_{cf} \sin\beta_1 - F_{cf} \sin\beta_2 - F_{sf} \sin\alpha - F_{cl1} \cos\beta_1 \\ &\quad - F_{cl2} \cos\beta_2 - F_{sl} \sin\alpha \\ \sum Y &= F_t - F_{dr} - F_{cf1} \cos\beta_1 - F_{cf2} \cos\beta_2 - F_{sf} \cos\alpha \\ &\quad - F_{cn1} \sin\beta_1 - F_{cn2} \sin\beta_2 - F_{sl} \sin\alpha \\ \sum N &= -F_{cf1} \cos\beta_1 \ell - F_{cn2} \sin\beta_2 \ell + F_{cf1} \cos\beta_1 \ell + F_{cn1} \sin\beta_1 \ell \\ &\quad - F_{d\ell} k + k F_{sf} \sin\alpha + k F_{sl} \cos\alpha \end{aligned} \quad (A.7.2.3)$$

Where F_{sl} , F_{sf} are the cornering force and rolling resistance on the steering wheel, F_{dr} , F_{dt} , $F_{d\ell}$ are the rolling resistance, tractive force and cornering force on the driving wheel, F_{cf1} , F_{cn1} are the rolling resistance

and cornering force on caster 1, and F_{cf2} , F_{cn2} are the rolling resistance and cornering force on caster 2.

Simplifying equations (A.7.2.1) by introducing $S\alpha = \sin\alpha$, $C\alpha = \cos\alpha$, $S\beta_1 = \sin\beta_1$, $C\beta_1 = \cos\beta_1$, $S\beta_2 = \sin\beta_2$, and $C\beta_2 = \cos\beta_2$.

$$\sum X = -F_{cf1} S\beta_1 - F_{cf2} S\beta_2 - F_{sf} S\alpha - F_{cn1} C\beta_1 - F_{cn2} C\beta_2 - F_{sl} C\alpha - F_{dl}$$

$$\sum Y = F_t - F_{df} - F_{cf1} C\beta_1 - F_{cf2} C\beta_2 - F_{sf} C\alpha - F_{cn1} S\beta_1 - F_{cn2} S\beta_2 - F_{sl} S\alpha$$

$$\sum N = -F_{cf2} C\beta_2 - F_{cn2} S\beta_2 l + F_{cf1} C\beta_1 l + F_{cn1} S\beta_1 l - F_{dl} k + F_{sf} S\alpha k + F_{sl} C\alpha k$$

(A.7.2.4)

The external forces are calculated using the following formulae:

tractive force

$$F_t = \frac{n}{r_d} (K_t I - \frac{Jn}{r_d} \dot{V} - \frac{Dn}{r_d} V - T_f)$$

rolling resistance

$$F_f = (k_1 + k_2 V) N$$

cornering force

$$F_l = \alpha \cdot C$$

sliding friction

$$F_n = k_l \cdot N \cdot \text{sign}(\text{atan}(\frac{V_x}{V_y}) - \alpha_c)$$

Thus the external forces of the AGV are

$$F_{cf1} = \{ k_1 + k_2 [(V_y - \Omega_z l) \cos\beta_1 + V_x \sin\beta_1] \} N_{c1} \quad (A.7.2.5)$$

$$F_{cf2} = \{ k_1 + k_2 [(V_y + \Omega_z l) \cos\beta_2 + V_x \sin\beta_2] \} N_{c2} \quad (A.7.2.7)$$

$$F_{sf} = \{ k_1 + k_2 [V_y \cos\alpha + (V_x - \Omega_z k) \sin\alpha] \} N_s \quad (A.7.2.8)$$

$$F_{df} = (k_1 + k_2 V_y) N_d \quad (A.7.2.9)$$

$$F_{cl1} = k_{cn} N_{c1} \text{sign}(\text{atan}(\frac{V_x}{V_y}) - \beta_1) \quad (A.7.2.10)$$

$$F_{d2} = k_{cn} N_{c2} \text{sign}(\text{atan}(\frac{V_x}{V_y}) - \beta_2) \quad (\text{A.7.2.11})$$

$$F_{s1} = \{\text{atan}(\frac{V_x - W_z k}{V_y}) - \alpha_s\} C_s \quad (\text{A.7.2.12})$$

$$F_{d1} = -\text{atan}(\frac{V_x - W_z k}{V_y}) C_d \quad (\text{A.7.2.13})$$

$$F_{dt} = \frac{n}{r_d} \{k_t I - \frac{J n}{r_d} \dot{V}_y - \frac{D n}{r_d} V_y - T_f\} \quad (\text{A.7.2.14})$$

Let

$$K_{d1}[1] = k_{d1} N_{d1} \quad K_{d2}[1] = k_{d2} N_{d1}$$

$$K_{s1}[1] = k_{s1} N_s \quad K_{s2}[1] = k_{s2} N_s$$

$$K_{c1}[1] = k_{c1} N_{c1} \quad K_{c2}[1] = k_{c2} N_{c1}$$

$$K_{c1}[2] = k_{c1} N_{c2} \quad K_{c2}[2] = k_{c2} N_{c2}$$

$$K_{cn}[1] = k_{cn} N_{c1} \quad F_{cn}[2] = F_{cn} N_{c2}$$

Substituting the external forces and K_{j1}, K_{j2} ($j = d, s, c$) into equation

(A.7.2.4). Then

$$\begin{aligned} \sum X = & -\{K_{d1}[1] + K_{d2}[1]\}[(V_y - \Omega_z \ell) C\beta_1 + V_x S\beta_1] S\beta_1 \\ & - \{K_{d1}[2] + K_{d2}[2]\}[(V_y + \Omega_z \ell) C\beta_2 + V_x S\beta_1] S\beta_2 \\ & - \{K_{s1} + K_{s2}\}[(V_y C\alpha_1 + (V_x - \Omega_z k) S\alpha_1)] S\alpha \\ & - K_{cn}[1] \text{sign}(\text{atan}(\frac{V_x}{V_y}) - \beta_1) C\beta_1 \\ & - K_{cn}[2] \text{sign}(\text{atan}(\frac{V_x}{V_y}) - \beta_2) C\beta_2 \\ & - \{\text{atan}(\frac{V_x - W_z k}{V_y}) - \alpha_s\} C_s C\alpha + \text{atan}(\frac{V_x - W_z k}{V_y}) C_d \\ \sum Y = & K_{et} I - M_o \dot{V}_y - D_o V_y - T_{ef} \\ & - \{K_{c1}[1] + K_{c2}[1]\}[(V_y - \Omega_z \ell) C\beta_1 + V_x S\beta_1] C\beta_1 \\ & - \{K_{c1}[2] + K_{c2}[2]\}[(V_y + \Omega_z \ell) C\beta_2 + V_x S\beta_2] C\beta_2 \end{aligned}$$

$$\begin{aligned}
& -(K_{s1} + K_{s2}[V_y C\alpha + (V_x - \Omega_z \cdot k) S\alpha]) C\alpha \\
& -K_{cn}[1]\text{sign}(\text{atan}(\frac{V_x}{V_y}) - \beta_1) S\beta_1 \\
& -K_{cn}[2]\text{sign}(\text{atan}(\frac{V_x}{V_y}) - \beta_2) S\beta_2 \\
& -(\text{atan}(\frac{V_x - \Omega_z k}{V_y}) - \alpha_s) C_s S\alpha \\
\sum N = & -(K_{c1}[2] + K_{c2}[2] [(V_y + \Omega_z \ell) C\beta_2 + V_x S\beta_2]) C\beta_2 \ell \\
& -K_{cn}[2]\text{sign}(\text{atan}(\frac{V_x}{V_y}) - \beta_2) S\beta_2 \ell \\
& + (K_{c1}[1] + K_{c2}[1] [(V_y + \Omega_z \ell) C\beta_1 + V_x S\beta_1]) C\beta_1 \ell \\
& -K_{cn}[1]\text{sign}(\text{atan}(\frac{V_x}{V_y}) - \beta_1) S\beta_1 \ell \\
& -\text{atan}(\frac{V_x + \Omega_z \ell}{V_y}) C_d k \\
& + (K_{s1} + K_{s2}[V_y C\alpha + (V_x - \Omega_z k) S\alpha]) S\alpha k \\
& + (\text{atan}(\frac{V_x + \Omega_z \ell}{V_y}) - \alpha_s) C_s C\alpha k
\end{aligned} \tag{A.7.2.15}$$

Rearranging the equations (A.7.2.15), they are written as follows:

$$\begin{aligned}
\sum X = & -(K_{c2}[1] C\beta_1 S\beta_1 + K_{c2}[2] C\beta_2 S\beta_2 + K_{s2} C\alpha S\alpha) V_y \\
& -(-K_{c2}[1] \cdot \ell C\beta_1 S\beta_1 + K_{c2}[2] \cdot \ell C\beta_2 S\beta_2 - K_{s2} \cdot k S\alpha^2) \Omega_z \\
& -(K_{c2}[1] S^2\beta_1 + K_{c2}[2] S^2\beta_2 + K_{s2} S^2\alpha) V_x \\
& -[K_{d1}[1] S\beta_1 + K_{d2}[2] S\beta_2 + K_{s1} S\alpha] - \\
& (K_{cn}[1]\text{sign}(\text{atan}(\frac{V_x}{V_y}) - \beta_1) C\beta_1
\end{aligned}$$

$$\begin{aligned}
& + K_{cn}[2] \text{sign} \left[\text{atan} \left(\frac{V_x}{V_y} \right) - \beta_2 \right] C\beta_2 \} \\
& - \text{atan} \left(\frac{V_x - W_z k}{V_y} \right) C_s C\alpha + \alpha_s C_s C\alpha \\
\sum Y = & K_{et} I - M_o \dot{V}_y \\
& - [K_{d2} + K_{c2}[1] C^2\beta_1 + K_{c2}[2] C^2\beta_2 + K_{s2} C^2\alpha + D_o] V_y \\
& - [-K_{c2}[1] \cdot \ell C^2\beta_1 + K_{c2}[2] \cdot \ell^2 C\beta_2 - K_{s2} \cdot k S\alpha C\alpha] \Omega_z \\
& - [K_{c2}[1] S\beta_1 C\beta_1 + K_{c2}[2] \cdot \ell S\beta_2 C\beta_2 + K_{s2} \cdot k S\alpha C\alpha] V_x \\
& - (K_{d1} + K_{c1}[1] \text{sign} \left[\text{atan} \left(\frac{V_x}{V_y} \right) - \beta_1 \right] C\beta_1 + \\
& K_{c2}[2] \text{sign} \left[\text{atan} \left(\frac{V_x}{V_y} \right) - \beta_2 \right] C\beta_2) - K_{s1} C\alpha + T_{ef} \\
& - (K_{cn}[1] \text{sign} \left[\text{atan} \left(\frac{V_x}{V_y} \right) - \beta_1 \right] S\beta_1 \\
& + K_{cn}[2] \text{sign} \left[\text{atan} \left(\frac{V_x}{V_y} \right) - \beta_2 \right] S\beta_2) \\
& - \frac{V_x - W_z k}{V_y} C_s S\alpha + \alpha_s C_s S\alpha \\
\sum N = & - (K_{c1}[2] + K_{c2}[2] [(V_y + \Omega_z \ell) C\beta_2 + V_x S\beta_2]) C\beta_2 \ell \\
& - K_{cn}[2] \text{sign} \left(\text{atan} \left(\frac{V_x}{V_y} \right) - \beta_2 \right) S\beta_2 \ell \\
& + (K_{c1}[1] + K_{c2}[1] [(V_y + \Omega_z \ell) C\beta_1 + V_x S\beta_1]) C\beta_1 \ell \\
& - K_{cn}[1] \ell \text{sign} \left[\text{atan} \left(\frac{V_x}{V_y} \right) - \beta_1 \right] S\beta_1 \ell \\
& - \text{atan} \left(\frac{V_x + \Omega_z \ell}{V_y} \right) C_d k \\
& + (K_{s1} + K_{s2} [V_y C\alpha + (V_x - \Omega_z k) S\alpha]) S\alpha k
\end{aligned}$$

$$+ \left\{ \left(\operatorname{atan}\left(\frac{V_x + \Omega_z \ell}{V_y}\right) - \alpha_s \right) C_s \right\} C_\alpha k$$

(A.7.2.16)

So the equations of motion of this diamond-shaped AGV are:

$$\begin{aligned} m(\dot{V}_x - \Omega_z V_y) = & -(K_{c2}[1] C\beta_1 S\beta_1 + K_{c2}[2] C\beta_2 S\beta_2 + K_{s2} C\alpha S\alpha) V_y \\ & - (-K_{c2}[1] \cdot \ell C\beta_1 S\beta_1 + K_{c2}[2] \cdot \ell C\beta_2 S\beta_2 - K_{s2} \cdot k S\alpha^2) \Omega_z \\ & - (K_{c2}[1] S^2\beta_1 + K_{c2}[2] S^2\beta_2 + K_{s2} S^2\alpha) V_x \\ & - [K_{d1}[1] S\beta_1 + K_{d2}[2] S\beta_2 + K_{s1} S\alpha] \\ & - K_{cn}[1] \operatorname{sign}\left(\operatorname{atan}\left(\frac{V_x}{V_y}\right) - \beta_1\right) C\beta_1 \\ & + K_{cn}[2] \operatorname{sign}\left(\operatorname{atan}\left(\frac{V_x}{V_y}\right) - \beta_2\right) C\beta_2 + \operatorname{atan}\left(\frac{V_x - W_z k}{V_y}\right) C_s C\alpha \\ & + \alpha_s C_s C\alpha + \left(\frac{V_x - W_z k}{V_y}\right) C_d \end{aligned}$$

$$\begin{aligned} m(\dot{V}_y + \Omega_z V_x) = & K_{et} I - M_e \dot{V}_y \\ & - [K_{d2} + K_{c2}[1] C^2\beta_1 + K_{c2}[2] C^2\beta_2 + K_{s2} C^2\alpha + D_e] V_y \\ & - [-K_{c2}[1] \cdot \ell C^2\beta_1 + K_{c2}[2] \cdot \ell C^2\beta_2 - K_{s2} \cdot k S\alpha C\alpha] \Omega_z \\ & - [K_{c2}[1] S\beta_1 C\beta_1 + K_{c2}[2] \cdot \ell S\beta_1 C\beta_2 + K_{s2} \cdot k S\alpha C\alpha] V_x \\ & - (K_{d1} + K_{c1}[1] C\beta_1 + K_{c2}[2] C\beta_2 + K_{s1} C\alpha + T_{ef}) \\ & - (K_{cn}[1] \operatorname{sign}\left(\operatorname{atan}\left(\frac{V_x}{V_y}\right) - \beta_1\right) S\beta_1 \\ & + K_{cn}[2] \operatorname{sign}\left(\operatorname{atan}\left(\frac{V_x}{V_y}\right) - \beta_2\right) S\beta_2 \\ & + \frac{V_x - W_z k}{V_y} C_s S\alpha) + \alpha_s C_s S\alpha \end{aligned}$$

$$\begin{aligned}
I_z \dot{\Omega}_z = & [K_{c2}[1] C\beta_1^2 \ell - K_{c2}[2] C\beta_2^2 \ell + K_{s2} C\alpha S\alpha k] V_y \\
& - [K_{c2}[1] C\beta_1 \ell^2 - K_{c2}[2] C\beta_2^2 \ell^2 + K_{s2} C\alpha S\alpha k^2] \Omega_z \\
& + [K_{c2}[1] S\beta_1 C\beta_1 \ell - K_{c2}[2] S\beta_2 C\beta_2 \ell + K_{s2} S\alpha^2 k] V_x \\
& + \ell \{K_{c1}[1] C\beta_1 \ell - K_{c1}[2] C\beta_2 \ell + K_{s1} S\alpha k \\
& - K_{cn}[1] \text{sign}[\text{atan}(\frac{V_x}{V_y}) - \beta_1] S\beta_1 \\
& - K_{cn}[2] \text{sign}[\text{atan}(\frac{V_x}{V_y}) - \beta_2] S\beta_2\} \\
& - \text{atan}(\frac{V_x + \Omega_z k}{V_y}) C_d k + \text{atan}(\frac{V_x - \Omega_z k}{V_y}) C_s C\alpha k \\
& - \alpha_s C_s C\alpha k
\end{aligned}
\tag{A.7.2.17}$$

GENERAL PROCEDURE

Using the general procedure, the equations of motion are derived in four steps. The equations of motion of a 3 d-o-f AGV (forward, lateral and yaw) are as follows:

$$\begin{aligned}
\sum X = m(\dot{V}_x - r V_y) &= \sum_1^{\ell} F_{dx}[i] + \sum_1^m F_{sx}[i] + \sum_1^n F_{dsx}[i] + \sum_1^k F_{cx}[i] \\
\sum Y = m(\dot{V}_y + r V_x) &= \sum_1^{\ell} F_{dy}[i] + \sum_1^m F_{sy}[i] + \sum_1^n F_{dsy}[i] + \sum_1^k F_{cy}[i] \\
\sum N = I_z \dot{\Omega}_z &= - \sum_1^{\ell} F_{dx}[i] \cdot Y_d[i] - \sum_1^m F_{sx}[i] \cdot Y_s[i] - \sum_1^n F_{dsx}[i] \cdot Y_{ds}[i] - \\
&\quad \sum_1^k F_{cx}[i] \cdot Y_c[i] + \sum_1^{\ell} F_{dy}[i] \cdot X_d[i] + \\
&\quad \sum_1^m F_{sy}[i] \cdot X_s[i] + \sum_1^n F_{dsy}[i] \cdot X_{ds}[i] + \sum_1^k F_{cy}[i] \cdot X_c[i]
\end{aligned}
\tag{A.7.2.18}$$

STEP 1 --- system information

Fig. A.9 shows the configuration of the AGV. It has two casters on two sides (left is wheel 1 and right is wheel 2), one steering wheel at front, and one driving wheel at rear. Thus

$$k = 2;$$

$$m = 1;$$

$$\ell = 1.$$

The coordinates for the wheel are

$$\text{caster 1 } [0, -\ell];$$

$$\text{caster 2 } [0, \ell];$$

$$\text{driving wheel } [-k, 0]$$

$$\text{steering wheel } [k, 0]$$

STEP TWO --- system parameters

wheel type	δ_1	δ_2	system parameters
$C_1(0, -\ell)$	$\delta_{c1}[1] = -\ell$	$\delta_{c2}[1] = 0$	$K_{c1}[1] \quad K_{c2}[1]$
$C_2(0, \ell)$	$\delta_{c1}[2] = \ell$	$\delta_{c2}[2] = 0$	$K_{c1}[2] \quad K_{c2}[2]$
$S_1(k, 0)$	$\delta_{s1}[1] = 0$	$\delta_{s2}[1] = -k$	$K_{s1}[1] \quad K_{s2}[1]$
$D_1(-k, 0)$	$\delta_{d1}[1] = 0$	$\delta_{d2}[1] = k$	K_{et}, J_e, D_e K_{d1}, K_{d2}, T_{ef}

Where

$$K_{et} = \frac{nk_t[1]}{r_d[1]}$$

$$M_e = \frac{Jn^2[1]}{r^2[1]}$$

$$D_e = \frac{Dn^2[1]}{r_d^2[1]}$$

$$T_{ef} = \frac{n}{r_d} T_f[1]$$

$$K_{s1}[1] = k_{s1}[1] N_s[1]$$

$$K_{s2}[1] = k_{s2}[1] N_s[1]$$

$$K_{c1}[1] = k_{c1}[1] N_c[1]$$

$$K_{c2}[1] = k_{c2}[1] N_c[1]$$

$$K_{c1}[2] = k_{c1}[2] N_c[2]$$

$$K_{c2}[2] = k_{c2}[2] N_c[2]$$

$$K_{cn}[1] = k_{cn}[1] N_c[1]$$

$$K_{cn}[2] = k_{cn}[2] N_c[2]$$

STEP THREE --- the formulation of the external forces

Casters:

From equations (A.5.13), the external forces on the casters are:

$$\begin{aligned}
 F_{cx}[1] &= -K_{c1}[1] \sin\beta[1] - K_{c2}[1] \cos\beta[1] \sin\beta[1] V_y \\
 &\quad - K_{c2}[1] \sin^2\beta[1] V_x - K_{c2}[1] \sin\beta[1] [\cos\beta[1](-\ell_1) \cdot \Omega_z \\
 &\quad - K_{cn}[1] \text{sign}\left(\text{atan}\left(\frac{V_x}{V_y}\right) - \beta[1]\right) \cdot \cos\beta[1] \\
 F_{cx}[2] &= -K_{c1}[2] \sin\beta[2] - K_{c2}[2] \cos\beta[2] \sin\beta[2] V_y \\
 &\quad - K_{c2}[2] \sin^2\beta[2] V_x - K_{c2}[2] \sin\beta[2] [\cos\beta[2](-\ell_1) \cdot \Omega_z \\
 &\quad - K_{cn}[2] \text{sign}\left(\text{atan}\left(\frac{V_x}{V_y}\right) - \beta[2]\right) \cdot \cos\beta[2] \quad (7.2.19)
 \end{aligned}$$

$$\begin{aligned}
 F_{cy}[1] &= -K_{c1}[1] \cos\beta[1] - K_{c2}[1] \cos^2\beta[1] V_y \\
 &\quad - K_{c2}[1] \sin\beta[1] \cos\beta[1] V_x - K_{c2}[1] \cos^2\beta[1] (-\ell_1) \cdot \Omega_z \\
 &\quad - K_{cn}[1] \text{sign}\left(\text{atan}\left(\frac{V_x}{V_y}\right) - \beta[1]\right) \cdot \sin\beta[1] \\
 F_{cy}[2] &= -K_{c1}[2] \cos\beta[2] - K_{c2}[2] \cos^2\beta[2] V_y \\
 &\quad - K_{c2}[2] \sin\beta[2] \cos\beta[2] V_x - K_{c2}[2] \cos^2\beta[2] (-\ell_1) \cdot \Omega_z \\
 &\quad - K_{cn}[2] \text{sign}\left(\text{atan}\left(\frac{V_x}{V_y}\right) - \beta[2]\right) \cdot \sin\beta[2] \quad (7.2.20)
 \end{aligned}$$

Steering Wheels:

From equations (5.16), the forces on the steering wheel are:

$$\begin{aligned}
 F_{sx} &= -K_{s1} \sin\alpha - K_{s2} \cos\alpha \sin\alpha \cdot V_y - K_{s2} \sin^2\alpha \cdot V_x - K_{s2} \sin^2\alpha \ell_2 \Omega_z \\
 &\quad - C_s \cos\alpha \left[\alpha_s - \text{atan}\left(\frac{V_x - k\Omega_z}{V_y}\right) \right]
 \end{aligned}$$

$$\begin{aligned}
F_{sy} = & -K_{s1} \sin \alpha - K_{s2} \cos^2 \alpha \cdot V_y - K_{s2} \sin \alpha \cos \alpha \cdot V_x \\
& + K_{s2} \sin \alpha \cos \alpha \ell_2 \Omega_z + C_s \cos \alpha \left[\alpha - \arctan\left(\frac{V_x - k\Omega_z}{V_y}\right) \right]
\end{aligned}
\tag{A.7.2.21}$$

Driving wheel

The static friction moment T_{fr} is considered to be negligible in current study, therefore, the external forces on the driving wheel are obtained from equations (A.5.15).

$$\begin{aligned}
F_{dx} = & -C_d \tan\left(\frac{V_x + k\Omega_z}{V_y}\right) \\
F_{dy} = & K_{et} I_1 - M_e \cdot \dot{V} - (D_e + K_{d2}) V - K_{d1}
\end{aligned}
\tag{A.7.2.22}$$

STEP FOUR --- the dynamic equations

The equations of motion of the AGV may be obtained by substituting the external forces into the following equations.

$$\begin{aligned}
\sum X = & m(\dot{V}_x - \Omega_z V_y) \\
\sum Y = & m(\dot{V}_y - \Omega_z V_x) \\
\sum N = & I_z \dot{\Omega}_z
\end{aligned}$$

The equations of motion are:

$$\begin{aligned}
 \Sigma X &= \Sigma F_{cx}[i] + F_{dx} + F_{sx} \\
 &= - (K_{c1}[1]\sin\beta[1] + K_{c1}[2]\sin\beta[2]) - (K_{c2}[2]\sin\beta[1]\cos\beta[1] + \\
 &\quad K_{c2}[2]\sin\beta[2]\cos\beta[2])V_y - (K_{c2}[1]\sin^2\beta[1] + K_{c2}[2]\sin^2\beta[2])V_x \\
 &\quad - l(-K_{c2}[1]\cos\beta[1]\sin\beta[1] + K_{c2}[2]\cos\beta[2]\sin\beta[2])\Omega_z \\
 &\quad - (K_{cn}[1]\text{sign}(\text{atan}(\frac{V_x}{V_y}) - \beta[1])\cos\beta[1] \\
 &\quad + K_{cn}[2]\text{sign}(\text{atan}(\frac{V_x}{V_y}) - \beta[2])\cos\beta[2] \\
 &\quad - K_{s1}\sin\alpha - K_{s2}\cos\alpha\sin\alpha V_y \\
 &\quad - K_{s2}\sin^2\alpha V_x + K_{s2}\sin^2\alpha k\Omega_z - C_s\alpha\cos\alpha \\
 &\quad - C_d\text{atan}(\frac{V_x + k\Omega_z}{V_y}) - C_s\text{atan}(\frac{V_x - k\Omega_z}{V_y})\cos\alpha
 \end{aligned}$$

$$\begin{aligned}
 \Sigma Y &= \Sigma F_{cy}[i] + F_{sy} + F_{dy} \\
 &= (K_{c1}[1]\cos\beta[1] + K_{c1}[1]\cos\beta[2]) - (K_{c2}[2]\cos^2\beta[1] \\
 &\quad + K_{c2}[2]\cos^2\beta[2])V_y \\
 &\quad - (K_{c2}[1]\cos\beta[1]\sin\beta[1] + K_{c2}[2]\cos\beta[2]\sin\beta[2])V_x \\
 &\quad + K_{c2}(K_{c2}[1]\cos^2\beta[1] - K_{c2}[2]\cos^2\beta[2])\Omega_z \\
 &\quad + K_{cn}[1]\text{sign}(\text{atan}(\frac{V_x}{V_y}) - \beta[1])\sin\beta[1] \\
 &\quad + K_{cn}[2]\text{sign}(\text{atan}(\frac{V_x}{V_y}) - \beta[2])\sin\beta[2] \\
 &\quad - K_{s1}\cos\alpha - K_{s2}\cos^2\alpha V_y - K_{s2}\sin\alpha\cos\alpha k\Omega_z + \\
 &\quad C_s\sin\alpha(\alpha + C_s\text{atan}(\frac{V_x - k\Omega_z}{V_y}))
 \end{aligned}$$

$$\begin{aligned}
\sum N = & - \{ - C_d \operatorname{atan}\left(\frac{V_x + k\Omega_z}{V_y}\right) \cdot (-k) + [-K_{s1} \sin\alpha \\
& - K_{s2} \cos\alpha \sin\alpha V_y - K_{s2} \sin^2\alpha V_x + K_{s2} \sin^2\alpha k \Omega_z \\
& - C_s \cos\alpha [\alpha + \operatorname{atan}\left(\frac{V_x - k\Omega_z}{V_y}\right)] \} k \\
& + (K_{c1}[1] \cos\beta[1] - K_{c2}[1] \cos^2\beta[1] V_y - K_{c2}[1] \cos\beta[1] \sin\beta[1] V_x \\
& + K_{c2}[1] \cos^2\beta[1] \ell_1 \Omega_z \\
& + K_{cn}[1] \operatorname{sign}\left(\operatorname{atan}\left(\frac{V_x}{V_y}\right) - \beta[1]\right) \sin\beta[1] \cdot (-\ell) \\
& + \{-K_{c1} \cos\beta[2] - K_{c2}[2] \cos^2\beta[2] V_y - K_{c2}[2] \cos\beta[2] \sin\beta[2] V_x \\
& - K_{c2}[2] \cos^2\beta[2] \ell \cdot \Omega_z + K_{cn}[2] \operatorname{sign}\left(\operatorname{atan}\left(\frac{V_x}{V_y}\right) - \beta[2]\right) \sin\beta[2] \} \ell
\end{aligned}
\tag{A.7.2.23}$$

Rearranging the equation we have:

$$\begin{aligned}
m(\dot{V}_x - \Omega_z V_y) = & - [K_{s2} \cos\alpha \sin\alpha + (K_{c2}[1] \cos\beta[1] \sin\beta[1] \\
& + K_{c2}[2] \cos\beta[2] \sin\beta[2])] V_y \\
& - [K_{s2} \sin^2\alpha + (K_{c2}[1] \sin^2\beta[1] + K_{c2}[2] \sin^2\beta[2])] V_x \\
& - [\ell(K_{c2}[2] \cos\beta[2] \sin\beta[2] - K_{c2}[1] \cos\beta[1] \sin\beta[1]) \\
& - K_{s2} \cdot k \sin^2\alpha] \Omega_z \\
& - [(K_{c1}[1] \sin\beta[1] + K_{c1}[2] \sin\beta[2]) + K_{s1} \sin\alpha] - \\
& \{C_s \cos\alpha [\alpha - \operatorname{atan}\left(\frac{V_x - k\Omega_z}{V_y}\right)] + C_d \operatorname{atan}\left(\frac{V_x + k\Omega_z}{V_y}\right)\}
\end{aligned}$$

$$\begin{aligned}
m(\dot{V}_y - \Omega_z V_x) = & K_{et} I_1 - M_e \dot{V}_y - [(D_e + K_{d2}) \\
& + K_{s2} \cos^2 \alpha + (K_{c2}[1] \cos^2 \beta[1] + K_{c2}[2] \cos^2 \beta[2])] V_y \\
& - [K_{s2} \cos \alpha \sin \alpha + (K_{c2}[1] \cos \beta[1] \sin \beta[1] \\
& + K_{c2}[2] \cos \beta[2] \sin \beta[2])] V_x + \\
& [k K_{s2} \cos \alpha \sin \alpha + \ell (K_{c2}[1] \cos^2 \beta[1] - K_{c2}[2] \cos^2 \beta[2])] \Omega_z \\
& - [K_{s1} \cos \alpha + (K_{c1}[1] \cos \beta[1] + K_{c1}[2] \cos \beta[2])] \\
& + C_s \sin \alpha \left[\alpha - \operatorname{atan}\left(\frac{V_x - k \Omega_z}{V_y}\right) \right] \\
& + K_{cn}[1] \operatorname{sign}\left(\operatorname{atan}\left(\frac{V_x}{V_y}\right) - \beta[1]\right) \sin \beta[1] \\
& + K_{cn}[2] \operatorname{sign}\left(\operatorname{atan}\left(\frac{V_x}{V_y}\right) - \beta[2]\right) \sin \beta[2] - K_d
\end{aligned}$$

$$\begin{aligned}
I_z \dot{\Omega} = & [-K_{s2} k^2 \sin \alpha + \ell^2 (K_{c2}[1] \cos^2 \beta[1] + K_{c2}[2] \cos^2 \beta[2])] \Omega_z \\
& - [-K_{s2} \ell \sin^2 \alpha - K_{c2}[1] \ell \cos \beta[1] \sin \beta[1] \\
& + K_{c2}[2] \ell \cos \beta[2] \sin \beta[2]] V_x - \\
& [-K_{s2} k \cos \alpha \sin \alpha - K_{c2}[1] \ell \cos^2 \beta[1] + K_{c2}[2] \ell \cos^2 \beta[2]] V_y \\
& + [K_{s1} k \sin \alpha + K_{c1}[1] \ell \cos \beta[1] - K_{c1}[2] \ell \cos \beta[2]] \\
& - [k C_d \operatorname{atan}\left(\frac{V_x + k \Omega_z}{V_y}\right) - C_s \cos \alpha k \left[\alpha - \operatorname{atan}\left(\frac{V_x - k \Omega_z}{V_y}\right) \right] \\
& + \ell [K_{cn}[1] \operatorname{sign}\left(\operatorname{atan}\left(\frac{V_x}{V_y}\right) - \beta[1]\right) \\
& - K_{cn}[2] \operatorname{sign}\left(\operatorname{atan}\left(\frac{V_x}{V_y}\right) - \beta[2]\right)]
\end{aligned}$$

(A.7.2.24)

Comparison of the results of the regular approach and the general approach

Compared with equations (A.7.1.17), and noted that:

$$\begin{aligned}C\alpha &= \cos\alpha; & S\alpha &= \sin\alpha; \\C\beta[1] &= \cos\beta[1]; & C\beta[2] &= \cos\beta[2]; \\S\beta[1] &= \sin\beta[1]; & S\beta[2] &= \sin\beta[2],\end{aligned}$$

then the equations of motion of this diamond-shaped fore-and-aft driving steering AGV obtained the general approach (A.7.2.24) are as the same as those by the regular approach.

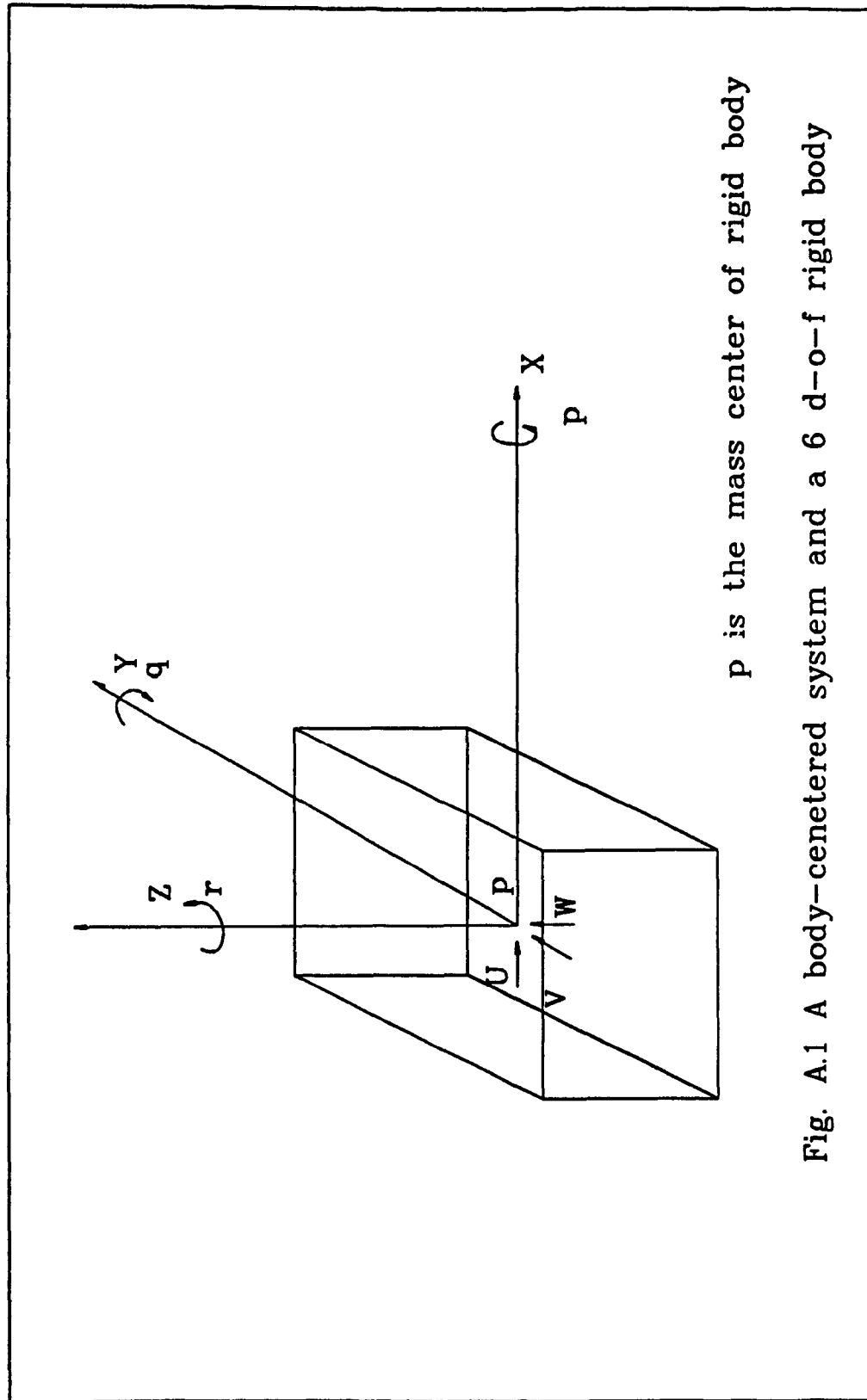


Fig. A.1 A body-centered system and a 6 d-o-f rigid body

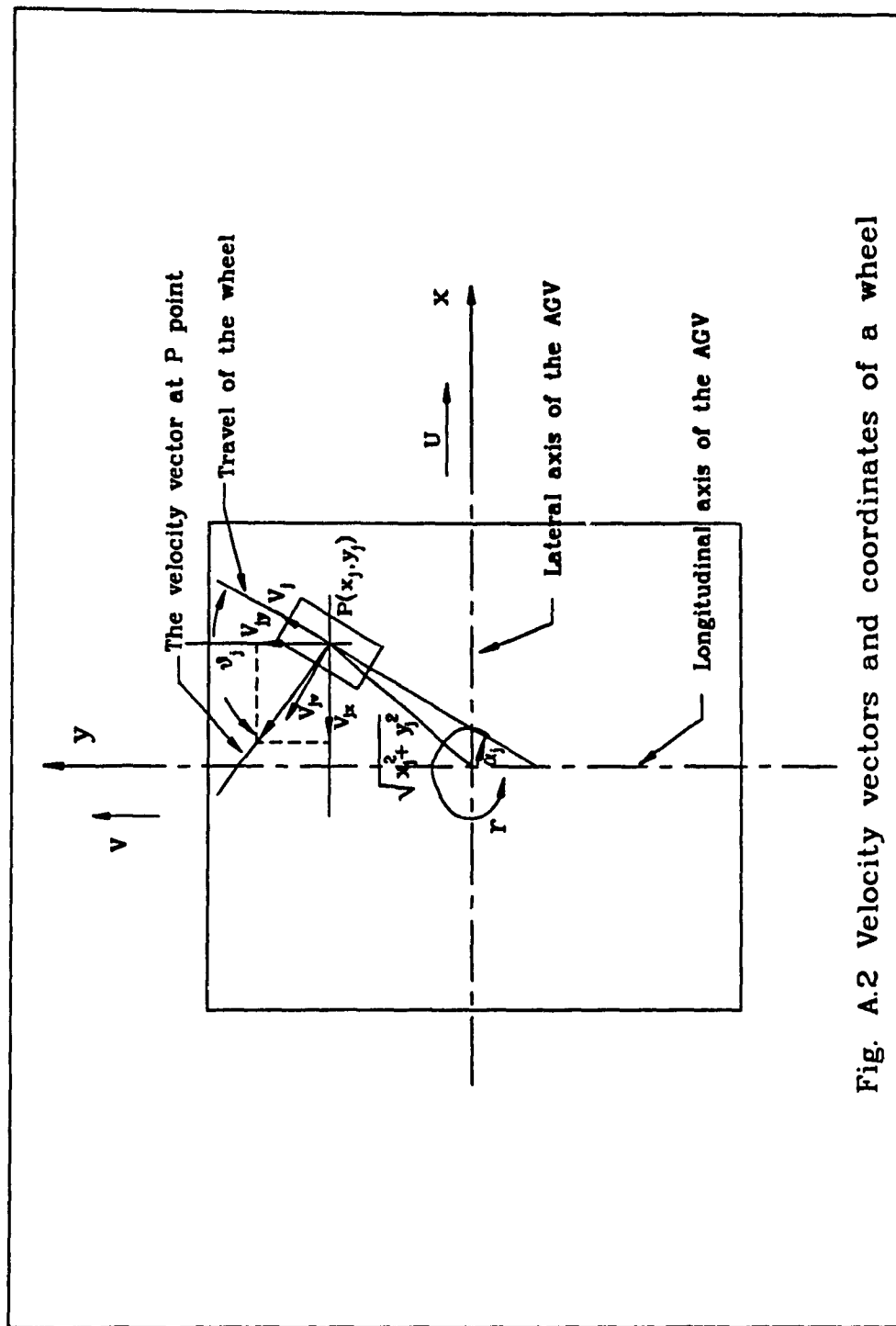


Fig. A.2 Velocity vectors and coordinates of a wheel

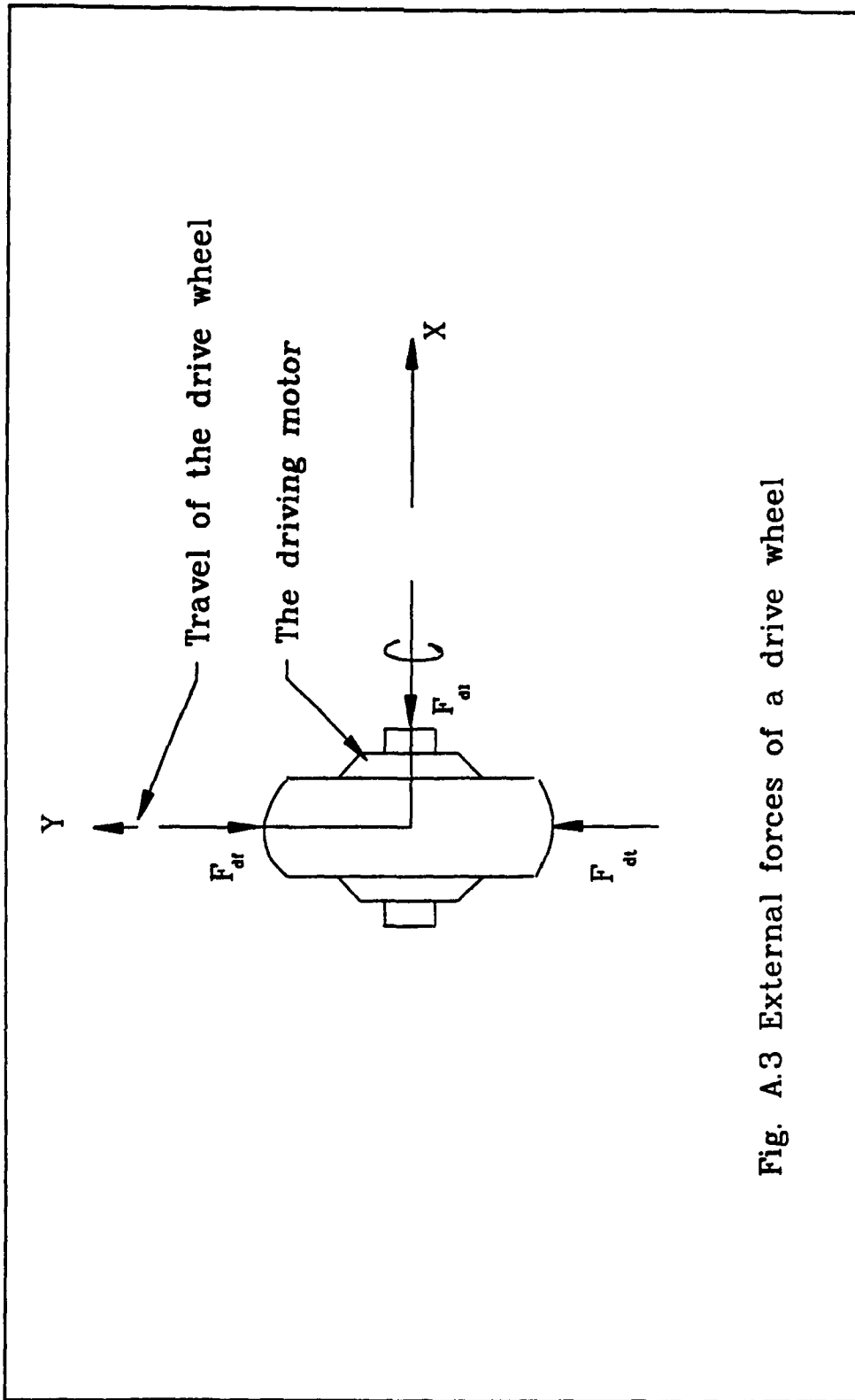


Fig. A.3 External forces of a drive wheel

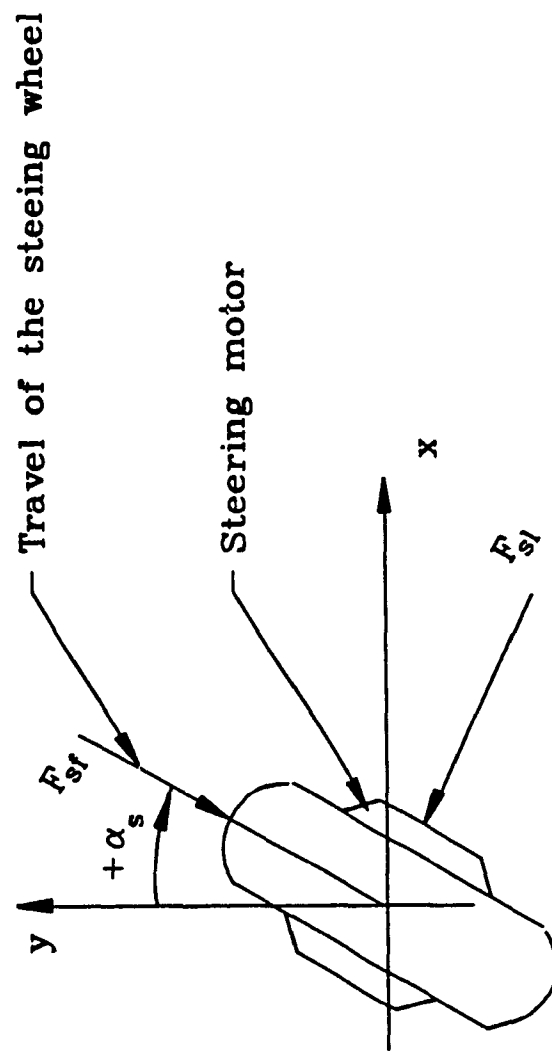


Fig. A.4 External forces of a steering wheel

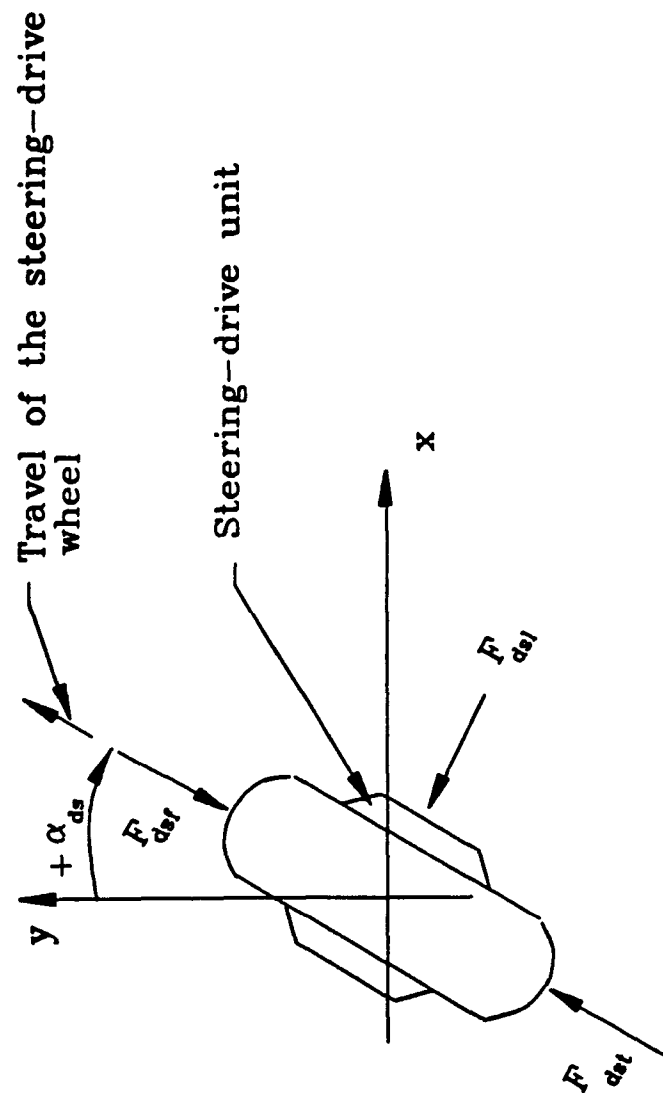


Fig. A.5 External forces of a steering-drive wheel

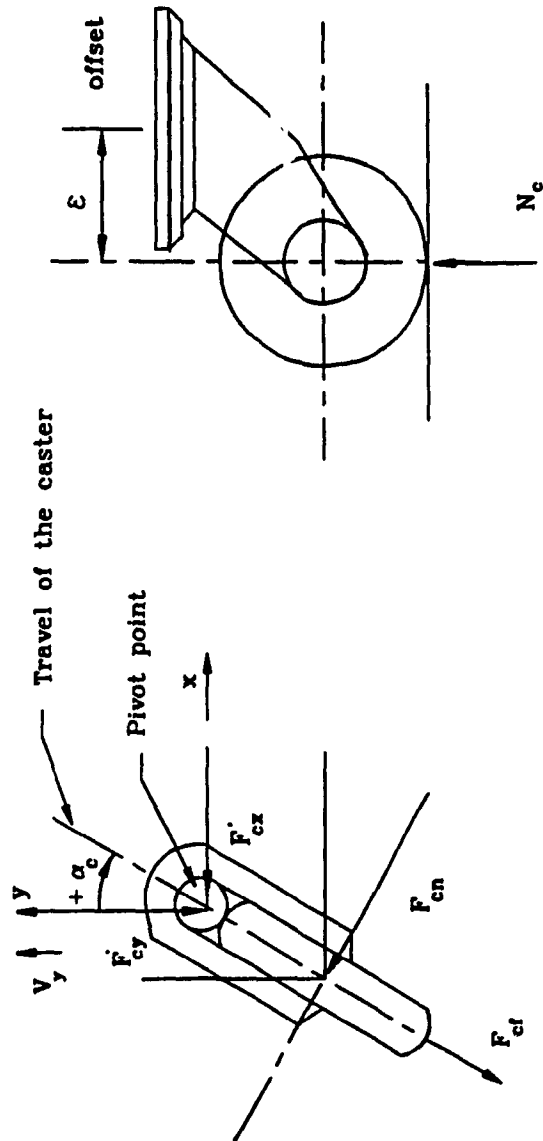


Fig. A.6 External forces of a caster

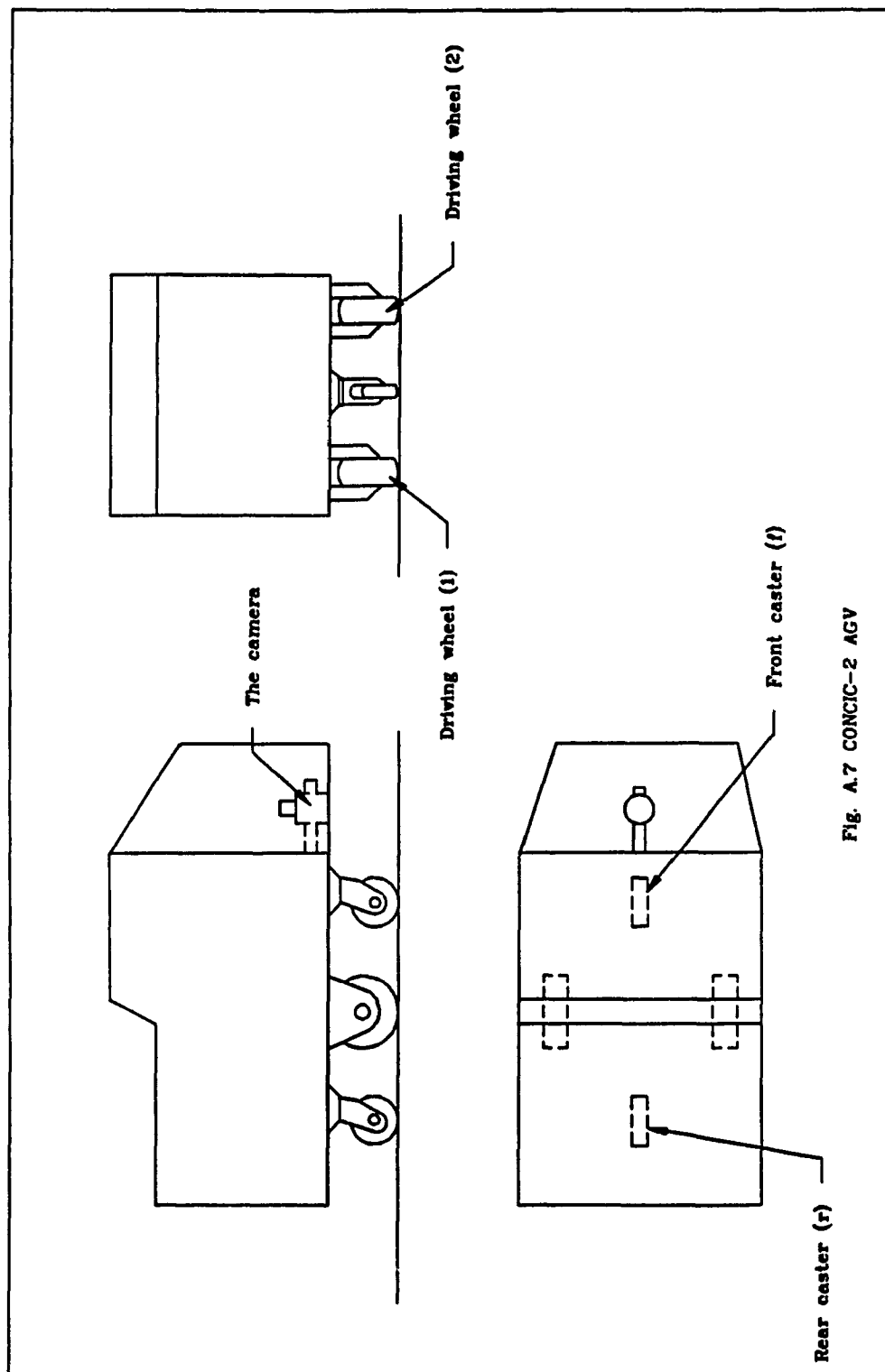
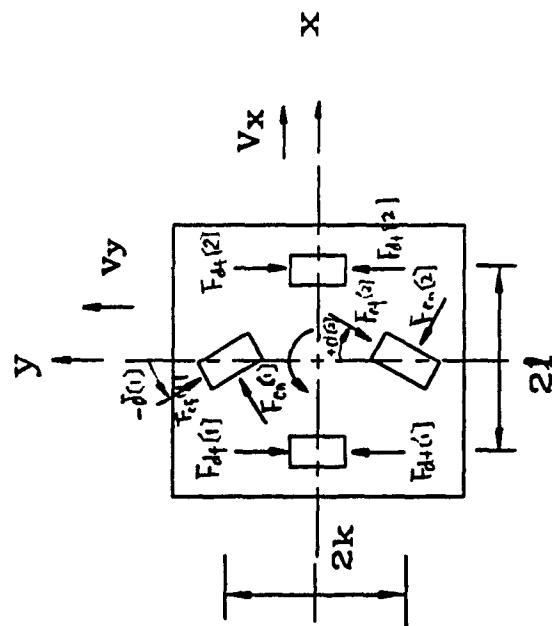
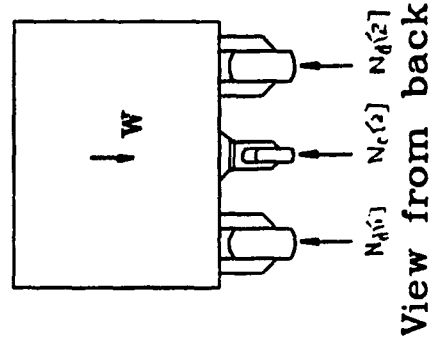


Fig. A.7 CONCIC-2 AGV



View from top



View from back

Fig. A.8 External forces for CONCIC-2 AGV

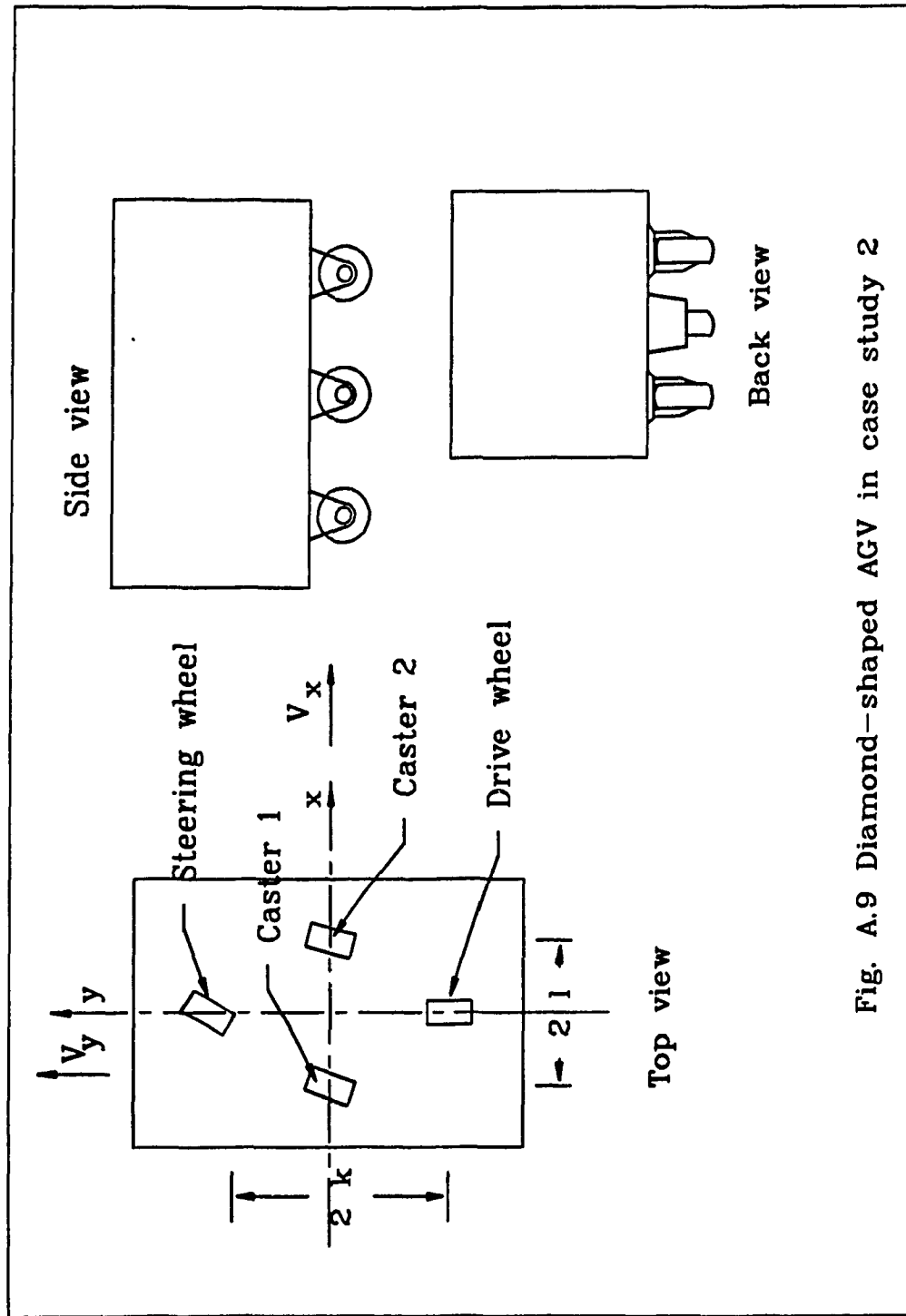


Fig. A.9 Diamond-shaped AGV in case study 2

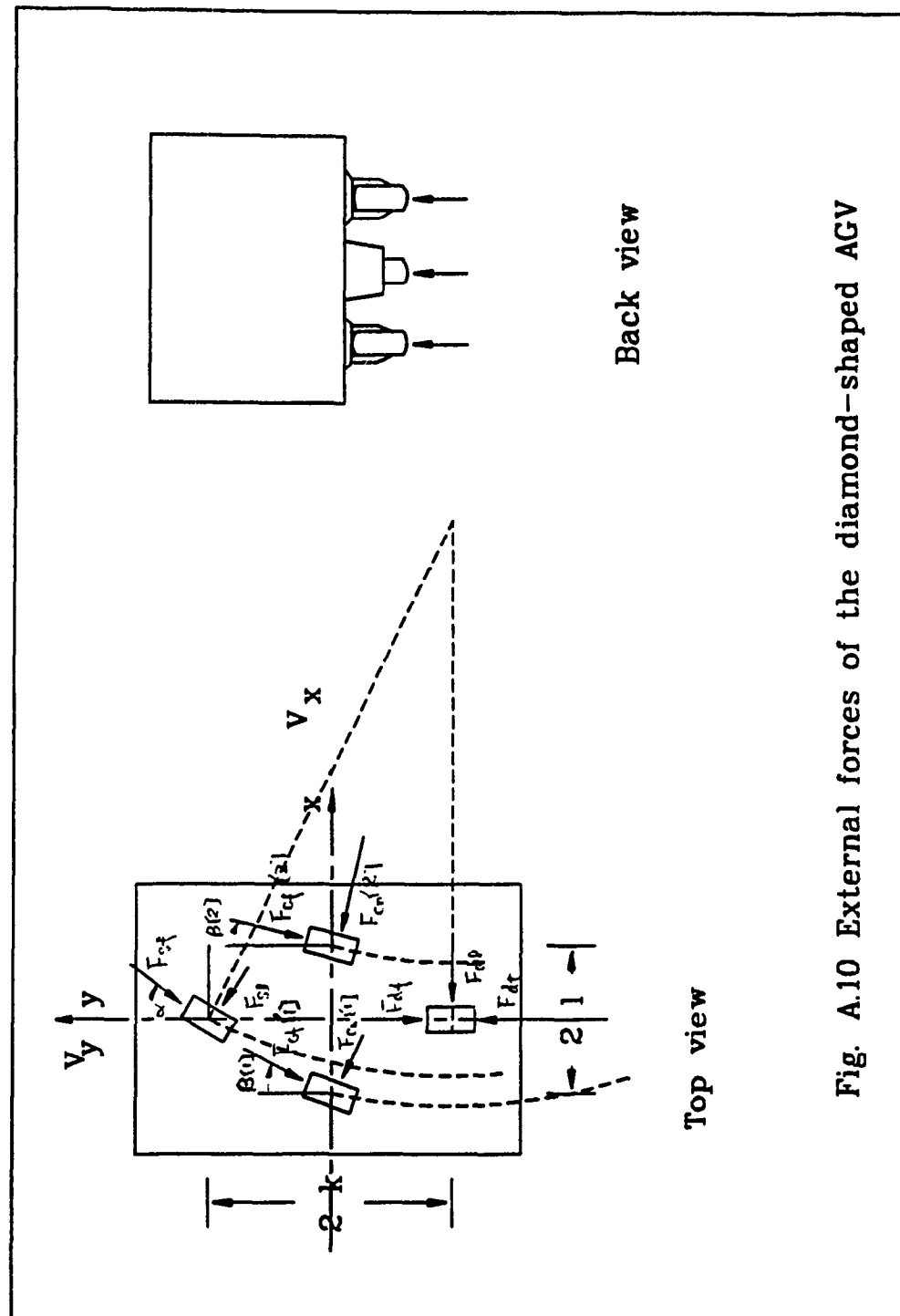


Fig. A.10 External forces of the diamond-shaped AGV

APPENDIX B

Motor-In-Wheel-Drive (Motor-Wheel) Units

Most of the industrial and research AGVs employ non-integral driving arrangement to power the driving and steering wheels. This arrangement, which consists dc servo motors, external chain, belt, or gear train to drive the wheels, requires complex mechanical system, extensive design requirements and more space for mounting.

As the results of these limitation, an integral driving unit is employed in CONCIC-2 AGV. This unit is specially design for AGVs by the Schabmuller Corporation in West Germany and are currently used by most of the AGV manufacturers in Europe. These units are known as Motor-in wheel-drive units (or motor-wheel units). Fig. B.1, Fig. B.2, and Fig. B.3 illustrates one of such unit in CONCIC-2. this unit has a driving motor, a speed reduction gearing arrangement, an hardened rubber wheel, a steering motor with speed reducer, and feedback elements for the driving and steering motors.

B.1 The driving arrangement

The driving motor is a permanent magnet (PM) brush type 24 volts dc motor. Its characteristics is illustrated in Fig.B.4. The maximum speed the motor can attain is 1350 rpm. The gear ratio provides a speed reduction of 1:9.9, and hence the maximum speed the wheel can have is 145 rpm. The wheel diameter is 0.150 m, the width of the tire is 0.025 m and the maximum linear speed come to 1.2 m/s (211 ft/min). The load capacity of the tire is 200 kg. The tire material has a static friction coefficient of 0.02 .

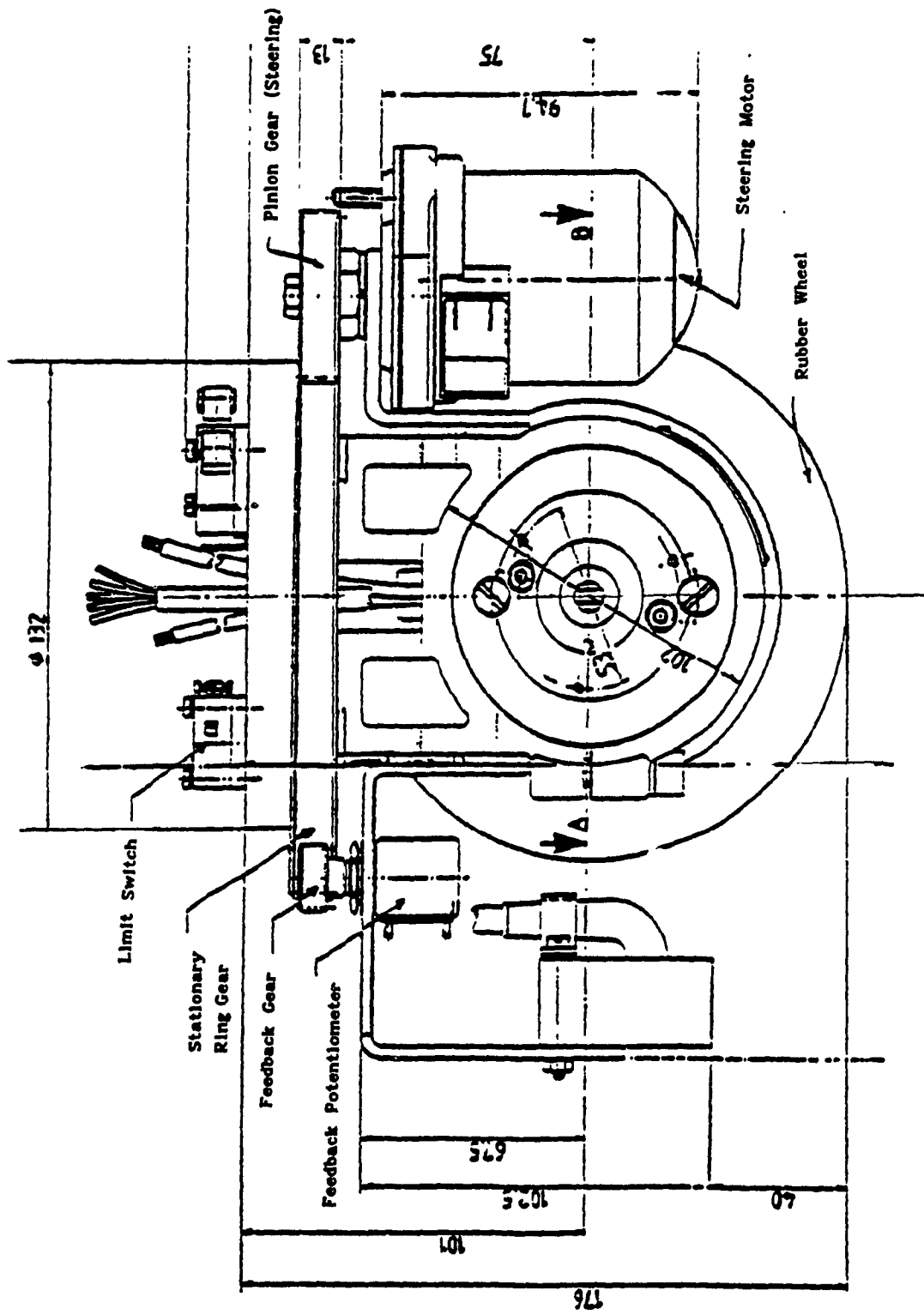


Fig.B.2 Motor-in-Wheel-Drive Unit (Side Elevation)

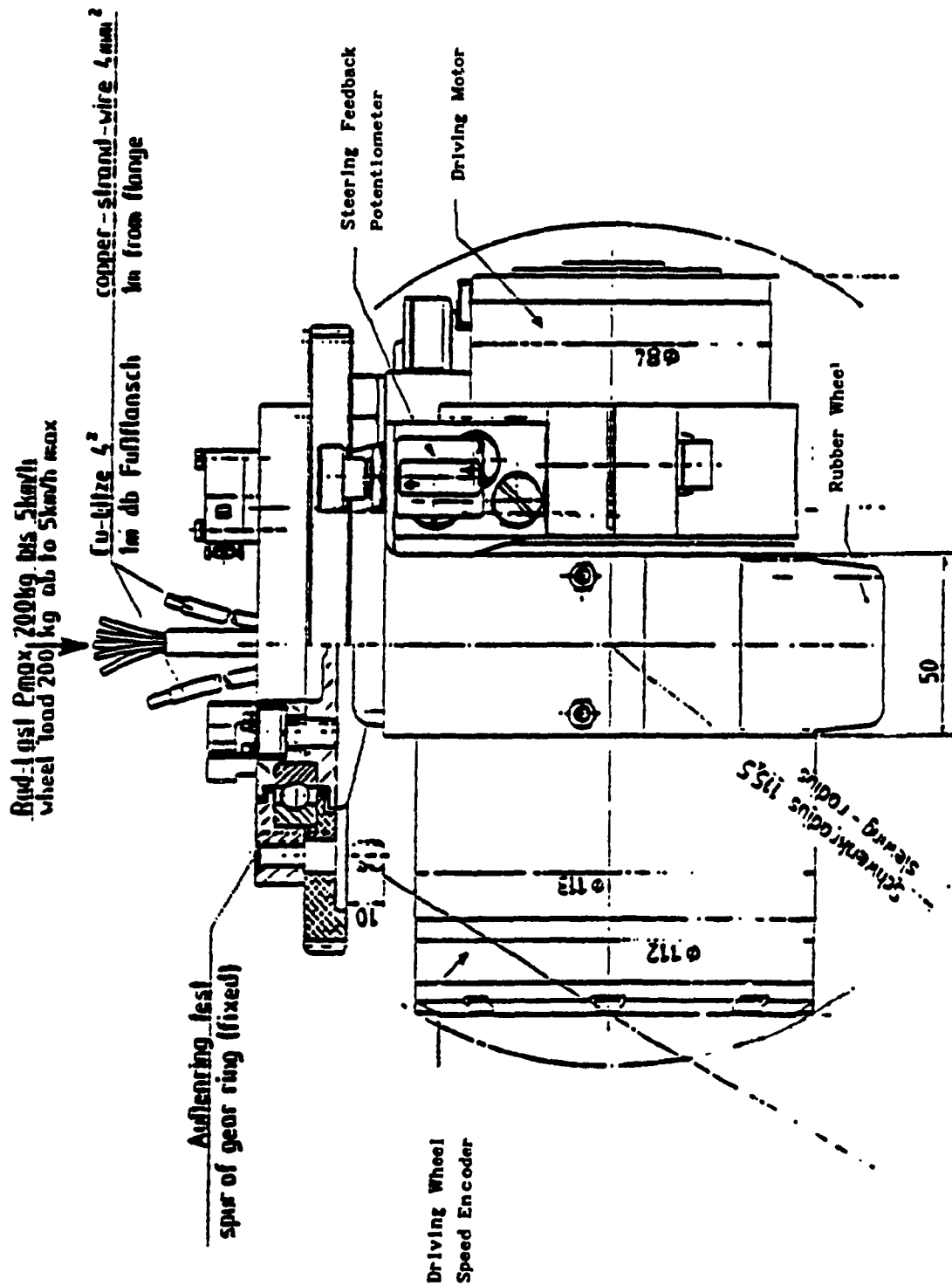


Fig.B.3 Motor-in-Wheel-Drive Unit (Front Elevation)

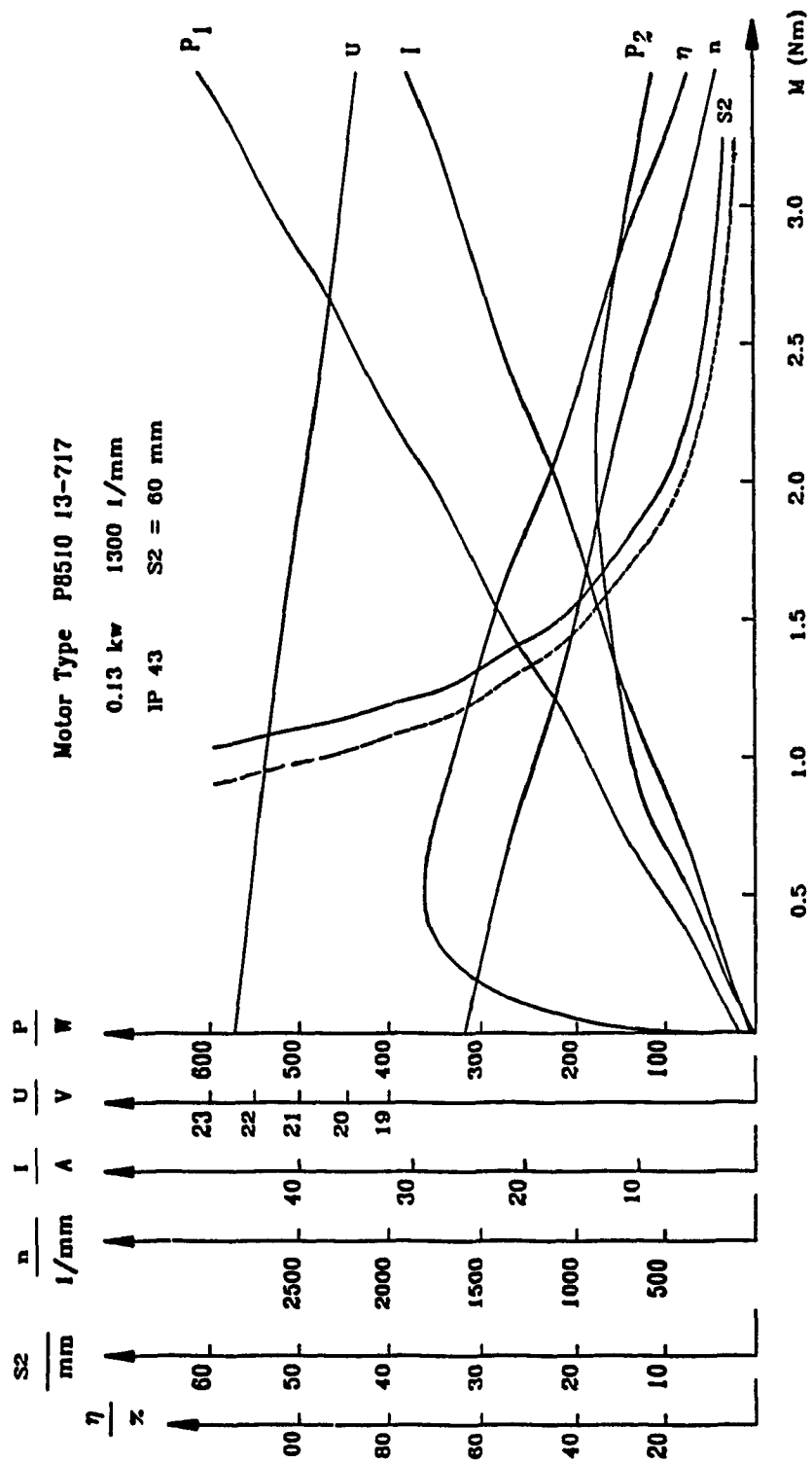


Fig.B.4 The Characteristics of Driving Motor

The drive motor parameters are calculated from the characteristics curves, the torque constant of the motor is computed as below:

$$\text{Torque Constant } k_t = \frac{3-1.35 \text{ Nm}}{26.4-12 \text{ A}} = 0.114 \text{ Nm /A} \quad (\text{B.1})$$

The velocity constant k_e presents the relationship between the velocity and the back EMF voltage is derive from the curves as follows:

$$\text{Ratio between motor torque and voltage} = \frac{22.5-0 \text{ Volt}}{0-3.2 \text{ Nm}} = -7.031 \text{ Volts/Nm}$$

$$\text{Ratio between motor torque and speed} = \frac{1250-500 \text{ rpm}}{1-2.82 \text{ Nm}} = -412.088 \text{ rpm/Nm}$$

then

$$k_e = \frac{7.031 \text{ V/Nm}}{412.088 \text{ rpm/Nm}} = 0.0171 \text{ Volts/rpm} = 0.163 \text{ Volts/(rad/s)} \quad (\text{B.2})$$

The stall torque (T_s), the static friction torque (T_f), and the no load speed (N_f) of the motor can be deduced from the graph as:

$$\text{Stall torque } T_s = 4.05 \text{ Nm} = 4.05 \text{ Kg} \cdot \text{m}^2/\text{sec}^2 \quad (\text{B.3})$$

$$\text{Static Friction torque } T_f = 8.2 \text{ Nm} = 8.2 \text{ Kg} \cdot \text{m}^2/\text{sec}^2 \quad (\text{B.4})$$

$$\text{No load speed } N_f = 1700 \text{ rpm} = 178.03 \text{ rad/sec}$$

From the manufacturer's specifications, the moment of inertia of the rotor J_m is

$$\text{Rotor inertia } J_m = 0.002 \text{ Kg/m}^2$$

The mechanical damping factor (D_m) and the time constant (τ_m) are evaluated from the mechanical parameters from the motor a below.

$$\text{Damping factor } D_m = \frac{T_s}{N_f} = \frac{4.05 \text{ Nm}}{178.03 \text{ rad/s}} = 0.0228 \text{ Kg} \cdot \text{m}^2/\text{s} \quad (\text{B.5})$$

$$\text{Mechanical time constant } \tau_m = \frac{J_m}{D_m} = 0.088 \text{ sec} \quad (\text{B.6})$$

The electrical parameters of the motor are:

Rated Voltage	$V = 22 \text{ Volts}$
Maximum Power Input	$P_{in} = 198 \text{ Watts}$
Maximum Power Output	$P_{out} = 130 \text{ Watts}$
Continuous Current	$I_c = \text{Power Input/Rated Voltage} = 9.0 \text{ A}$
Starting (Peak) Current	$I_p = 45.5 \text{ A}$
Armature Inductance	$L = 4.7 \text{ mH}$
Armature Resistance	$R = 0.602 \Omega$

From the above parameters, the electrical time constant of the motor τ_e is calculated by

$$\text{Electrical time constant } \tau_e = \frac{L}{R} = 0.0078 \text{ sec.} \quad (\text{B.7})$$

B.2 The Steering Arrangement

The overall assembly of the drive unit with a steer motor is illustrated on Fig.B.5. It is seen that an aluminum bracket in the shape of an inverted L houses a bearing for the steering unit. One end of the aluminum bracket is attached to the stator casing of the drive motor. The inner race of the bearing is attached to the bracket. A lock plate is also attached to the inner race to prevent any axial movement of the bearing. The outer race of the bearing is fixed in position by lock ring. The lock ring also locks a large speed reduction gear. The lock ring with the gear forms the stationary components of the steering unit. The lock ring can be attached to a fixed body in the system (Vehicle body). The power for the steering motor is provided by a permanent magnet dc motor with a rating of 42 watts. The power delivered by the motor is 13 watts. The steer motor is a

self-contained unit with a speed reduction gearing unit. This motor is fixed to the body of the aluminum L-bracket mentioned above. The speed reducer shaft of the steer motor carries a plastic gear which engages with a stationary large gear. Hence whenever the steer motor rotates, this pinion also rotates as the large gear is stationary, the wheel body along with the steer and drive motor turns (to left and right). The gear ratio of the system is 62.7:1.

The characteristics curves and other specification of the steer motor are provided in Fig. B.6 and Table B.1.

From these curves, the torque constant of the motor can be computed as

$$\text{Torque Constant } k_t = \frac{8 - 12 \text{ Nm}}{3 - 1 \text{ A}} = 3 \text{ Nm/A} \quad (\text{B.8})$$

the relationship between the torque and the speed is given by

$$\frac{15-47.5 \text{ rpm}}{13-2 \text{ Nm}} = -2.955 \text{ rpm/Nm} \quad (\text{B.9})$$

The stall torque T_s , and the no-load speed N_f of the motor can be deduced from the graph as:

$$\text{Stall torque } T_s = 18.0 \text{ Nm} = 18.0 \text{ Kg} \cdot \text{m}^2/\text{s}^2$$

$$\text{No-load speed } N_f = 45 \text{ rpm}$$

The electrical parameters of the steer motor are:

Rated Voltage	$V = 24 \text{ Volts}$
Maximum Power Input	$P_{in} = 42 \text{ Watts}$
Maximum Power Output	$P_{out} = 13 \text{ Watts}$
Continuous Current	$I_c = 1.75 \text{ A}$
Armature Inductance	$L = 4.135 \text{ mH}$
Armature Resistance	$R = 10.9 \Omega$

The electrical time constant τ_e is computed by

$$\text{Electrical time constant } \tau_e = \frac{L}{R} = 0.376 \text{ sec.}$$

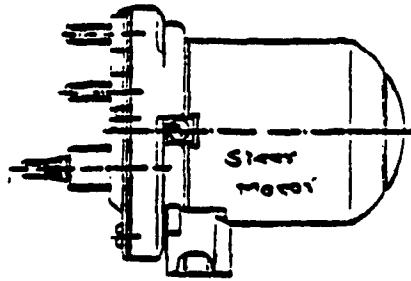


Fig.B.5 The steering Unit

Type	V	I _a	M _a	I _f		I _a	I _f		Winding	Schematic	Armature	
72734	12	2	10	45	10.4	42	13		W12	S9	K23	360°
403 040	12	2	10	45	10.4	42	13		W12	S11	K23	360°
402 828	24	2.5	10	45	12.7	42	13		W12	S3	K23	Continuous
402 901	24	2.5	10	45	12.7	42	13		W25	S3	K23	
402 916	24	2.5	10	45	12.7	42	13		W28	S3	K23	
402 981	24	2.5	10	45	10.4	42	13		W12	S10	K23	360°
403 042	24	2.5	10	45	10.4	42	13		W12	S11	K23	360°

Table B.1 Steering Motor Parameters

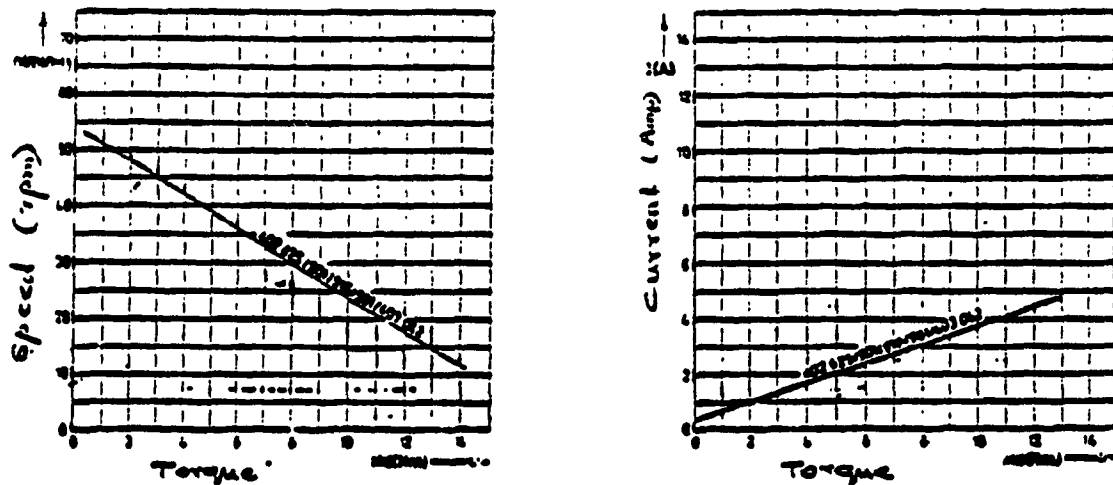


Fig.B.6 Steering Motor Characteristics

APPENDIX C

LM628/LM629 Precision Motion Controller

LM628 motion controllers in the servo loops of the CONCIC-2 AGV are used to provide the servo control functions. More detailed information is given in the following paragraphs about the characteristics, the theory of operation, and the user command sets of LM628/LM629.

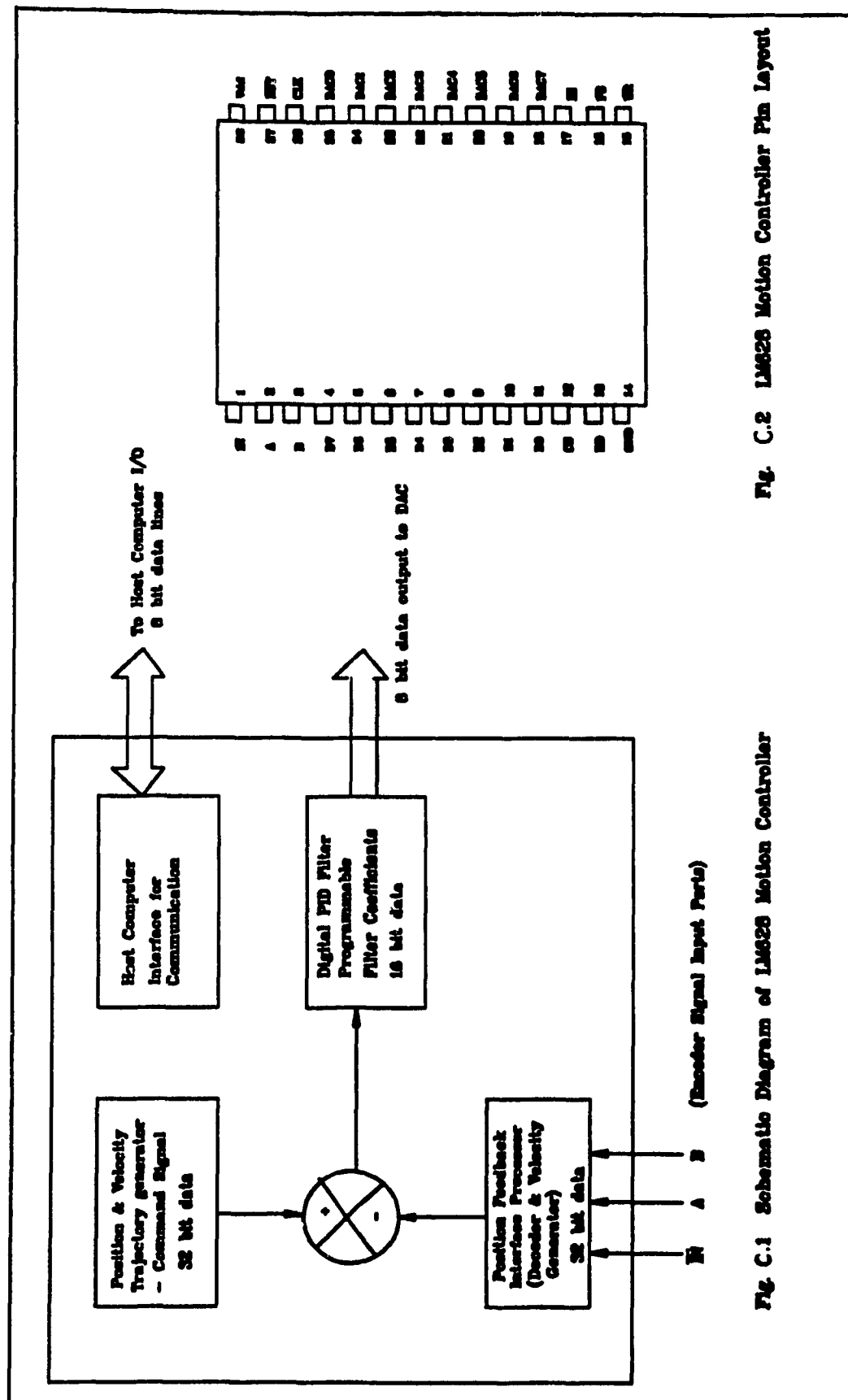
GENERAL DESCRIPTION

The LM628/LM629 are dedicated motion-control processors designed for use with a variety of DC and brushless DC servo motors, and other servo mechanisms which provide a quadrature incremental position feedback signal. The parts perform the intensive, real-time computation tasks required for high performance digital motion control. The host control software interface is facilitated by a high-level command set. The LM628 has an 8-bit output which can drive either an 8-bit or a 12-bit DAC. The components required to build a servo system are reduced to the DC motor/actuator, an incremental encoder, a DAC, an amplifier, and the LM628. An LM629-based system is similar, except that it provides an 8-bit PWM output for directly driving H-switches. The parts are fabricated in NMOS and packaged in a 28-pin dual in-line package. They incorporate an SDA core processor and cells designed by SDA.

FEATURES

- 32-bit position, velocity, and acceleration registers
- 750 kHz encoder-state capture rate

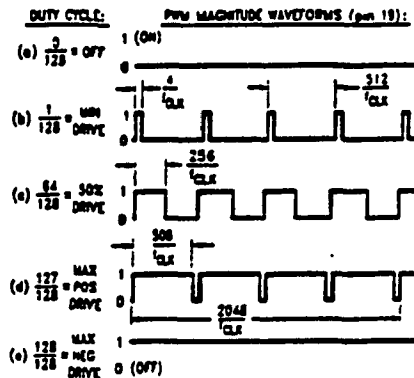
- 341 μ s sampling interval
- Programmable digital PID filter with 16-bit coefficients
- 8- or 12-bit DAC output data (LM628)
- 8-bit sign-magnitude PWM output data (LM629)
- Internal trapezoidal velocity profile generator
- Velocity, target position, and filter parameters may be changed during motion
- Position and velocity modes of operation
- Real-time programmable host interrupts
- 8-bit parallel asynchronous host interface
- Quadrature incremental encoder interface with index pulse input
- Programmable derivative sampling interval (341 μ s to 87,381 μ s, or $341.33 \times 256 \mu$ s)
- Operates at 6 MHz clock frequency



Theory of Operation (Continued)

The LM629 provides 8-bit, sign and magnitude PWM output signals for directly driving switch-mode motor-drive amplifiers.

Figure 11 shows the format of the PWM magnitude output signal.



TLV6219-13

Note: Sign output (pin 18) not shown

FIGURE 11. PWM Output Signal Format

User Command Set

GENERAL

The following paragraphs describe the user command set of the LM628. Some of the commands can be issued alone and some require a supporting data structure. As examples, the command STT (STArT motion) does not require additional data; command LFIL (Load FILter parameters) re-

quires additional data (derivative-term sampling interval and/or filter parameters).

Commands are categorized by function: initialization, interrupt control, filter control, trajectory control, and data reporting. The commands are listed in Table II and described in

TABLE II. LM628 User Command Set

Command	Type	Description	Hex	Data Bytes	Note
RESET	Initialize	Reset LM628	00	0	1
PORT8	Initialize	Select 8-Bit Output	05	0	2
PORT12	Initialize	Select 12-Bit Output	06	0	2
DFH	Initialize	Define Home	02	0	1
SIP	Interrupt	Set Index Position	03	0	1
LPEI	Interrupt	Interrupt on Error	1B	2	1
LPES	Interrupt	Stop on Error	1A	2	1
SBPA	Interrupt	Set Breakpoint, Absolute	20	4	1
SBPR	Interrupt	Set Breakpoint, Relative	21	4	1
MSKI	Interrupt	Mask Interrupts	1C	2	1
RSTI	Interrupt	Reset Interrupts	1D	2	1
LFIL	Filter	Load Filter Parameters	1E	2 to 10	1
UDF	Filter	Update Filter	04	0	1
LTRJ	Trajectory	Load Trajectory	1F	2 to 14	1
STT	Trajectory	Start Motion	01	0	3
RDSTAT	Report	Read Status Byte	None	1	1, 4
RDSIGS	Report	Read Signals Register	0C	2	1
RDIP	Report	Read Index Position	09	4	1
RDDP	Report	Read Desired Position	08	4	1
RDRP	Report	Read Real Position	0A	4	1
RDDV	Report	Read Desired Velocity	07	4	1
RDRV	Report	Read Rel Velocity	0B	2	1
RDSUM	Report	Read Integration Sum	0D	2	1

Note 1: Commands may be executed "On the Fly" during motion.

Note 2: Commands not applicable to execution during motion.

Note 3: Command may be executed during motion if acceleration parameter was not changed.

Note 4: Command needs no code because the command port status-byte read is totally supported by hardware.

the following paragraphs. Along with each command name is its command-byte code, the number of accompanying data bytes that are to be written (or read), and a comment as to whether the command is executable during motion.

Initialization Commands

The following four LM628 user commands are used primarily to initialize the system for use.

RESET COMMAND: RESET the LM628

Command Code: 00 Hex
Data Bytes: None
Executable During Motion: Yes

This command (and the hardware reset input, Pin 27) results in setting the following data items to zero: filter coefficients and their input buffers, trajectory parameters and their input buffers, and the motor control output. A zero motor control output is a half-scale, offset-binary code: 80 hex for the 8-bit output mode; 800 hex for 12-bit mode). During reset, the DAC port outputs 800 hex to "zero" a 12-bit DAC and reverts to 80 hex to "zero" an 8-bit DAC. The command also clears five of the six interrupt masks (only the SBPA/SBPR interrupt is masked), sets the output port size to 8 bits, and defines the current absolute position as home. Reset, which may be executed at any time, will be completed in less than 1.5 ms. Also see commands PORT8 and PORT12.

PORT8 COMMAND: Set Output PORT Size to 8 Bits

Command Code: 05 Hex
Data Bytes: None
Executable During Motion: Not Applicable

The default output port size of the LM628 is 8 bits; so the PORT8 command need not be executed when using an 8-bit DAC. This command must not be executed when using a 12-bit converter; it will result in erratic, unpredictable motor behavior. The 8-bit output port size is the required selection when using the LM629, the PWM-output version of the LM628.

PORT12 COMMAND: Set Output PORT Size to 12 Bits

Command Code: 06 Hex
Data Bytes: None
Executable During Motion: Not Applicable

When a 12-bit DAC is used, command PORT12 should be issued very early in the initialization process. Because use of this command is determined by system hardware, there is only one foreseen reason to execute it later: if the RESET command is issued (because an 8-bit output would then be selected as the default) command PORT12 should be immediately executed. This command must not be issued when using an 8-bit converter or the LM629, the PWM-output version of the LM628.

DFH COMMAND: DeFINE Home

Command Code: 02 Hex
Data Bytes: None
Executable During Motion: Yes

This command declares the current position as "home", or absolute position 0 (Zero). If DFH is executed during motion it will not affect the stopping position of the on-going move unless command STT is also executed.

Interrupt Control Commands

The following seven LM628 user commands are associated with conditions which can be used to interrupt the host computer. In order for any of the potential interrupt conditions to

actually interrupt the host via Pin 17, the corresponding bit in the interrupt mask data associated with command MSKI must have been set to logic high (the non-masked state).

The identity of all interrupts is made known to the host via reading and parsing the status byte. Even if all interrupts are masked off via command MSKI, the state of each condition is still reflected in the status byte. This feature facilitates polling the LM628 for status information, as opposed to interrupt driven operation.

SIP COMMAND: Set Index Position

Command Code: 03 Hex
Data Bytes: None
Executable During Motion: Yes

After this command is executed, the absolute position which corresponds to the occurrence of the next index pulse input will be recorded in the index register, and bit 3 of the status byte will be set to logic high. The position is recorded when both encoder-phase inputs and the index pulse input are logic low. This register can then be read by the user (see description for command RDIP) to facilitate aligning the definition of home position (see description of command DFH) with an index pulse. The user can also arrange to have the LM628 interrupt the host to signify that an index pulse has occurred. See the descriptions for commands MSKI and RSTI.

LPEI COMMAND: Load Position Error for Interrupt

Command Code: 1B Hex
Data Bytes: Two
Data Range: 0000 to 7FFF Hex
Executable During Motion: Yes

An excessive position error (the output of the loop summing junction) can indicate a serious system problem; e.g., a stalled rotor. Instruction LPEI allows the user to input a threshold for position error detection. Error detection occurs when the absolute magnitude of the position error exceeds the threshold, which results in bit 5 of the status byte being set to logic high. If it is desired to also stop (turn off) the motor upon detecting excessive position error, see command LPES, below. The first byte of threshold data written with command LPEI is the more significant. The user can have the LM628 interrupt the host to signify that an excessive position error has occurred. See the descriptions for commands MSKI and RSTI.

LPES COMMAND: Load Position Error for Stopping

Command Code: 1A Hex
Data Bytes: Two
Data Range: 0000 to 7FFF Hex
Executable During Motion: Yes

Instruction LPES is essentially the same as command LPEI above, but adds the feature of turning off the motor upon detecting excessive position error. The motor drive is not actually switched off, it is set to half-scale, the offset-binary code for zero. As with command LPEI, bit 5 of the status byte is also set to logic high. The first byte of threshold data written with command LPES is the more significant. The user can have the LM628 interrupt the host to signify that an excessive position error has occurred. See the descriptions for commands MSKI and RSTI.

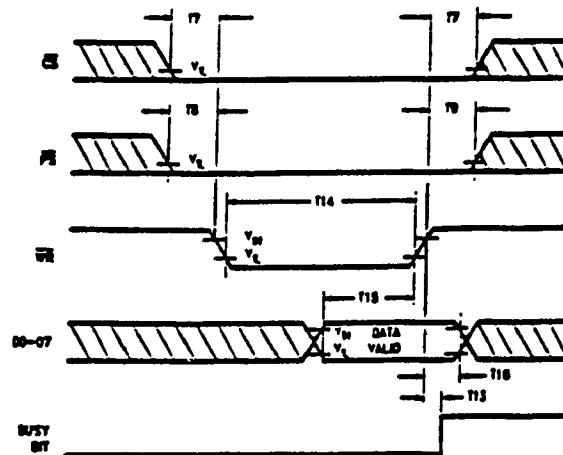


FIGURE 5. Command Byte Write Timing

TL/M/9218-7

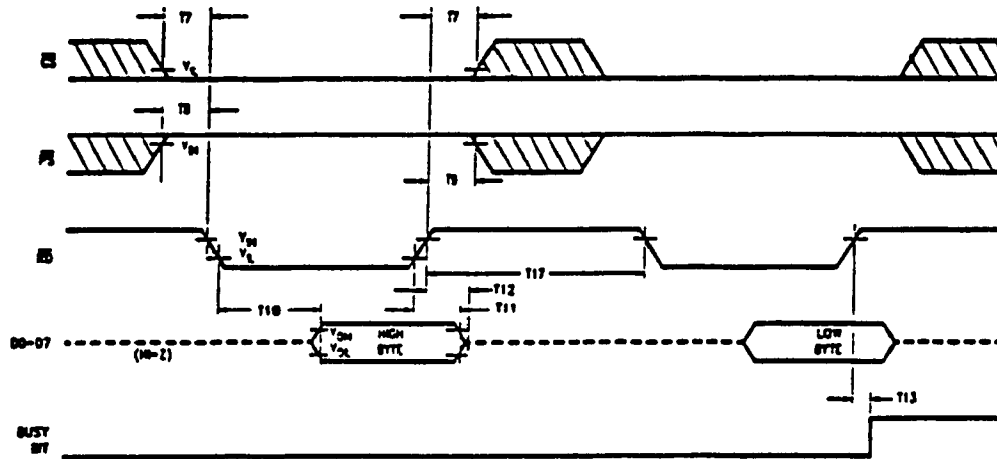


FIGURE 6. Data Word Read Timing

TL/M/9218-8

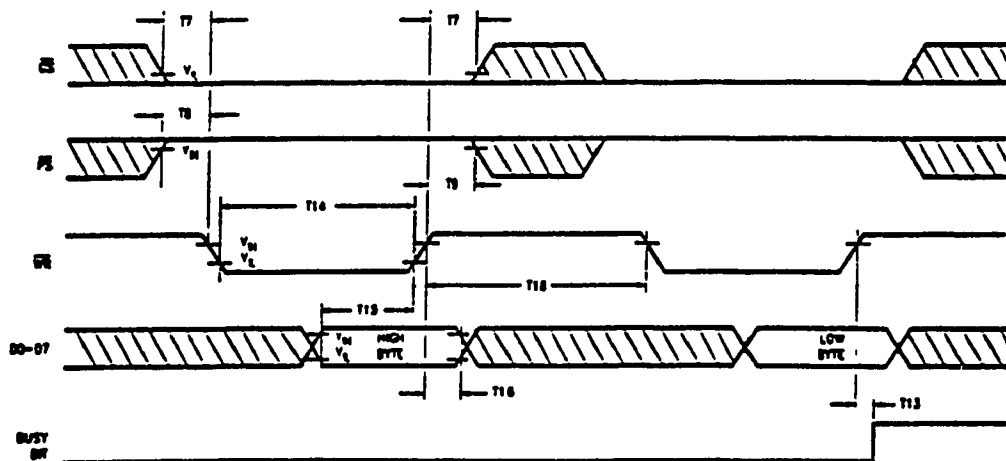


FIGURE 7. Data Word Write Timing

TL/M/9218-9

Pinout Description (See Connection Diagrams)

Pin 1, Index (IN) Input: Receives optional index pulse from the encoder. Must be used high if not used. The index position is read when Pins 1, 2, and 3 are low.

Pins 2 and 3, Encoder Signal (A, B) Inputs: Receive the two-phase quadrature signals provided by the incremental encoder. When the motor is rotating in the positive ("forward") direction, the signal at Pin 2 leads the signal at Pin 3 by 90 degrees. Note that the signals at Pins 2 and 3 must remain at each encoder state (See Figure 9) for a minimum of 8 clock periods in order to be recognized. Because of a four-to-one resolution advantage gained by the method of decoding the quadrature encoder signals, this corresponds to a maximum encoder-state capture rate of 1.0 MHz. For other clock frequencies the encoder signals must also remain at each state a minimum of 8 clock periods.

Pins 4 to 11, Host I/O Port (D0 to D7): Bi-directional data port which connects to host computer/processor. Used for writing commands and data to the LM628, and for reading the status byte and data from the LM628, as controlled by CS (Pin 12), PS (Pin 16), RD (Pin 13), and WR (Pin 15).

Pin 12, Chip Select (CS) Input: Used to select the LM628 for writing and reading operations.

Pin 13, Read (RD) Input: Used to read status and data.

Pin 14, Ground (GND): Power-supply return pin.

Pin 15, Write (WR) Input: Used to write commands and data.

Pin 16, Port Select (PS) Input: Used to select command or data port. Selects command port when low, data port when high. The following modes are controlled by Pin 16:

1. Commands are written to the command port (Pin 16 low),
2. Status byte is read from command port (Pin 16 low), and
3. Data is written and read via the data port (Pin 16 high).

Pin 17, Host Interrupt (HI) Output: This active-high signal alerts the host (via a host interrupt service routine) that an interrupt condition has occurred.

Pins 18 to 25, DAC Port (DAC0 to DAC7): Output port which is used in three different modes:

1. LM628 (8-bit output mode): Outputs latched data to the DAC. The MSB is Pin 18 and the LSB is Pin 25.

2. LM628 (12-bit output mode): Outputs two, multiplexed 6-bit words. The less-significant word is output first. The MSB is on Pin 18 and the LSB is on Pin 23. Pin 24 is used to demultiplex the words: Pin 24 is low for the less-significant word. The positive-going edge of the signal on Pin 25 is used to strobe the output data. Figure 8 shows the timing of the multiplexed signals.

3. LM629 (sign/magnitude outputs): Outputs a PWM sign signal on Pin 18, and a PWM magnitude signal on Pin 19. Pins 20 to 25 are not used in the LM629. Figure 11 shows the PWM output signal format. Connect pin 25 to ground.

Pin 26, Clock (CLK) Input: Receives 6 MHz system clock.

Pin 27, Reset (RST) Input: Active-low, positive-edge triggered, resets the LM628 to the internal conditions shown below. Note that the reset pulse must be logic low for a minimum of 8 clock periods. Reset does the following:

1. Filter coefficient and trajectory parameters are zeroed.
2. Sets position error threshold to maximum value (7FFF hex), and effectively executes command LPEI.
3. The SBPA/SBPR interrupt is masked (disabled).
4. The five other interrupts are unmasked (enabled).
5. Initializes current position to zero, or "home" position.
6. Sets derivative sampling interval to $2048/f_{CLK}$ or 341 μs for a 6.0 MHz clock.
7. DAC port outputs 800 hex to "zero" a 12-bit DAC and then reverts to 80 hex to "zero" an 8-bit DAC.

Immediately after releasing the reset pin from the LM628, the status port should read '00'. If the reset is successfully completed, the status word will change to hex '84' or 'C4' within 1 ms. If the status word has not changed from hex '00' to '84' or 'C4' within 1 ms, perform another reset and repeat the above steps. To be certain that the reset was properly performed, execute a RSTi command. If the chip has reset properly, the status byte will change from hex '84' or 'C4' to hex '80'. If this does not occur, perform another reset and repeat the above steps.

Pin 28, Supply Voltage (VDD): Power supply voltage (+5V).

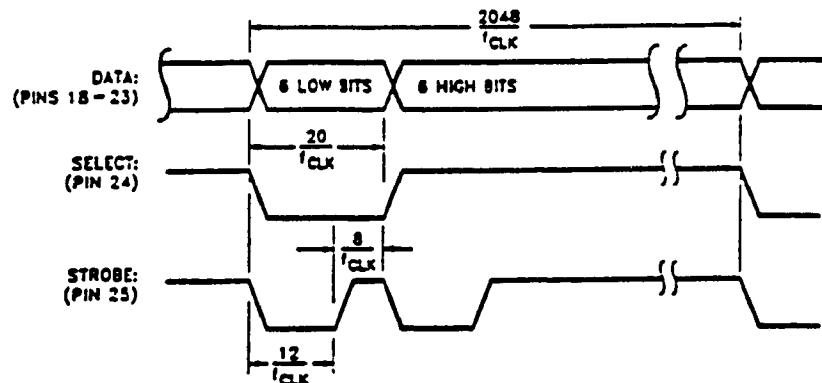


FIGURE 8. 12-Bit Multiplexed Output Timing

TLW6218-10

Theory of Operation (Continued)

```

let P = target position (units = encoder counts)
let R = encoder lines * 4 (system resolution)
then R = 500 * 4 = 2000
and P = 2000 * desired number of revolutions
P = 2000 * 100 revs = 200,000 counts (value to load)
P (coding) = 00030D40 (hex code written to LM628)

let V = velocity (units = counts/sample)
let T = sample time (seconds) = 341 μs (with 6 MHz clock)

let C = conversion factor = 1 minute/60 seconds
then V = R * T * C * desired rpm
and V = 2000 * 341E-6 * 1/60 * 600 rpm
V = 6.82 counts/sample
V (scaled) = 6.82 * 65,536 = 446,955.52
V (rounded) = 446,956 (value to load)
V (coding) = 0006D1EC (hex code written to LM628)

let A = acceleration (units = counts/sample/sample)
A = R * T * T * desired acceleration (rev/sec/sec)
then A = 2000 * 341E-6 * 341E-6 * 1 rev/sec/sec
and A = 2.33E-4 counts/sample/sample
A (scaled) = 2.33E-4 * 65,536 = 15.24
A (rounded) = 15 (value to load)
A (coding) = 0000000F (hex code written to LM628)

```

The above position, velocity, and acceleration values must be converted to binary codes to be loaded into the LM628. The values shown for velocity and acceleration must be multiplied by 65,536 (as shown) to adjust for the required integer/fraction format of the input data. Note that after scaling the velocity and acceleration values, literal fractional data cannot be loaded; the data must be rounded and converted to binary. The factor of four increase in system resolution is due to the method used to decode the quadrature encoder signals; see Figure 9.

PID COMPENSATION FILTER

The LM628 uses a digital Proportional Integral Derivative (PID) filter to compensate the control loop. The motor is held at the desired position by applying a restoring force to the motor that is proportional to the position error, plus the integral of the error, plus the derivative of the error. The following discrete-time equation illustrates the control performed by the LM628:

$$u(n) = kp \cdot e(n) - k_i \sum_{N=0}^n e(n) -$$

$$kd[e(n') - e(n' - 1)] \quad (\text{Eq. 1})$$

where $u(n)$ is the motor control signal output at sample time n , $e(n)$ is the position error at sample time n , n' indicates sampling at the derivative sampling rate, and kp , k_i , and k_d are the discrete-time filter parameters loaded by the users.

The first term, the proportional term, provides a restoring force proportional to the position error, just as does a spring obeying Hooke's law. The second term, the integration term, provides a restoring force that grows with time, and thus ensures that the static position error is zero. If there is

a constant torque loading, the motor will still be able to achieve zero position error.

The third term, the derivative term, provides a force proportional to the rate of change of position error. It acts just like viscous damping in a damped spring and mass system (like a shock absorber in an automobile). The sampling interval associated with the derivative term is user-selectable; this capability enables the LM628 to control a wider range of inertial loads (system mechanical time constants) by providing a better approximation of the continuous derivative. In general, longer sampling intervals are useful for low-velocity operations.

LM628 READING AND WRITING OPERATIONS

The host processor writes commands to the LM628 via the host I/O port when Port Select (PS) input (Pin 16) is logic low. The desired command code is applied to the parallel port line and the Write (WR) input (Pin 15) is strobed. The command byte is latched into the LM628 on the rising edge of the WR input. When writing command bytes it is necessary to first read the status byte and check the state of a flag called the "busy bit" (Bit 0). If the busy bit is logic high, no command write may take place. The busy bit is never high longer than 100 μs, and typically falls within 15 μs to 25 μs.

The host processor reads the LM628 status byte in a similar manner: by strobing the Read (RD) input (Pin 13) when PS (Pin 16) is low; status information remains valid as long as RD is low.

Writing and reading data to/from the LM628 (as opposed to writing commands and reading status) are done with PS (Pin 16) logic high. These writes and reads are always an integral number (from one to seven) of two-byte words, with the first byte of each word being the more significant. Each byte requires a write (WR) or read (RD) strobe. When transferring data words (byte-pairs), it is necessary to first read the status byte and check the state of the busy bit. When the busy bit is logic low, the user may then sequentially transfer both bytes comprising a data word, but the busy bit must again be checked and found to be low before attempting to transfer the next byte pair (when transferring multiple words). Data transfers are accomplished via LM628-internal interrupts (which are not nested); the busy bit informs the host processor when the LM628 may not be interrupted for data transfer (or a command byte). If a command is written when the busy bit is high, the command will be ignored.

The busy bit goes high immediately after writing a command byte, or reading or writing a second byte of data (See Figures 5 thru 7).

MOTOR OUTPUTS

The LM628 DAC output port can be configured to provide either a latched eight-bit parallel output or a multiplexed 12-bit output. The 8-bit output can be directly connected to a flow-through (non-input-latching) D/A converter; the 12-bit output can be easily demultiplexed using an external 6-bit latch and an input-latching 12-bit D/A converter. The DAC output data is offset-binary coded; the 8-bit code for zero is 80 hex and the 12-bit code for zero is 800 hex. Values less than these cause a negative torque to be applied to the motor and, conversely, larger values cause positive motor torque. The LM628, when configured for 12-bit output, provides signals which control the demultiplexing process. See Figure 8 for details.

Theory of Operation

INTRODUCTION

The typical system block diagram (See Figure 1) illustrates a servo system built using the LM628. The host processor communicates with the LM628 through an I/O port to facilitate programming a trapezoidal velocity profile and a digital compensation filter. The DAC output interfaces to an external digital-to-analog converter to produce the signal that is power amplified and applied to the motor. An incremental encoder provides feedback for closing the position servo loop. The trapezoidal velocity profile generator calculates the required trajectory for either position or velocity mode of operation. In operation, the LM628 subtracts the actual position (feedback position) from the desired position (profile generator position), and the resulting position error is processed by the digital filter to drive the motor to the desired position. Table I provides a brief summary of specifications offered by the LM628/LM629:

POSITION FEEDBACK INTERFACE

The LM628 interfaces to a motor via an incremental encoder. Three inputs are provided: two quadrature signal inputs, and an index pulse input. The quadrature signals are used to keep track of the absolute position of the motor. Each

time a logic transition occurs at one of the quadrature inputs, the LM628 internal position register is incremented or decremented accordingly. This provides four times the resolution over the number of lines provided by the encoder. See Figure 8. Each of the encoder signal inputs is synchronized with the LM628 clock.

The optional index pulse output provided by some encoders assumes the logic-low state once per revolution. If the LM628 is so programmed by the user, it will record the absolute motor position in a dedicated register (the index register) at the time when all three encoder inputs are logic low.

If the encoder does not provide an index output, the LM628 index input can also be used to record the home position of the motor. In this case, typically, the motor will close a switch which is arranged to cause a logic-low level at the index input, and the LM628 will record motor position in the index register and alert (interrupt) the host processor. When using the index input in this manner, the user should assure that the index input does not remain logic low during shaft rotation because LM628 internal interrupts are generated every time all three encoder inputs are logic low. These internal interrupts will cause the LM628 to malfunction if the velocity is faster than about 15,000 counts/second (when using a 6 MHz clock).

TABLE I. System Specifications Summary

Position Range	- 1,073,741,824 to 1,073,741,823 counts
Velocity Range	0 to 1,073,741,823/2 ¹⁶ counts/sample; i.e. 0 to 16,383 counts/sample, with a resolution of 1/2 ¹⁶ counts/sample
Acceleration Range	0 to 1,073,741,823/2 ¹⁶ counts/sample/sample; i.e. 0 to 16,383 counts/sample/sample, with a resolution of 1/2 ¹⁶ counts/sample/sample
Motor Drive Output	LM628: 8-bit multiplexed output to DAC, or 12-bit multiplexed output to DAC LM629: 8-bit PWM sign/magnitude signals
Operating Modes	Position and Velocity
Feedback Device	Incremental Encoder (quadrature signals; support for index pulse)
Control Algorithm	Proportional Integral Derivative (PID) (plus programmable integration limit)
Sample Intervals	Derivative Term: Programmable from 2048/f _{CLK} to (2048 * 256)/f _{CLK} in steps of 2048/f _{CLK} (341 to 87,381 μs for a 6.0 MHz clock). Proportional and Integral: 2048/f _{CLK}

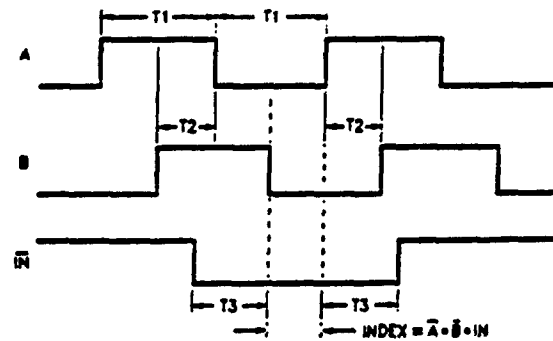


FIGURE 2. Quadrature Encoder Input Timing

TL/M/9218-4

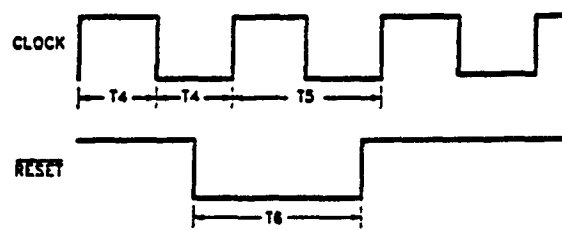


FIGURE 3. Clock and Reset Timing

TL/M/9218-5

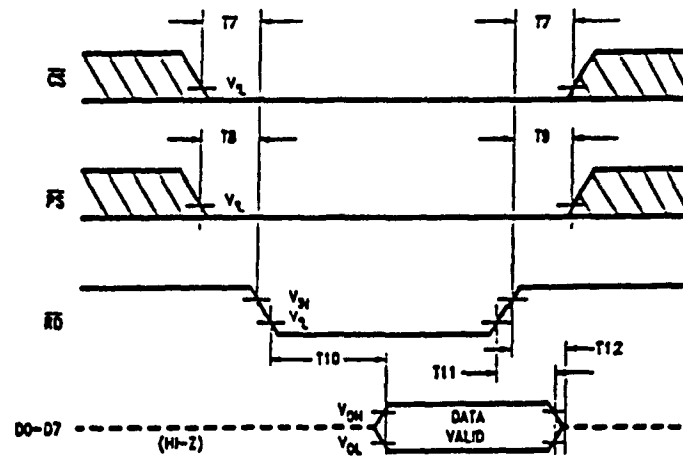


FIGURE 4. Status Byte Read Timing

TL/M/9218-6

AC Electrical Characteristics (Continued)

(V_{DD} and T_A per Operating Ratings; f_{CLK} = 8 MHz; C_{LOAD} = 50 pF, Input Test Signal t_r = t_f = 10 ns)

Timing Interval	T	Tested Limits		Units
		Min	Max	
COMMAND BYTE WRITE TIMING (See Figure 5)				
Chip-Select Setup/Hold Time	T7	0		ns
Port-Select Setup Time	T8	30		ns
Port-Select Hold Time	T9	30		ns
Busv Bit Delay	T13		(Note 2)	ns
WR Pulse Width	T14	100		ns
Write Data Setup Time	T15	50		ns
Write Data Hold Time	T16	100		ns
DATA WORD READ TIMING (See Figure 6)				
Chip-Select Setup/Hold Time	T7	0		ns
Port-Select Setup Time	T8	30		ns
Port-Select Hold Time	T9	30		ns
Read Data Access Time	T10		180	ns
Read Data Hold Time	T11	0		ns
RD High to Hi-Z Time	T12		180	ns
Busv Bit Delay	T13		(Note 2)	ns
Read Recovery Time	T17	120		ns
DATA WORD WRITE TIMING (See Figure 7)				
Chip-Select Setup/Hold Time	T7	0		ns
Port-Select Setup Time	T8	30		ns
Port-Select Hold Time	T9	30		ns
Busv Bit Delay	T13		(Note 2)	ns
WR Pulse Width	T14	100		ns
Write Data Setup Time	T15	50		ns
Write Data Hold Time	T16	120		ns
Write Recovery Time	T18	120		ns

Note 1: Absolute Maximum Ratings indicate limits beyond which damage to the device may occur. DC and AC electrical specifications do not apply when operating the device beyond the above Operating Ratings.

Note 2: In order to read the busy bit, the status byte must first be read. The time required to read the busy bit far exceeds the time the chip requires to set the busy bit. It is, therefore, impossible to test actual busy bit delay. The busy bit is guaranteed to be valid as soon as the user is able to read it.

Absolute Maximum Ratings (Note 1)

If Military/Aerospace specified devices are required, contact the National Semiconductor Sales Office/Distributors for availability and specifications.

Voltage at Any Pin with Respect to GND (Pin 14)	-0.3V to +7.0V
Ambient Storage Temperature	-65°C to +150°C
Lead Temperature (Soldering, 4 sec.)	260°C
Maximum Power Dissipation	550 mW
ESD Tolerance	
(C _{ZAP} = 120 pF, R _{ZAP} = 1.5k)	2000V

Operating Ratings

Temperature Range	-40°C < T _A < +85°C
Clock Frequency:	
LM628N-8, LM629N-8	1.0 MHz < f _{CLK} < 8.0 MHz
V _{DD} Range	4.5V < V _{DD} < 5.5V

DC Electrical Characteristics (V_{DD} and T_A per Operating Ratings; f_{CLK} = 6 MHz)

Symbol	Parameter	Conditions	Tested Limits		Units
			Min	Max	
I _{DD}	Supply Current	Outputs Open		100	mA
INPUT VOLTAGES					
V _{IH}	Logic 1 Input Voltage		2.0		V
V _{IL}	Logic 0 Input Voltage			0.8	V
I _{IN}	Input Currents	0 ≤ V _{IN} ≤ V _{DD}	-10	10	μA
OUTPUT VOLTAGES					
V _{OH}	Logic 1	I _{OH} = -1.6 mA	2.4		V
V _{OL}	Logic 0	I _{OH} = 1.6 mA		0.4	V
I _{OUT}	TRI-STATE Output Leakage Current	0 ≤ V _{OUT} ≤ V _{DD}	-10	10	μA

AC Electrical Characteristics

(V_{DD} and T_A per Operating Ratings; f_{CLK} = 6 MHz; C_{LOAD} = 50 pF; Input Test Signal t_r = t_f = 10 ns)

Timing Interval	T	Tested Limits		Units
		Min	Max	
ENCODER AND INDEX TIMING (See Figure 2)				
Motor-Phase Pulse Width	T1	2.67		μs
Dwell-Time Per State	T2	1.33		μs
Index Pulse Setup and Hold (Relative to A and B Low)	T3	0.0		μs
CLOCK AND RESET TIMING (See Figure 3)				
Clock Pulse Width	T4	78		ns
Clock Period	T5	166	1000	ns
Reset Pulse Width	T6	$\frac{8}{f_{CLK}}$		ns
STATUS BYTE READ TIMING (See Figure 4)				
Chip-Select Setup/Hold Time	T7	0		ns
Port-Select Setup Time	T8	30		ns
Port-Select Hold Time	T9	30		ns
Read Data Access Time	T10		180	ns
Read Data Hold Time	T11	0		ns
RD High to Hi-Z Time	T12		180	ns

Typical Applications (Continued)

Two approaches exist for avoiding this problem. If one is using hardware interrupts, they should be disabled at the host prior to issuing any LM628 command sequence, and re-enabled after each command sequence. The second approach is to avoid hardware interrupts and poll the LM628 status byte for "interrupt" status. The status byte always reflects the interrupt-condition status, independent of whether or not the interrupts have been masked.

Typical Host Computer/Processor Interface

The LM628 is interfaced with the host computer/processor via an 8-bit parallel bus. Figure 12 shows such an interface and a minimum system configuration.

As shown in Figure 12, the LM628 interfaces with the host data, address and control lines. The address lines are decoded to generate the LM628 CS input; the host address LSB directly drives the LM628 PS input. Figure 12 also shows an 8-bit DAC and an LM12 Power Op Amp interfaced to the LM628.

LM628 and High Performance Controller (HPC) Interface

Figure 13 shows the LM628 interfaced to a National HPC High Performance Controller. The delay and logic associated with the WR line is used to effectively increase the write-data hold time of the HPC (as seen at the LM628) by causing the WR pulse to rise early. Note that when clocking the HPC at 12 MHz, the CK2 output provides the required 6 MHz clock for the LM628. The 74LS245 is used to decrease the read-data hold time, which is necessary when interfacing to fast host busses.

Interfacing a 12-bit DAC

Figure 14 illustrates use of a 12-bit DAC with the LM628. The 74LS378 hex gated-D flip-flop and an inverter demultiplex the 12-bit output. DAC offset must be adjusted to minimize DAC linearity and monotonicity errors. Two methods exist for making this adjustment. If the DAC1210 has been socketed, remove it and temporarily connect a 15 k Ω resistor between Pins 11 and 13 of the DAC socket (Pins 2 and 6 of the LF358) and adjust the 25 k Ω potentiometer for 0V at Pin 6 of the LF358.

If the DAC is not removable, the second method of adjustment requires that the DAC1210 inputs be presented an all-zeros code. This can be arranged by commanding the appropriate move via the LM628, but with no feedback from the system encoder. When the all-zeros code is present, adjust the pot for 0V at Pin 6 of the LF358.

A Monolithic Linear Drive Using LM12 Power Op Amp

Figure 15 shows a motor-drive amplifier built using the LM12 Power Operational Amplifier. This circuit is very simple and can deliver up to 6A at 30V (using the LM12L/LM12CL). Resistors R1 and R2 should be chosen to set the gain to provide maximum output voltage consistent with maximum input voltage. This example provides a gain of 2.2, which allows for amplifier output saturation at $\pm 22V$ with a $\pm 10V$ input, assuming power supply voltages of $\pm 30V$. The amplifier gain should not be higher than necessary because the system is non-linear when saturated, and because gain should be controlled by the LM628. The LM12 can also be configured as a current driver, see 1987 Linear Databook, Vol. 1, p. 2-280.

Typical PWM Motor Drive Interfaces

Figure 16 shows an LM18298 dual full-bridge driver interfaced to the LM629 PWM outputs to provide a switch-mode power amplifier for driving small brush/commutator motors. Figure 17 shows an LM621 brushless motor commutator interfaced to the LM629 PWM outputs and a discrete device switch-mode power amplifier for driving brushless DC motors.

Incremental Encoder Interface

The incremental (position feedback) encoder interface consists of three lines: Phase A (Pin 2), Phase B (Pin 3), and Index (Pin 1). The index pulse output is not available on some encoders. The LM628 will work with both encoder types, but commands SIP and RDIP will not be meaningful without an index pulse (or alternative input for this input... be sure to be Pin 1 high if not used).

Some consideration is merited relative to use in high Gaussian-noise environments. If noise is added to the encoder inputs (either or both inputs) and is such that it is not sustained until the next encoder transition, the LM628 decoder logic will reject it. Noise that mimics quadrature counts or persists through encoder transitions must be eliminated by appropriate EMI design.

Simple digital "filtering" schemes merely reduce susceptibility to noise (there will always be noise pulses longer than the filter can eliminate). Further, any noise "filtering" scheme reduces decoder bandwidth. In the LM628 it was decided (since simple filtering does not eliminate the noise problem) to not include a noise filter in favor of offering maximum possible decoder bandwidth. Probably the most effective countermeasure to noise induction can be had by using balanced-line drivers and receivers on the encoder inputs. Figure 18 shows circuitry using the DS26LS31 and DS26LS32.

Data Reporting Commands (Continued)

There is no identification code; it is directly supported by the hardware and may be executed at any time. The single-byte status read is selected by placing CS, PS and RD at logic zero. See Table VII.

TABLE VII. Status Byte Bit Allocation

Bit Position	Function
Bit 7	Motor Off
Bit 6	Breakpoint Reached (Interrupt)
Bit 5	Excessive Position Error (Interrupt)
Bit 4	Wraparound Occurred (Interrupt)
Bit 3	Index Pulse Observed (Interrupt)
Bit 2	Trajectory Complete (Interrupt)
Bit 1	Command Error (Interrupt)
Bit 0	Busy Bit

Bit 7, the motor-off flag, is set to logic one when the motor drive output is off (at the half-scale, offset-binary code for zero). The motor is turned off by any of the following conditions: power-up reset, command RESET, excessive position error (if command LPES had been executed), or when command LTRJ is used to manually stop the motor via turning the motor off. Note that when bit 7 is set in conjunction with command LTRJ for producing a manual, motor-off stop, the actual setting of bit 7 does not occur until command STT is issued to affect the stop. Bit 7 is cleared by command STT, except as described in the previous sentence.

Bit 6, the breakpoint-reached interrupt flag, is set to logic one when the position breakpoint loaded via command SBPA or SBPR has been exceeded. The flag is functional independent of the host interrupt mask status. Bit 6 is cleared via command RSTL.

Bit 5, the excessive-position-error interrupt flag, is set to logic one when a position-error interrupt condition exists. This occurs when the error threshold loaded via command LPEI or LPES has been exceeded. The flag is functional independent of the host interrupt mask status. Bit 5 is cleared via command RSTL.

Bit 4, the wraparound interrupt flag, is set to logic one when a numerical "wraparound" has occurred. To "wraparound" means to exceed the position address space of the LM628, which could occur during velocity mode operation. If a wrap-around has occurred, then position information will be in error and this interrupt helps the user to ensure position data integrity. The flag is functional independent of the host interrupt mask status. Bit 4 is cleared via command RSTL.

Bit 3, the index-pulse acquired interrupt flag, is set to logic one when an index pulse has occurred (if command SIP had been executed) and indicates that the index position register has been updated. The flag is functional independent of the host interrupt mask status. Bit 3 is cleared by command RSTL.

Bit 2, the trajectory complete interrupt flag, is set to logic one when the trajectory programmed by the LTRJ command and initiated by the STT command has been completed. Because of overshoot or a limiting condition (such as commanding the velocity to be higher than the motor can achieve), the motor may not yet be at the final commanded position. This bit is the logical OR of bits 7 and 10 of the

Signals Register, see command RDSIGS below. The flag functions independently of the host interrupt mask status. Bit 2 is cleared via command RSTL.

Bit 1, the command-error interrupt flag, is set to logic one when the user attempts to read data when a write was appropriate (or vice versa). The flag is functional independent of the host interrupt mask status. Bit 1 is cleared via command RSTL.

Bit 0, the busy flag, is frequently tested by the user (via the host computer program) to determine the busy/ready status prior to writing and reading any data. Such writes and reads may be executed only when bit 0 is logic zero (not busy). Any command or data writes when the busy bit is high will be ignored. Any data reads when the busy bit is high will read the current contents of the I/O port buffers, not the data expected by the host. Such reads or writes (with the busy bit high) will not generate a command-error interrupt.

RDSIGS COMMAND: Read Signals Register

Command Code: 0C Hex
Bytes Read: Two
Data Range: See Text
Executable During Motion: Yes

The LM628 internal "signals" register may be read using this command. The first byte read is the more significant. The less significant byte of this register (with the exception of bit 0) duplicates the status byte. See Table VIII.

TABLE VIII. Signals Register Bit Allocation

Bit Position	Function
Bit 15	Host Interrupt
Bit 14	Acceleration Loaded (But Not Updated)
Bit 13	UDF Executed (But Filter Not yet Updated)
Bit 12	Forward Direction
Bit 11	Velocity Mode
Bit 10	On Target
Bit 9	Turn Off upon Excessive Position Error
Bit 8	Eight-Bit Output Mode
Bit 7	Motor Off
Bit 6	Breakpoint Reached (Interrupt)
Bit 5	Excessive Position Error (Interrupt)
Bit 4	Wraparound Occurred (Interrupt)
Bit 3	Index Pulse Acquired (Interrupt)
Bit 2	Trajectory Complete (Interrupt)
Bit 1	Command Error (Interrupt)
Bit 0	Acquire Next Index (SIP Executed)

Bit 15, the host interrupt flag, is set to logic one when the host interrupt output (Pin 17) is logic one. Pin 17 is set to logic one when any of the six host interrupt conditions occur (if the corresponding interrupt has not been masked). Bit 15 (and Pin 17) are cleared via command RSTL.

Bit 14, the acceleration-loaded flag, is set to logic one when acceleration data is written to the LM628. Bit 13 is cleared by the STT command.

Bit 13, the UDF-executed flag, is set to logic one when the UDF command is executed. Because bit 12 is cleared at the end of the sampling interval in which it has been set, this signal is very short-lived and probably not very profitable for monitoring.

Data Reporting Commands (Continued)

Bit 12, the forward direction flag, is meaningful only when the LM628 is in velocity mode. The bit is set to logic one to indicate that the desired direction of motion is "forward"; zero indicates "reverse" direction. Bit 12 is set and cleared via command LTRJ. The actual setting and clearing of bit 12 does not occur until command STT is executed.

Bit 11, the velocity mode flag, is set to logic one to indicate that the user has selected (via command LTRJ) velocity mode. Bit 11 is cleared when position mode is selected (via command LTRJ). The actual setting and clearing of bit 11 does not occur until command STT is executed.

Bit 10, the on-target flag, is set to logic one when the trajectory generator has completed its functions for the last-issued STT command. Bit 10 is cleared by the next STT command.

Bit 9, the turn-off on-error flag, is set to logic one when command LPES is executed. Bit 9 is cleared by command LPEI.

Bit 8, the 8-bit output flag, is set to logic one when the LM628 is reset, or when command PORT8 is executed. Bit 8 is cleared by command PORT12.

Bits 0 through 7 replicate the status byte (see Table VII), with the exception of bit 0. Bit 0, the acquire next index flag, is set to logic one when command SIP is executed; it then remains set until the next index pulse occurs.

RDIP COMMAND: Read Index Position

Command Code: 09 Hex
Bytes Read: Four
Data Range: C0000000 to 3FFFFFFF Hex
Executable During Motion: Yes

This command reads the position recorded in the index register. Reading the index register can be part of a system error checking scheme. Whenever the SIP command is executed, the new index position minus the old index position, divided by the incremental encoder resolution (encoder lines times four), should always be an integral number. The RDIP command facilitates acquiring these data for host-based calculations. The command can also be used to identify/verify home or some other special position. The bytes are read in most-to-least significant order.

RDDP COMMAND: Read Desired Position

Command Code: 08 Hex
Bytes Read: Four
Data Range: C0000000 to 3FFFFFFF Hex
Executable During Motion: Yes

This command reads the desired (current) position output of the profile generator. This is the "set-point" input to the loop summing junction. The bytes are read in most-to-least significant order.

RDRP COMMAND: Read Real Position

Command Code: 0A Hex
Bytes Read: Four
Data Range: C0000000 to 3FFFFFFF Hex
Executable During Motion: Yes

This command reads the current actual position of the motor. This is the feedback input to the loop summing junction. The bytes are read in most-to-least significant order.

RDDV COMMAND: Read Desired Velocity

Command Code: 07 Hex
Bytes Read: Four
Data Range: 00000000 to 3FFFFFFF Hex
Executable During Motion: Yes

This command reads the desired (instantaneous) velocity as used to generate the position profile. The first byte read is the more significant. Note that the 16 least significant bits of the result represent fractional velocity; therefore, it is necessary to divide the resulting output by 65,536 (shift right 16 bits) to relate it to integer velocity values.

RDRV COMMAND: Read Real Velocity

Command Code: 0B Hex
Bytes Read: Two
Data Range: 8000 to 7FFF Hex. See Text
Executable During Motion: Yes

This command reads the integer portion (the more-significant two bytes) of the actual (instantaneous) velocity of the motor. The result must be multiplied by 65,536 (2^{16}) to be scaled for comparison with the result obtained by executing command RDDV or for comparison with the input value. There is no fractional portion in the actual velocity result. The first byte read is the more significant.

RDSUM COMMAND: Read Integration-Term SUMmation Value

Command Code: 0D Hex
Bytes Read: Two
Data Range: 00000 Hex to \pm the Current Value of the Integration Limit
Executable During Motion: Yes

This command reads the value to which the integration term has accumulated. The ability to read this value may be helpful in initially or adaptively tuning the system.

Typical Applications

Programming LM628 Host Handshaking (Interrupts)

A few words regarding the LM628 host handshaking will be helpful to the system programmer. As indicated in various portions of the above text, the LM628 handshakes with the host computer in two ways: via the host interrupt output (Pin 17), or via polling the status byte for "interrupt" conditions. When the hardware interrupt is used, the status byte is also read and parsed to determine which of six possible conditions caused the interrupt.

When using the hardware interrupt it is very important that the host interrupt service routine does not interfere with a command sequence which might have been in progress when the interrupt occurred. If the host interrupt service routine were to issue a command to the LM628 while it is in the middle of an ongoing command sequence, the ongoing command will be aborted (which could be detrimental to the application).

T11450210-10

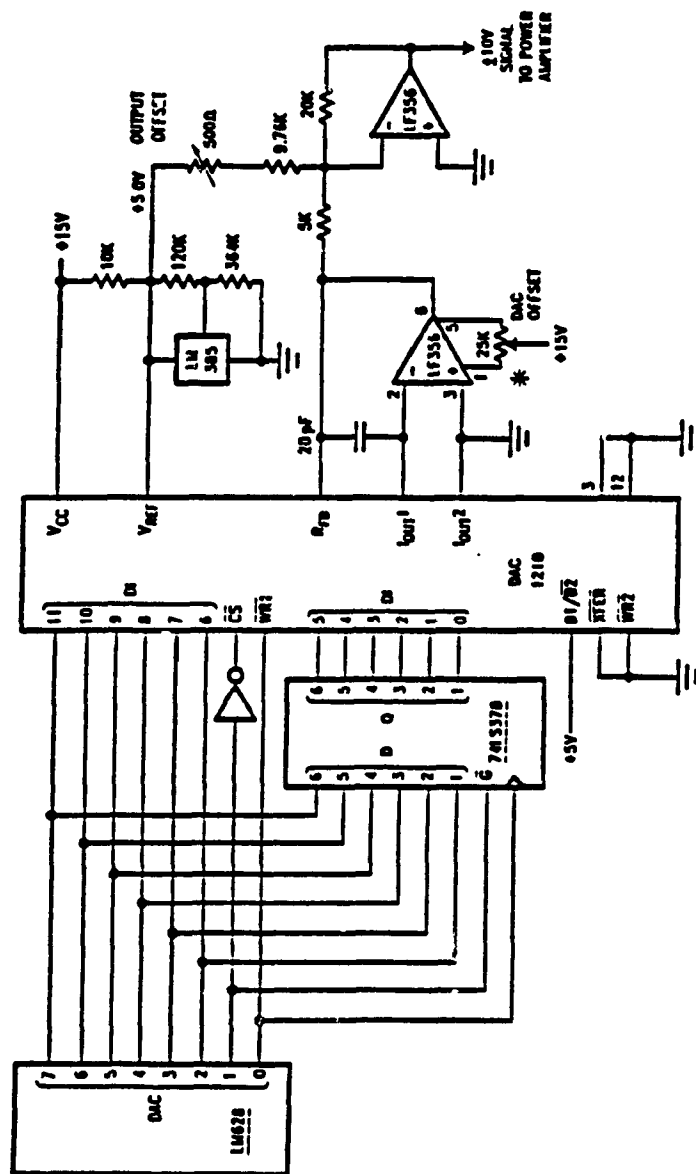


FIGURE 14. Interleaving a 12-Bit DAC and LM528

*DAC offset must be adjusted to minimize DAC linearity and monotonicity errors. See text.

Typical Applications (Continued)

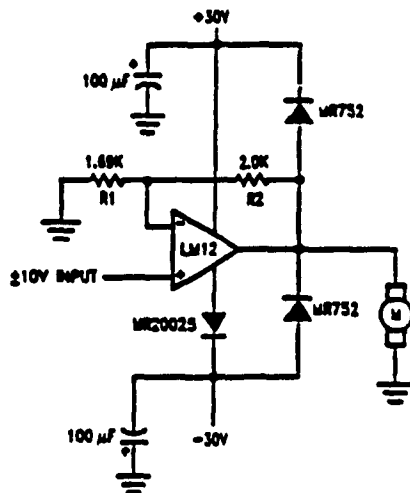


FIGURE 15. Driving a Motor with the LM12 Power Op Amp

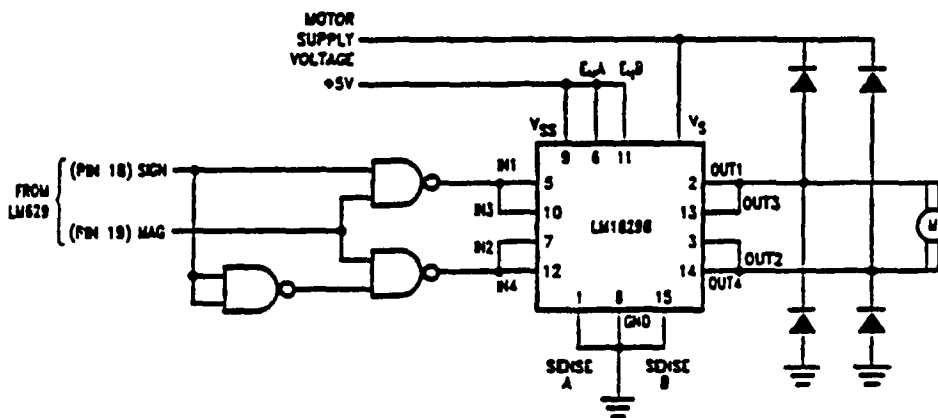


FIGURE 16. PWM Drive for Brush/Commutator Motors

Typical Applications (Continued)

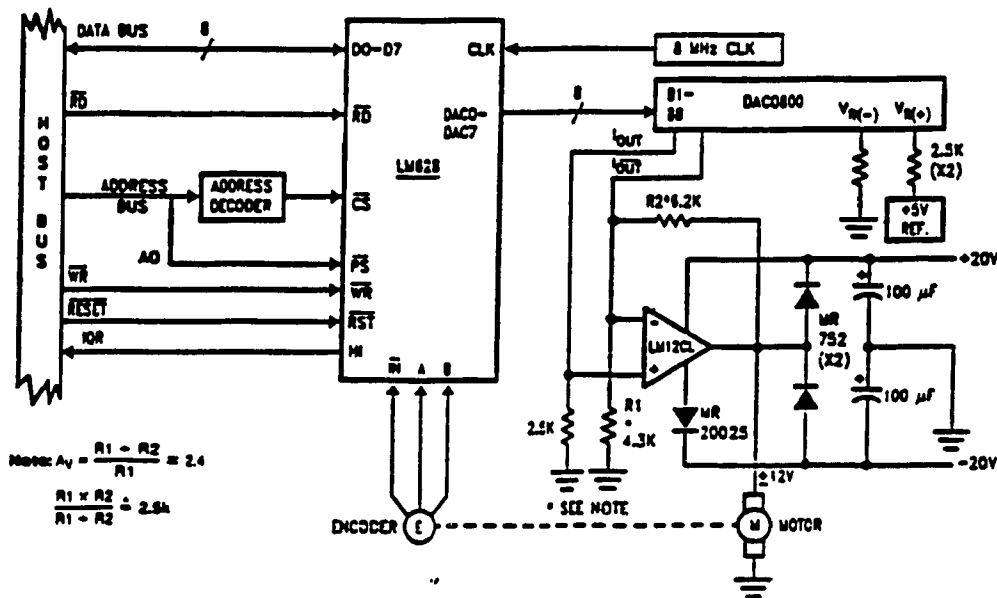


FIGURE 12. Host Interface and Minimum System Configuration

TJH/R219-14

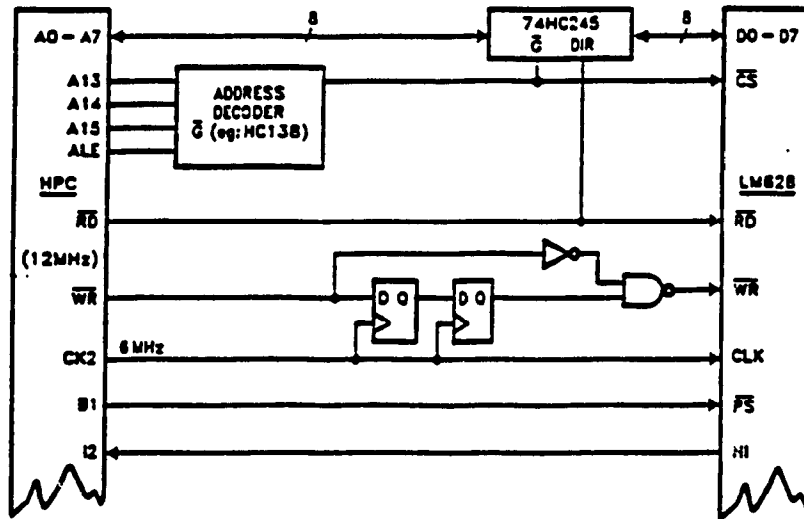


FIGURE 13. LM628 and HPC Interface

TLW/2219-12

Trajectory Control Commands (Continued)

The trajectory control parameters which are written to the LM628 to control motion are: acceleration, velocity, and position. In addition, indications as to whether these three parameters are to be considered as absolute or relative inputs, selection of velocity mode and direction, and manual stopping mode selection and execution are programmable via this command. After writing the command code, the first two data bytes that are written specify which parameter(s) is/are being changed. The first byte written is the more significant. Thus the two data bytes constitute a trajectory control word that informs the LM628 as to the nature and number of any following data bytes. See Table VI.

TABLE VI. Trajectory Control Word Bit Allocation

Bit Position	Function
Bit 15	Not Used
Bit 14	Not Used
Bit 13	Not Used
Bit 12	Forward Direction (Velocity Mode Only)
Bit 11	Velocity Mode
Bit 10	Stop Smoothly (Decelerate as Programmed)
Bit 9	Stop Abruptly (Maximum Deceleration)
Bit 8	Turn Off Motor (Cuts Off Zero Drive)
Bit 7	Not Used
Bit 6	Not Used
Bit 5	Acceleration Will Be Loaded
Bit 4	Acceleration Data is Relative
Bit 3	Velocity Will Be Loaded
Bit 2	Velocity Data is Relative
Bit 1	Position Will Be Loaded
Bit 0	Position Data is Relative

Bit 12 determines the motor direction when in the velocity mode. A logic one indicates forward direction. This bit has no effect when in position mode.

Bit 11 determines whether the LM628 operates in velocity mode (Bit 11 logic one) or position mode (Bit 11 logic zero). Bits 8 through 10 are used to select the method of manually stopping the motor: bit 8 is set to one to stop the motor via turning off the motor drive output (outputting the appropriate offset-binary code to apply zero drive to the motor); bit 9 is set to one to stop the motor abruptly (at maximum deceleration, via setting the target position equal to the current position); and bit 10 is set to one to stop the motor smoothly using the current user-programmed acceleration value (the normal way of manually stopping the motor). Bits 8 through 10 are to be used exclusively; only one bit should be a logic one at any time.

Bits 0 through 5 inform the LM628 as to whether any or all of the trajectory controlling parameters are about to be written, and whether the data should be interpreted as absolute or relative. The user may choose to update any or all (or none) of the trajectory parameters. Those chosen for updating are so indicated by logic one(s) in the corresponding bit position(s). Any parameter may be changed while the motor is in motion; however, if acceleration is changed then the next STT command must not be issued until the LM628 has completed the current move or has been manually stopped.

The data bytes specified by and immediately following the trajectory control word are written in pairs which comprise 16-bit words. Each data item (parameter) requires two 16-bit words; the word and byte order is most-to-least significant.

The order of sending the parameters to the LM628 corresponds to the descending order shown in the above description of the trajectory control word; i.e., beginning with acceleration, then velocity, and finally position.

Acceleration and velocity are 32 bits, positive only, but range only from 0 (00000000 hex) to $[2^{30}] - 1$ (3FFFFFF hex). The bottom 16 bits of both acceleration and velocity are scaled as fractional data; therefore, the least-significant integer data bit for these parameters is bit 16 (where the bits are numbered 0 through 31). To determine the coding for a given velocity, for example, one multiplies the desired velocity (in counts per sample interval) times 65,536 and converts the result to binary. The units of acceleration are counts per sample per sample. Position is a signed, 32-bit integer, but ranges only from $-[2^{30}]$ (C0000000 hex) to $[2^{30}] - 1$ (3FFFFFF hex).

The required data is written to the primary buffers of a double-buffered scheme by the above described operations; it is not transferred to the secondary (working) registers until the STT command is executed. This fact can be used advantageously; the user can input numerous data ahead of their actual use. This simple pipeline effect can relieve potential host computer data communications bottlenecks, and facilitates easier synchronization of multiple-axis controls.

Before using LTRJ to issue a new acceleration value, a "motor off" command must first be executed (LTRJ command with bit 8 of the Trajectory Control Word set). This procedure is only necessary if the acceleration value is being changed.

STT COMMAND: Start Motion Control

Command Code: 01 Hex
Data Bytes: None
Executable During Motion: Yes, if acceleration has not been changed

The STT command is used to execute the desired trajectory, the specifics of which have been programmed via the LTRJ command. Synchronization of multi-axis control (to within one sample interval) can be arranged by loading the required trajectory parameters for each (and every) axis and then simultaneously issuing a single STT command to all axes. This command may be executed at any time, unless the acceleration value has been changed and a trajectory has not been completed or the motor has not been manually stopped. If STT is issued during motion and acceleration has been changed, a command error interrupt will be generated and the command will be ignored.

Data Reporting Commands

The following seven LM628 user commands are used to obtain data from various registers in the LM628. Status, position, and velocity information are reported. With the exception of ROSTAT, the data is read from the LM628 data port after first writing the corresponding command to the command port.

ROSTAT COMMAND: Read STATUS Byte

Command Code: None
Byte Read: One
Data Range: See Text
Executable During Motion: Yes

The ROSTAT command is really not a command, but is listed with the other commands because it is used very frequently to control communications with the host computer.

Theory of Operation (Continued)

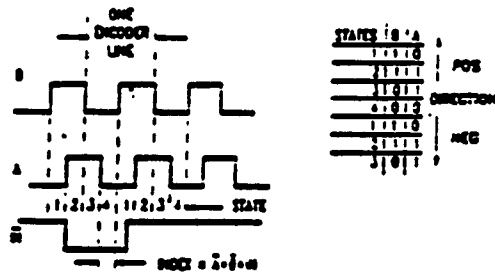


FIGURE 9. Quadrature Encoder Signals

TLW9219-11

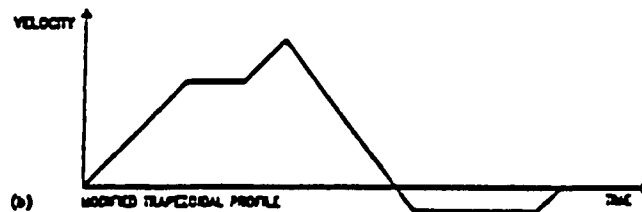
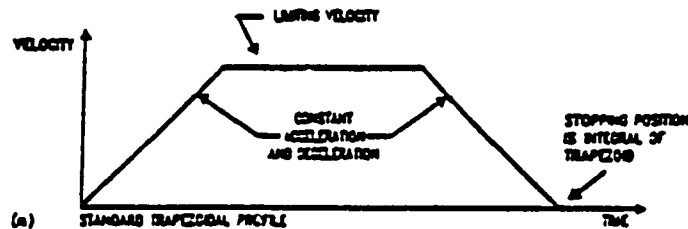


FIGURE 10. Typical Velocity Profiles

TLW9219-12

VELOCITY PROFILE (TRAJECTORY) GENERATION

The trapezoidal velocity profile generator computes the desired position of the motor versus time. In the position mode of operation, the host processor specifies acceleration, maximum velocity, and final position. The LM629 uses this information to affect the move by accelerating as specified until the maximum velocity is reached or until deceleration must begin to stop at the specified final position. The deceleration rate is equal to the acceleration rate. At any time during the move the maximum velocity and/or the target position may be changed, and the motor will accelerate or decelerate accordingly. Figure 10 illustrates two typical trapezoidal velocity profiles. Figure 10 (a) shows a simple trapezoid, while Figure 10 (b) is an example of what the trajectory looks like when velocity and position are changed at different times during the move.

When operating in the velocity mode, the motor accelerates to the specified velocity at the specified acceleration rate and maintains the specified velocity until commanded to stop. The velocity is maintained by advancing the desired position at a constant rate. If there are disturbances to the motion during velocity mode operation, the long-time average velocity remains constant. If the motor is unable to maintain the specified velocity (which could be caused by a locked rotor, for example), the desired position will continue to be increased, resulting in a very large position error. If this

condition goes undetected, and the impeding force on the motor is subsequently released, the motor could reach a very high velocity in order to catch up to the desired position (which is still advancing as specified). This condition is easily detected; see commands LPEI and LPES.

All trajectory parameters are 32-bit values. Position is a signed quantity. Acceleration and velocity are specified as 16-bit, positive-only integers having 16-bit fractions. The integer portion of velocity specifies how many counts per sampling interval the motor will traverse. The fractional portion designates an additional fractional count per sampling interval. Although the position resolution of the LM629 is limited to integer counts, the fractional counts provide increased average velocity resolution. Acceleration is treated in the same manner. Each sampling interval the commanded acceleration value is added to the current desired velocity to generate a new desired velocity (unless the command velocity has been reached).

One determines the trajectory parameters for a desired move as follows. If, for example, one has a 500-line shaft encoder, desires that the motor accelerate at one revolution per second per second until it is moving at 600 rpm, and then decelerate to a stop at a position exactly 100 revolutions from the start, one would calculate the trajectory parameters as follows:

Interrupt Control Commands (Continued)

SBPA COMMAND:

Command Code: 20 Hex
Data Bytes: Four
Data Range: C0000000 to 3FFFFFFF Hex
Executable During Motion: Yes

This command enables the user to set a breakpoint in terms of absolute position. Bit 6 of the status byte is set to logic high when the breakpoint position is reached. This condition is useful for signaling trajectory and/or filter parameter updates. The user can also arrange to have the LM628 interrupt the host to signify that a breakpoint position has been reached. See the descriptions for commands MSKI and RSTI.

SBPR COMMAND:

Command Code: 21 Hex
Data Bytes: Four
Data Range: See Text
Executable During Motion: Yes

This command enables the user to set a breakpoint in terms of relative position. As with command SBPA, bit 6 of the status byte is set to logic high when the breakpoint position (relative to the current commanded target position) is reached. The relative breakpoint input value must be such that when this value is added to the target position the result remains within the absolute position range of the system (C0000000 to 3FFFFFFF hex). This condition is useful for signaling trajectory and/or filter parameter updates. The user can also arrange to have the LM628 interrupt the host to signify that a breakpoint position has been reached. See the descriptions for commands MSKI and RSTI.

MSKI COMMAND: MaSK Interrupts

Command Code: 1C Hex
Data Bytes: Two
Data Range: See Text
Executable During Motion: Yes

The MSKI command lets the user determine which potential interrupt condition(s) will interrupt the host. Bits 1 through 6 of the status byte are indicators of the six conditions which are candidates for host interrupt(s). When interrupted, the host then reads the status byte to learn which condition(s) occurred. Note that the MSKI command is immediately followed by two data bytes. Bits 1 through 6 of the second (less significant) byte written determine the masked/unmasked status of each potential interrupt. Any zero(s) in this 6-bit field will mask the corresponding interrupt(s); any one(s) enable the interrupt(s). Other bits comprising the two bytes have no effect. The mask controls only the host interrupt process; reading the status byte will still reflect the actual conditions independent of the mask byte. See Table III.

TABLE III. Mask and Reset Bit Allocations for Interrupts

Bit Position	Function
Bits 15 thru 7	Not Used
Bit 6	Breakpoint Interrupt
Bit 5	Position-Error Interrupt
Bit 4	Wrap-Around Interrupt
Bit 3	Index-Pulse Interrupt
Bit 2	Trajectory-Complete Interrupt
Bit 1	Command-Error Interrupt
Bit 0	Not Used

RSTI COMMAND: ReSeT Interrupts

Command Code: 1D Hex
Data Bytes: Two
Data Range: See Text
Executable During Motion: Yes

When one of the potential interrupt conditions of Table III occurs, command RSTI is used to reset the corresponding interrupt flag bit in the status byte. The host may reset one or all flag bits. Resetting them one at a time allows the host to service them one at a time according to a priority programmed by the user. As in the MSKI command, bits 1 through 6 of the second (less significant) byte correspond to the potential interrupt conditions shown in Table III. Also see description of RDCSTAT command. Any zero(s) in this 6-bit field reset the corresponding interrupt(s). The remaining bits have no effect.

Filter Control Commands

The following two LM628 user commands are used for setting the derivative-term sampling interval, for adjusting the filter parameters as required to tune the system, and to control the timing of these system changes.

LFIL COMMAND: Load FiLter Parameters

Command Code: 1E Hex
Data Bytes: Two to Ten
Data Ranges ...
Filter Control Word: See Text
Filter Coefficients: 0000 to 7FFF Hex (Pos Only)
Integration Limit: 0000 to 7FFF Hex (Pos Only)

Executable During Motion: Yes

The filter parameters (coefficients) which are written to the LM628 to control loop compensation are: k_p , k_i , k_d , and I (integration limit). The integration limit (I) constrains the contribution of the integration term

$$\left[k_i \cdot \sum_{x=0}^n e(x) \right]$$

(see Eq. 1) to values equal to or less than a user-defined maximum value; this capability minimizes integral or reset "wind-up" (an overshooting effect of the integral action). The positive-only input value is compared to the absolute

Filter Control Commands (Continued)

magnitude of the integration term; when the magnitude of integration term value exceeds *i*, the *i* value (with appropriate sign) is substituted for the integration term value.

The derivative-term sampling interval is also programmable via this command. After writing the command code, the first two data bytes that are written specify the derivative-term sampling interval and which of the four filter parameters is/are to be written via any forthcoming data bytes. The first byte written is the more significant. Thus the two data bytes constitute a filter control word that informs the LM628 as to the nature and number of any following data bytes. See Table IV.

TABLE IV. Filter Control word Bit Allocation

Bit Position	Function
Bit 15	Derivative Sampling Interval Bit 7
Bit 14	Derivative Sampling Interval Bit 6
Bit 13	Derivative Sampling Interval Bit 5
Bit 12	Derivative Sampling Interval Bit 4
Bit 11	Derivative Sampling Interval Bit 3
Bit 10	Derivative Sampling Interval Bit 2
Bit 9	Derivative Sampling Interval Bit 1
Bit 8	Derivative Sampling Interval Bit 0
Bit 7	Not Used
Bit 6	Not Used
Bit 5	Not Used
Bit 4	Not Used
Bit 3	Loading <i>k_p</i> Data
Bit 2	Loading <i>k_i</i> Data
Bit 1	Loading <i>k_d</i> Data
Bit 0	Loading <i>i</i> Data

Bits 8 through 15 select the derivative-term sampling interval. See Table V. The user must locally save and restore these bits during successive writes of the filter control word. Bits 4 through 7 of the filter control word are not used.

Bits 0 to 3 inform the LM628 as to whether any or all of the filter parameters are about to be written. The user may choose to update any or all (or none) of the filter parameters. Those chosen for updating are so indicated by logic one(s) in the corresponding bit position(s) of the filter control word.

The data bytes specified by and immediately following the filter control word are written in pairs to compose 16-bit words. The order of sending the data words to the LM628 corresponds to the descending order shown in the above description of the filter control word; i.e., beginning with *k_p*, then *k_i*, *k_d* and *i*. The first byte of each word is the more-significant byte. Prior to writing a word (byte pair) it is necessary to check the busy bit in the status byte for readiness. The required data is written to the primary buffers of a double-buffered scheme by the above described operations; it is not transferred to the secondary (working) registers until the UDF command is executed. This fact can be used advantageously; the user can input numerous data ahead of their actual use. This simple pipeline effect can relieve potential host computer data communications bottlenecks, and facilitates easier synchronization of multiple-axis controls.

UDF COMMAND: Update Filter

Command Code: 04 Hex
Data Bytes: None
Executable During Motion: Yes

The UDF command is used to update the filter parameters, the specifics of which have been programmed via the LFIL command. Any or all parameters (derivative-term sampling interval, *k_p*, *k_i*, *k_d*, and/or *i*) may be changed by the appropriate command(s), but command UDF must be executed to affect the change in filter tuning. Filter updating is synchronized with the calculations to eliminate erratic or spurious behavior.

Trajectory Control Commands

The following two LM628 user commands are used for setting the trajectory control parameters (position, velocity, acceleration), mode of operation (position or velocity), and direction (velocity mode only) as required to describe a desired motion or to select the mode of a manually directed stop, and to control the timing of these system changes.

LTRJ COMMAND: Load TRAJectory Parameters

Command Code: 1F Hex
Data Bytes: Two to Fourteen
Data Ranges . . .
Trajectory Control Word: See Text
Position: C0000000 to 3FFFFFFF Hex
Velocity: 00000000 to 3FFFFFFF Hex (Pos Only)
Acceleration: 00000000 to 3FFFFFFF Hex (Pos Only)
Executable During Motion: Conditionally, See Text

TABLE V. Derivative-Term Sampling Interval Selection Codes

	Bit Position								Selected Derivative Sampling Interval
	15	14	13	12	11	10	9	8	
	0	0	0	0	0	0	0	0	341.33 μ s
	0	0	0	0	0	0	0	1	682.66 μ s
	0	0	0	0	0	0	1	0	1024.00 μ s
	0	0	0	0	0	0	1	1	1365.33 μ s, etc. . .
thru	1	1	1	1	1	1	1	1	87,381.33 μ s

Note: Sampling intervals shown are when using a 4.0 MHz clock. The 341.33 corresponds to 2048/6 MHz; sample intervals must be scaled for other clock frequencies.